Library Declaration and Deposit Agreement

1. STUDENT DETAILS

Please complete the following:

Full name: Andrew Timothy Grigg

 University ID number: 0513932

2. THESIS DEPOSIT

2.1 I understand that under my registration at the University, I am required to deposit my thesis with the University in BOTH hard copy and in digital format. The digital version should normally be saved as a single pdf file.

2.2 The hard copy will be housed in the University Library. The digital version will be deposited in the University's Institutional Repository (WRAP). Unless otherwise indicated (see 2.3 below) this will be made openly accessible on the Internet and will be supplied to the British Library to be made available online via its Electronic Theses Online Service (EThOS) service.
[At present, theses submitted for a Master's degree by Research (MA, MSc, LLM, MS or MMedSci) are not being deposited in WRAP and not being made available via EthOS. This may change in future.]

2.3 In exceptional circumstances, the Chair of the Board of Graduate Studies may grant permission for an embargo to be placed on public access to the hard copy thesis for a limited period. It is also possible to apply separately for an embargo on the digital version. (Further information is available in the *Guide to Examinations for Higher Degrees by Research.*)

2.4 *If you are depositing a thesis for a Master's degree by Research, please complete section (a) below. For all other research degrees, please complete both sections (a) and (b) below:*

(a)   Hard Copy

I hereby deposit a hard copy of my thesis in the University Library to be made publicly available to readers (please delete as appropriate) EITHER immediately OR after an embargo period of ....……. months/years as agreed by the Chair of the Board of Graduate Studies.

I agree that my thesis may be photocopied.   YES / NO (*Please delete as appropriate*)

(b)   Digital Copy

I hereby deposit a digital copy of my thesis to be held in WRAP and made available via EThOS.

Please choose one of the following options:

EITHER   My thesis can be made publicly available online.   YES / NO (*Please delete as appropriate*)

OR   My thesis can be made publicly available only after…..[date] (Please give date)
                                                                                                    YES / NO (*Please delete as appropriate*)

OR   My full thesis cannot be made publicly available online but I am submitting a   separately identified   additional, abridged version that can be made available online.
                                                                                                    YES / NO (*Please delete as appropriate*)

OR   My thesis cannot be made publicly available online.   YES / NO (*Please delete as appropriate*)

3. **GRANTING OF NON-EXCLUSIVE RIGHTS**

Whether I deposit my Work personally or through an assistant or other agent, I agree to the following:

Rights granted to the University of Warwick and the British Library and the user of the thesis through this agreement are non-exclusive. I retain all rights in the thesis in its present version or future versions. I agree that the institutional repository administrators and the British Library or their agents may, without changing content, digitise and migrate the thesis to any medium or format for the purpose of future preservation and accessibility.

4. **DECLARATIONS**

(a)   I DECLARE THAT:

- I am the author and owner of the copyright in the thesis and/or I have the authority of the authors and owners of the copyright in the thesis to make this agreement. Reproduction of any part of this thesis for teaching or in academic or other forms of publication is subject to the normal limitations on the use of copyrighted materials and to the proper and full acknowledgement of its source.

- The digital version of the thesis I am supplying is the same version as the final, hard-bound copy submitted in completion of my degree, once any minor corrections have been completed.

- I have exercised reasonable care to ensure that the thesis is original, and does not to the best of my knowledge break any UK law or other Intellectual Property Right, or contain any confidential material.

- I understand that, through the medium of the Internet, files will be available to automated agents, and may be searched and copied by, for example, text mining and plagiarism detection software.

(b)   IF I HAVE AGREED (in Section 2 above) TO MAKE MY THESIS PUBLICLY AVAILABLE DIGITALLY, I ALSO DECLARE THAT:

- I grant the University of Warwick and the British Library a licence to make available on the Internet the thesis in digitised format through the Institutional Repository and through the British Library via the EThOS service.

- If my thesis does include any substantial subsidiary material owned by third-party copyright holders, I have sought and obtained permission to include it in any version of my thesis available in digital format and that this permission encompasses the rights that I have granted to the University of Warwick and to the British Library.

5. **LEGAL INFRINGEMENTS**

I understand that neither the University of Warwick nor the British Library have any obligation to take legal action on behalf of myself, or other rights holders, in the event of infringement of intellectual property rights, breach of contract or of any other right, in the thesis.

Please sign this agreement and return it to the Graduate School Office when you submit your thesis.

Student's signature: ....… Date: 9th October 2013
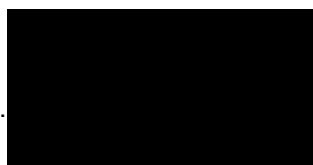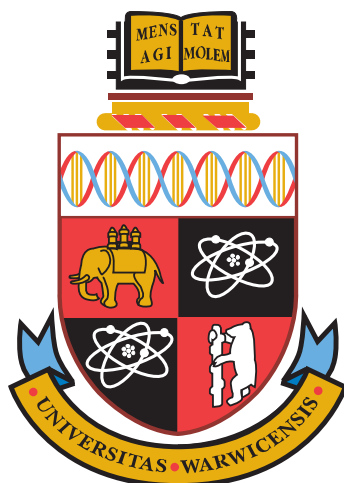
The structure of divalent and trivalent cation substituted β-tricalcium phosphate

by

Andrew Timothy Grigg

Thesis

Submitted to the University of Warwick

for the degree of

Doctor of Philosophy

Department of Physics

October MMXIII

THE UNIVERSITY OF
WARWICK

CONTENTS

LIST OF TABLES

LIST OF FIGURES

ACKNOWLEDGMENTS

DECLARATION AND PUBLISHED WORK

I declare that the work presented in this thesis is my own except where stated otherwise, and was carried out entirely at the University of Warwick, during the period of September 2009 to March 2013, under the supervision of Dr Diane Holland. The research reported here has not been submitted, either wholly or in part, in this or any other academic institution for admission to a higher degree.

Some parts of the work reported and other work not reported in this thesis will be submitted for publication in due course.

ABSTRACT

Current methods of nuclear waste disposal are not suitable for the immobilisation of novel defence-based waste due to the high halogen content resulting from pyrochemical reprocessing. The objective of this thesis was to investigate β-tricalcium phosphate (β-TCP, $Ca_3(PO_4)_2$) encapsulated in a sodium aluminoborophosphate glass (NABP) matrix as a potential host for this waste using a variety of structural probes. Samples were prepared to determine the structural changes in β-TCP as components of the simulated waste streams were substituted into the material. Zn, Mg, Al, and Ga incorporation was investigated.

A combination of X-ray and neutron diffraction was used to determine the changes in long-range order as a function of Zn and Mg substitution up to 13 % and 25 % cation substitution respectively. Both Zn and Mg substitution caused a contraction of the unit cell up to complete substitution of the Ca(5) site, at which point the contraction ceased. Under further substitution on the Ca(4) site, the *a* lattice parameter continued to decrease, while the *c* lattice parameter *increased*, resulting in an unchanged unit cell volume. Evidence of tricalcium trimagnesium phosphate second phase was observed for the Mg-based compositions above $Ca_{2.8}Mg_{0.2}(PO_4)_2$, as has been previously documented, however single phase samples were observed for all Zn-based compositions, in contrast to previous studies. ^{31}P NMR was used to confirm this Ca(5)-Ca(4) substitution model for the Zn-based β-TCP compositions by tightly constrained simulations as a function of composition.

A combination of solid-state NMR techniques were used to identify the substitution mechanism of Al and Ga in β-TCP up to the composition $Ca_9M(PO_4)_7$, where M is Al or Ga respectively. The ^{31}P and ^{43}Ca NMR spectra were simulated as with the divalent cations mentioned above to determine the origin of each resonance in the spectra. Subsequently, ^{27}Al-$\{^{31}P\}$ and ^{71}Ga-$\{^{31}P\}$ R^3-HMQC experiments were performed to explicitly identify substitution on the Ca(5) site only.

Studies were also performed to model the NABP:β-TCP interface formed as a result of the encapsulation process, for both pure β-TCP and Ga-substituted β-TCP. To simulate the range of compositions expected at this interface, calcium phosphate and NABP preparations were mixed in proportions from 10 wt.% to 80 wt.% (Ga-substituted) β-TCP. ^{31}P NMR and Raman spectroscopy showed a progressive depolymerisation of the phosphorus network, consistent with the replacement of Al^{3+} and Na^+ with Ca^{2+}. The Al^{3+} was shown to exist primarily in a 4 coordinated state, showing a tendency to exist within the phosphorus network, whereas ^{11}B NMR showed the B to move from a 4 coordinated site in NABP to a B-rich 3 coordinated environment.

Differential thermal analysis showed an increase in the temperature of the two recrystallisation events as a function of both β-TCP and Ga-substituted β-TCP. Studies of the phases present after recrystallisation of the pure β-TCP-based samples showed calcium sodium phosphate and Na Al co-substituted β-TCP for the lower and higher crystallisation temperatures with β-TCP incorporation. For the Ga-containing samples, Na Al Ga co-substituted β-TCP was observed for both crystallisation temperatures. Critically, Ga was shown to displace Al in the β-TCP phase.

GLOSSARY AND ABBREVIATIONS

DTA	Differential thermal analysis
EDX	Energy dispersive X-ray (spectroscopy)
EFG	Electric field gradient
FWHM	Full width at half maximum
HLW	High level waste
HILW	Halogenated intermediate level waste
ILW	Intermediate level waste
LLRN	Long-lived radionuclide
LLW	Low level waste
MAS	Magic angle spinning
N_4	The fraction of boron units that are four-coordinated
NABP	Sodium aluminoborophosphate
ND	Neutron diffraction
NMR	Nuclear magnetic resonance
nn	Nearest neighbour
nnn	Next-nearest neighbour
Q^n	[PO_4] tetrahedra with n bridging oxygen atoms
R^3-HMQC	Rotary resonance recoupled heteronuclear multiple quantum coherence
SEM	Scanning electron microscope
SLRN	Short-lived radionuclide
β-TCP	Beta-tricalcium phosphate
β-TCAP	Aluminium substituted β-TCP
β-TCGP	Gallium substituted β-TCP
β-TCMP	Magnesium substituted β-TCP
β-TCZP	Zinc substituted β-TCP
T_x	Crystallisation temperature
T_g	Glass transition temperature
$T(r)$	Total correlation function
t-o-f	Time of flight
XRD	X-ray diffraction

CHAPTER 1

INTRODUCTION

"Treat the earth well: it was not given to you by your parents, it was loaned to you by your children."

— Native American Proverb

1.1 Overview

Since the advent of the nuclear age, waste radioactive material has been produced in ever increasing quantities. Despite the great leaps forward in creating both energy and destruction with nuclear material, there is comparatively little knowledge of how to dispose of the resulting waste. Various methods have been investigated previously, including borosilicate and phosphate glasses, glass-ceramics and crystalline ceramics, but as the problems created by the waste are solved, a new type of waste is created which is incompatible with the previous solution. The method investigated here consists of chemical substitution of the active cations into the β-tricalcium phosphate (β-TCP) structure, followed by encapsulation of this waste into an alumino-phosphate glass. This is hoped to secure the waste both chemically and physically. Samples were prepared by heat treating reactants to create β-TCP substituted by the desired cation. The structure was then probed using nuclear magnetic resonance (NMR), X-ray diffraction (XRD) and neutron diffraction (ND).

1.2   Aims

The aim of this work is to investigate the effects on the structure of β-TCP under the substitution of various divalent and trivalent cations. Samples of β-TCP were prepared, substituted with the cations under investigation and then analysed by various experimental techniques.

The most ubiquitous and readily available technique for investigating the structure of crystalline materials is XRD, and has formed a key component of the analysis presented in this work. The pattern produced by XRD can give information not only on the size of the unit cell of the material, but also the positions of the atoms within the unit cell, and potentially the occupancy and range of thermal motion of these atoms. However, due to the large size of β-TCP, other techniques were required.

NMR is ideal for investigating the structure of substituted β-TCP, since it is extremely sensitive to subtle changes in the local atomic environment. ^{43}Ca is the naïve choice for investigation of the Ca environments of a calcium phosphate, however due to the inherent difficulties in performing ^{43}Ca NMR, ^{31}P is the main nucleus used in this study. It is a highly abundant nucleus with a high receptivity, and is sensitive to the next-nearest neighbours, i.e. the Ca atoms. Experiments were also performed on the substituent atoms themselves if they were sufficiently NMR active, and the possibility of 2-dimensional NMR experiments was also exploited between ^{31}P and these substituent cations.

1.3   Structure of the thesis

This thesis is comprised of nine chapters, which are summarised here to give an outline of the presented work.

Chapter 2 introduces the problems associated with nuclear waste, and the current methods employed to mitigate and solve these problems. The unique problems of halogenated nuclear waste are established and the solutions proposed by AWE are discussed, focussing on encapsulating the calcined waste in a sodium aluminoborophosphate (NABP) glass.

In chapter 3, the theory relevant to the thesis is discussed. This includes X-ray

and neutron diffraction, Rietveld refinement, nuclear magnetic resonance, and Raman spectroscopy.

Chapters 4 to 7 present the results of characterisation experiments on β-TCP, Zn-substituted, Mg-substituted, and finally Al-substituted and Ga-substituted β-TCP. Each chapter begins with a literature review of published results, and then goes forward to detail the experimental procedures used for each sample. Finally, the results are interpreted and compared to the existing knowledge of the system.

Chapter 8 deals with the dissolution of β-TCP and Ga-substituted β-TCP in an NABP melt at a range of compositions, simulating the distribution of compositions at the β-TCP-NABP interface.

Finally, chapter 9 summarises the results and conclusions in the previous five chapters, as well as discussing future compositions and experiments that will allow further study of the β-TCP system.

CHAPTER 2

NUCLEAR WASTE ENCAPSULATION

2.1 Nuclear waste

When nuclear fission was first discovered in 1938, the idea of a nuclear 'chain reaction' had already been envisioned by Leó Szilárd and Enrico Fermi. They proposed a ^{235}U-based nuclear reactor (pile) which, with the addition of graphite as a moderator, could create and maintain a chain reaction. This would result in a seemingly limitless source of clean energy, at least when compared to the output of contemporary fossil fuel power stations [1]. However, it has always been known that the by-products of these reactions would produce dangerous levels of nuclear waste. In addition to induced radioactivity, caused by neutron capture, in the reactor structure, fuel, coolant and cladding, high quantities of intrinsically radioactive material is produced [2]. Waste has always been the major problem with nuclear power, and is mostly responsible for the limited use of fission reactors worldwide, despite their myriad advantages. The dangers of nuclear waste, and the potential problems this can create, are strongly in the public perception as shown by coverage in newspapers and popular science journals [3–5]. If the problem of nuclear waste can be solved, then one of the major objections to nuclear power is eliminated.

Additionally, nuclear waste is produced by both university and commercial research, hospitals, defence reprocessing, and the mining of uranium ore [6, Chapter 3]. The precise composition of nuclear waste is heavily dependent on both these sources and the reprocessing techniques used.

Nuclear waste is generally classified into three groups by activity. High level waste (HLW) has the highest activity of the three groups, and is defined by the actively cooled

storage facilities required to counteract the increase in temperature produced by the radioactive decay.

Intermediate level waste (ILW) is, as the name suggests, less active than HLW and is not expected to increase in temperature as the waste decays. ILW is composed of materials that have induced radioactivity as a result of being in close proximity to the reactor core, such as shielding and cladding. Both HLW and ILW are highly radiotoxic, and require very careful handling and storage.

The least active classification of nuclear waste is known as low level waste (LLW). This is typically composed of inactive materials that have been in the vicinity of active areas. This includes paper, tools, and clothing which have been used on a site which also contains high levels of active material. LLW does not require shielding, and some can be disposed in landfill. However, by volume, LLW is the largest category of waste and this is the main source of difficulty. A more thorough description of the varieties of waste is given in [7, Chapter 9].

There is an additional distinction between different types of nuclear waste, based on the expected lifetime of the active nuclides contained within the waste. The distinction between short-lived waste and long-lived waste is made based on the half-life of ^{137}Cs, i.e. 30 years. Any radionuclides with a half-life less than this are designated short-lived radionuclide (SLRN), and any with a half-life greater are designated long-lived radionuclide (LLRN) [7, Chapter 9]. Short-lived ILW and LLW will be below background radiation after 200 years (6 half-lives), and hence expensive long-term immobilisation and encapsulation is not required. The more dangerous LLRNs generally have high levels of actinide concentration, including plutonium, neptunium, americium and curium. Therefore, if these LLRNs can be removed from the ILW and HLW waste streams, a short-lived waste product is created, with a much simpler containment demand [8]. The half-lives of LLRNs are given in table 2.1.

2.2 Methods of waste elimination

Recovery and reprocessing of nuclear waste, with an aim of recycling the useful materials, is a key aspect in managing nuclear waste. Of the 10 000 t of spent nuclear fuel produced every year from nuclear power plants, only around 5 % of the U and Pu is

Table 2.1   Half-lives of the main LLRNs present in ILW and HLW waste streams. Nuclides taken from [9], with updated values from [10, Table 4.6.1]

Radionuclides	Half-life / yr^{-1}	Radionuclides	Half-life / yr^{-1}
β-particle sources		*α-particle sources*	
^{79}Se	3.56×10^5	^{237}Np	2.144×10^6
^{93}Zr	1.53×10^6	^{239}Pu	2.41×10^4
^{99}Tc	2.111×10^5	^{238}Pu	8.774×10^1
^{107}Pd	6.5×10^6	^{240}Pu	6.561×10^3
^{126}Sn	2.30×10^5	^{242}Pu	3.73×10^5
^{129}I	1.61×10^7	^{241}Am	4.326×10^2
^{135}Cs	2.3×10^6	^{243}Am	7.37×10^3
^{137}Cs	3.0×10^1	^{245}Cm	8.5×10^3
^{151}Sm	9.0×10^1		

'burnt' in the lifetime of the fuel. However, most spent fuel is treated as HLW with no attempt to reclaim the remaining fuel, due to the difficulties in reprocessing highly active materials. Despite this, reprocessing is currently performed in the UK and France.

The International Atomic Energy Authority (IAEA) defines immobilisation as the conversion of a nuclear waste into a wasteform by solidification, embedding, or encapsulation. This is done to make transportation and ultimate storage and disposal easier and safer. Immobilisation of waste is achieved by dissolution into a ceramic, either vitreous (figure 2.1a) or crystalline (figure 2.1c,d), such that the chemical properties of the wasteform are desirable for storage. The immobilised wasteform can then be encapsulated in concrete or bitumen, such that the radioactive elements are isolated from the environment. Presently, borosilicate-based glass is commonly used for immobilisation by dissolution, where the waste streams are dissolved in the molten glass, and then quenched to produce a monolithic wasteform. A type of hybrid wasteform is also possible, where waste particles are encapsulated in a glass matrix (figure 2.1b), thus rendering them isolated from the environment [11].

Many different wasteform compositions have been investigated, and are summarised in [12]. These include, but are not limited to, silicates, aluminosilicates, borosilicates, sodium aluminium phosphates, and lanthanide borosilicate glasses. Borosilicate glasses were chosen internationally for the monolithic encapsulation of nuclear waste in the late 1970s and early 1980s, due to their familiarity from use in industry, excellent ability to act as a solvent for HLW streams, and relative ease of processing [12].
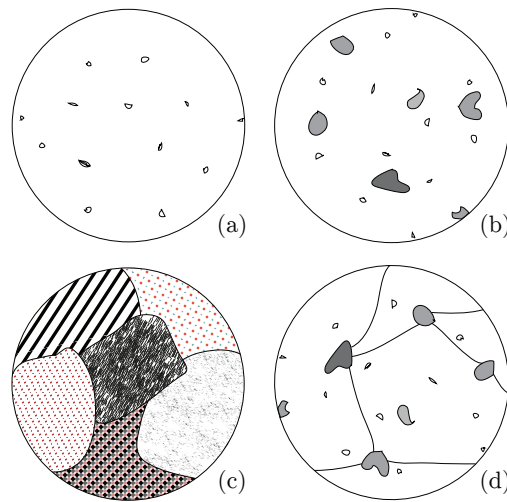
Figure 2.1 Four different possible wasteforms: (a) Vitreous wasteform, with some small inclusions; (b) polycrystalline particles encapsulated in a glass matrix; (c) ceramic phases in solid solution; (d) particles encapsulated in a ceramic matrix. Figure based on [11].

2.3 Halogenated intermediate level waste

The ILW dealt with by the Atomic Weapons Establishment (AWE) and defence organisations in general, however, is somewhat distinct from the majority of HLW and ILW produced as a result of nuclear reactors. In most nuclear waste reprocessing, electrolysis is used to separate the radioactive material from the bulk waste. There are numerous established techniques for removing the waste; the most widely used techniques are based on the plutonium and uranium recovery by extraction (PUREX) method and use water and organic solvents [13].

The PUREX method is not suitable for the reprocessing of decommissioned nuclear weapons however, due to the importance of reclaiming all actinides in the waste, including americium and curium. The pyroprocessing method used for the reprocessing of this waste uses a liquid salt solvent. This creates a highly halogenated ILW (HILW) stream, with high levels of actinide and chloride ions. Common methods of immobilising ILW, as introduced in section 2.2, are not suitable for use with HILW, due to the poor solubility of actinides and chlorides in the ubiquitous borosilicate-based glass used to immobilise the aforementioned nuclear power plant waste [14].

During testing of the immobilisation and encapsulation methods, simulant waste streams are created to model the real HILW, without the dangers and expense inherent in

Table 2.2   Simulant waste streams produced by AWE. The highlighted rows indicate elements investigated in this thesis. Data taken from [15].

Component / mass %	Waste Stream Type			
	I	II	III	IV
Oxides				
HfO_2	-	20.7	62.2	11.4
Ga_2O_3	-	28.0	9.4	10.5
Al_2O_3	-	9.8	1.7	2.2
Sm_2O_3	-	4.6	11.7	1.0
MgO	-	6.3	-	10.1
FeO	-	1.5	-	0.7
Ta_2O_5	-	1.3	-	0.7
NiO	-	1.3	-	0.7
ZnO	-	-	-	35.7
SiO_2	-	-	-	0.8
B_2O_3	-	-	-	0.8
Halides				
$CaCl_2$	80.0	-	-	-
$SmCl_3$	20.0	-	-	-
CaF_2	-	10.4	5.0	8.5
KCl	16.3	10.0	16.9	-

working with active samples. The simulant streams specifically produced by AWE are shown in table 2.2, with hafnium or samarium oxide used as a surrogate for plutonium or americium oxides respectively. Waste stream I contains the highest concentration of chlorides, whilst streams II - IV contain high levels of actinides and halides [15].

A two-stage storage technique has been developed at AWE [16, 17]. Initially, the waste is calcined with tricalcium phosphate ($Ca_3(PO_4)_2$) to produce chlorapatite ($Ca_5(PO_4)_3Cl$) and spodiosite ($Ca_2(PO_4)Cl$) phases. Due to the friability of this powdered product, this resulting powder is encased in a sodium aluminophosphate glass matrix [14], creating a hybrid wasteform, as in figure 2.1b. Additionally, this method has the added benefit of immobilising all four simulant waste streams. Initial results are very positive, and show that all waste products are successfully incorporated into the wasteform. However, since the composition of the production waste streams can vary substantially, it is essential to determine the limits of substitution for each significant component of the waste streams. This is the aim of this project, to create similar phases with a single substituent component, and to determine both the limit of substitution, and the nature of the ceramic phase created.

Figure 2.2 An example of naturally occurring whitlockite, on display at the Royal Ontario Museum, Canada.

2.4   β-TCP

β-TCP is found as a naturally occurring mineral called whitlockite, which was discovered in the Palermo quarry in New Hampshire, USA and named in honour of Herbert P. Whitlock, curator of minerals and gems in the American Museum of Natural History [18]. An example of whitlockite is shown in figure 2.2. Whitlockite has also been observed in lunar rocks [19] and chondrite meteorites [20], where it is known as merrillite. These naturally occurring β-TCP-based phases often contain many other elements, including magnesium, iron, fluorine, and hydrogen. It is these properties of β-TCP, that it can host a variety of elements, and can exist in a vast variety of environments, that is of interest for nuclear waste encapsulation. The detailed nature of the structure is introduced in chapter 4; an overview of the relevant literature follows.

β-TCP has been the subject of a great deal of previous study, as to the effects of substituent cations on both the crystallographic structure and the temperatures of the phase changes. Work initially done by Ando [21], and furthered by Enderlea et al. [22] has

defined the phase change of β-TCP to α-TCP and α′-TCP as a function of temperature, and also of magnesium substitution, one of the most actively investigated substituent cations. The substitution of magnesium into β-TCP, forming β-TCMP, is of great interest to the biomedical industry. This is due to the ability of magnesium to stabilise the high-temperature α-TCP phase, which has much higher biological re-absorption rates into natural tissues. β-TCP has potential applications in dentistry, maxillofacial surgery and orthopaedics, whereas α-TCP's higher rate of reabsorption is exploited in hydraulic bone cements [23–25].

In addition to the substitution of magnesium, the ability for β-TCP to accept many other cations into its structure has been investigated. Lazoryak has published many papers throughout the late 1980s and 1990s on the substitution of trivalent cations into the β-TCP structure, such as aluminium, iron, gallium and europium [26–32]. The study of divalent cations such as sodium and zinc in addition to magnesium, with a view to investigating the modified β-TCP structure has also been a very active area of research, with work starting in the 1970s with the advent of Rietveld refinement, and continuing to the present day [33–46].

Within the last three years, Grimes has published calculations of the β-TCP structure, with regards to understanding the energetics of the system [47, 48]. Using the GULP code [49] and the BFGS algorithm [50], the energetics of both the intrinsic β-TCP structure, and the modified structure under the addition of substituent cations were understood for the first time. This has only become possible recently, since the need to consider supercells of the β-TCP structure, which contains almost 200 atoms in a single unit cell, requires significant computing power.

2.5   Sodium aluminoborophosphate glass

Despite the prevalence of borosilicate glass in the world of nuclear waste disposal, the glass under investigation in this study is a sodium aluminophosphate (NAP) glass, due to the poor solubility of chloride and actinide wastes in borosilicate glass (section 2.3). NAP glass has previously been shown to be durable [51], and was used by the former Soviet Union to encapsulate high sulfide-containing waste resulting from reprocessing reactor fuel [52, 53]. As a result, there is much interest in determining the structural

composition of aluminophosphate glasses. Brow et al. [54, 55] determined the structure of the network over the full compositional range and, supported by numerous other studies making use of a wide variety of techniques, the nature of the Na_2O-Al_2O_3-P_2O_5 system is well understood [56–59].

There are many features of NAP glass which make it desirable as a waste encapsulation material, such has the high dissolution rates of waste materials into the network, and the low temperatures needed for processing. However, poor thermal stability results in devitrification with only small additions of waste materials [17]. Since the great strength of a vitrified wasteform is its high resistance to radiation damage and chemical durability due to its amorphous nature, any crystalline regions are potential sites of attack, which reduce the overall chemical and physical durability of the wasteform.

Initially, the concept of removing the Na_2O from the glass composition was examined, which resulted in an acceptable monolithic wasteform comprising a calcium iron phosphate glass [60]. However, Donald et al. [61] investigated the change in thermal parameters of the NAP glass under B_2O_3 and Fe_2O_3 addition, and found that each resulted in a much more thermally stable glass, with only a minor decrease in the chemical stability of the wasteform. However, it is prudent to understand the effect of these modifications on the structure of the glass. A similar effect was seen in sodium iron phosphate glasses by Yu et al., and attributed to the formation of P-O-Fe bonds replacing P-O-P bonds [62].

The solution under investigation in this thesis is the encapsulation of a β-TCP wasteform in a sodium aluminoborophosphate (NABP) glass matrix, as described in [14]. It is important to stress the difference in this case between immobilisation and encapsulation. Borosilicate glass has been used to *immobilise* the waste by *dissolution*, resulting in a *homogeneous* wasteform. The NAP glass is expected to *encapsulate* the polycrystalline ceramic, resulting in a *heterogeneous* wasteform.

Early tests have proved to be successful, and leaching tests showed no release of the immobilized waste cations in the β-TCP structure, even under high α-particle flux [63]. However, it is prudent to observe the effects on both the β-TCP and NABP structures in simpler, more controlled circumstances. In particular, the consequence of interactions at interfaces between β-TCP-rich regions and the surrounding glass are important to examine in detail.

References

[1] S. M. Rashad and F. H. Hammad, *Applied Energy* **65** (1-4), (2000), 211–229.

[2] C. F. Smith and W. E. Kastenberg, *Nuclear Engineering and Design* **39**, (1976), 293–333.

[3] L. Gray, *Who will bury Britain's nuclear waste in their backyard?*, The Telegraph, 17th May 2012.

[4] M. L. Wald, *Uranium substitute is no longer needed, but its disposal may pose security risk*, The New York Times, 23rd September 2012.

[5] S. Reardon, *US nuke plant delay fails to solve storage conundrum*, New Scientist, August 2012.

[6] R. Roy, *Radioactive Waste Disposal Volume 1: The Waste Package* (Pergamon Press, New York, 1982).

[7] M. I. Ojovan and W. E. Lee, *An Introduction to Nuclear Waste Immobilisation* (Elsevier Science, 2005).

[8] C. Madic, M. Lecomte, P. Baron and B. Boullis, *Comptes Rendus Physique* **3** (7-8), (2002), 797–811.

[9] P. Trocellier, *Annales de Chimie Science des Materiaux* **26** (2), (2001), 113–130.

[10] G. W. C. Kaye and T. H. Laby, Tables of Physical & Chemical Constants .

[11] I. W. Donald, B. L. Metcalfe and R. N. J. Taylor, *Journal of Materials Science* **32** (22), (1997), 5851–5887.

[12] I. W. Donald, *Glass technology* **48** (4), (2007), 155–163.

[13] H. H. Anderson and L. B. Asprey, *Solvent extraction process for plutonium*, U.S. Patent 2 924 506, filed 8th May 1947, issued 9th May 1960.

[14] I. W. Donald, B. L. Metcalfe, S. K. Fong, L. A. Gerrard, D. M. Strachan and R. D. Scheele, *Journal of Nuclear Materials* **361** (1), (2007), 78–93.

[15] S. K. Fong, I. W. Donald and B. L. Metcalfe, *Journal of Alloys and Compounds* **444-445**, (2007), 424–428.

[16] B. L. Metcalfe, I. W. Donald, R. D. Scheele and D. M. Strachan, *Materials Research Society Symposium Proceedings* **757**, (2003), 255–260.

[17] I. W. Donald, B. L. Metcalfe and R. S. Greedharee, *Materials Research Society Symposium Proceedings* **713**, (2002), 287–293.

[18] C. Frondel, *American Mineralogist* **26** (3), (1941), 145–152.

[19] G. H. Heiken, D. T. Vaniman and B. M. French, *Lunar sourcebook, a user's guide to the moon* (Cambridge University Press, Cambridge, 1991), 1st ed.

[20] L. Fuchs, *Science* **137** (3528), (1962), 425–426.

[21] J. Ando, *Bulletin of the Chemical Society of Japan* **31**, (1958), 201–205.

[22] R. Enderlea, F. Gotz-Neunhoeffer, M. Gobbels, F. A. Müller and P. Greil, *Biomaterials* **26**, (2005), 3379–3384.

[23] M. Bohner, *Injury* **31** (Suppl D), (2000), 37–47.

[24] S. V. Dorozhkin, *Journal of Materials Science* **43** (9), (2008), 3028–3057.

[25] R. G. Carrodeguas and S. de Aza, *Acta biomaterialia* **7** (10), (2011), 3536–46.

[26] B. I. Lazoryak, V. N. Golubev, R. Salmon, C. Parent and P. Hagenmuller, *European Journal of Solid State Inorganic Chemistry* **26**, (1989), 455–463.

[27] V. N. Golubev, B. N. Viting, O. B. Dogadin, B. I. Lazoryak and R. G. Aziev, *Russian Journal of Inorganic Chemistry* **35** (12), (1990), 1724–1726.

[28] B. I. Lazoryak, L. N. Ivanov, T. V. Strunenkova, V. N. Golubev and B. N. Viting, *Neorganicheskii Materialy* **26** (2), (1990), 341–345.

[29] V. N. Golubev and B. I. Lazoryak, *Inorganic Materials* **27**, (1991), 576.

[30] B. I. Lazoryak, V. A. Morozov and A. A. Belik, *Journal of Solid State Chemistry* **122** (1), (1996), 15–21.

[31] B. I. Lazoryak, N. Khan, V. A. Morozov, A. A. Belik and S. S. Khasanov, *Journal of Solid State Chemistry* **145** (1), (1999), 345–355.

[32] B. I. Lazoryak, V. A. Morozov, A. A. Belik, S. Y. Stefanovich, V. V. Grebenev, I. A. Leonidov, E. B. Mitberg, S. A. Davydov, O. I. Lebedev and G. Van Tendeloo, *Solid State Sciences* **6** (2), (2004), 185–195.

[33] B. Dickens, L. W. Schroeder and W. E. Brown, *Journal of Solid State Chemistry* **10** (3), (1974), 232–248.

[34] L. W. Schroeder, B. Dickens and W. E. Brown, *Journal of Solid State Chemistry* **22** (3), (1977), 253–262.

[35] R. A. Terpstra, F. C. M. Driessens, H. G. Schaeken and R. M. H. Verbeeck, *Zeitschrift fur anorganische und allgemeine Chemie* **507** (12), (1983), 206–212.

[36] A. Bigi, L. Compostella, A. M. Fichera, E. Foresti, M. Gazzano, A. Ripamonti and N. Roveri, *Journal of Inorganic Biochemistry* **34**, (1988), 75–82.

[37] A. Bigi, G. Falini, E. Foresti, A. Ripamonti, M. Gazzano and N. Roveri, *Zeitschrift fur Kristallographie* **211**, (1996), 13–16.

[38] A. Bigi, E. Foresti, M. Gandolfi, M. Gazzano and N. Roveri, *Journal of Inorganic Biochemistry* **66** (4), (1997), 259–265.

[39] R. J. B. Jakeman, A. K. Cheetham, N. J. Clayden and C. M. Dobson, *Journal of Solid State Chemistry* **78** (1), (1989), 23–34.

[40] A. A. Baird, J. Kagan, T. Gaudette, K. A. Walz, N. Hershlag and D. A. Boas, *NeuroImage* **16** (4), (2002), 1120–1126.

[41] R. Famery, N. Richard and P. Boch, *Ceramics International* **20**, (1994), 327–336.

[42] L. Obadia, P. Deniard, B. Alonso, T. Rouillon, M. Julien, D. Massiot, B. Bujoli and J.-M. Bouler, *Chemistry of Materials* **18** (7), (2006), 1425–1433.

[43] C. Tardei, F. Grigore, I. Pasuk and S. Stoleriu, *Journal of Optoelectronics and Advanced Materials* **8** (2), (2006), 568 – 571.

[44] S. Kannan, J. M. Ventura and J. M. F. Ferreira, *Ceramics International* **33**, (2007), 637–641.

[45] J. Marchi, A. C. S. Dantas, P. Greil, J. C. Bressiani, A. H. A. Bressiani and F. A. Müller, *Materials Research Bulletin* **42** (6), (2007), 1040–1050.

[46] D. Lee, C. Sfeir and P. N. Kumta, *Materials Science and Engineering* **C29**, (2009), 69–77.

[47] E. E. Jay, E. M. Michie, D. Parfitt, M. J. D. Rushton, S. K. Fong, P. M. Mallinson, B. L. Metcalfe and R. W. Grimes, *Journal of Solid State Chemistry* **183** (10), (2010), 2261–2267.

[48] E. E. Jay, P. M. Mallinson, S. K. Fong, B. L. Metcalfe and R. W. Grimes, *Journal of Nuclear Materials* **414** (3), (2011), 367–373.

[49] J. D. Gale, *Journal of the American Ceramic Society, Faraday Transactions* **93** (4),

(1997), 629–637.

[50] J. Nocedal and S. J. Wright, *Numerical Optimization* (Springer, New York, 2006).

[51] H. G. Grimm and P. Huppert, *Vitreous Composition*, U.S. Patent 1 964 629, filed 26th August 1931, issued 26th June 1934.

[52] A. S. Polyakov, G. B. Borisov, N. I. Moiseenko, V. I. Osnovin, E. G. Dzekun, G. M. Medvedev, V. A. Bel'tyukov, S. A. Dubkov and S. N. Filippov, *Atomic Energy* **76** (3), (1994), 181–185.

[53] S. V. Stefanovsky, I. A. Ivanova and A. N. Gulin, *Materials Research Society Symposium Proceedings* **353**, (1994), 101.

[54] R. K. Brow, *Journal of the American Ceramic Society* **76** (4), (1993), 913–918.

[55] R. K. Brow, R. J. Kirkpatrick and G. L. Turner, *Journal of the American Ceramic Society* **76** (4), (1993), 919–928.

[56] A. Belkébir, J. Rocha, A. Esculcas, P. Berthet, B. Gilbert, Z. Gabelica, G. Llabres, F. Wijzen and A. Rulmont, *Spectrochimica Acta Part A: Molecular and Biomolecular Spectroscopy* **55** (7-8), (1999), 1323–1336.

[57] L. Zhang and H. Eckert, *Journal of Physical Chemistry B* **110** (18), (2006), 8946–58.

[58] M. Elisa, C. Vasiliu, C. Grigorescu, B. Sava, A. Diaconu, H. J. Trodahl and M. Dalley, *Glass Technology-European Journal of Glass Science and Technology Part A* **48** (5), (2007), 247–251.

[59] L. van Wüllen, G. Tricot and S. Wegner, *Solid State Nuclear Magnetic Resonance* **32** (2), (2007), 44–52.

[60] B. L. Metcalfe, S. K. Fong and I. W. Donald, *Glass Technology* **46** (2), (2005), 130–133.

[61] I. W. Donald, B. L. Metcalfe, S. K. Fong and L. A. Gerrard, *Journal of Non-Crystalline Solids* **352** (28-29), (2006), 2993–3001.

[62] X. Yu, D. E. Day, G. J. Long and R. K. Brow, *Journal of Non-Crystalline Solids* **215** (1), (1997), 21–31.

[63] B. L. Metcalfe, I. W. Donald, S. K. Fong, L. A. Gerrard, D. M. Strachan and R. D. Scheele, *Journal of Nuclear Materials* **385** (2), (2009), 485–488.

CHAPTER 3

EXPERIMENTAL BACKGROUND

3.1 X-ray diffraction

Diffraction as a general phenomenon occurs when a wave's motion is interrupted by an object, and there is a relative phase difference between portions of the reflected or transmitted wave as a function of angle. For a monochromated light source, there is an angular dependence on the intensity of the radiation detected. This relation is shown in equation 3.1, and is known as Bragg's law [1]

$$n\lambda = 2d\sin\theta, \tag{3.1}$$

where λ is the wavelength, n is the order of the diffraction, d is the distance between the lattice planes, and θ is the angle between the incident beam and the lattice plane. This is illustrated in figure 3.1. X-ray diffraction (XRD) makes use of the long range crystallographic order of the material to create an X-ray pattern [2, section 3.3]. X-rays are used since their wavelengths are comparable to inter-atomic distances. The XRD performed in this work is specifically X-ray powder diffraction, although it will be referred to as XRD for brevity. Since a powder is used, the assumption can be made that all possible orientations of the crystal are present. This results in a superposition of the peaks from all possible single crystal patterns into a one dimensional pattern, containing all information about the crystal. This information can be extracted to various extents, by different methods.

The intensity of the diffraction peaks can be derived by first considering the individual atomic scattering factors $f(\mathbf{s})$ of the atoms in the lattice such that [3]

$$f(\mathbf{s}) = \int_{-\infty}^{\infty} \rho(\mathbf{r})e^{2\pi i(\mathbf{r}\cdot\mathbf{s})}d\mathbf{r} = f(s), \tag{3.2}$$
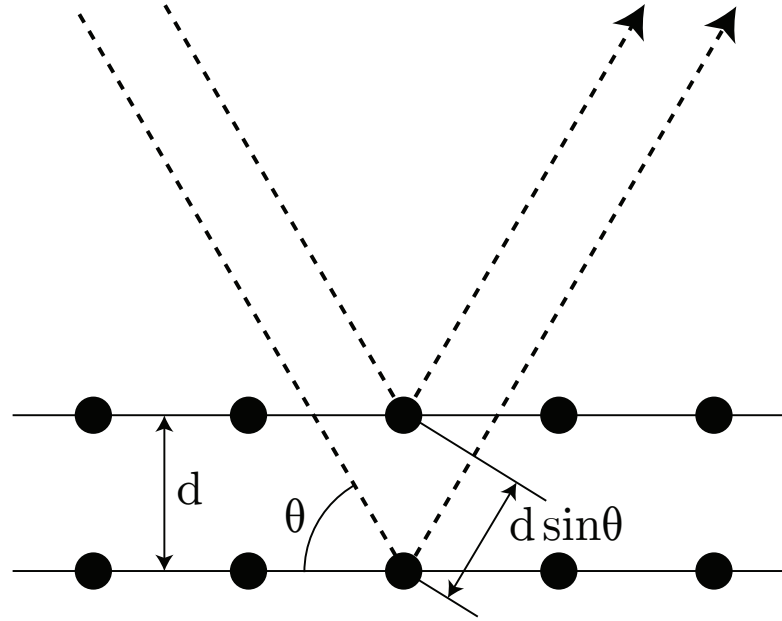
Figure 3.1   A single lattice plane undergoing diffraction. The X-rays are shown at an incident angle θ, with a lattice plane distance d. Half the path difference $d \sin \theta$ is indicated.

where $\mathbf{s} = \hat{\mathbf{s}} \sin \theta / \lambda$, and $\rho(\mathbf{r})$ is the electron density a distance $\mathbf{r}$ from the centre of the distribution. The atom scattering factor $f(\mathbf{s})$ can be treated as being dependent on only the magnitude of $\mathbf{s}$ since the electron distribution in an isolated atom is approximately spherically symmetric. One can now define the structure factor $F(\mathbf{h})$ in terms of a sum over the scattering factors of the N atoms in the unit cell such that

$$F(\mathbf{h}) = \sum_{i=1}^{N} f_i(s) e^{2\pi i (\mathbf{h} \cdot \mathbf{x_i})}, \tag{3.3}$$

where the vector $\mathbf{h}$ is defined by the dimensionless Miller indices (hkl), and $f_i(s)$ is the scattering factor of atom i at the position $\mathbf{x_i}$. The structure factor is also dependent on the thermal motion of the atoms in the structure, and so a correction to the structure factor $F(\mathbf{h})$ is applied such that

$$F(\mathbf{h}) = \sum_{i=1}^{N} f_i(s) e^{2\pi i (\mathbf{h} \cdot \mathbf{x_i})} e^{-8\pi^2 s^2 \langle u_i^2 \rangle}, \tag{3.4}$$

where $\langle u_i^2 \rangle$ is the isotropic thermal parameter of the ith atom, defined as the mean square displacement from its equilibrium position $\mathbf{x_i}$, and referred to as U_{iso} for an individual site. However, in the case where the thermal motion of the atom cannot be described accurately by an isotropic value, the more accurate modification can be used, where the

16

structure factor $F(\mathbf{h})$ is further corrected such that

$$F(\mathbf{h}) = \sum_{i=1}^{N} f_i(s)e^{2\pi i(\mathbf{h}\cdot\mathbf{x_i})}e^{-2\pi^2\alpha}, \tag{3.5}$$

where $\alpha = U_{11}\,h^2 a^{*2} + U_{22}\,k^2 b^{*2} + U_{33}\,l^2 c^{*2} + 2U_{12}\,hk\,a^* b^* + 2U_{13}\,hl\,a^* c^* + 2U_{23}\,kl\,b^* c^*$, and a^*, b^*, and c^* are the vectors perpendicular to the bc, ac, and ab planes respectively. It then follows that the intensity $I(\mathbf{h})$ due to a reflection from the individual scattering centres in a crystal is given simply by the self convolution of structure factor $F(\mathbf{h})$, such that

$$I(\mathbf{h}) = F(\mathbf{h})F^*(\mathbf{h}). \tag{3.6}$$

3.2 Time of flight neutron diffraction

Instead of using photons for diffraction, neutrons can also be used as a medium to probe the periodic structure of crystalline materials. Unlike X-rays, neutrons are not scattered by the electron cloud surrounding an atom. Due to the mass of the neutron, it is instead scattered strongly by the nucleus of the atom, and as a result can scatter more strongly from 'light' elements, such as oxygen, than X-rays.

In a semi-classical model, the scattering of neutrons can be treated in a similar fashion to X-rays, where the wavelength of the neutron is given by the de Broglie wavelength [4]

$$\lambda = \frac{h}{m_n v}, \tag{3.7}$$

where h is Planck's constant, m_n is the mass of the neutron, and v is the speed of the neutron. Hence, the wavelength λ of the neutrons can effectively be 'tuned' by controlling the speed, or energy of the neutrons. This is performed via a process known as moderation, which is usually given in units of temperature, using the relation

$$\frac{1}{2}m_n v^2 = k_B T, \tag{3.8}$$

where k_B is Boltzmann's constant, and T is the temperature of the moderator. Hence, thermal (room temperature) neutrons produced by a moderator at 290 K have a speed of $2200\,\mathrm{m\,s^{-1}}$, corresponding to a wavelength of 1.8 Å by equation 3.7. It is somewhat coincidental that 1.8 Å happens to be of the order of the interatomic spacing in most

common materials, rendering thermal neutrons very effective for neutron scattering experiments.

Moderation produces a range of neutron energies, and hence wavelengths, due to the complex nature of the moderation process. It is possible to monochromate the neutron beam, however this has the obvious side effect of rejecting the vast majority of the neutron flux. Instead of monochromating the neutrons, a wide range of energies can be used, as long as the energy dispersion is accounted for. This is known as time of flight (t-o-f) neutron diffraction. In the case of t-o-f neutron diffraction, the neutron wavelengths are calculated based on the time required for the neutrons to arrive at the detector and the scattering angle, where the time taken

$$t = \frac{m_n}{h} L\lambda, \tag{3.9}$$

and L is the flight path from the moderator to the detector, via the sample [5]. By this technique, a range of neutron wavelengths can be used, utilising a large fraction of the total flux available, with excellent resolution.

In this study, the total neutron diffractometer GEM (General Materials Diffractometer) was used to collect the data, using neutrons supplied by the ISIS neutron source. ISIS is an accelerator-based neutron source, which creates pulses of neutrons by spallation. Initially, H^- ions are accelerated in a linac up to $70\,MeV$, before passing through alumina foil which removes the electrons from the ions, producing H^+ ions, or protons. These are then accelerated further up to an energy of $800\,MeV$ in a synchrotron, before being diverted to the tungsten spallation target. A $50\,Hz$ repetition frequency is used, providing a proton current of up to $200\,\mu A$. Neutrons are produced by spallation, and are then moderated to create maximum intensity at the desired wavelength range [6].

The GEM diffractometer is one of the most advanced t-o-f detectors in the world, due to its very large solid angle coverage. Detectors cover scattering angles from $1.2°$ to $171.4°$, with an azimuthal angle of $\pm 45°$, covering $30\,\%$ of all possible scattering directions from the sample. The detector banks are shown in figure 3.2. Since the detectors cover a wide scattering angle range, they also cover a very high Q range: from 0.1 to $60\,Å^{-1}$, where Q is the momentum transfer defined in terms of the scattering vector $\mathbf{k}$. GEM receives neutrons from a liquid methane moderator at $110\,K$, corresponding to a wavelength of $2.94\,Å$. GEM also features a relatively long primary flight path from
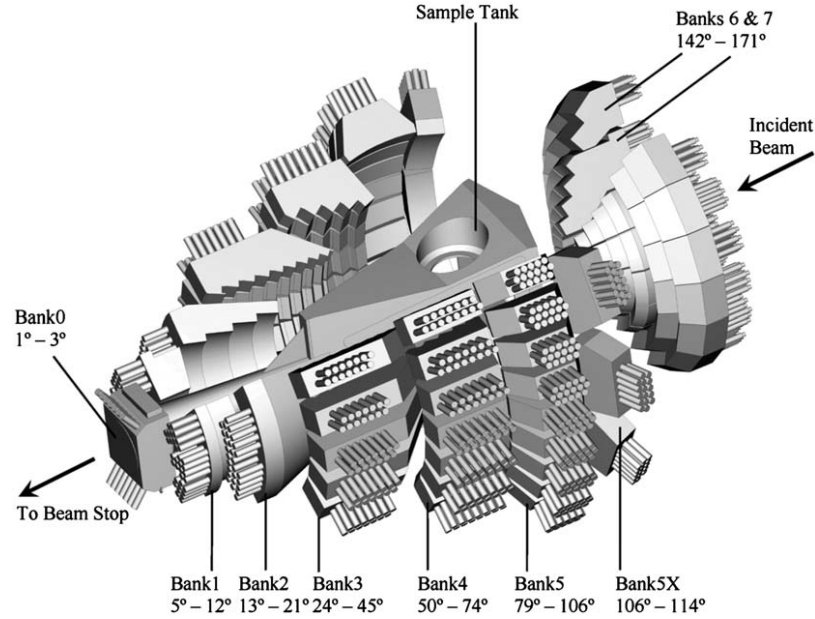
Figure 3.2 The GEM diffractometer. All detector banks are shown, with the beam travelling from right to left. Reproduced from [6].

moderator to sample of 17 m, which reduces the contributions of t-o-f acceptance in the ultimate resolution of the experiment [6].

A total neutron diffractometer measures the differential cross section

$$\left(\frac{\mathrm{d}\sigma}{\mathrm{d}\Omega}\right)_{\text{total}} = I(Q) = \frac{R_{\text{total}}}{N\Phi\mathrm{d}\Omega}, \tag{3.10}$$

where R_{total} is the rate of scattering at a solid angle $\mathrm{d}\Omega$, N is the number of atoms in the sample and Φ is the neutron flux. This can be expressed in terms of a self scattering component $I^s(Q)$ and distinct scattering component $i(Q)$, such that

$$I(Q) = I^s(Q) + i(Q). \tag{3.11}$$

The self-scattering can be determined by considering the composition and density of the sample, and hence can be subtracted from the total scattering to yield the distinct scattering. It is generally the case that the distinct scattering, when plotted as a function of Q, oscillates about zero, with a period based on the interatomic distances of the atoms. Hence, a Fourier transform can be taken, moving from reciprocal space into real space, such that

$$T(r) = T^0(r) + \frac{2}{\pi} \int_0^\infty Q\,i(Q)\,M(Q)\,\sin(rQ)\,\mathrm{d}Q, \tag{3.12}$$

where $T(r)$ is known as the total correlation function. $T^0(r)$ is the average density contribution to the total correlation function, which is a linear function of r, and $M(Q)$

is a window function to reduce artefacts arising as a result of the finite maximum Q value (Q_{max}) used in the Fourier transform.

In the current study, a Lorch modification function was used, where

$$M(Q) = \begin{cases} 0 & \text{if } Q > Q_{max} \\ \dfrac{\sin Q\Delta r}{Q\Delta r} & \text{if } Q \leq Q_{max}. \end{cases} \qquad (3.13)$$

The total correlation function can also be expressed as a weighted sum of partial correlation functions, such that

$$T(r) = \sum_l \sum_{l'} c_l \bar{b}_l \bar{b}_{l'} \, t_{ll'}(r), \qquad (3.14)$$

where $t_{ll'}$ is the partial correlation between atoms l and l', $\bar{b}_l$ and $\bar{b}_{l}'$ are the coherent scattering lengths of the elements l and l' respectively, and c_l is the atomic fraction of element l. Each partial correlation function can be thought of as the average number of atoms of element l' which are in a given spherical shell of radius r from element l, as shown in figure 3.3 [5].
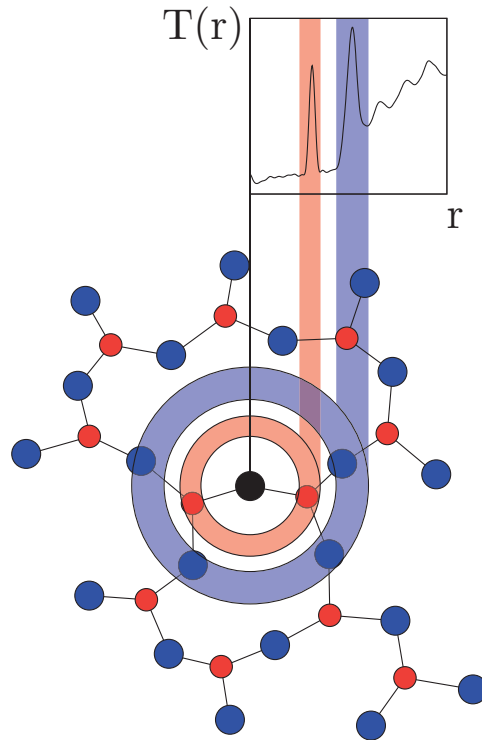
Figure 3.3 An imaginary network of two different atoms, with the resulting total scattering pattern plotted above. The bond lengths are clearly visible in the real space total scattering plot. Modified from [5].

It is possible to fit the observed total correlation function in terms of its partial correlation functions at short r, so as to remain within the first coordination shell. A Gaussian convoluted with the effects of a finite Q_{max} and Lorch window function is used, with an area $A_{ll'}$ and position $r_{ll'}$. These results can be used to extract the coordination number $n_{ll'}$ of atom l with respect to atom l', using the relation

$$n_{ll'} = \frac{r_{ll'} A_{ll'}}{(2 - \delta_{ll'}) c_l \bar{b}_l \bar{b}_{l'}}, \tag{3.15}$$

where $\delta_{ll'}$ is the Kronecker delta.

3.3   Rietveld refinement

Rietveld refinement is based on postulating a hypothesized crystal structure, in terms of a space group, unit cell dimensions, and the crystallographic parameters (position, site occupancy, thermal parameters) of the constituent atoms, and then refining these aspects of the structure to match the observed XRD pattern as closely as possible [7]. Once the refined pattern is reasonably close to the experimental pattern, it can be assumed that the atomic positions are a reasonable representation of the crystal structure. The technique does, however, require an accurate idea of the initial structure. At the very least, a space group and constituent atoms are required as initial conditions. If the space group is not known, a Pawley refinement can be carried out to determine the most likely space groups to make the powder pattern [8, 9]. This requires much less initial information than a Rietveld refinement, but can only give a list of the most likely space groups, and the intensity of each observed reflection. Since the β-TCP structure is well known, Rietveld refinement was used exclusively in this thesis.

3.3.1   XRD Rietveld refinement

In addition to the equations governing the reflection positions and intensities described above, there are corrections which must be applied to the model to correctly account for subtleties with the experiment. For example, a Lorenz polarisation factor arising from the Ge(111) monochromater which affects reflection intensity, and a zero and height offset which result in linear and cosinusoidal offsets to the peak position respectively. A background term is also included, which fits the slowly changing baseline of the pattern,

in this case with a polynomial function. Finally, a peakshape is convoluted with the impulses simulated by the structure and corrections, which seeks to approximate the complex behaviour of the detector and optics. There is an additional correction known as the simple axial model, which models the aberration caused by the defocusing of the X-ray beam at low angle [10, Chapter 1].

There are various peakshapes available for Rietveld refinement; in this thesis the Pearson VII peakshape was used exclusively, the analytical formula of which is given by

$$I(2\theta) = \left[\frac{h^2}{h^2 + (2^{1/m} - 1)(2\theta - 2\theta_c)^2} \right]^m, \tag{3.16}$$

where $2h = h_a + h_b \tan\theta + h_c \sec\theta$, and $m = 0.6 + m_a + m_b \tan\theta + m_c \sec\theta$ [11]. These six h and m terms are refinable parameters, and are dependent on θ, modelling the change in peakshape as a function of angle [12].

XRD patterns are the most simple source of data for Rietveld refinement. This is mostly due to the widespread use of X-ray diffractometers all based around a similar radiation source, resulting in a large market for X-ray based Rietveld refinement software designed specifically for this purpose. Additionally, the generation and focussing of X-rays is far simpler than the neutron case discussed below, resulting in a more tightly focussed X-ray beam and hence a small instrumental broadening factor on the observed reflections. As a result, the resolution of XRD can be very high, with the instrumental peak width as low as $0.05°$ 2θ corresponding to a distribution in d-spacing of the order of 10^{-4} Å for CuKα_1. This in turn results in less overlap between reflections, and hence the pattern is simpler to fit with less uncertainty in the position of the peaks and their relative amplitudes. Also, since the X-ray form factor scales with Z^2, diffraction involving heavy atoms ($Z > 10$) is very sensitive.

Despite these advantages of XRD Rietveld refinement, there are issues with the technique. The main problem arises when an atom has a small electron cloud. Since X-rays scatter from the electron cloud, this atom will scatter X-rays relatively weakly. In other words, the X-ray refinement is relatively insensitive to changes in the atomic position and thermal parameters of these atoms. This is particularly problematic in the case of oxygen, which is a major component of the majority of materials.

3.3.2 Neutron diffraction Rietveld refinement

A potential solution is neutron Rietveld refinement. Since neutrons scatter from the nucleus as opposed to the electron cloud, the presence or absence of electrons is irrelevant to the scattering of neutrons, which is a complex function of the nucleus. Whilst it is incorrect to state that the neutron scattering is *always* larger than X-ray scattering for light nuclei, in the case of oxygen the neutron scattering length *is* significantly greater than the X-ray form factor. Hence, in order to determine accurate O positions with high precision, ND is a vital tool. Additionally, ND can also reveal far more information than XRD about the anisotropic thermal motion of the atoms within the structure, highlighting any disorder and preferred directionality.

The same basic technique is used for refinement of neutron data, with background corrections and offsets used to account for any errors in the calibration of the diffractometer. Due to the fundamental difference in the t-o-f based neutron experiment to the monochromated X-ray based experiment however, the impulse used is no longer assumed to be a simple function. The Ikeda-Carpenter function [13], [10, Chapter 11.5] is used to model the effects of a pulsed neutron source with a moderator, which takes the form given in equation 3.17.

$$I(t) = \frac{\alpha}{2}\left[(1-R) * (t\alpha)^2 \exp(-t\alpha) + 2R\frac{\alpha^2\beta}{(\alpha-\beta)^2}\right] \tag{3.17}$$

where $\alpha^{-1} = \alpha_0 + \lambda\alpha_1$, $R = \exp\left\{-\dfrac{1}{\kappa\lambda^2}\right\}$, $\beta = \frac{1}{\beta_0}$, and $*$ denotes a convolution. In this impulse, the refinable α_0 and α_1 terms correspond to the dispersion in energy of the neutrons emerging during thermalisation, and the refinable β_0 term is the inverse of the thermalised neutron decay time constant. The refinable κ term corresponds to the contribution of the thermalised neutron decay to the overall impulse, and is a function of the moderator temperature. R is referred to as the 'storage' term; the fraction of neutrons that are held in the moderator, and decay with a time constant β. This function describes the flux of neutrons reaching the sample as a function of the t-o-f, and has a characteristic shape which is present in the observed diffraction patterns. This impulse is then convoluted with a pseudo-Voigt lineshape, which accounts for the instrumental broadening of the diffractometer, and any disorder in the sample itself. An example of a typical Ikeda-Carpenter-based peakshape can be seen in figure 3.4.
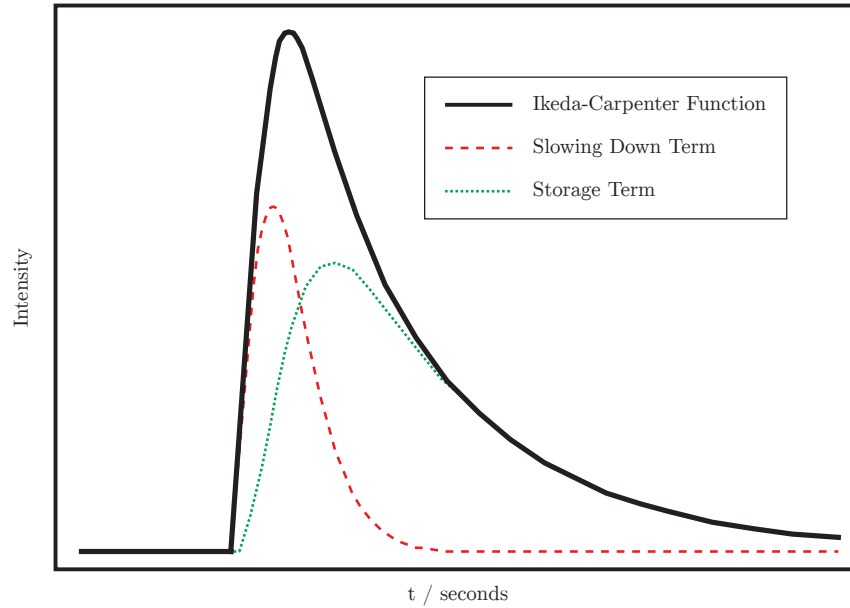
Figure 3.4 The Ikeda-Carpenter function as a function of time-of-flight. The total function is a sum of the relatively narrow, initial slowing down term, and the broader, wavelength independent thermalised neutron decay. Modified from [13].

Due to the range in wavelengths of the neutrons used however, the resolution of a neutron diffraction pattern is generally worse than that of an XRD pattern over a similar d-spacing range. To combat this, a combined treatment is also possible [10, Chapter 12]. Rietveld refinement can be performed on multiple diffraction patterns of the same sample, including different scattering techniques. In this work, to achieve a combination of precise lattice parameters and good contrast between species, a combination of neutron and XRD patterns were used in the same Rietveld refinement.

3.3.3 Goodness of fit

It is often difficult to discriminate between 'good' fits and 'bad' fits produced during Rietveld refinement, especially in the case of large unit cells and overlapping peaks. It is hence useful to define a series of goodness of fit parameters, which are displayed in table 3.1. The functions are defined in terms of y_{oi} and y_{ci}, the observed and calculated intensities at the ith step, I_{ok} and I_{ck}, the kth observed and calculated Bragg reflection intensities, and w_i, a weighting factor equal to $\frac{1}{y_{oi}}$. The goodness of fit functions have been reproduced based on the formulation printed in the TOPAS technical reference [12], since it is this software that was used to perform the Rietveld refinements [14].

Table 3.1 Goodness of fit functions. For brevity, only the first summation is given explicitly, all others are over the same parameter and range. These functions have been reproduced from the TOPAS technical reference [12].

Name	Function
R-pattern	$R_p = \sqrt{\dfrac{\sum_{i=1}^{n} w_i \left(y_{oi} - y_{ci}\right)^2}{\sum y_{oi}}}$
R-weighted pattern	$R_{wp} = \sqrt{\dfrac{\sum \left|y_{oi} - y_{ci}\right|}{\sum w_i y_{oi}^2}}$
R-expected	$R_{exp} = \sqrt{\dfrac{\sum \left(M - P\right)}{\sum w_i y_{oi}^2}}$
Goodness of fit	$\chi^2 = \dfrac{R_{wp}}{R_{exp}} = \sqrt{\dfrac{\sum \left(y_{oi}^2 - y_{ci}^2\right)}{\left(M - P\right)}}$
R-Bragg	$R_B = \dfrac{\sum_{k=1}^{m} \left|I_{ok} - I_{ck}\right|}{\sum I_{ok}}$

The R_p and R_{wp} parameters are measures of how well the observed pattern is fitted by the calculated pattern, based on the summed differences over each step. These values are compared with R_{exp}, which calculates the best fit possible based on the number of steps M and the parameters used in the model P. The goodness of fit, or χ^2 parameter is given as the ratio of the R_{wp} and R_{exp} parameters. If $R_{wp} = R_{exp}$, $\chi^2 = 1$, showing the model is a perfect fit to the data. In any real system however, R_{wp} is greater than R_{exp}, resulting in $\chi^2 > 1$. The R_B parameter treats each Bragg reflection as a data point, and expresses the residual based only on the phase being modelled, with no contribution from other phases.

3.4 Nuclear magnetic resonance

All nuclei have intrinsic quantum mechanical spin in multiples of $\frac{\hbar}{2}$. This can range from zero spin, for nuclei such as $^{16}_{8}O$ and $^{40}_{20}Ca$, to $\frac{7\hbar}{2}$ for $^{43}_{20}Ca$ and $6\hbar$ for $^{50}_{23}V$. The variety of nuclear spin arises from the pairing of protons and neutrons in the nucleus. In the case where both the number of protons and number of neutrons are even, there is zero net nuclear spin. In the case where either one or both are odd, a net nuclear spin

forms [15, Chapter 1], which is expressed as an angular momentum $\mathbf{I}$. These nuclear spins $\mathbf{I}$ possess a magnetic moment μ given by

$$\mu = \gamma \mathbf{I} \hbar. \tag{3.18}$$

If the magnetic field is defined as being applied in the $\hat{\mathbf{z}}$ direction, the vectors can be eliminated to reveal [16, Chapter 1.A]

$$\mu_z = \gamma I_z \hbar. \tag{3.19}$$

However, due to the quantization of the angular momentum with respect to the maximum direction, there are $2I + 1$ distinct values of $\mathbf{I}$, and hence μ. I_z is commonly quantized in terms of m, which can take values from $-2I$ to $2I$, in units of I, where m is the quantized z projection of the angular momentum I. Hence

$$\mu_z = \gamma m_z \hbar. \tag{3.20}$$

In the absence of an external magnetic field, these states all have equal energy. However, under the application of an external magnetic field, the degeneracy is lifted by the Zeeman effect, which creates an energy differential based on the orientation of the nucleus to the external field. Classically, this can be thought of as $-\mu \cdot B$, however, since μ is quantized to specific angles, the more appropriate equation is [15, Chapter 2.2]

$$E = -\mu_z B_0 = -\gamma m_z \hbar B_0. \tag{3.21}$$

If we only allow single quantum transitions, (i.e. $\Delta m = 1$), then

$$\Delta E = -\gamma \hbar B_0. \tag{3.22}$$

If quanta of energy are applied that match a value ΔE, a photon may be absorbed. This results in an increase in the energy of the nucleus. This absorbed energy is re-emitted at a frequency characteristic of the environment of the nucleus, which can be detected and analysed. The energy of the emitted photon is given by [15, Chapter 2.5]

$$\Delta E = -\gamma \hbar B_0 = \hbar \omega_0, \tag{3.23}$$

so the frequency ω_0 is given by

$$\omega_0 = -\gamma B_0. \tag{3.24}$$

3.4.1 The Bloch Equations

Most NMR performed at the present day is pulse NMR. In the most general sense, this involves perturbing an ensemble of spins aligned with B_0 (at equilibrium) with a radiofrequency (RF) pulse, thus creating an excited state. This can be visualised as rotating the magnetisation vector from the z direction, about a vector perpendicular to this z direction. The spins are then allowed to return to equilibrium, through a process known as relaxation [15, Chapter 2.6-2.7]. As this relaxation takes place, the re-emitted energy is detected, giving information about the environment of the spins.

There are two types of relaxation from this excited state, spin-spin relaxation and spin-lattice relaxation. Spin-spin relaxation occurs when the transverse magnetisation (perpendicular to z) de-phases and decays to zero. It is caused by the individual nuclear spins relaxing with respect to each other due to the presence of a spatially dependent magnetic field, and hence by equation 3.24, a spatially dependent Larmor frequency. It is assumed for convenience that the magnetisation is initially in the y direction ($\mathbf{M} = (0, M_y, 0)$), after having been rotated about the x direction. This relaxation process is governed by equation 3.25,

$$
\begin{aligned}
\mathrm{M}_x(t) &= \mathrm{M}_x(0)\sin\omega t \exp\left(-\frac{t}{\mathrm{T}_2}\right) \\
\mathrm{M}_y(t) &= \mathrm{M}_y(0)\cos\omega t \exp\left(-\frac{t}{\mathrm{T}_2}\right),
\end{aligned}
\tag{3.25}
$$

where the spin-spin magnetisation at time t, denoted by $M_x(t)$ and $M_y(t)$, exponentially decays to zero at a rate related to T_2, while rotating in the xy plane at the Larmor frequency ω_0. T_2 is known as the spin-spin relaxation time, and is the time required for the transverse magnetisation to reduce by a factor of 2. It is important to note that even once the transverse magnetisation has decayed completely, the individual spins still each have a transverse component, i.e. the longitudinal magnetisation has still not fully returned to equilibrium.

Spin-lattice relaxation is due to the magnetisation re-aligning with B_z. This process is governed by equation 3.26,

$$
\mathrm{M}_z(t) = \mathrm{M}_z(0)\left\{1 - \exp\left(-\frac{t}{\mathrm{T}_1}\right)\right\}
\tag{3.26}
$$

where the magnetisation in the $\hat{\mathbf{z}}$ direction, M_z, increases to its maximum value M_0, i.e. the magnetisation at equilibrium, as t becomes very long on the scale of T_1. Equa-
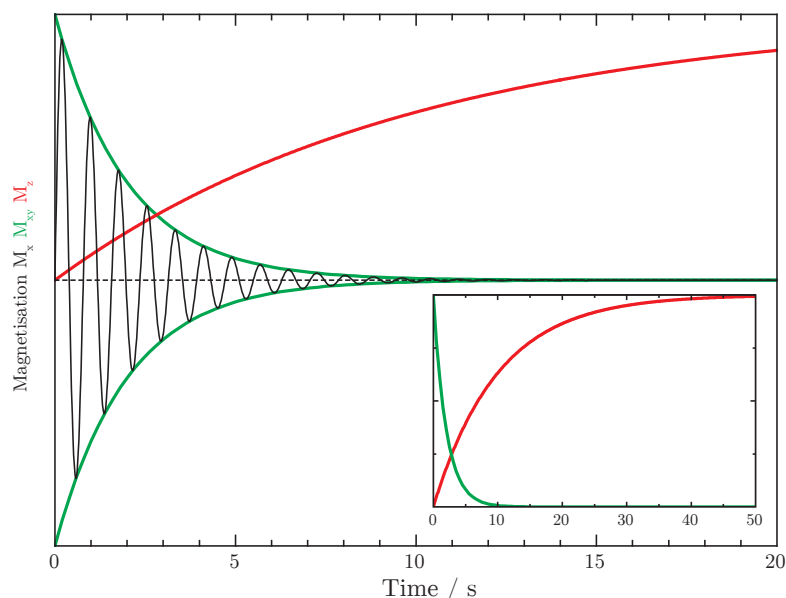
Figure 3.5 The transverse and longitudinal magnetisation as a function of time. Both are presented in the rotating frame, with the transverse magnetisation also shown in the laboratory frame. In this case, the Larmor frequency is greatly reduced to less than 1 Hz.

tions 3.25 and 3.26 are collectively known as the Bloch equations, after Felix Bloch [17, 18]. A plot of both equation 3.25 and 3.26 can be seen in figure 3.5.

3.4.2 Acquiring an NMR Spectrum

As the spins precess about their equilibrium axis at the Larmor frequency, a characteristic signal known as a free induction decay (FID) is detected by the receiving coil around the sample [15, Chapter 2.8]. This signal is a measure of the transverse magnetisation of the ensemble in the laboratory frame, and hence oscillates between positive and negative values in the time domain at the Larmor frequency. The oscillation is damped with a time constant equal to the T_2 relaxation time, resulting in a spectrum resembling figure 3.5.

An FID of a real sample is rarely as clear as figure 3.5 however. It usually comprises a variety of different frequencies, superposed into a single signal, resulting in beat patterns. Despite containing information on all the magnetic environments comprising the sample, it is very hard for the human mind to make sense of it when displayed in the time domain.

A Fourier transform can be applied to the FID signal, moving from the time domain

to the frequency domain [15, Chapter 5] [16, Chapter 1.D]. It is now trivial to see each individual magnetic environment as a peak in the spectrum at the specific Larmor frequency of that environment. It is convenient to convert from an angular frequency in rad s^{-1} into a chemical shift in ppm, defined in equation 3.27.

$$\delta = \frac{\omega - \omega_{\text{ref}}}{\omega_{\text{ref}}} \times 10^6 \text{ ppm} \tag{3.27}$$

The chemical shift δ is a function of the observed Larmor frequency ω and a reference frequency ω_{ref}, and is usually expressed as a dimensionless value in ppm (parts per million). The reference frequency is recorded by performing NMR on a standard reference for each nucleus, and assigning that chemical shift to a specific ppm value. For primary references, this is $0\,\text{ppm}$. Primary references are not always used however, due to safety concerns. For example, the primary reference for ^{31}P NMR is phosphoric acid, at 85% concentration. Instead of using this corrosive acid, ammonium dihydrogen phosphate (ADP) is used, which produces a sharp resonance peak at 0.7 ppm.

The chemical shift scale is chosen because it is convenient for expressing the very small frequency variations observed, and is also independent of field strength, allowing easy comparison of spectra taken using different equipment.

3.4.3   The Pertubations on the Zeeman Effect

So far, the Zeeman interaction is the only interaction we have *explicitly* considered between the spin system and the magnetic field, despite *implicitly* considering the chemical shift interaction above. If the Zeeman interaction were the only interaction present, NMR would not be useful as a spectroscopic technique, since each isotope would have one unvarying resonant frequency, regardless of its environment. Without other interactions, it is impossible to describe the widely varying types of spectra that can be observed with NMR.

3.4.3.1   The Chemical Shift

The electrons in the structure under investigation can cause the magnetic field B_z to vary on very short length scales, typically causing each atom to 'feel' a slightly different magnetic field. This effect is a two step process, where the external magnetic field induces currents in the electron clouds, which then induce a magnetic field, usually

acting to shield the nucleus from the main external field. As a result, each nucleus in a different environment will possess a slightly different Larmor frequency, which will be observable in the FID, and hence as a different position in the Fourier transformed spectrum.

Since it can be expected that the induced electric currents will have preferred directions, around rings for example, the change in local magnetic field will be a function of the angle of the material to the magnetic field. The induced magnetic field $B^{induced}$ is given by

$$\mathbf{B}_j^{induced} = \delta_{ij}\mathbf{B}_i, \tag{3.28}$$

where δ is a second rank tensor, known as the chemical shift tensor. It is usually diagonalised by choosing a principal axis system (PAS), and the isotropic (δ_{iso}), span (Ω) and skew (κ) components are defined:

$$\delta_{iso} = \tfrac{1}{3}\left(\delta_{11} + \delta_{22} + \delta_{33}\right)$$
$$\Omega \approx \delta_{11} - \delta_{33} \tag{3.29}$$
$$\kappa = \frac{3(\delta_{22} - \delta_{iso})}{\Omega},$$

where

$$\delta = \begin{pmatrix} \delta_{11} & 0 & 0 \\ 0 & \delta_{22} & 0 \\ 0 & 0 & \delta_{33} \end{pmatrix}, \tag{3.30}$$

the PAS is defined such that $|\delta_{11}| \geq |\delta_{22}| \geq |\delta_{33}|$, and all other matrix elements are zero. This is known as the Herzfeld-Berger convention [19], and is currently considered to be the most widely used. There are numerous other conventions for the definition of the CSA tensor given in equation 3.30, but it is trivial to convert between them. The rotation from the magnetic field system to the PAS is a function of the angle between the two systems. If a single crystal is examined, the spectrum remains sharp, with the position dependent on the orientation of the PAS tensor to the B_0 field. In the case of many small crystallites however, which cover every angle to the B_0 field, a characteristic broad lineshape is observed. A typical lineshape is shown in figure 3.6.

Fitting this pattern in principle allows all the parameters in equations 3.29 to be extracted, providing a wealth of information about the crystal structure. However, each distinct magnetic environment has its own δ tensor, and as a result its own peak. The
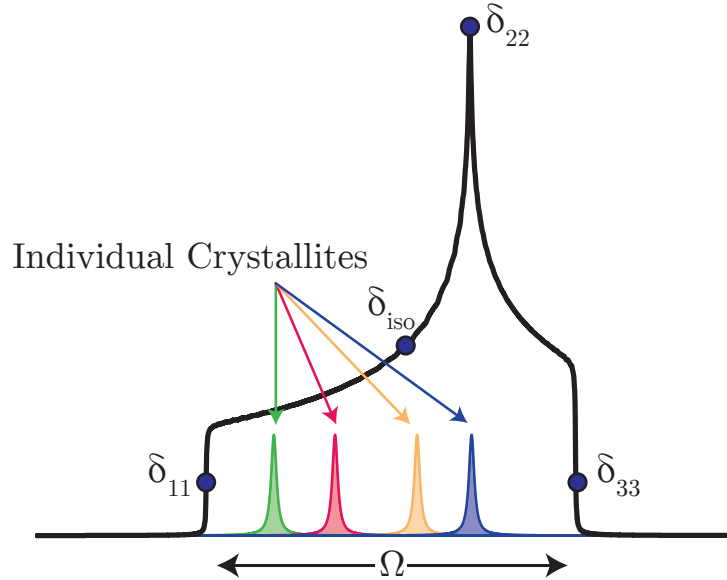
Figure 3.6 A typical CSA lineshape, where $\kappa = 0.65$. Individual single crystal peaks are shown, where each crystallite (and hence its chemical shift tensor) is at a different angle to the B_0 field. The matrix elements and δ_{iso} are labelled.

width of the CSA lineshape is generally broader than the distance between the peaks themselves, and as a result will overlap. This makes fitting the resulting spectrum very difficult, and rarely unambiguous.

3.4.3.2 The Dipolar Interaction

The dipolar interaction has an analogue of two bar magnets in close proximity. If they are held with like poles nearest, they are considered to be in a high energy configuration, and vice versa. In the case of classical electrodynamics, the interaction energy E between two magnetic dipoles μ_1 and μ_2 separated by a vector $\mathbf{r}$ is given by

$$E = (\mu_1 \cdot \mu_2)\, r^{-3} - 3\, (\mu_1 \cdot \mathbf{r}) (\mu_2 \cdot \mathbf{r})\, \mathbf{r}^{-5}. \tag{3.31}$$

If the dipoles have the same alignment with respect to the vector $\mathbf{r}$ (i.e. in a very strong B_0 field), then equation 3.31 becomes

$$E = -2\, (\mu_1 \cdot \mu_2)\, r^{-3} \{P_2 (\cos\theta)\}, \tag{3.32}$$

where P_2 is the second order Legendre polynomial, and is discussed in greater detail in section 3.4.4. The resulting lineshape is known as a Pake doublet [20], and is shown in
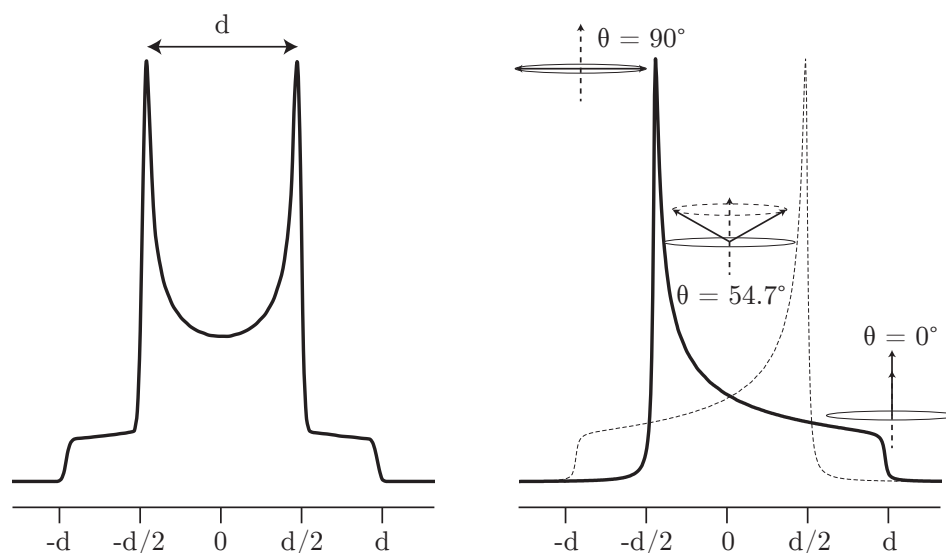
Figure 3.7 A typical dipolar lineshape. On the left, a total lineshape is shown, with symmetry about the centre. On the right, both components are shown, with the dipolar vector shown relative to the B_0 field at both extremes, and the crossover of the two components, where the strength of the dipolar coupling is zero.

figure 3.7. Since the coupled dipoles μ_1 and μ_2 can be aligned either parallel or anti-parallel, there are two possible energies, and hence Larmor frequencies, for each site. For each alignment, a lineshape similar to the CSA lineshape shown in figure 3.6 results, and the Pake doublet is effectively two CSA lineshapes overlaid, with one reflected about the isotropic chemical shift δ_{iso}. Again, information about the structure can be extracted if the lineshape can be fitted, but generally, if two or more environments are present, they will overlap, causing problems for lineshape fitting.

3.4.3.3 The Quadrupolar Interaction

The quadrupolar interaction is generally the largest interaction (excluding the Zeeman interaction), and is dependent on the charge distribution of the nucleus, which becomes progressively more complex as I increases. For spin $\frac{1}{2}$ nuclei, the charge distribution is spherical, and hence the contribution is zero, since the energy is independent of the orientation of the nucleus. For nuclei with I greater than $\frac{1}{2}$, the contribution is non-zero. It is proportional to the magnitude and direction of the electric field gradient of the surrounding field. An example of this dependence in the case of a 'cigar-shaped' nucleus is given in figure 3.8.

Low energy ——

High energy - - - - -
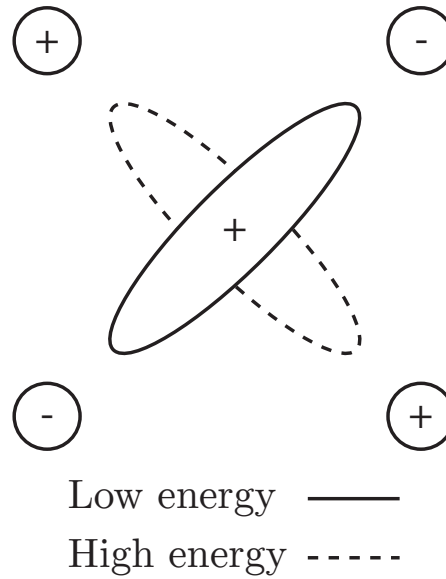
Figure 3.8 The high and low energy configuration of a 'cigar-shaped' nucleus in an EFG. The strength of the quadrupolar interaction clearly depends on the orientation of the nucleus within the EFG.

Initially we can restrict ourselves to the situation where the quadrupole interaction is an order of a magnitude smaller than the Zeeman interaction. In this case all energy levels are perturbed by the quadrupole interaction to first order.

Since the quadrupolar coupling, and hence the energy, depends on the orientation of the nucleus, any quadrupolar nucleus-containing powders will have their NMR line-shape significantly broadened, depending on the strength of the quadrupolar coupling. This is strongly related to the strength and direction of the electric field gradient (EFG) at the nucleus, which is defined in the PAS of the EFG, such that $|V_{zz}| \geq |V_{xx}| \geq |V_{yy}|$, and all other matrix elements are zero, similar to the CSA interaction described previously.

$$V = \begin{pmatrix} V_{xx} & 0 & 0 \\ 0 & V_{yy} & 0 \\ 0 & 0 & V_{zz} \end{pmatrix} \tag{3.33}$$

The quadrupolar interaction is then described in terms of the quadrupolar coupling constant

$$C_q = \frac{e^2 q_{zz} Q}{h} = \frac{eQV_{zz}}{h}, \tag{3.34}$$

and the asymmetry parameter

$$\eta_q = \frac{V_{yy} - V_{xx}}{V_{zz}}. \tag{3.35}$$

33

The strength of the quadrupolar coupling is given by

$$\Omega_q = \frac{3C_q\pi}{2I(2I-1)}, \tag{3.36}$$

where Ω_q is the energy of the quadrupolar interaction given in rad s^{-1}, also known as the quadrupolar frequency. The first order change in energy of the previously degenerate Zeeman energy levels is given by

$$\Delta E_m^{(1)} = \frac{1}{2}\Delta\omega_q(\theta,\phi)\left[m^2 - \frac{1}{3}I(I+1)\right], \tag{3.37}$$

where $\Delta\omega_q$ is given by

$$\Delta\omega_q(\theta,\phi) = \frac{1}{2}\omega_q\left[3\cos^2\theta - 1 - \eta\,\sin^2\theta\,\cos(2\phi)\right] \tag{3.38}$$

and is a function of θ and ϕ, the two Euler angles used to rotate the PAS of the quadrupolar interaction into the lab frame of the Zeeman interaction (i.e. the direction of the B_0 magnetic field). If the case of a single quantum transition is taken, the modification to the transition $m \leftrightarrow m+1$ is given by

$$\Delta\omega_{m\leftrightarrow m+1}^{(1)} = \Delta\omega_q(\theta,\phi)\left(m + \frac{1}{2}\right), \tag{3.39}$$

where m is the quantum number of the lower of the two states. Since the central transition is from $m = -\frac{1}{2}$ to $m = +\frac{1}{2}$, $\Delta\omega_{m\leftrightarrow m+1}^{(1)} = 0$. The central transition is therefore unchanged to first order, for any EFG [16, Chapter II.D].

However, in most quadrupolar cases, this simplistic first order is not sufficient to explain the lineshapes seen in experiment, and the second order perturbations must be considered. The change in energy levels as a function of m for the second order contribution is given by

$$\Delta E_m^{(2)} = -\frac{\omega_q^2}{9\omega_0}m\left\{2\left[I(I+1) - 2m^2 - \frac{1}{4}\right]\left(\frac{|V_1|}{eq}\right)^2 - \left[I(I+1) - m^2 - \frac{1}{2}\right]\left(\frac{|V_2|}{eq}\right)^2\right\}. \tag{3.40}$$

For brevity, only the modification to the central transition is given,

$$\Delta\omega_{-1/2\leftrightarrow 1/2}^{(2)} = -\frac{\omega_q^2}{9\omega_0}2m\left[I(I+1) - \frac{3}{4}\right]\times\left[2\left(\frac{|V_1|}{eq}\right)^2 - \left(\frac{|V_2|}{eq}\right)^2\right], \tag{3.41}$$

which is critically non-zero and results in the energy levels presented in figure 3.9 [15, Chapter 17.4]. As a result, the energy of the central transition is a function of angle
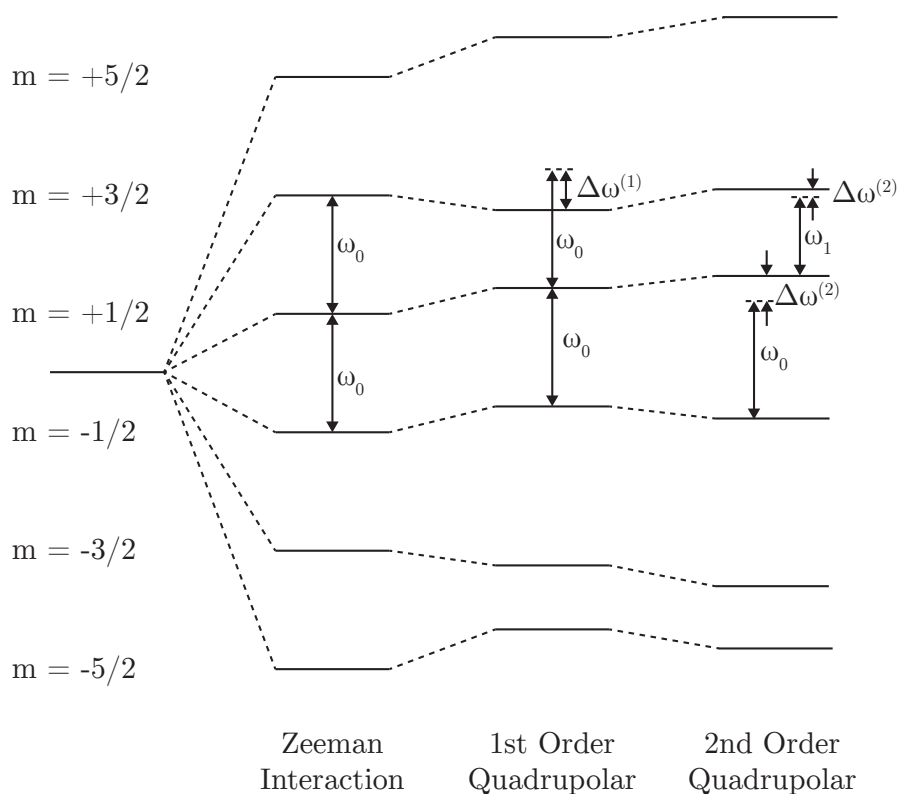
Figure 3.9   The energy levels for different *m* quantum numbers of a quadrupolar nucleus, considered with just the Zeeman interaction, and both first and second order quadrupolar interactions. The modifications to the previous energy difference are shown in the diagram.

with regards to the B_0 field. If a powdered sample is used, as is the case in this research, then a full range of angles are encountered, which results in a broadening dependent on the strength of the EFG. It can be shown (but is beyond the scope of this thesis) that the angular dependence has the form of the fourth-order Legendre polynomial: $P_4(\cos\theta)$ [21].

3.4.4   Magic Angle Spinning

Solid state NMR is a widely-practised technique, but is more involved than the solution state case. Solutions undergo rapid molecular motion and, as such, any anisotropy is averaged on a time-scale much faster than the Larmor time-scales associated with NMR. This leads to very narrow lines ($<1\,\text{ppm}$) unaffected by the broadening mechanisms presented in the three previous sections. To first order, these effects are all proportional

to a root of the second order Legendre polynomial,

$$P_2 \left(\cos \theta \right) = 0$$

$$3\cos^2\theta - 1 = 0 \tag{3.42}$$

$$\theta = 54.7°$$

If the sample is mechanically spun about an axis at 54.7° to the magnetic field, at a speed in excess of 1000 rotations a second, these interactions can be averaged out similarly to the solution case. This technique is known as magic angle spinning (MAS). Due to the effects of rotation, spinning sidebands appear at a position displaced from the 'real' peak by the spinning frequency, both to the positive and negative sides of the spectrum, with intensities governed by the envelope of the static lineshape.

Second order effects however, do not have the same angular dependence. They depend on the fourth order Legendre polynomial,

$$P_4 \left(\cos \theta \right) = 0$$

$$35\cos^4\theta - 30\cos^2\theta + 3 = 0 \tag{3.43}$$

$$\theta = 30.6°.$$

As a result, spinning a sample at a single angle where the 2nd order quadrupolar coupling is significant will not remove all broadening, and a residual broadening will remain [21]. Some advanced techniques are available to further narrow the lineshape, including dynamic angle rotation, double rotation, and multiple quantum MAS experiments, however these are not featured in this thesis.

3.4.5   NMR Experiments

There are an almost limitless number of NMR experiments that can be performed, generally with their own pulse sequences. These range from a simple single pulse experiment, to complex pulse sequences with hundreds of pulses at dynamic frequencies. At their core however, all experiments rely on manipulating the spin system in a known way, and observing the resulting spectrum. In this thesis, only a few simple pulse sequences are discussed.

3.4.5.1 Single Pulse

A single pulse is applied in the *xy* plane and acts to rotate the net magnetisation about an axis mutually orthogonal to the *z* and pulse directions. In the majority of single pulse experiments it is not necessary, and may even be detrimental, to rotate the magnetisation fully into the *xy* plane. As the magnetisation precesses about the *z* axis, it induces a current in the detection coils. Since each nucleus is at a different energy due to the interactions discussed previously, they precess at a different frequency. When the Fourier transform is performed, a spread of peaks is acquired, forming a spectrum [18].

3.4.5.2 Spin-Echo

For some systems, single pulse experiments are not ideal for collecting data. Since, in virtually all pulsed NMR experiments, the receiving coil also transmits the high power pulse, there is a period of dead time before the signal acquisition can begin due to the 'ringing' of the coil. This only lasts around 5 μs, however the relaxation of some samples can be significantly faster than this. Signals from these samples will not be detected.

To combat this effect, a technique known as a spin-echo can be used. A 90° pulse is applied, rotating the ensemble of spins into the *xy* plane. Since some spins are in a stronger magnetic field than others, they precess at a slightly higher rate than others, and the initially focussed magnetisation defocus. Once this has occurred, a 180° pulse is applied, reversing the orientation of the spins in the system. The spins now refocus, resulting in an echo. The time intervals between the two pulses is adjusted, reaching a compromise between the effects of the transverse and longitudinal relaxation [15, Chapter 11.2][16, Chapter 1.C]. Additionally, if the sample being examined has multiple environments, it must be ensured that they do not differ excessively in relaxation. If one of the environments relaxes more quickly than another, it will have a lower intensity in the resulting spectrum.

The time domain spin-echo can then be Fourier transformed as before, with the added advantage that the transform can be phased to contain a purely real spectrum, with no imaginary component. The pulse sequence is shown in figure 3.10. If a spin-echo is used in conjunction with MAS, it is vital that the evolution period τ is an integer number of rotor periods. If this is not the case, a distorted lineshape can result.
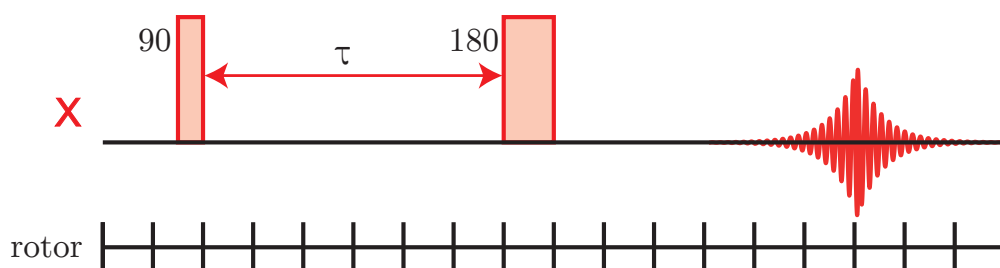
Figure 3.10   A rotor synchronised spin echo under MAS.

3.4.5.3   Heteronuclear multiple-quantum coherence

Rotary resonance recoupled heteronuclear multiple-quantum coherence (R^3-HMQC) is a multidimensional heteronuclear correlation (HETCOR) experiment which reveals through-space connectivities by virtue of the dipolar coupling inherent in the structure. The magnetisation of one nucleus is observed whilst the other is modulated in such a way as to reintroduce the desired heteronuclear couplings (dependent on distance), which are normally averaged to zero by magic angle spinning (MAS).

The simplest HMQC experiment consists of four pulses and was first demonstrated by Bax et al. [22]. A spin-echo experiment is performed on the observe nucleus, which is modulated by two pulses on the indirect nucleus creating a single quantum coherence, the length of which is incremented, providing the second time dimension. The R^3 modification consists of two pulses applied to the spin 1/2 nucleus, before and after the two HMQC pulses. The nutation frequency ν_1 of these pulses is chosen to be resonant with the MAS rotor frequency ν_R, such that $\nu_1 = q\nu_R$ and this reintroduces dipolar coupling. For HETCOR spectra, $q = 2$ is used, since then an exclusively heteronuclear coupling is recoupled [23]. The complete pulse sequence is shown in figure 3.11.

To determine the physical power level required to produce the correct nutation frequency, a spin lock-based experiment is performed. Initially a 90° pulse is applied in the x direction, resulting in a rotation of the magnetisation into the y direction. Secondly, a pulse is applied in the y direction. Since the magnetisation is already in this direction, the spin ensemble is 'held' artificially, and does not relax. If the power of this spin lock pulse is on resonance with the conditions discussed above, the relaxation occurs *via* dipolar coupling. The output from this spin lock optimisation is shown in figure 3.12 as a function of spin lock energy.
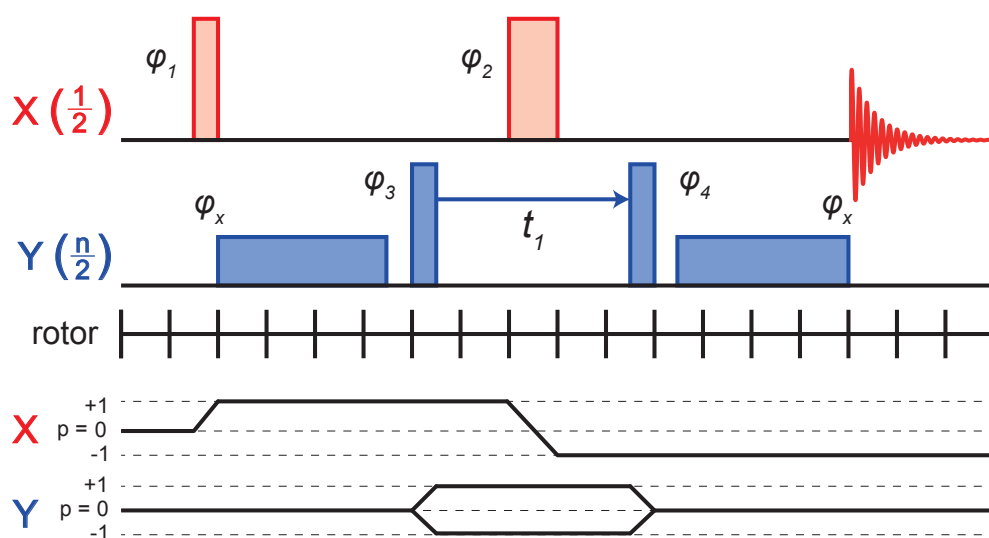
Figure 3.11 The R^3-HMQC pulse sequence for two nuclei X and Y.
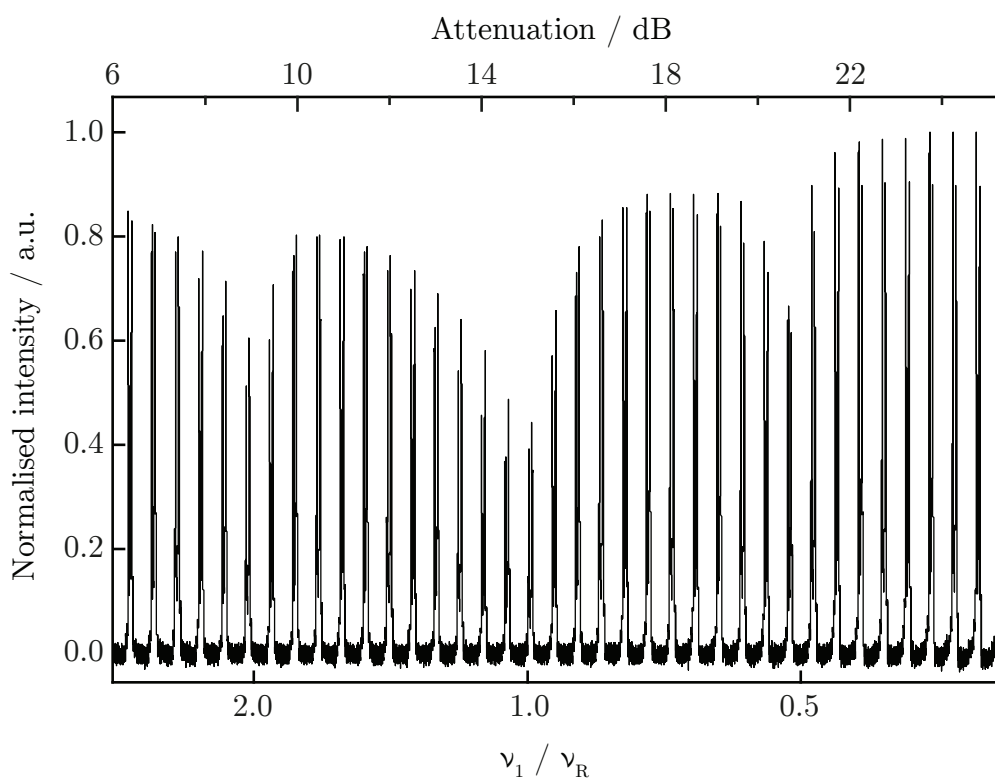
Figure 3.12 The normalised ^{31}P NMR spectral intensity of β-TCAP as a function of the power of the spin-lock pulse. The *x* axis is given in terms of the *q* resonance conditions and the attenuation in dB applied to the amplifier output in the NMR spectrometer.

3.4.5.4 Signal enhancement techniques

There are various techniques available for enhancing the signal observed in NMR experiments. In this thesis two such techniques are used, rotary assisted population transfer (RAPT) and adiabatic chirp pulses. RAPT was developed by Yao et al. [24], and enhances the signal of quadrupolar nuclei by increasing the population difference of the central transition. At equilibrium the population difference between the individual Zeeman states of the nucleus are given by the Boltzmann distribution, which at room temperature is small. A train of Gaussian pulses offset from the central transition in frequency are prefixed to the pulse sequence, which have the effect of saturating the satellite transitions. This enhances the population difference between the $m = -\frac{1}{2}$ and $m = \frac{1}{2}$ by a maximum factor of $I + \frac{1}{2}$, where I is the nuclear spin. The effect of this selective satellite saturation is shown in figure 3.13. Pulses of varying frequency, known as chirp pulses, can be used in place of the Gaussian RAPT pulses to achieve a similar effect.

3.4.6 Fitting ^{31}P NMR spectra of β-TCP

Due to the disorder inherent in the ^{31}P NMR spectrum of β-TCP, the individual resonances are broadened such that they overlap significantly. This makes fitting the spectrum a problem, since there is a high degree of correlation between the fitting parameters. To simplify the problem, some fitting parameters should be calculated independently of the spectrum. The structure of β-TCP is known, and hence the relative intensities of the resonances can be calculated. However, calculation of chemical shift is much
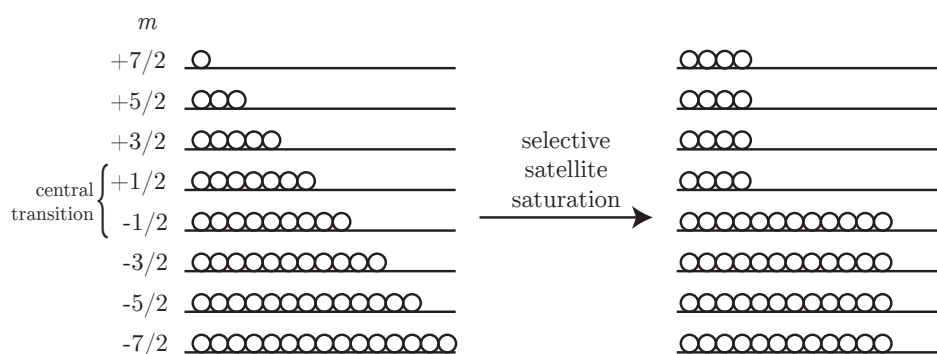
Figure 3.13 The effect of the RAPT population enhancement on a spin-$\frac{7}{2}$ nucleus.

more complex, since it is highly sensitive to subtle changes in precise bond lengths and angles in the structure and the very large unit cell requires extensive computational power.

As a result, a fit was employed where the areas of the peaks were fixed, but the line widths (and hence amplitudes) and positions were allowed to vary. It rapidly became apparent that a multitude of different results were possible, each with a fitting quality indistinguishable from one another.

Unique results *were* possible however for the four different substitutions studied throughout this thesis, since the relative areas of the peaks are modulated with composition in a predictable way based on the substitution model. All four compositional series were fitted independently and when the fits were extrapolated back to zero substitution, a common solution was found.

3.5   Raman spectroscopy

The Raman effect was discovered by C. V. Raman in 1928 [25], and is used ubiquitously as a probe of the structure of materials. The effect occurs when a sample is illuminated by a monochromatic beam of light, and the resulting scattered light is observed as a function of wavelength. The scattered light results mostly from elastic processes, however a small fraction, generally of the order of 10^{-7}, is scattered to higher and lower frequencies by an inelastic interaction. Those components at a lower frequency are known as Stokes components, and those at a higher frequency are known as anti-Stokes components. These two transitions are shown in figure 3.14. Measurements are usually made of the stronger Stokes components, due to the Boltzmann distribution [26].

The states discussed above are most commonly vibrational or rotational states occurring between atoms or groups of atoms. Some simple 'building-blocks' of materials have been well studied, for example the $[PO_4]^{3-}$ phosphate group, and their vibrations and rotations in free space are known, as well as the effects of surrounding cations. These oscillations are expressed in terms of a Raman shift Δw, measured in units of cm^{-1}, where the Raman shift is defined by

$$\Delta w = \left(\frac{1}{\lambda_0} - \frac{1}{\lambda_1} \right) \times 10^7, \tag{3.44}$$

where λ_0 is the incident wavelength and λ_1 is the scattered wavelength, both in nm.

ω ω_s ω ω_a

Raman Stokes   Raman anti-Stokes
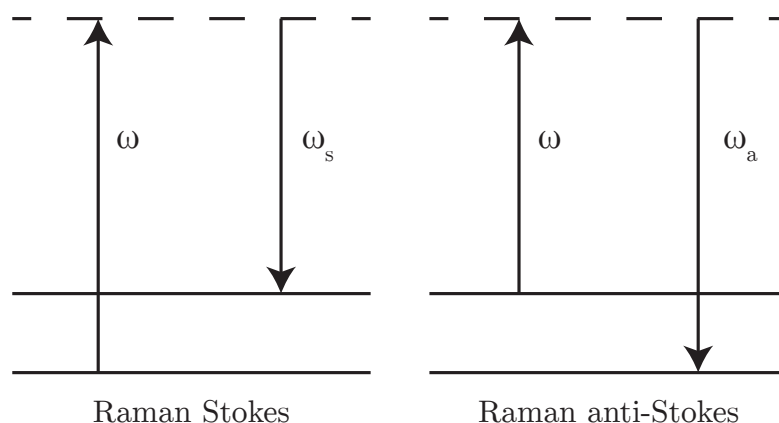
Figure 3.14 Energy level diagrams illustrating Raman Stokes and anti-Stokes scattering.

References

[1] W. L. Bragg, *Proceedings of the Cambridge Philosophical Society* **17**, (1914), 43–57.

[2] A. R. West, *Basic Solid State Chemistry* (Wiley-Blackwell, 2002), 2nd ed.

[3] R. B. Von Dreele and J. Rodriguez-Carvajal, in: *Powder Diffraction Theory and Practice*, edited by R. E. Dinnebier and S. J. L. Billinge (RSC Publishing, Cambridge, 2008), chap. 3, pp. 58–88, 1st ed.

[4] L. de Broglie, *Recherches sur la théorie des quanta*, Ph.D. thesis, Paris 1924.

[5] A. C. Hannon, in: *Encyclopedia of Spectroscopy and Spectrometry*, edited by J. Lindon, J. Holmes and G. Tranter (Academic Press, 2000), vol. 2, pp. 1479–1503.

[6] A. C. Hannon, *Nuclear Instruments and Methods in Physics Research Section A: Accelerators, Spectrometers, Detectors and Associated Equipment* **551** (1), (2005), 88–107.

[7] H. M. Rietveld, *Journal of Applied Crystallography* **2** (2), (1969), 65–71.

[8] G. S. Pawley, *Journal of Applied Crystallography* **13** (6), (1980), 630–633.

[9] G. S. Pawley, *Journal of Applied Crystallography* **14** (6), (1981), 357–361.

[10] R. A. Young, H. M. Rietveld, E. Prince, T. M. Sabine, R. J. Hill, J. W. J. Richardson and R. L. Snyder, *The Rietveld Method* (Oxford University Press, Oxford, 1993).

[11] K. Pearson, *Philosophical Transactions of the Royal Society of London. Series A, Containing Papers of a Mathematical or Physical Character* **216**, (1916), 429–457.

[12] A. A. Coelho, TOPAS Academic Technical Reference 2007.

[13] S. Ikeda and J. M. Carpenter, *Nuclear Instruments and Methods in Physics Research* **A239** (3), (1985), 536–544.

[14] A. A. Coelho, TOPAS-Academic 2007.

[15] M. H. Levitt, *Spin Dynamics: Basics of Nuclear Magnetic Resonance* (John Wiley & Sons, Chichester, 2001), 1st ed.

[16] E. Fukushima and S. B. W. Roeder, *Experimental Pulse NMR: A Nuts and Bolts Approach* (Addison-Wesley, Reading, Massachusetts, 1981), 1st ed.

[17] F. Bloch, *Physical Review* **70**, (1946), 460–474.

[18] F. Bloch, W. W. Hansen and M. Packard, *Physical Review* **70**, (1946), 474–485.

[19] J. Herzfeld and A. E. Berger, *The Journal of Chemical Physics* **73** (12), (1980), 6021.

[20] G. E. Pake, *The Journal of Chemical Physics* **16** (4), (1948), 327.

[21] A. P. M. Kentgens, *Geoderma* **80**, (1997), 271–306.

[22] A. Bax, R. H. Griffey and B. L. Hawkins, *Journal of the American Chemical Society* **105** (24), (1983), 7188–7190.

[23] J. Trébosc, B. Hu, J. P. Amoureux and Z. Gan, *Journal of Magnetic Resonance* **186** (2), (2007), 220–7.

[24] Z. Yao, H.-T. Kwak, D. Sakellariou, L. Emsley and P. J. Grandinetti, *Chemical Physics Letters* **327** (1-2), (2000), 85–90.

[25] C. V. Raman and K. S. Krishnan, *Nature* **121**, (1928), 501–502.

[26] R. W. Boyd, in: *Nonlinear optics* (Academic Press, Burlington, 2008), chap. 10, pp. 473–509, 3rd ed.

CHAPTER 4

β-TRICALCIUM PHOSPHATE

4.1 Introduction

β-TCP has a crystal structure shown schematically in figure 4.1. It belongs to the $R3c$ space group, with unit cell parameters most recently reported as $a = b = 10.4183(5)$ Å and $c = 37.346(2)$ Å [1]. There are 5 structurally distinct calcium sites with very different coordination numbers and average Ca-O bond lengths, shown in table 4.1 and figure 4.2. The structure is composed of two distinct columns in the c direction, with Ca(4), Ca(5) and P(1) sites occupying column A, and Ca(1), Ca(2), Ca(3), P(2) and P(3) sites occupying column B. The columns appear in the proportions A : B = 1 : 3 respectively. The Wyckoff positions are $18b$ for Ca(1), Ca(2) and Ca(3), and $6a$ for Ca(4) and Ca(5). Since the Ca(4) site has an occupancy factor of 0.5 to preserve charge neutrality, the 5 calcium sites appear in the ratios 18:18:18:3:6 respectively. β-TCP is stable at room temperature and pressure, and undergoes a phase transition to α-TCP at 1150 °C. There is a further poorly-defined phase change to α′-TCP over the range 1150 °C to 1775 °C, before melting at 1775 °C [2].

Numerous studies have been published on the structure of β-TCP, discussed previously in section 2.4. The purpose of the work presented in this chapter is to introduce and assess the techniques proposed for the examination of the substituted β-TCP samples, and to act as a common starting point for any observed trends. XRD and ND were used both independently, in the form of relative phase quantification and total scattering plots, and together, in a Rietveld co-refinement. ^{31}P and [43]Ca solid-state NMR was also performed; [43]Ca NMR has not been performed successfully on β-TCP and so is of great interest even when isolated from the potential applications of this work.
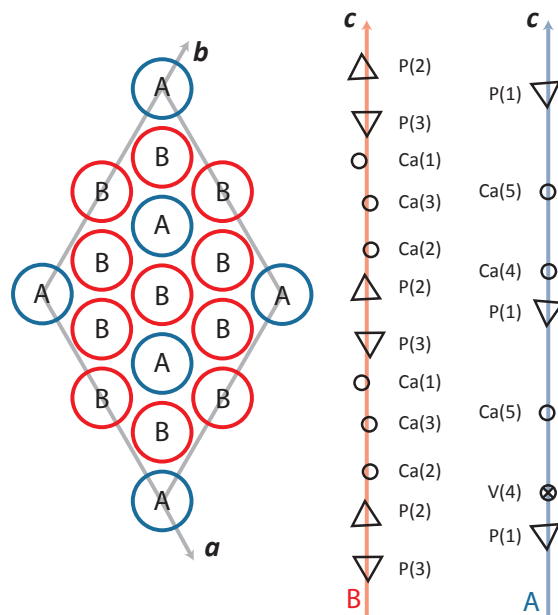
Figure 4.1 The unit cell of β-TCP shown in a simplified form. The structure of β-TCP is typified by a pair of columns in the *c* lattice direction, here labelled A and B. On the left is the unit cell viewed down the *c* axis, and on the right is a projection of the two distinct columns A and B with the a axis into the plane. Inspired by [3].

(a) Ca(1)   **(b)** Ca(2)   **(c)** Ca(3)

(d) Ca(4)   **(e)** Ca(5)
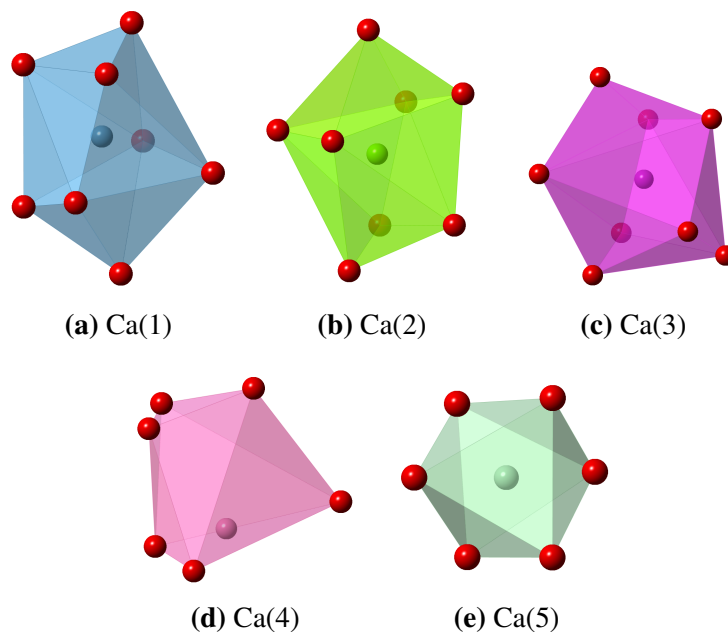
Figure 4.2 The 5 Ca-O polyhedra. All except Ca(4) are shown with *c* into the page; the Ca(4) octahedron has been rotated for clarity. Note how, in the case of Ca(4), the Ca cation is displaced towards the base of the octahedron. Based on [4].

Table 4.1 Average Ca-O bond lengths and coordination numbers from the crystal structure presented by [5].
[†] A coordination number of 3 or 6 is possible, depending on Ca-O distance cut-off used.

Ca Site	Coordination number	Average Ca-O bond length / Å [5]
Ca(1)	8	2.433
Ca(2)	8	2.481
Ca(3)	8	2.543
Ca(4)[†]	3	2.530
Ca(4)[†]	6	2.825
Ca(5)	6	2.262

4.2 Sample preparation

The β-TCP used in this study was prepared by solid-state sintering, with stoichiometric amounts of $CaHPO_4$ (Alfa Aesar, 98+ %) and $CaCO_3$ (Alfa Aesar, 99.5+ %), as in the equation

$$CaCO_3 + 2CaHPO_4 \rightarrow Ca_3(PO_4)_2 + H_2O + CO_2. \tag{4.1}$$
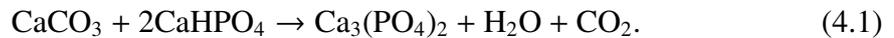
The powders were weighed on an analytical balance to ± 1 mg, before being mixed in a pestle and mortar for 10 minutes. The mixture was sintered in an alumina crucible with a heating rate of $300 \,°C \, h^{-1}$ up to $1050 \,°C$, before dwelling at this temperature for 4 hours. The temperature was then reduced to room temperature, again at $300 \,°C \, h^{-1}$. However, despite repeated mixing and re-sintering for a total of four heat treatments, a significant quantity of hydroxyapatite (HAp) still remained. It was decided to attempt a wet ball-milling method, wherein the powders are placed in a plastic container, with the addition of alumina milling balls and pure ethanol, and placed on a pair of rotating rollers. The mixture was ball-milled for 72 hours, before being dried at $70 \,°C$. The resulting powder was re-ground, in a pestle and mortar, before being heat treated as before. Both an alumina and a platinum crucible were used with the same powder mixture and heated in the same furnace concurrently, to determine if there was any aluminium diffusion from the alumina crucible into the β-TCP structure.

4.3 Experimental methods

4.3.1 X-ray diffraction

All XRD scans presented in this work unless stated otherwise were performed on a PANalytical X'Pert Pro MPD. The instrument was configured with a focussing Johansson Ge(111) monochromator, giving high resolution $CuK\alpha_1$ radiation with a wavelength of 1.5406 Å. The diffractometer was set up in Bragg-Brentano ($\theta - 2\theta$) mode, with a rotating sample stage to average any in-plane anisotropic effects. A PIXcel solid-state detector was used with an angular width of 3.347°. A step size of 0.007° was chosen over a scan range of 10° to 70° covering in excess of 100 reflections of the β-TCP structure. XRD patterns were collected for both the platinum and alumina crucible fired samples with simple lattice parameter refinements to determine if there was any difference in the lattice parameters, indicating small amounts of cation substitution.

4.3.2 Neutron diffraction

All ND scans presented in this work were performed at the ISIS pulsed neutron source located at the Rutherford Appleton Laboratory. The GEM diffractometer was used due to its very high scattering angle coverage giving excellent resolution at high Q, resulting in excellent spatial resolution. Due to time constraints only the alumina crucible fired sample was used for diffraction, due to the lower level of HAp second phase in this sample, detailed in section 4.3. The sample was loaded into an 8.3 mm vanadium can made with 25 μm foil, and the sample was weighed and the volume was measured to determine the effective density of the powder, vital for correct normalisation of the data. The data were collected until the total accumulated proton beam current had reached 1000 μA h, to ensure excellent statistics. Background scans were also collected of an empty vanadium can, a vanadium rod of known dimensions, and the empty diffractometer. The data were normalised using the GudrunN software which, in addition to normalising the data, corrects for background, absorption, inelastic and multiple scattering effects [6], resulting in a t-o-f diffraction pattern for each bank of detectors. The self-scattering was then computed and subtracted, before the data from the different detector banks were merged using the ATLAS suite of programs [7].

4.3.3 Rietveld refinement

Both XRD and ND patterns were used in a Rietveld co-refinement. Due to the complexity of the β-TCP structure and the number of reflections visible in each pattern, the order of refining certain parameters was observed to be critical in avoiding false minima and instabilities. The TOPAS-Academic software was used [8], and examples of input files and custom macros are given in appendix A. The order used for the β-TCP Rietveld refinements shown in figure 4.8 was as follows, where no variable is fixed once allowed to refine unless explicitly stated, and resulted in a system with 212 degrees of freedom:

1. XRD background terms, simple axial model, height displacement, lattice parameters, XRD scale, peakshape terms

2. Bank 4 background terms, x-axis calibration terms, peakshape terms

3. Bank 5 background terms, x-axis calibration terms (zero timing offset constrained to be equal to bank 4), peakshape terms (constrained to be equal to bank 4)

4. Ca atom positions

5. P atom positions

6. O(1-5) atom positions

7. O(6-10) atom positions

8. Ca thermal parameters (Ca(1-3) constrained to be equal)

9. P thermal parameters (P(2-3) constrained to be equal)

10. O(1-5) thermal parameters (All constrained to be equal)

11. O(6-10) thermal parameters (O(1-10) constrained to be equal)

12. Ca(1-3) occupancy (constrained to be equal)

13. Constraints lifted on O(1), O(9) and O(10)

14. Anisotropic thermal parameters added to Ca(4)

4.3.4 ^{31}P NMR

The most accessible nucleus for NMR in β-TCP is ^{31}P, due to its high abundance and non-quadrupolar nuclear spin $I = \frac{1}{2}$, which generally result in intense, narrow resonances. The ^{31}P spectrum was acquired at 202.43 MHz with a $\pi/8$ pulse length of

1.1 µs. A delay of 720 s between pulses was used despite the small tip angle, due to the long T_1 of ^{31}P NMR and the necessity for a fully quantitative spectrum. The spectra were referenced to solid ammonium dihydrogen phosphate ($NH_4H_2PO_4$) under MAS at 0.9 ppm with respect to the primary reference 85% aq. H_3PO_4.

4.3.5 ^{43}Ca NMR

One might expect that the most useful nucleus for NMR study of β-TCP would be the Ca nucleus. After all, the Ca environments are the most varied in the structure and are directly involved in cation substitution, a major topic of this research. ^{43}Ca *is* of interest, however there are a number of problems that must be overcome. The major problem is one of signal. The ^{43}Ca isotope has a very low natural abundance (0.135 %). The cost of isotopic enrichment is prohibitive, so this problem can only be mitigated, not eliminated. Additionally, ^{43}Ca has a low gyromagnetic ratio γ (-1.80×10^7 rad T^{-1} s^{-1} *cf.* ^{31}P: 10.84×10^7 rad T^{-1} s^{-1}) resulting in a relatively low polarisation. In this work a large sample size was used, combined with a high field and the RAPT pulse sequence as described in section 3.4.5.4. These steps allowed a spectrum to be collected within two days, with a signal to noise ratio of 30.

Natural abundance ^{43}Ca NMR was performed on a Bruker Avance III 850 MHz spectrometer at 57.22 MHz (20 T). A delay of 5 s between pulses was used, with 7 mm rotors at an MAS spinning rate of 5 kHz. The rotary-assisted population-transfer (RAPT)[9] sequence was included before the main excitation pulse (5 pairs of Gaussian shaped pulses offset by ±200 kHz). A 1.5 µs solids $\pi/2$ pulse was used, with 20 000 acquisitions, resulting in a total experimental time of 28 hours. The spectrum was referenced to the primary reference 0.1 mol aq. $CaCl_2 \cdot H_2O$.

4.4   Results

4.4.1   X-ray diffraction

A different time per step was used for the two different crucible fired samples due to experimental time constraints, however, the data were normalised to give an intensity in counts per second. The two diffraction patterns are shown in figure 4.3.
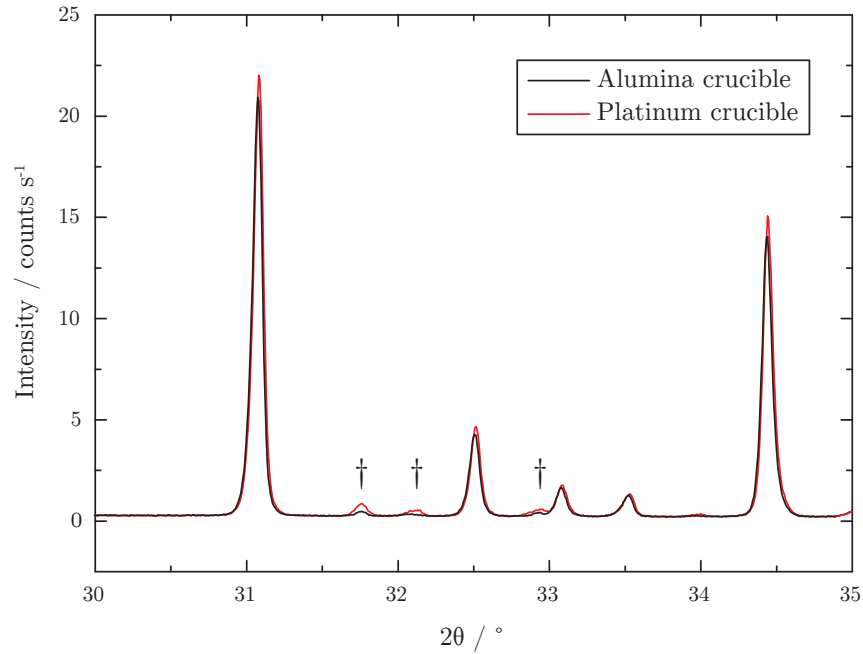
Figure 4.3 Two XRD patterns of β-TCP prepared in either a platinum crucible or an alumina crucible, after sample displacement correction. The lattice parameters and lineshapes are identical within experimental error, but there is a clear difference in the proportion of HAp second phase.

4.4.2 Neutron diffraction

The normalised reciprocal space data of the β-TCP sample are shown in figure 4.4. The data were Fourier transformed with the Lorch window function discussed in section 3.2, to reduce termination artefacts of the Fourier transform. Total scattering plots were prepared as a function of the maximum Q value, Q_{max}, to illustrate the effect which this has on the spatial resolution, and are shown in figure 4.5.

The P-O correlation was fitted to extract the coordination number of the P environment n_{PO}, which refined to 3.93(2). The fit is shown in figure 4.7.
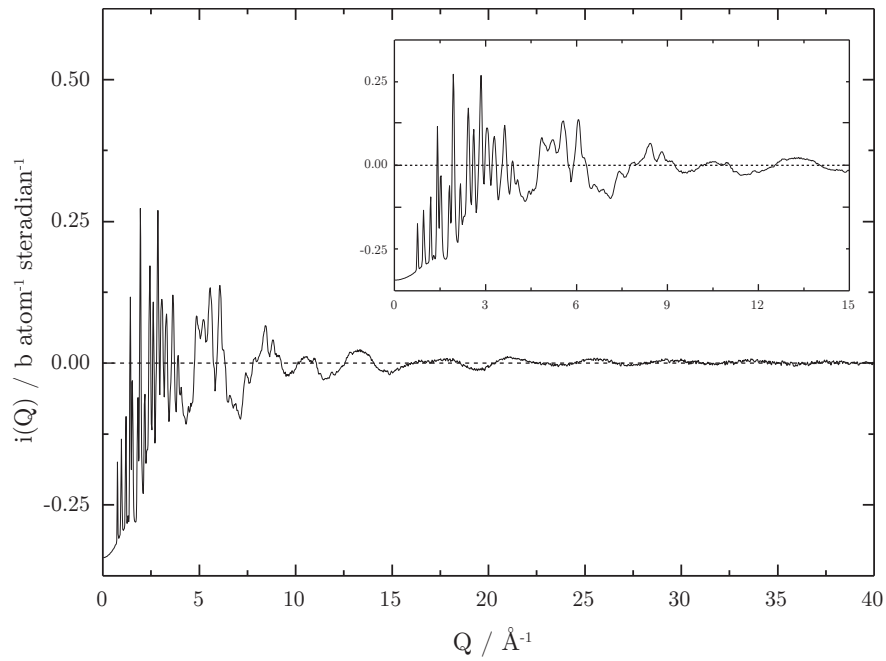
Figure 4.4 The distinct scattering $i(Q)$ as a function of Q. The region from $0 < Q < 0.5$ has been fitted to a polynomial function to remove any discontinuities at low Q.
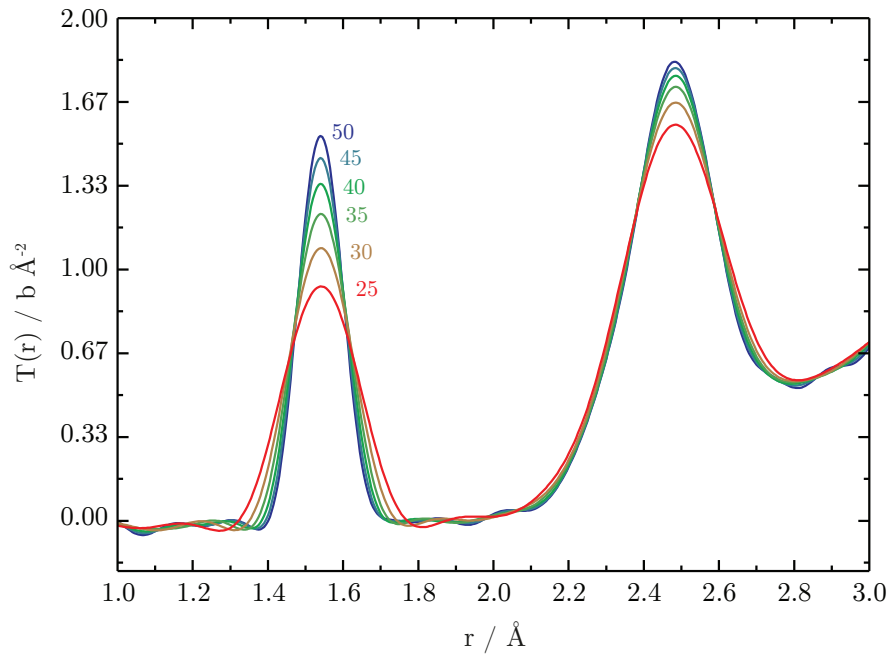
Figure 4.5 Total scattering plots of β-TCP as a function of Q_{max}. As Q_{max} decreases the spatial resolution worsens, and the positions of the small features either side of the main peaks move, confirming them as Fourier transform artefacts.
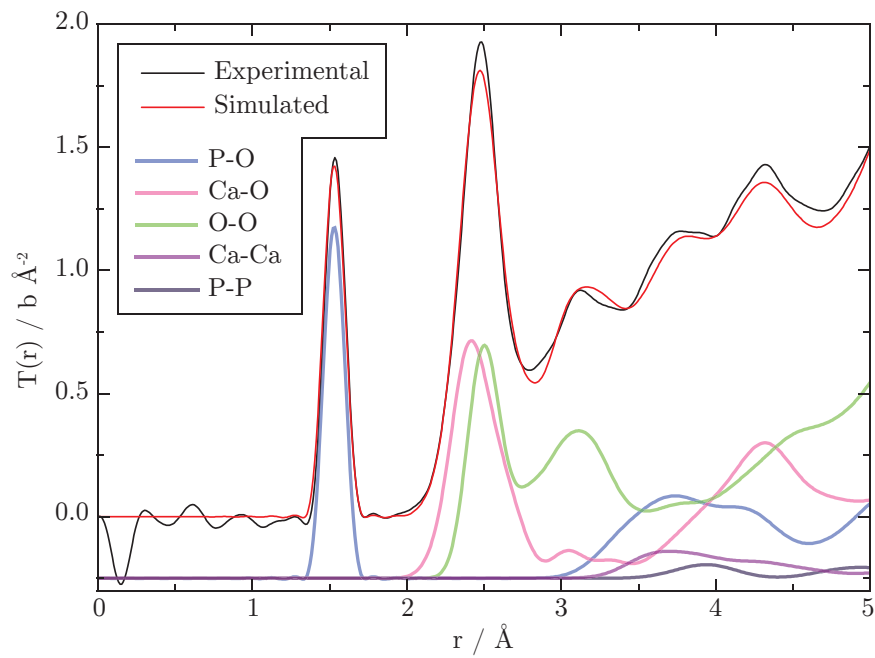
Figure 4.6 A simulation of the total scattering for β-TCP, based on the structure presented by Yashima et al. [5], where Q_{max} is set to $40\,\text{Å}^{-1}$, and the Lorch window is used. The individual correlations are labelled.
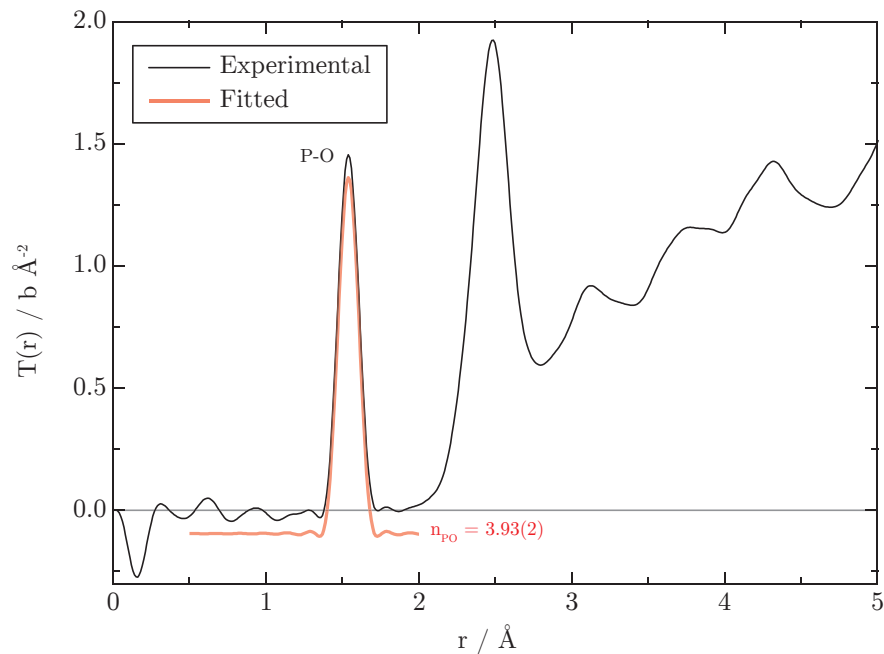
Figure 4.7 A fit of the total scattering plot where Q_{max} is set to $40\,\text{Å}^{-1}$. The fitted P-O correlation is labelled, and the resulting coordination number n_{PO} was calculated as 3.93(20). The fit is displaced $-0.1\,\text{b}\,\text{Å}^{-2}$ from zero.

4.4.3   Rietveld Refinement

A combined XRD and ND approach was taken when analysing the β-TCP structure, due to the relative merits of each technique discussed in section 3.3. The lattice parameters refined to $a = 10.4135(2)$ Å, $c = 37.376(1)$ Å. The uncertainties were estimated based on the difference between the alumina and platinum crucible fired samples. The resulting fits are shown in figure 4.8, and the structural parameters are shown in table 4.2.

Table 4.2   The structure of β-TCP from Rietveld refinement. The Ca(4) anisotropic thermal parameters are shown below the table.

Site	x	y	z	Species	Occupancy	U_{iso}
Ca1	0.725 87(62)	0.848 05(182)	0.167 06(59)	Ca^{2+}	1.0180(49)	0.5026(375)
Ca2	0.616 05(52)	0.797 33(181)	−0.032 39(38)	Ca^{2+}	1.0180(49)	0.5026(375)
Ca3	0.729 10(45)	0.843 85(143)	0.061 69(37)	Ca^{2+}	1.0180(49)	0.5026(375)
Ca4	0	0	−0.082 98(76)	Ca^{2+}	0.5	†
Ca5	0	0	0.734 79(47)	Ca^{2+}	1	1.7783(2679)
P1	0	0	0	P^{5+}	1	1.7440(4444)
P2	0.680 34(200)	0.863 40(167)	0.867 81(56)	P^{5+}	1	0.5263(323)
P3	0.649 59(102)	0.855 80(159)	0.766 93(40)	P^{5+}	1	0.5263(323)
O1	0.721 54(93)	−0.090 84(138)	−0.092 97(48)	O^{2-}	1	1.5553(789)
O2	0.758 22(200)	0.773 31(157)	0.855 04(48)	O^{2-}	1	1.0400(232)
O3	0.723 61(144)	0.011 80(194)	0.845 49(56)	O^{2-}	1	1.0400(232)
O4	0.520 94(177)	0.758 31(235)	0.857 44(38)	O^{2-}	1	1.0400(232)
O5	0.603 55(148)	−0.040 34(223)	0.778 27(50)	O^{2-}	1	1.0400(232)
O6	0.579 07(46)	0.691 93(226)	0.784 25(21)	O^{2-}	1	1.0400(232)
O7	0.079 11(42)	0.899 98(43)	0.776 14(19)	O^{2-}	1	1.0400(232)
O8	0.628 26(40)	0.823 47(50)	0.726 86(17)	O^{2-}	1	1.0400(232)
O9	0.010 81(55)	0.869 06(36)	−0.012 13(21)	O^{2-}	1	1.6828(4185)
O10	0	0	0.043 52(29)	O^{2-}	1	1.6562(9493)

† $U_{11} = 0.000\,02(532)$, $U_{22} = 0.000\,02(532)$, $U_{33} = 0.119\,40(3863)$, $U_{12} = 0.000\,00(266)$, $U_{13} = 0$, $U_{23} = 0$
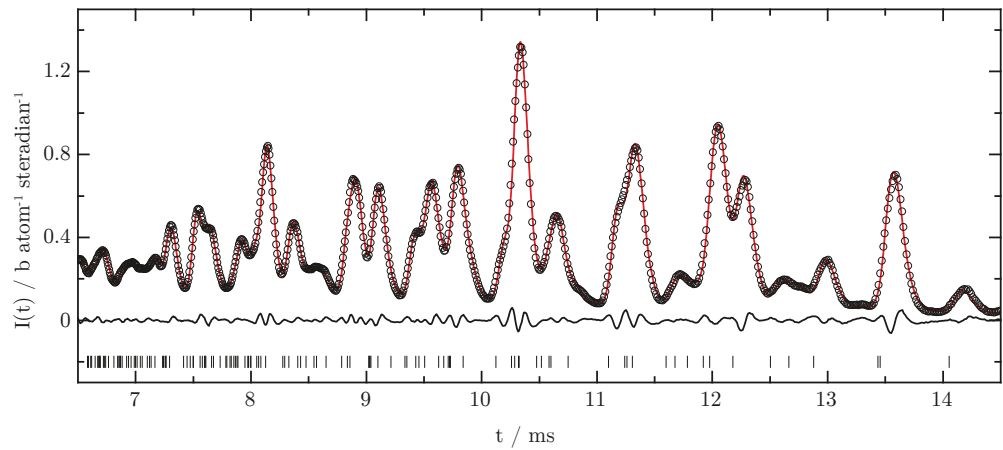
(a) ND: Bank 4
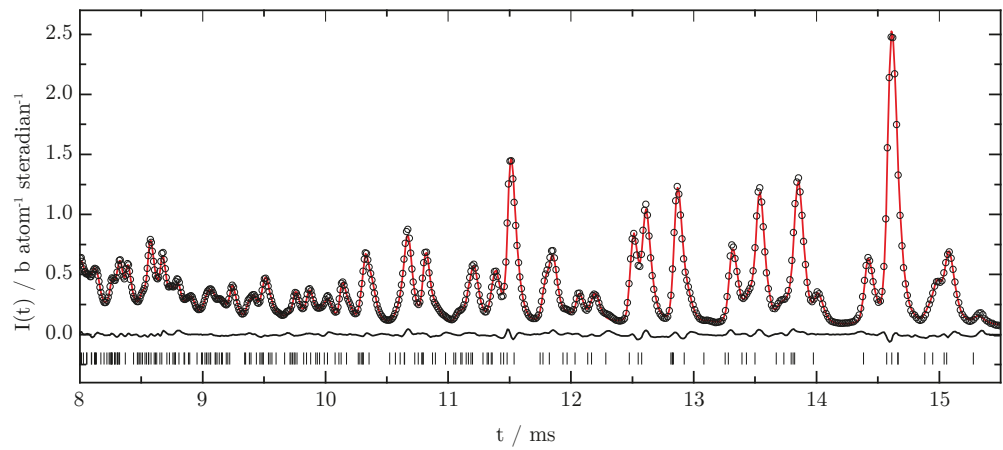
(b) ND: Bank 5
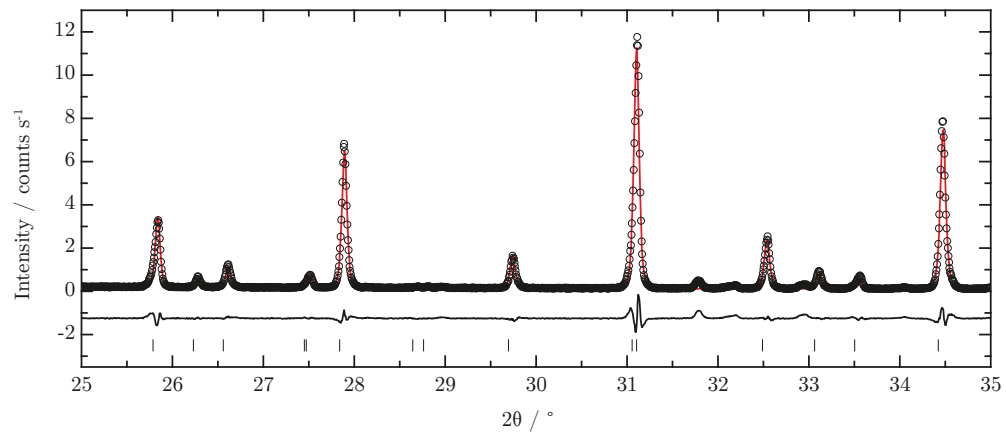
(c) XRD

Figure 4.8 Results of Rietveld refinement for β-TCP, with two ND data sets, and an XRD dataset. Data points are shown in blue, the fit is shown in black, the residual is shown in grey, and reflections are shown as tick marks.

4.4.4 ^{31}P NMR

The β-TCP spectrum is shown in figure 4.9 and compared with a tightly constrained iterative fit made using 5 Gaussian profiles, corresponding to the 5 sites as explained in figure 4.10. During the fitting procedure each peak was allowed to optimise individually in terms of its position, intensity and line width. Peaks were only allowed to refine individually due to instabilities and high degrees of correlation caused by the complexity of the spectrum. The fitting was performed in the Bruker TopSpin software, and the resulting fitted parameters are given in table 4.3.

The importance of allowing complete relaxation between pulses was shown, since different regions of the spectrum have different T_1 relaxation times. An example of two spectra collected with different pulse delays is shown in figure 4.11. The difference in the integrated areas of the two spectra is only 3 %, however this could be a significant proportion of an individual, saturated environment.
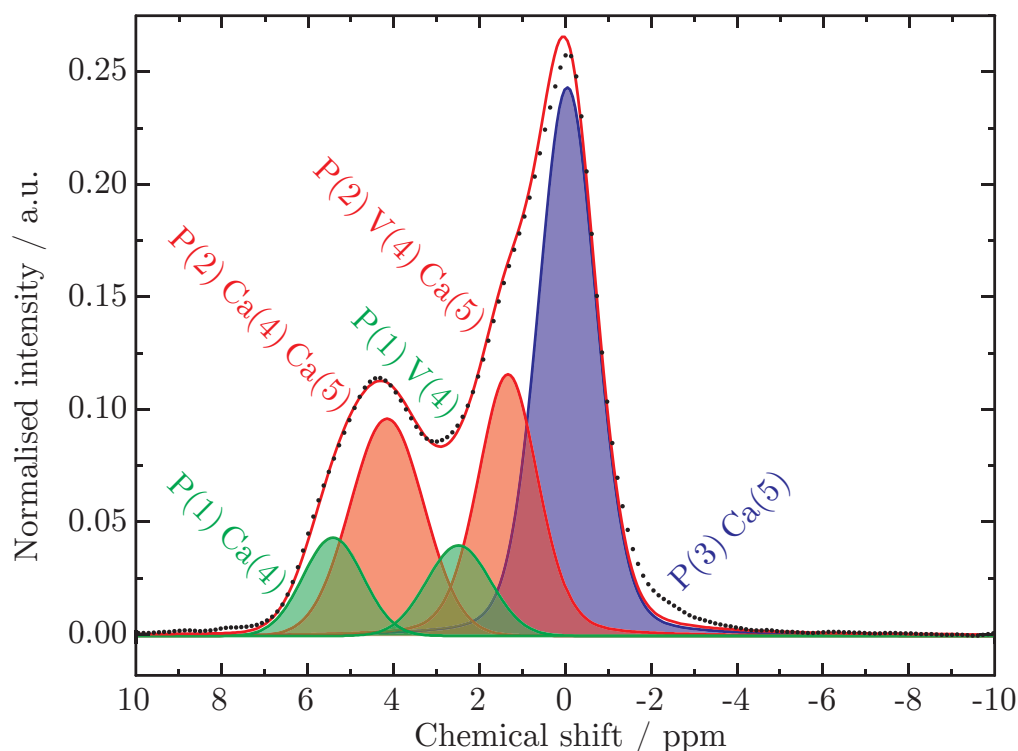
Figure 4.9 The ^{31}P NMR spectrum of β-TCP, compared with a fit made to five Gaussian profiles, with areas constrained by the model shown in figure 4.10.

Table 4.3   Results of the ^{31}P NMR fit shown in figure 4.9. Results previously published by Obadia et al. [10] are given for comparison.

Phosphorus Site	δ_{iso} ±0.1 ppm	FWHM ±10 Hz	Observed Area ±1 %	Predicted Area / %	Area in Obadia et al. / %
P(1) V(4)	2.9	350	7.5	7.0	4.2
P(1) Ca(4)	5.7	375	7.0	7.0	7.1
P(2) V(4) Ca(5)	1.6	400	22.0	21.5	19.1
P(2) Ca(4) Ca(5)	4.4	470	21.5	21.5	22.8
P(3)	0.2	400	42.0	43.0	46.8
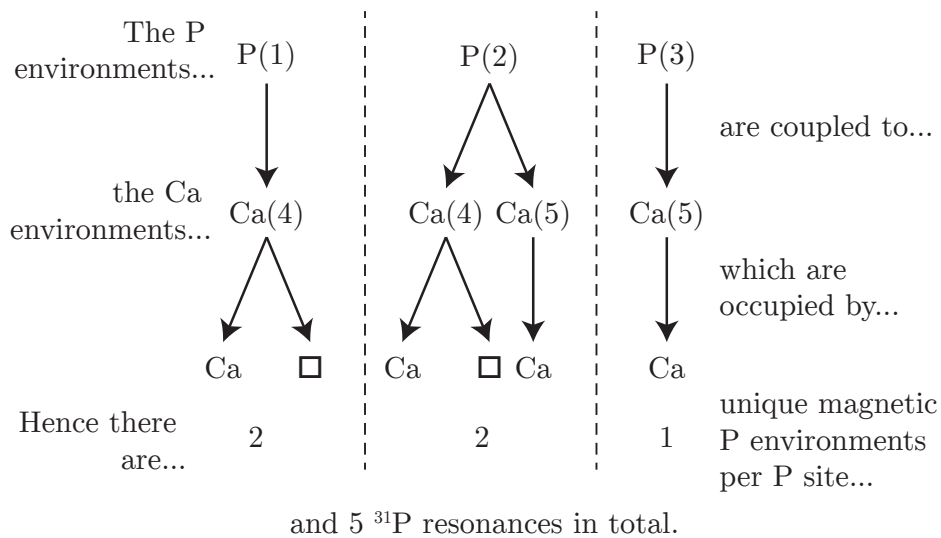
Figure 4.10   An illustration showing how the 3 crystallographic P sites give rise to 5 ^{31}P resonances.
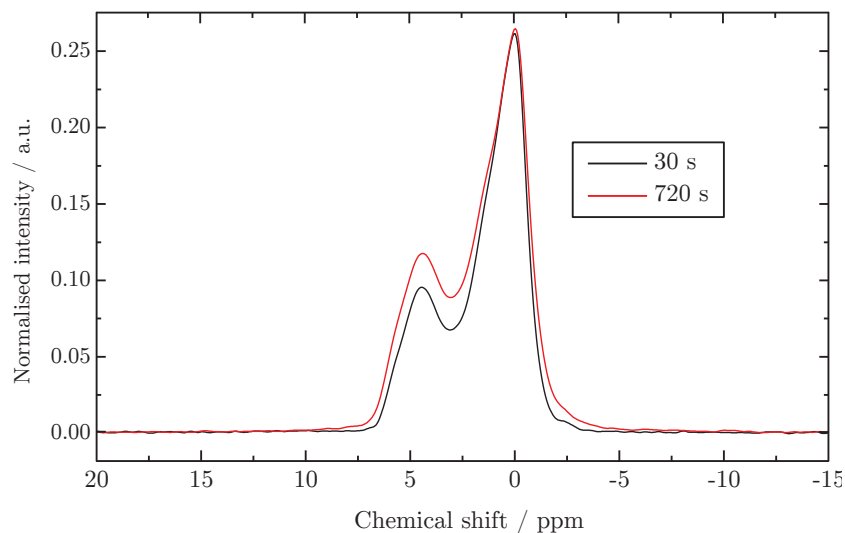
Figure 4.11   Two ^{31}P β-TCP spectra collected with different relaxation times. The environments at higher chemical shift are not fully relaxed with a shorter pulse delay, resulting in the saturation of some environments and a reduction in their intensity.

4.4.5 ^{43}Ca NMR

The ^{43}Ca NMR spectrum shown in figure 4.12 was fitted to 5 Gaussian lineshapes, with areas constrained by the relative multiplicities of the Ca sites in the β-TCP structure.
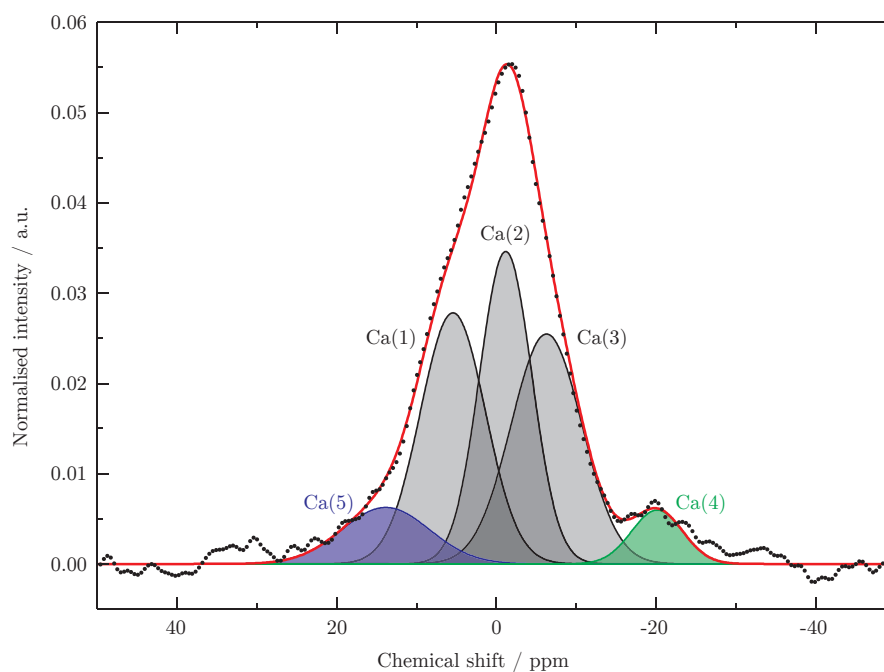
Figure 4.12 A ^{43}Ca NMR spectrum of β-TCP, fitted to 5 Gaussian profiles. A similar colour coding is used to figure 4.9, where the Ca and P environments share colours if they are the exclusive nnn of each other.

Table 4.4 Areas of the peaks in figure 4.12. The parameters correspond closely to those expected for pure β-TCP. Gaussian lineshapes were used in the fit, with the area column rounded to 0.5 % precision.

Ca Site	δ_{iso} ± 0.5 / ppm	FWHM ± 10 / Hz	Observed Area ± 1 %	Predicted Area / %	Average Ca-O Bond Length / Å [5]
Ca(1)	5.7	550	29.0	28.5	2.433
Ca(2)	−1.0	440	29.0	28.5	2.481
Ca(3)	−6.1	600	28.5	28.5	2.543
Ca(4)	−20.0	430	5.0	5.0	2.825
Ca(5)	14.0	740	8.5	9.5	2.262

4.5 Discussion

4.5.1 The crucible material

HAp second phase is visible in the XRD patterns of both samples (figure 4.3), denoted by [†], however the relative amount of HAp is greater in the platinum crucible fired sample. It is possible that this is due to a temperature gradient within the furnace (since the crucibles were placed one in front of the other), or is a direct result of the different crucible materials. A difference in the heights of the β-TCP reflections is also visible, albeit by a lesser factor than the difference between the HAp reflections. There is very little difference between the strain and particle size in the phases however, since the peak shapes vary by less than the step size. Critically, however, there is no difference in lattice parameters, indicating no diffusion of Al from the alumina crucible into the β-TCP structure. Therefore, due to the significantly reduced amount of HAp second phase and the availability of alumina crucibles, these were used for the sample preparation throughout this work.

4.5.2 Short range structure

One of the major ongoing questions related to the structure of β-TCP is the *disorder* intrinsic in the structure, and whether there is any evidence of a reduction of this disorder under substitution. ND is used extensively as a probe of short-range structure in amorphous materials, and hence has been employed here. Specifically, the ND patterns were transformed into real space to investigate the structure on the order of individual atoms.

For neutron diffraction, it was decided that a Q_{max} of $40\,\text{Å}^{-1}$ gave an ideal compromise between spatial resolution and termination artefacts, and hence was chosen for all subsequent ND data processing. The P-O correlation can be labelled unambiguously, due to its characteristic bond length of ~1.5 Å distinct from any other correlations. The Ca-O and O-O correlations however, are too similar in r to be assigned from figure 4.5 alone. Brese & o'Keeffe [11] published tables of experimentally determined bond-valence parameters, which can be used to give approximate values for the 6 and 8 coordinated Ca-O correlation lengths, however the O-O coordination is unique to the

geometry of the material. A T(r) plot was simulated using the structure previously published by Yashima et al. [5]. The XTAL program was used, which calculates radial distribution functions from the structure, and then broadens the resulting plot to simulate thermal motion and finite resolution [12]. The results of this simulation are shown in figure 4.6, with the individual correlations labelled.

The simulation is similar to the experimental data, showing direct evidence that the T(r) plot has been correctly prepared and is a good representation of the structure. A feature of the simulation, and hence the T(r) plot itself, is the nature of the peak widths as a function of r. Two thermal parameters were used for each correlation to model the random thermal vibrations of the atoms in the lattice, with a smaller parameter at short r and a larger parameter at long r. Since the bonding between nearest neighbours is very strong, the atoms within the first coordination shell of each other tend to behave as a rigid body, and so the distance between these atoms does not change significantly. This rigid body behaviour breaks down rapidly however, such that atoms which are more than 3 Å distant vibrate approximately independent of each other.. Since there is no correlation between their vibrations, the distance between them can vary over a greater range than that for nn, and the broadening is correspondingly larger.

The coordination number for P-O obtained from the fit is 3.93(2), which is close to the expected, or 'crystallographic' value of 4, given by the orthophosphate $[PO_4]^{3-}$ structure of the crystal. The value is not exactly equal to from the the crystallographic value however. This is probably a systematic error related to the technique, since total scattering plots of phosphate glasses by Hoppe et al. [13] show a similar effect. Orthophosphate-based glasses are shown to have P-O coordination numbers of 3.9(1), which again are differ by similar amount from the nominal value of 4.

4.5.3   Rietveld refinement

Any reduction in the constraints applied to the Rietveld co-refinement, or any additional refinement of the Ca(4) or Ca(5) occupancy resulted in an unstable system. The constraints were only enforced where the atoms were in similar environments, for example the 8 coordinated Ca(1,2,3) atoms, and the P(2,3) atoms which were not on special positions. Anisotropic thermal parameters were required on the Ca(4) site, otherwise non-physical U_{iso} values resulted on oxygen sites. It is unlikely that the anisotropic

thermal parameters have any physical meaning, but are merely included to correct for the short range disorder known to exist on the Ca(4) site caused by the partial occupancy. However, there is an indication of a displacement in the z direction only, which is consistent with the column-type structure of β-TCP. Most elements of the correlation matrix were small, except the z atomic positions which showed a strong positive correlation. This is again due to the columnar structure of β-TCP, and as such cannot be easily mitigated.

These issues and instabilities were reflected in the size of the χ^2 parameters for the individual datasets and the refinement as a whole. The χ^2 values were 2.257, 8.200, and 7.087 for the XRD, bank 4, and bank 5 ND data sets respectively. Generally a value over $\chi^2 = 2$ is considered to be a poor fit, and it is clear that in this case all χ^2 parameters are above this threshold. The most significant reason for this is due to the HAp second phase present in the sample. The TOPAS software does not allow a multiphase refinement with multiple data banks, and as a result it was not possible to perform a co-refinement with a correct model for the system. To mitigate this limitation, multiphase Rietveld refinements were performed on each data bank separately, resulting in very similar structures to the combined refinement. The lattice parameters for the XRD-based refinement were found to be a =10.4136(2) Å, c =37.375(1) Å, i.e. identical to the co-refinement, and results from the ND refinements were found to be a =10.410(12) Å, c =37.380(4) Å and a =10.413(6) Å, c =37.38(2) Å for bank 4 and 5 respectively, which are consistent with the combined results presented above, albeit with much larger uncertainties. Importantly, this treatment produced a significant reduction in the χ^2 parameters, reducing the values to 1.682, 3.612 and 4.025 again for the XRD, bank 4, and bank 5 ND data sets respectively.

The ND χ^2 parameters were still somewhat larger than would be expected for an ideal fit, and various methods were attempted to reduce this parameter, including optimisation of the peakshape and changes to the step size and scan ranges. A similar result was observed in a previous thesis by Mee [14], where it was assigned to a combination of an issue with the Ikeda-Carpenter peakshape and disorder in the β-TCP structure. The second explanation seems likely, however any deviation from the published structures would have to be extremely subtle, so as to only be observable with ND.

In terms of assessing the accuracy of the Rietveld refinement presented here, four

Table 4.5   Published sets of unit cell parameters for β-TCP. The results are presented in chronological order.

Publication	a / Å	c / Å
Frondel (1941) [15]	10.25(3)	36.9(1)
Dickens et al. (1974) [16]	10.439(1)	37.375(6)
Yashima et al. (2003) [5]	10.4352(2)	37.4029(50)
Ermrich & Peters (2006) [1]	10.4183(5)	37.346(2)
This work	10.4135(2)	37.376(1)

published unit cells are shown in table 4.5. There is significant difference in the most precise published data by Yashima et al. and Ermrich & Peters, even when accounting for their quoted experimental errors. This difference is of a similar magnitude to that between these parameters and the results presented here, hence indicating consistency between this sample of β-TCP and those previously examined. It is likely that the differences between the parameters presented in table 4.5 are due to a possible ordering of the vacancies in the structure and possible cation substitution in quantities too small to observe directly.

A T(r) plot was simulated as a comparison between published data and the structure resulting from the Rietveld refinement described above, using the method presented in section 4.4.2. This plot is shown in figure 4.13. There are subtle differences caused in most part by error in the oxygen positions. This is visible as a significant difference in the O-O correlation and smaller differences in the P-O and Ca-O correlations, in contrast to excellent agreement in the P-P and Ca-Ca correlations. This is due to the complex and overlapping nature of the patterns, caused by the low symmetry of the oxygen sites and the broad reflections in the t-o-f ND data.

4.5.4   A novel form of β-TCP

A potential candidate for this deviation from the established structure of β-TCP has recently been discovered, first observed with ^{31}P NMR by Obadia et al. [10], and subsequently with electron diffraction and synchrotron XRD by Mellier et al. [17]. The XRD pattern of this novel phase appears identical to the conventional β-TCP pattern apart from two extremely weak reflections at low d spacing, indicating a lower symmetry superstructure.
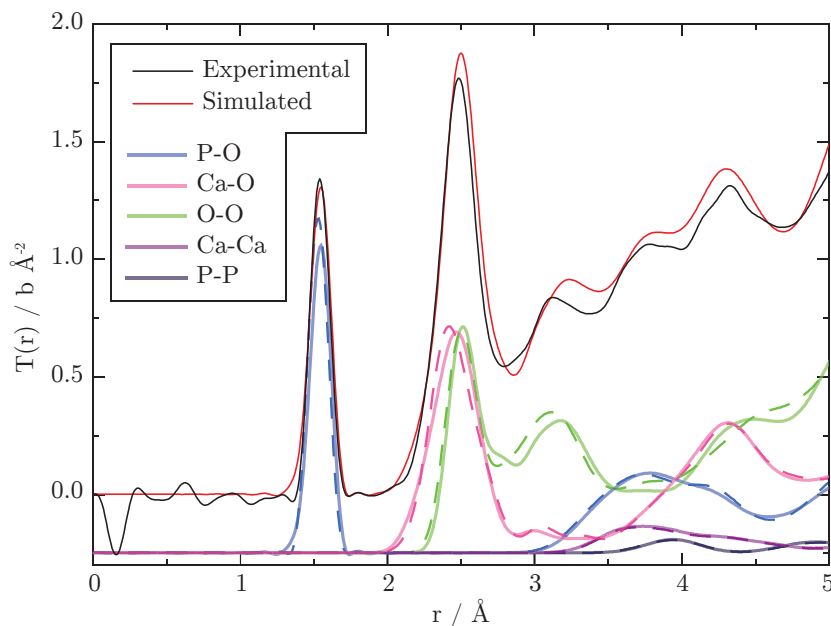
Figure 4.13 A total scattering simulation of the β-TCP structure from Rietveld refinement in table 4.2. The individual correlations plotted in figure 4.6 are shown as dashed lines for comparison.

This novel phase had also been prepared by a previous student of the group as a result of an alternative synthesis route using ammonium dihydrogen phosphate, however at the time it was mistakenly identified as α-TCP due to the superficial similarities of the ^{31}P NMR spectra. This sample was subsequently re-examined by the author to determine if the low d reflections observed by Mellier et al. were visible on a laboratory XRD instrument. A scan was performed on this sample over a range of 2° to 20°, with a step size of 0.007°. A time of 8000 s per step was used, resulting in a total experimental time of 14 hours. The reflections were observed at 12.7 Å and 10.6 Å, consistent with the results presented by Mellier et al. The XRD plot is compared to an XRD pattern of the β-TCP sample used throughout this chapter, and both are shown in figure 4.14. A $\log_{10}$ scale has been used to emphasize the low intensity reflections. There was no evidence of Bragg reflections over this range in the conventional β-TCP pattern, however a broad feature was visible at a similar d spacing. This indicates a slight deviation from the established structure of β-TCP on long-range distance scales. There is potential for this modification of the structure to affect the ND diffraction pattern, however the nature of this modification is beyond the scope of this work. For the rest of the thesis, the conventional β-TCP structure is assumed to be a sufficiently accurate representation, and as such the novel phase is not examined further.
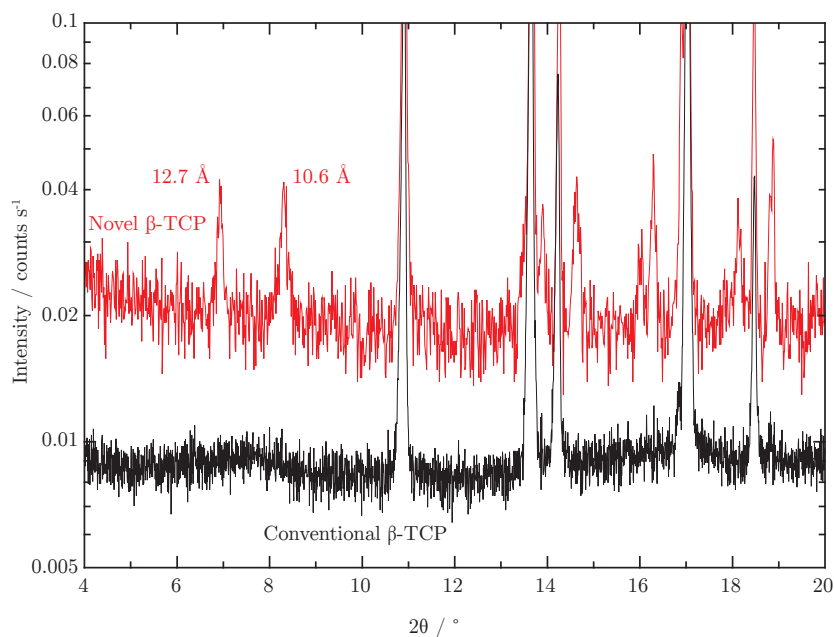
Figure 4.14 Diffraction patterns of the conventional and novel β-TCP samples. The extra reflections in the novel pattern above 10° are due to HAp second phase. Between 6° and 9° two reflections are seen in the novel sample, compared to a broad feature in the conventional sample.

4.5.5 Analysis of the NMR spectra

4.5.5.1 ^{31}P NMR

An assignment of the P(3) site to the magnetic environment at highest field can be made unambiguously with only the information in figure 4.9, since this is the most intense environment in the spectrum corresponding to the most abundant P site in the structure. The P(1) and P(2) sites are coupled to Ca(4) sites and hence, due to the partial occupancy of the Ca(4) site, each of the P(1) and P(2) sites have two magnetic environments. To determine which peaks are due to which environment, it is necessary to use the results which are presented in subsequent chapters, where the presence of substituted cations in the β-TCP structure modulates the areas of the P(1) and P(2) environments. Using this additional information, the spectrum in figure 4.9 can be assigned entirely.

This fit is in contrast to results previously published by Jakeman et al. [18] and Obadia et al. [10]. The deconvolution presented in Obadia et al. specifically uses a variety of linewidths and of pseudo-Voigt lineshapes, ranging from almost fully Gaussian to fully Lorentzian. The deconvolution presented in figure 4.9 is physically more realistic,

since the peaks from the different environments all have a similar line width and shape, which mirrors the similarity of the P environments in the structure. In addition, the fitting parameters can be used as a starting condition for the spectra for various cation substituted β-TCP systems, examined in subsequent chapters.

4.5.5.2 [43]Ca NMR

Due to the quadrupolar nature of the [43]Ca nucleus, the spectrum consists of a single broad feature, lacking the structure in the ^{31}P NMR spectrum presented above. Despite [43]Ca being a quadrupolar nucleus, Gaussian lineshapes were sufficient to fit the spectrum due to the large chemical shift dispersion masking any quadrupolar structure in the lineshapes. The resonances can be assigned to specific Ca sites by using the relationship between average Ca-O bond lengths [5] and chemical shifts presented by Gervais et al. [19]. The results of the fit are given in table 4.4. The correct position of the Ca(4) resonance results when the Ca(4) environment is assumed to be 6 coordinated, with 3 O sites at 2.53 Å, and 3 at 3.12 Å (*cf.* table 4.1).

4.6 Summary

β-TCP was successfully prepared as a pure material with < 1 mol% HAp second phase only after ball milling in ethanol prior to heating; mixing in a pestle and mortar was not sufficient to produce a single-phase product. It was then possible to perform a Rietveld co-refinement based on XRD and ND data where a stable minimum was reached, giving a structure consistent with previously published data. A significant deviance was observed in the ND patterns from the structure determined from XRD, potentially due to an ordering of the Ca(4) vacancies which is ND sensitive, but XRD insensitive.

The ^{31}P NMR spectrum of β-TCP was fitted to 5 Gaussian profiles. This fit differs from previously published data, however the result presented here appears more physically realistic. Additionally, the pure β-TCP simulation can be used as a basis for the spectrum of substituted simulations. A natural abundance [43]Ca NMR spectrum of β-TCP was collected, and fitted to 5 Gaussian profiles, again consistent with the crystallographic structure of β-TCP. The assignment of the environments could be made based on a published correlation between [43]Ca chemical shift and Ca-O bond length.

References

[1] M. Ermrich and F. Peters, *Materialwissenschaft und Werkstofftechnik* **37** (6), (2006), 526–529.

[2] R. Enderlea, F. Gotz-Neunhoeffer, M. Gobbels, F. A. Müller and P. Greil, *Biomaterials* **26**, (2005), 3379–3384.

[3] K. Yoshida, H. Hyuga, N. Kondo, H. Kita, M. Sasaki, M. Mitamura, K. Hashimoto and Y. Toda, *Journal of the American Ceramic Society* **89** (2), (2006), 688–690.

[4] E. E. Jay, P. M. Mallinson, S. K. Fong, B. L. Metcalfe and R. W. Grimes, *Journal of Nuclear Materials* **414** (3), (2011), 367–373.

[5] M. Yashima, A. Sakai, T. Kamiyama and A. Hoshikawa, *Journal of Solid State Chemistry* **175** (2), (2003), 272–277.

[6] A. K. Soper, *GudrunN and GudrunX : programs for correcting raw neutron and X-ray diffraction data to differential scattering cross section*, Tech. Rep. RAL-TR-2011-013, Rutherford Appleton Laboratory, Harwell, Oxford 2011.

[7] A. C. Hannon, W. S. Howells and A. K. Soper, *Institute of Physics Conference Series* **107**, (1990), 193–211.

[8] A. A. Coelho, TOPAS-Academic 2007.

[9] Z. Yao, H.-T. Kwak, D. Sakellariou, L. Emsley and P. J. Grandinetti, *Chemical Physics Letters* **327** (1-2), (2000), 85–90.

[10] L. Obadia, P. Deniard, B. Alonso, T. Rouillon, M. Julien, D. Massiot, B. Bujoli and J.-M. Bouler, *Chemistry of Materials* **18** (7), (2006), 1425–1433.

[11] N. E. Brese and M. O'Keeffe, *Acta Crystallographica Section B Structural Science* **47** (2), (1991), 192–197.

[12] A. C. Hannon, *XTAL: A program for calculating interatomic distances and coordination numbers for model structures*, Tech. rep., Rutherford Appleton laboratory, Harwell, Oxford 1993.

[13] U. Hoppe, R. K. Brow, B. Tischendorf, A. Kriltz, P. Jóvári, A. Schöps and A. Hannon, *Journal of Non-Crystalline Solids* **353** (18-21), (2007), 1802–1807.

[14] M. Mee, *Trivalent cation substitution of β-tricalcium phosphate*, Ph.D. thesis, University of Warwick 2011.

[15] C. Frondel, *American Mineralogist* **26** (3), (1941), 145–152.

[16] B. Dickens, L. W. Schroeder and W. E. Brown, *Journal of Solid State Chemistry* **10** (3), (1974), 232–248.

[17] C. Mellier, F. Fayon, V. Schnitzler, P. Deniard, M. Allix, S. Quillard, D. Massiot, J.-M. Bouler, B. Bujoli and P. Janvier, *Inorganic Chemistry* **50** (17), (2011), 8252–60.

[18] R. J. B. Jakeman, A. K. Cheetham, N. J. Clayden and C. M. Dobson, *Journal of Solid State Chemistry* **78** (1), (1989), 23–34.

[19] C. Gervais, D. Laurencin, A. Wong, F. Pourpoint, J. Labram, B. Woodward, A. P. Howes, K. J. Pike, R. Dupree and F. Mauri, *Chemical Physics Letters* **464** (1-3), (2008), 42–48.

CHAPTER 5

ZINC SUBSTITUTION

5.1 Introduction

The substitution of Zn^{2+} into the β-TCP structure is investigated here because it is a major component of one of the four waste streams produced in the pyrochemical reprocessing of nuclear waste, as outlined in section 2.3. It is therefore essential to understand the effect which this substitution has on the structure of β-TCP, which may affect its long term stability.

Kreidler and Hummel published the first work on Zn-substituted tricalcium phosphate (β-TCZP) [1]. They showed that, up to ~ 10 mol% substitution of $Zn_3(PO_4)_2$ (TZP) for β-TCP, the Zn^{2+} substituted into the β-TCP structure and resulted in a contraction of the unit cell, consistent with the incorporation of a smaller cation into the structure. Beyond ~ 10 mol%, a mixture of β-TCZP solid solution and monocalcium zinc phosphate ($CaZn_2(PO_4)_2$) was formed. However, since this work was performed in the early 1960s (before Rietveld refinement and high resolution solid-state NMR) they were not able to determine the structure of β-TCZP.

The Zn^{2+} cation is much smaller than the Ca^{2+} cation (Ca^{2+}: 1.0 Å, Zn^{2+}: 0.74 Å; 6-coordinated Pauling radii). Therefore, on size considerations alone, the Ca(5) site is a likely candidate for substitution, followed by the Ca(4) site. Experimentally, Jakeman et al. [2] confirmed this using ^{31}P NMR, and Bigi et al. [3] came to the same conclusion by considering unit cell parameters. This model of substitution is referred to here as the Ca(5)-Ca(4) model, and the aim of this chapter is to examine this model in more detail than the Jakeman and Bigi studies mentioned above. XRD and neutron diffraction will be combined in a Rietveld co-refinement, and ^{31}P NMR will be used as a sensitive probe

of the P environments. The sensitivity and precision of NMR has evolved a great deal since the publication of the work by Jakeman et al., and it is hoped that this increase in experimental power will yield more insight into the structure of β-TCZP.

5.2 Sample preparation

β-TCZP samples were prepared via a solid-state synthesis route similar to the pure β-TCP synthesis discussed in section 4.2. Again, $CaHPO_4$ and $CaCO_3$ were used, but with the addition of a Zn-containing compound. To determine a suitable Zn precursor, two Zn substituted samples were prepared to the formulae given below, using ZnO and $Zn_3(PO_4)_2 \cdot 4\,H_2O$ respectively:

$$0.8\,CaCO_3 + 2\,CaHPO_4 + 0.2\,ZnO \rightarrow$$
$$\rightarrow Ca_{2.8}Zn_{0.2}(PO_4)_2 + H_2O + 0.8\,CO_2 \tag{5.1}$$

and

$$0.933\,CaCO_3 + 1.867\,CaHPO_4 + 0.067\,Zn_3\,(PO_4)_2\,.4H_2O \rightarrow$$
$$\rightarrow Ca_{2.8}Zn_{0.2}(PO_4)_2 + 1.202\,H_2O + 0.933\,CO_2. \tag{5.2}$$
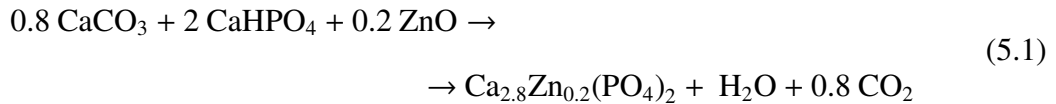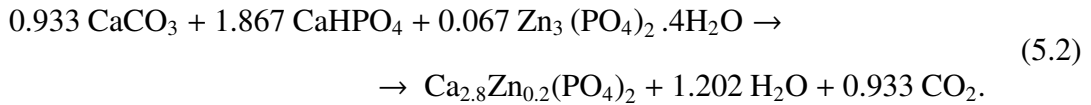
Both sets of powders were weighed on an analytical balance to ±1 mg, before being mixed in an agate pestle and mortar for 10 minutes. The mixed powders were sintered in alumina crucibles for 4 hours at 1050 °C, with heating and cooling rates of 300 °C h^{-1}. This process was repeated twice for a total of three heat treatments, with intermediate mixing in an agate pestle and mortar. XRD was performed on the resulting samples, and the patterns are shown in figure 5.1. The insert specifically highlights the region where the most intense second phase calcium pyrophosphate ($Ca_2P_2O_7$) reflections are seen. It is clear that these peaks are of much lower intensity in the $Zn_3(PO_4)_2 \cdot 4\,H_2O$-based β-TCZP than the ZnO-based sample, and a quantitative analysis was performed by means of a preliminary Rietveld refinement limited to instrumental parameters, lattice parameters and atom positions. The ZnO-based β-TCZP contained 4.5(3) wt.% $Ca_2P_2O_7$, compared to the $Zn_3PO_4 \cdot 4\,H_2O$-based β-TCZP with < 0.5 wt.%. Additionally, the reflections in the ZnO-based β-TCZP XRD pattern appear broader and less intense when normalised to counts/s, indicating smaller crystallite sizes, a more strained structure, or a combination of both. For these reasons, it was decided to use $Zn_3(PO_4)_2 \cdot 4\,H_2O$ as the precursor for the series of β-TCZP samples.
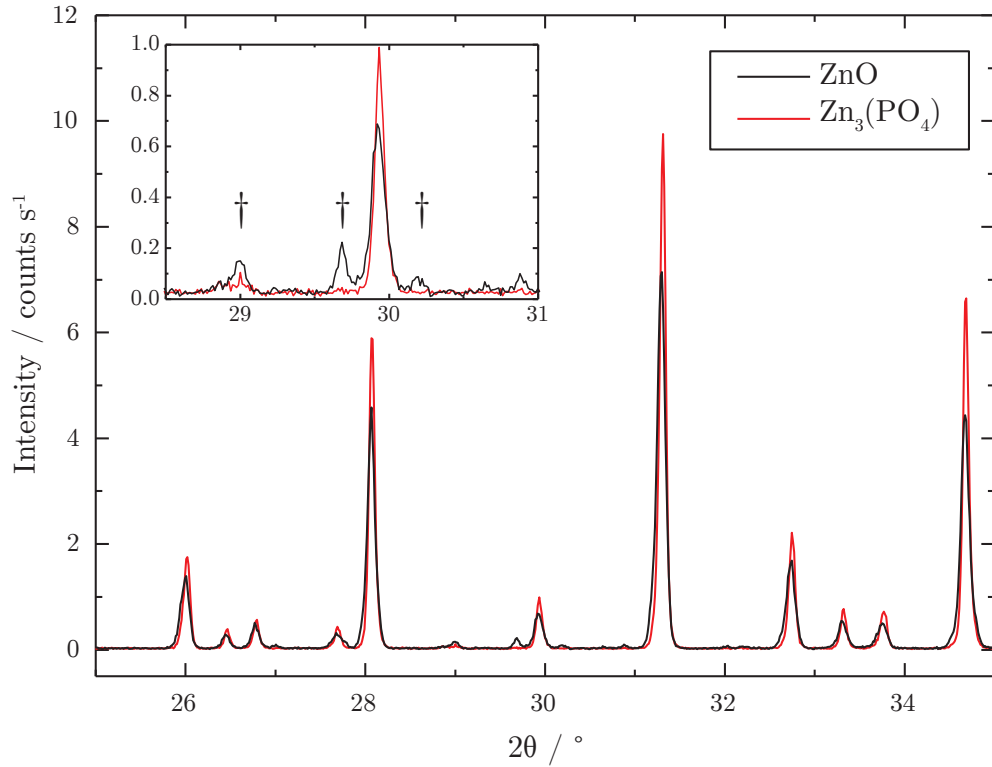
Figure 5.1 XRD patterns of the two $x = 0.200$ β-TCZP preparations, differing only in the Zn-based precursor used. The region from 25° to 35° 2θ is shown, with an insert illustrating the $Ca_2P_2O_7$ second phase reflections, denoted by †. These reflections constitute 4.5(3) wt.% of the sample.

Equation 5.2 was generalised as a function of the composition x, and 12 samples were prepared from $x = 0.033$ to 0.400 in increments of $x = 0.033$:

$$\left(1 - \frac{x}{3}\right) CaCO_3 + \left(2 - \frac{2x}{3}\right) CaHPO_4 + \left(\frac{x}{3}\right) Zn_3 (PO_4)_2 .(4H_2O) \rightarrow$$

$$\rightarrow Ca_{3-x}Zn_x(PO_4)_2 + (1 + x)\ H_2O + \left(1 - \frac{x}{3}\right) CO_2. \tag{5.3}$$
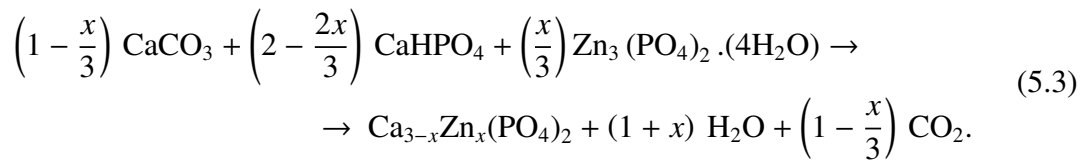
The samples were prepared as described earlier in this section, by mixing in a pestle and mortar before three cycles of sintering in an alumina crucible at 1050 °C for 4 hours, with heating and cooling rates of 300 °C h^{-1}.

5.3 Experimental methods

5.3.1 X-ray diffraction

XRD patterns were collected for all β-TCZP samples as described in section 4.3.1, with an XRD Rietveld refinement to determine the phase purity of the samples. The same

procedure for Rietveld refinement was used as in section 4.3.3, but without anisotropic thermal parameters and terms related to the Rietveld refinement of ND data. Additional Ca(5)/Zn(5) and Ca(4)/Zn(4) occupancy terms were included, fixed at the values predicted by the Ca(5)-Ca(4) model.

5.3.2   Neutron diffraction

ND patterns were collected for all β-TCZP samples as described in section 4.3.2 to examine real-space T(r) plots as a function of Zn concentration, and for Rietveld co-refinement.

5.3.3   Rietveld refinement

XRD and ND co-refinements were performed as in section 4.3.3, but with additional fixed Ca(5)/Zn(5) and Ca(4)/Zn(4) occupancy terms based on the nominal composition. In all but the initial case, the structure resulting from the previous refinement was used as a starting condition for the next refinement. Anisotropic thermal parameters were required on the Ca(4) site. The initial refinement was carried out as in section 4.3.3.

5.3.4 ^{31}P NMR

^{31}P NMR was used to examine the complete series of β-TCZP samples, using the results presented in section 4.4.4 as a starting condition. The spectra were referenced to solid ammonium dihydrogen phosphate ($NH_4H_2PO_4$) at 0.9 ppm with respect to the primary reference 85% aq. H_3PO_4. A stack plot of the NMR spectra is shown in figure 5.10.

5.4   Results

5.4.1   X-ray diffraction

XRD scans and preliminary Rietveld refinements were performed to determine the purity of the β-TCZP, and the resulting phase concentrations are shown in table 5.1. Due to the high levels of $Ca_2P_2O_7$ in the low substitution samples, the sintering temperature was raised by $100\,°C$ to $1150\,°C$. This had the effect of reducing the level of $Ca_2P_2O_7$ second phase to < 1wt.% for all samples. Ball milling was not required to obtain a

phase pure sample, unlike in the case of pure β-TCP. Stack plots of the patterns over two angular ranges are shown in figure 5.2.

Table 5.1   Levels of $Ca_2P_2O_7$ second phase as a result of sintering at 1050 °C. Due to the high quantities of second phase, a higher temperature of 1150 °C was subsequently used for the $x = 0.033$, 0.067, and 0.100 compositions. A '-' denotes second phase content < 0.5 wt.%.

x	$Ca_2P_2O_7$ wt.%
0.033	15
0.067	8
0.100	10
0.133	-
0.167	-
⋮	⋮

5.4.2   Neutron diffraction

T(r) plots were prepared to directly observe the Zn-O correlation in the material, and a stack plot of the data is shown in figure 5.3 with the P-O, Ca-O and Zn-O correlations labelled.

(a)

(b)
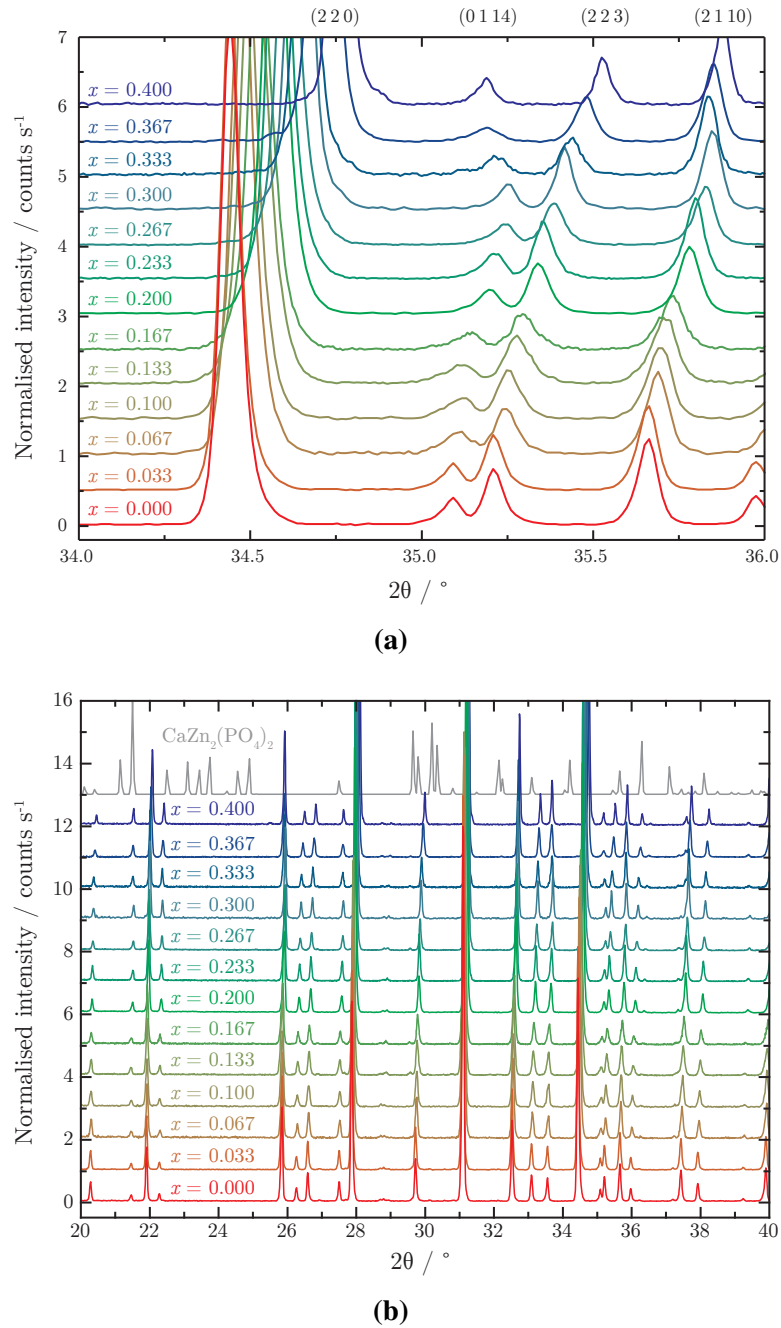
Figure 5.2 The XRD patterns over the complete compositional range, from pure β-TCP to x = 0.400 β-TCZP. The patterns are shown from 34° to 36° and from 20° to 40°, showing the trends of four labelled reflections and the absence of the $CaZn_2(PO_4)_2$ phase respectively. The (0 1 14) reflection shows a different trend to the other three reflections, which show a continual increase in 2θ, indicating a steady decrease in the unit cell size. The $CaZn_2(PO_4)_2$ pattern was computed from the structure published by Jakeman et al. [4], and there is no evidence this phase in the β-TCZP XRD patterns.

71
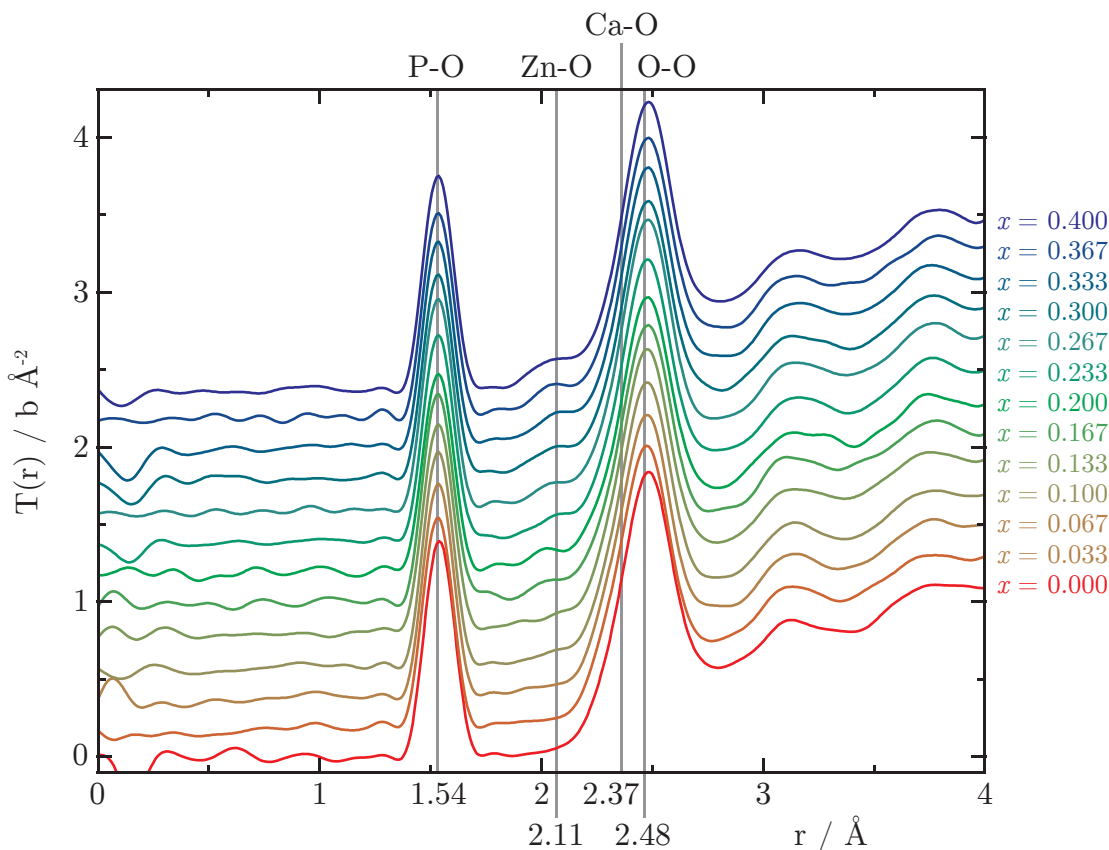
Figure 5.3 T(r) plots for the complete compositional range of β-TCZP. The correlation lengths are given for 4CN P-O (1.54 Å), 6CN Zn-O (2.11 Å), 6CN Ca-O (2.37 Å), and 8CN Ca-O (2.48 Å) from [5]. The Zn-O correlation clearly becomes more intense as a function of composition. Plots are offset from each other by 0.2 b Å^{-2}.

5.4.3 Rietveld co-refinement

The Ca(5)/Zn(5) or Ca(4)/Zn(4) occupancies were fixed for all refinements based on the occupancies predicted by the model. The results of the $x = 0.100$, $x = 0.200$, $x = 0.300$ and $x = 0.367$ refinements are shown in figures 5.4-5.7; the results for the other refinements are shown in appendix B and are summarised in table 5.6. The refined structural parameters of the $x = 0.100$, $x = 0.200$, $x = 0.300$ and $x = 0.367$ β-TCZP compositions are shown in tables 5.2-5.5. Total scattering plots were simulated as in section 4.4.2 for the four tabulated structures, and are shown in figure 5.9. A simulation of the $x = 0.400$ total scattering plot was prepared, however it was clear that the Rietveld refinement produced non-physical results with very short O-O correlations (~ 1.5 Å). The lattice parameters and unit cell volume are plotted in figure 5.8.
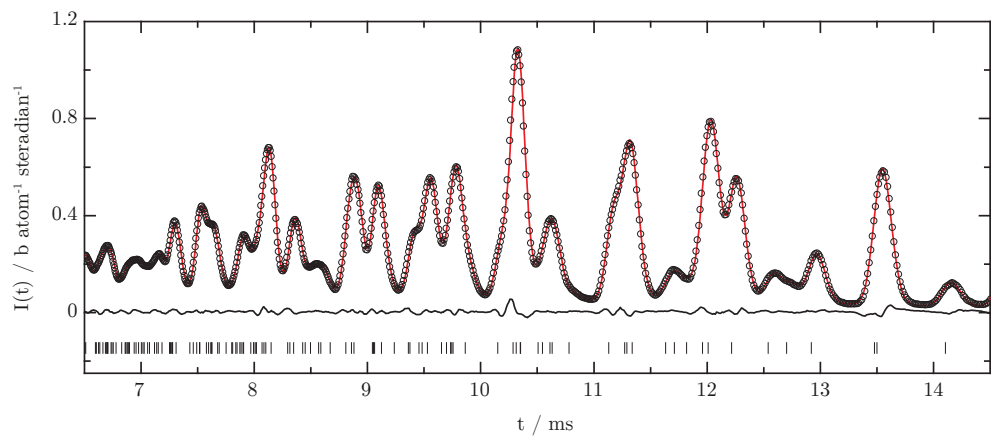
(a) ND: Bank 4
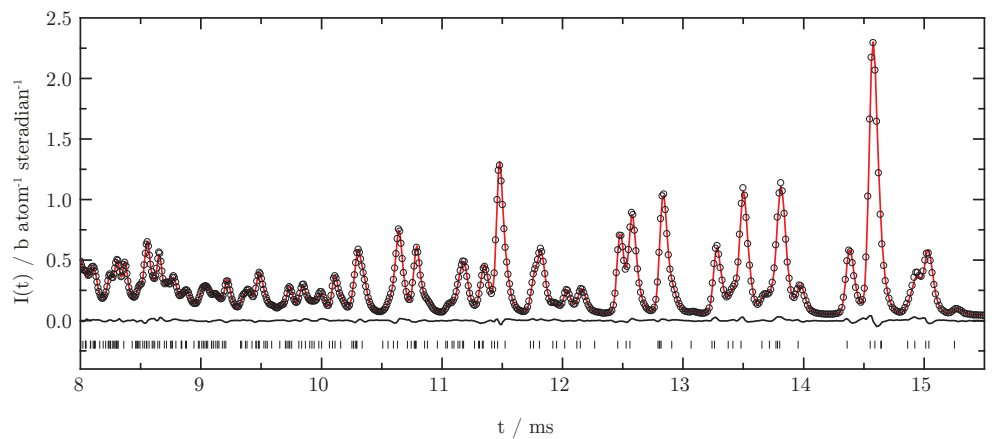
(b) ND: Bank 5
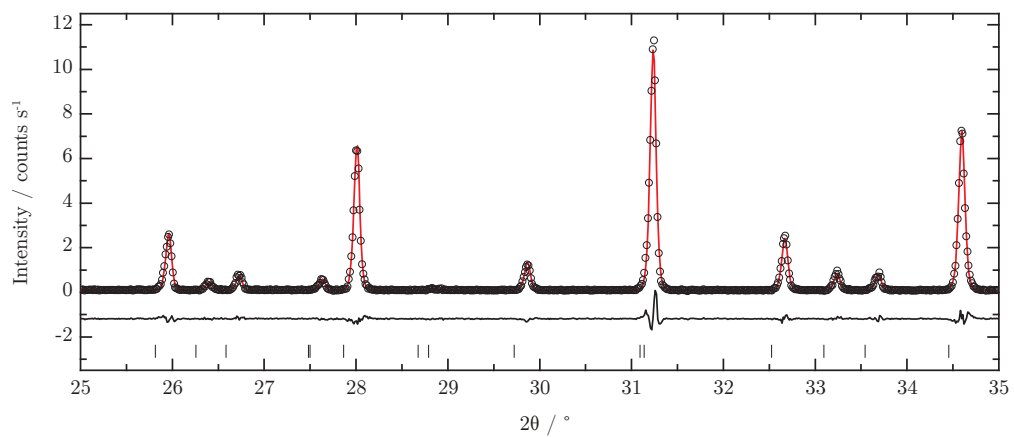
(c) XRD

Figure 5.4 Results of Rietveld refinement for β-TCZP $x = 0.100$. Data points are shown as empty black circles, the fit is shown in red, and reflections are shown as tick marks.

73
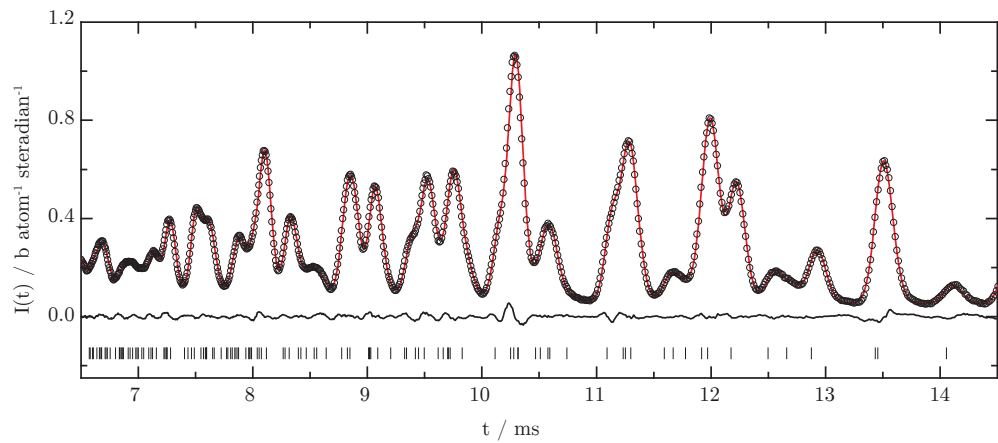
(a) ND: Bank 4

(b) ND: Bank 5

(c) XRD

Figure 5.5 Results of Rietveld refinement for β-TCZP x = 0.200. Data points are shown as empty black circles, the fit is shown in red, and reflections are shown as tick marks.

74
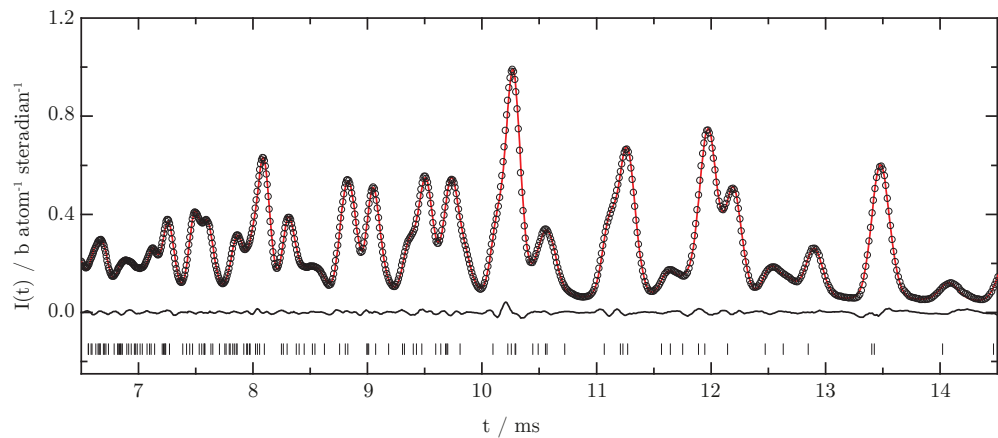
(a) ND: Bank 4

(b) ND: Bank 5

(c) XRD

Figure 5.6   Results of Rietveld refinement for β-TCZP x = 0.300. Data points are shown as empty black circles, the fit is shown in red, and reflections are shown as tick marks.
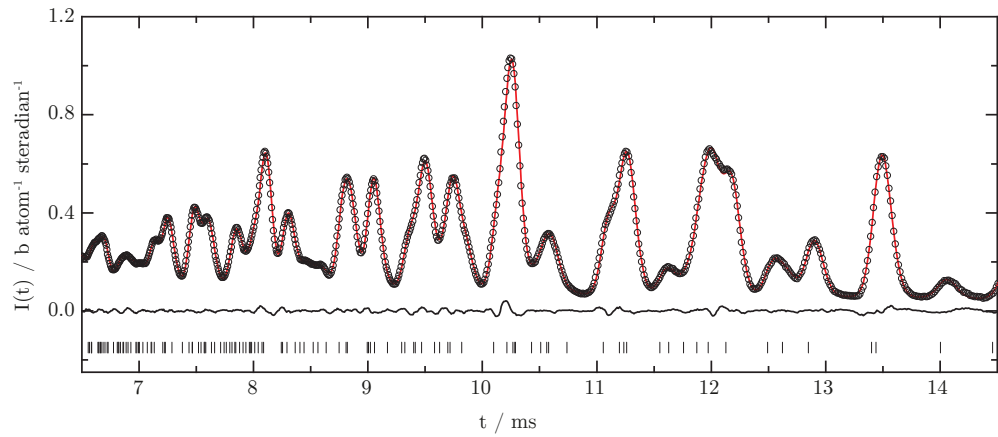
(a) ND: Bank 4
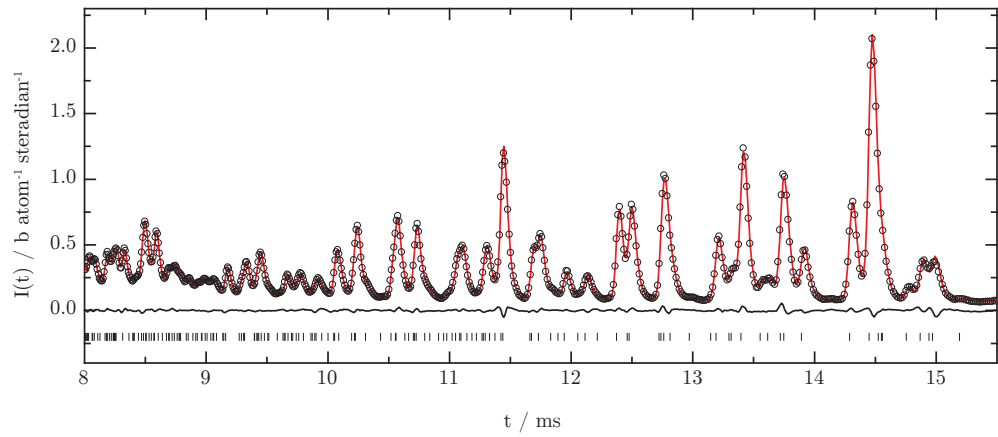
(b) ND: Bank 5
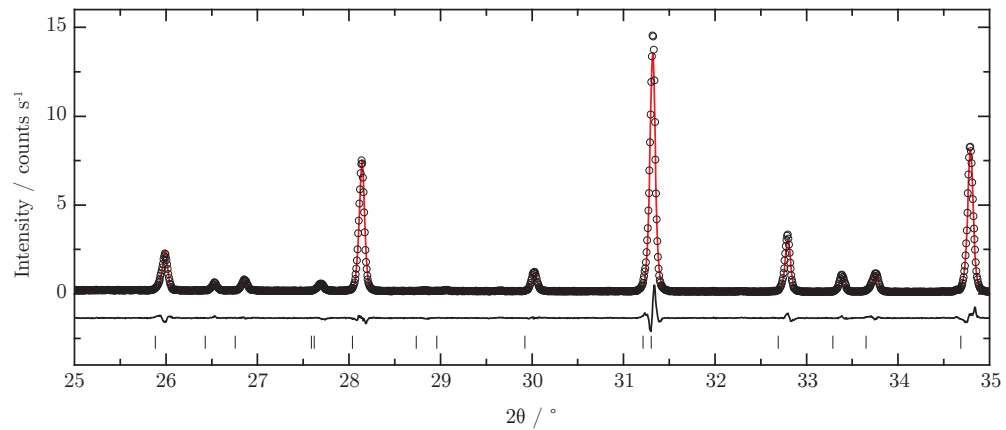
(c) XRD

Figure 5.7 Results of Rietveld refinement for β-TCZP x = 0.367. Data points are shown as empty black circles, the fit is shown in red, and reflections are shown as tick marks.
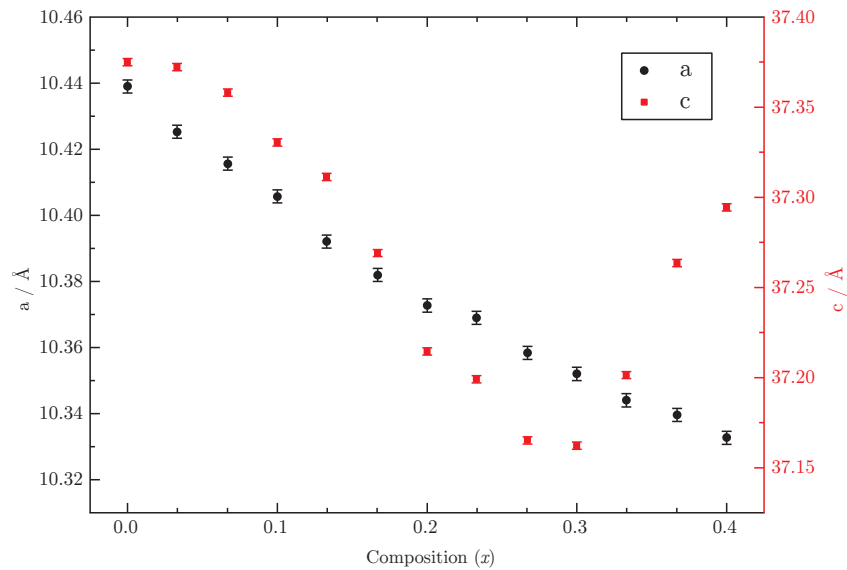
(a) Lattice parameters
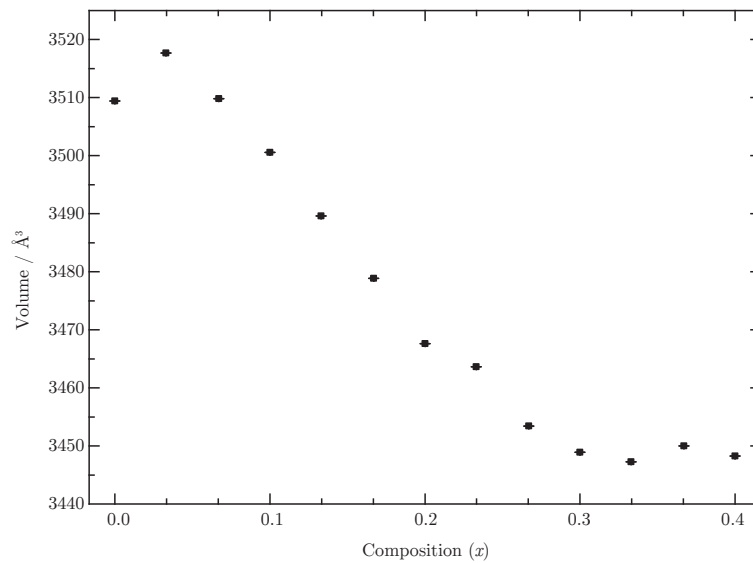
(b) Volume

Figure 5.8 The lattice parameters as a function of Zn concentration. In figure 5.8a, the c lattice parameter goes through a previously documented minimum at around $x = 0.300$. Combined with the approximately linear change in a, this leads to a unit cell volume, shown in figure 5.8b, which reaches a minimum at $x = 0.300$ with no further change.

(a) β-TCP

(b) β-TCZP $x = 0.100$

(c) β-TCZP $x = 0.200$

(d) β-TCZP $x = 0.300$

(e) β-TCZP $x = 0.367$
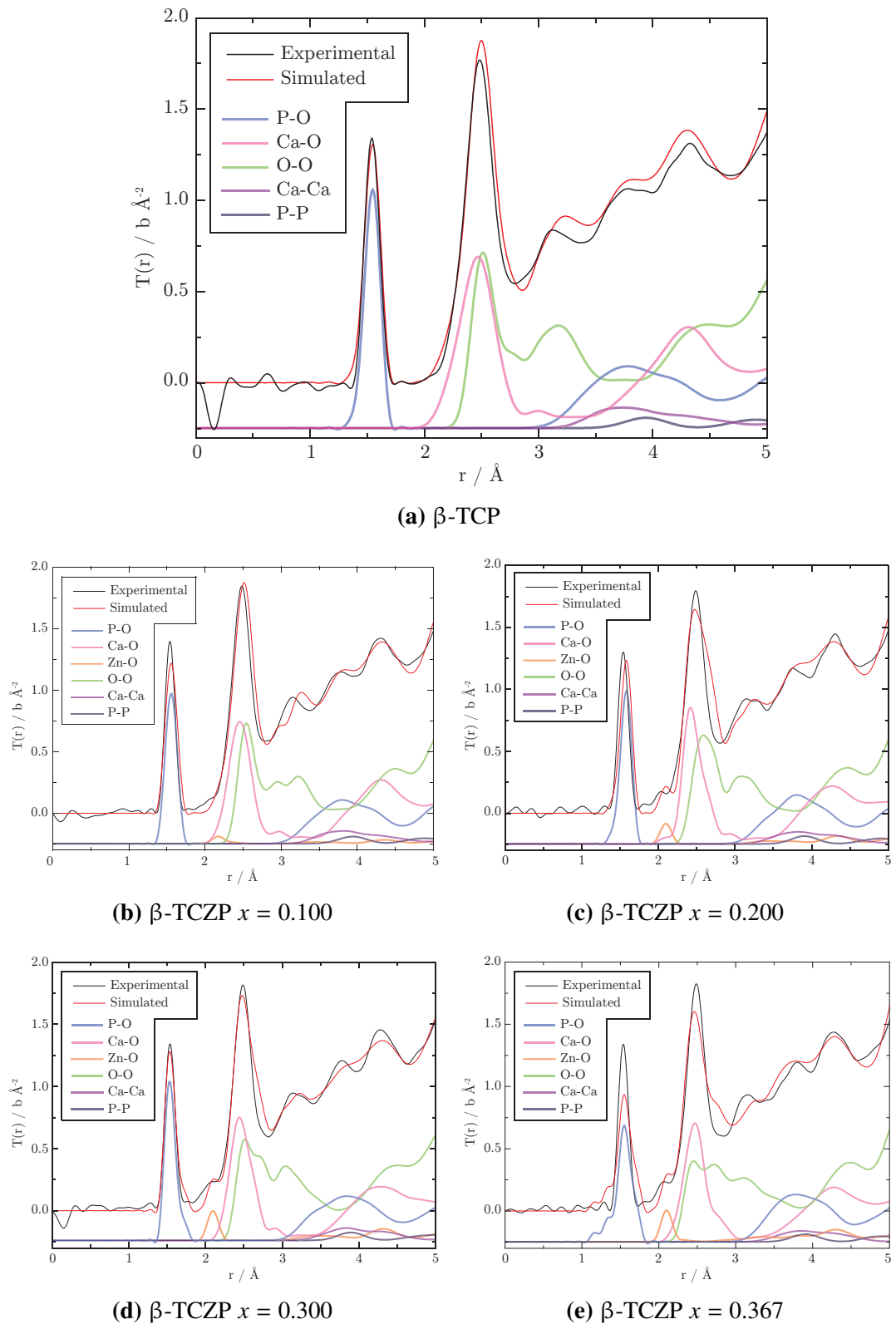
Figure 5.9 Simulated T(r) plots based on the output of Rietveld refinements for various values of x. The experimental T(r) plots are included for comparison.

Table 5.2 Refined structure of $x = 0.100$ β-TCZP. Values without uncertainties were not refined.

Site	x	y	z	Species	Occ.	U_{iso}
Ca1	0.713 41(90)	0.856 14(205)	0.166 54(94)	Ca^{2+}	1.0	0.4528(535)
Ca2	0.609 39(99)	0.827 33(66)	−0.031 04(47)	Ca^{2+}	1.0	0.4528(535)
Ca3	0.727 02(37)	0.851 30(51)	0.060 76(18)	Ca^{2+}	1.0	0.4528(535)
Ca4	0	0	−0.076 92(164)	Ca^{2+}	0.5	†
Ca5	0	0	0.737 55(29)	Zn^{2+}	0.35	1.0598(10839)
				Ca^{2+}	0.65	
P1	0	0	0	P^{5+}	1.0	1.6602(10539)
P2	0.687 30(178)	0.861 93(134)	0.869 67(19)	P^{5+}	1.0	0.4154(366)
P3	0.648 41(247)	0.858 75(111)	0.767 75(18)	P^{5+}	1.0	0.4154(366)
O1	0.719 74(57)	−0.081 60(390)	−0.091 82(35)	O^{2-}	1.0	−1.3496(1475)
O2	0.748 12(114)	0.769 99(86)	0.857 81(40)	O^{2-}	1.0	1.0754(372)
O3	0.718 30(103)	−0.004 36(113)	0.852 99(38)	O^{2-}	1.0	1.0754(372)
O4	0.523 98(376)	0.764 37(593)	0.862 86(25)	O^{2-}	1.0	1.0754(372)
O5	0.603 00(481)	−0.041 59(454)	0.778 61(144)	O^{2-}	1.0	1.0754(372)
O6	0.572 02(520)	0.689 45(603)	0.784 00(137)	O^{2-}	1.0	1.0754(372)
O7	0.073 82(562)	0.900 26(519)	0.775 94(138)	O^{2-}	1.0	1.0754(372)
O8	0.628 26(364)	0.823 03(468)	0.725 39(134)	O^{2-}	1.0	1.0754(372)
O9	0.006 90(465)	0.861 53(332)	−0.015 41(157)	O^{2-}	1.0	1.7038(1077)
O10	0	0	0.042 54(34)	O^{2-}	1.0	1.7358(2206)

† $U_{11} = 0.000\,00(2359)$, $U_{22} = 0.000\,00(2359)$, $U_{33} = 0.103\,06(8651)$, $U_{12} = 0.000\,00(1180)$, $U_{13} = 0$, $U_{23} = 0$

Table 5.3 Refined structure of $x = 0.200$ β-TCZP. Values without uncertainties were not refined.

Site	x	y	z	Species	Occ.	U_{iso}
Ca1	0.728 53(87)	0.856 63(88)	0.167 61(35)	Ca^{2+}	1.0	0.4241(588)
Ca2	0.616 56(59)	0.824 58(79)	−0.032 72(36)	Ca^{2+}	1.0	0.4241(588)
Ca3	0.727 96(39)	0.852 44(63)	0.061 31(35)	Ca^{2+}	1.0	0.4241(588)
Ca4	0	0	−0.077 91(242)	Ca^{2+}	0.5	†
Ca5	0	0	0.738 20(110)	Zn^{2+}	0.7	0.7007(2015)
				Ca^{2+}	0.3	
P1	0	0	0	P^{5+}	1.0	1.8714(4002)
P2	0.685 26(62)	0.860 04(91)	0.869 92(38)	P^{5+}	1.0	0.3046(511)
P3	0.656 34(108)	0.843 57(100)	0.766 68(38)	P^{5+}	1.0	0.3046(511)
O1	0.742 50(144)	−0.083 05(151)	−0.090 80(52)	O^{2-}	1.0	1.3932(4450)
O2	0.762 72(211)	0.774 61(188)	0.856 17(47)	O^{2-}	1.0	0.6319(487)
O3	0.725 68(190)	0.007 10(184)	0.847 61(46)	O^{2-}	1.0	0.6319(487)
O4	0.514 09(149)	0.761 92(207)	0.865 08(66)	O^{2-}	1.0	0.6319(487)
O5	0.602 31(183)	−0.044 99(164)	0.779 94(55)	O^{2-}	1.0	0.6319(487)
O6	0.575 06(190)	0.688 75(210)	0.785 90(52)	O^{2-}	1.0	0.6319(487)
O7	0.075 97(224)	0.904 40(204)	0.773 85(50)	O^{2-}	1.0	0.6319(487)
O8	0.624 93(133)	0.827 82(217)	0.730 66(84)	O^{2-}	1.0	0.6319(487)
O9	0.007 31(174)	0.854 21(133)	−0.019 78(49)	O^{2-}	1.0	1.6076(1555)
O10	0	0	0.044 94(78)	O^{2-}	1.0	1.4051(3304)

† $U_{11} = 0.000\,02(1088)$, $U_{22} = 0.000\,02(1088)$, $U_{33} = 0.114\,91(3135)$, $U_{12} = 0.000\,01(544)$, $U_{13} = 0$, $U_{23} = 0$

Table 5.4 Refined structure of $x = 0.300$ β-TCZP. Values without uncertainties were not refined.

Site	x	y	z	Species	Occ.	U_{iso}
Ca1	0.728 27(53)	0.858 20(53)	0.167 96(22)	Ca^{2+}	1.0	0.2654(531)
Ca2	0.621 28(56)	0.806 88(117)	−0.034 31(101)	Ca^{2+}	1.0	0.2654(531)
Ca3	0.736 02(59)	0.848 99(122)	0.064 84(36)	Ca^{2+}	1.0	0.2654(531)
Ca4	0	0	−0.047 51(442)	Ca^{2+}	0.45	†
				Zn^{2+}	0.05	
Ca5	0	0	0.732 24(66)	Zn^{2+}	1.0	0.9450(4245)
P1	0	0		P^{5+}	1.0	2.7203(2564)
P2	0.701 65(93)	0.844 03(118)	0.872 28(50)	P^{5+}	1.0	0.1410(352)
P3	0.671 25(120)	0.865 92(113)	0.768 08(45)	P^{5+}	1.0	0.1410(352)
O1	0.723 39(71)	−0.090 56(72)	−0.090 61(46)	O^{2-}	1.0	1.7351(2681)
O2	0.760 83(105)	0.764 37(77)	0.856 83(45)	O^{2-}	1.0	0.7629(354)
O3	0.719 98(108)	0.003 65(45)	0.847 39(19)	O^{2-}	1.0	0.7629(354)
O4	0.511 83(50)	0.758 26(46)	0.866 58(24)	O^{2-}	1.0	0.7629(354)
O5	0.604 01(50)	−0.044 20(50)	0.779 59(20)	O^{2-}	1.0	0.7629(354)
O6	0.578 90(63)	0.698 33(44)	0.786 97(21)	O^{2-}	1.0	0.7629(354)
O7	0.077 82(52)	0.901 61(47)	0.773 24(19)	O^{2-}	1.0	0.7629(354)
O8	0.620 78(43)	0.819 63(50)	0.725 77(16)	O^{2-}	1.0	0.7629(354)
O9	0.009 39(65)	0.864 59(41)	−0.011 99(23)	O^{2-}	1.0	2.1867(11399)
O10	0	0	0.042 83(36)	O^{2-}	1.0	1.4280(23270)

† $U_{11} = 0.000\,11(2181)$, $U_{22} = 0.000\,11(2181)$, $U_{33} = 0.017\,99(5959)$, $U_{12} = 0.000\,06(1091)$, $U_{13} = 0$, $U_{23} = 0$

Table 5.5 Refined structure of $x = 0.367$ β-TCZP. Values without uncertainties were not refined.

Site	x	y	z	Species	Occ.	U_{iso}
Ca1	0.726 38(41)	0.857 12(53)	0.169 01(25)	Ca^{2+}	1.0	0.2820(436)
Ca2	0.618 71(43)	0.817 39(174)	−0.032 16(31)	Ca^{2+}	1.0	0.2820(436)
Ca3	0.735 87(74)	0.852 74(52)	0.062 26(34)	Ca^{2+}	1.0	0.2820(436)
Ca4	0	0	−0.082 05(41)	Ca^{2+}	0.15	†
				Zn^{2+}	0.35	
Ca5	0	0	0.736 59(30)	Zn^{2+}	1.0	0.4533(939)
P1	0	0	0	P^{5+}	1.0	3.1164(3193)
P2	0.689 30(44)	0.859 21(185)	0.870 18(38)	P^{5+}	1.0	0.3568(422)
P3	0.659 97(101)	0.873 18(133)	0.767 17(36)	P^{5+}	1.0	0.3568(422)
O1	0.753 25(106)	0.086 31(169)	−0.088 84(48)	O^{2-}	1.0	3.2955(4072)
O2	0.742 77(113)	0.775 37(125)	0.860 27(41)	O^{2-}	1.0	0.7586(445)
O3	0.717 22(129)	0.003 50(118)	0.849 44(41)	O^{2-}	1.0	0.7586(445)
O4	0.529 50(137)	0.762 63(158)	0.870 07(49)	O^{2-}	1.0	0.7586(445)
O5	0.604 44(122)	0.037 45(125)	0.781 15(43)	O^{2-}	1.0	0.7586(445)
O6	0.576 24(122)	0.695 31(122)	0.789 12(39)	O^{2-}	1.0	0.7586(445)
O7	0.070 47(144)	0.898 33(126)	0.776 45(36)	O^{2-}	1.0	0.7586(445)
O8	0.615 00(114)	0.806 38(142)	0.730 07(39)	O^{2-}	1.0	0.7586(445)
O9	0.019 78(80)	0.874 49(68)	−0.005 60(46)	O^{2-}	1.0	6.2975(3573)
O10	0	0	0.040 56(27)	O^{2-}	1.0	4.1024(3414)

† $U_{11} = 0.023\,21(455)$, $U_{22} = 0.023\,21(455)$, $U_{33} = 0.054\,60(1322)$, $U_{12} = 0.011\,61(590)$, $U_{13} = 0$, $U_{23} = 0$

Table 5.6 Results of Rietveld refinements of β-TCZP series of compositions. The a and c lattice parameters have uncertainties of ±0.002 Å.

x	a / Å	c / Å	XRD χ^2	Bank 4 χ^2	Bank 5 χ^2	Overall χ^2
0.000	10.439	37.375	1.682	4.217	4.516	-
0.033	10.425	37.372	1.579	5.247	4.167	2.742
0.067	10.416	37.348	1.238	5.422	5.902	2.978
0.100	10.406	37.330	1.284	5.680	5.133	2.919
0.133	10.392	37.311	1.448	4.371	5.624	2.274
0.167	10.382	37.270	1.199	2.993	3.409	1.621
0.200	10.373	37.214	1.739	2.247	2.857	1.987
0.233	10.369	37.199	1.984	3.577	4.403	2.381
0.267	10.358	37.165	1.855	5.448	5.103	2.600
0.300	10.352	37.162	1.233	4.328	4.616	2.461
0.333	10.344	37.201	1.409	5.958	5.769	2.542
0.367	10.340	37.263	1.825	2.891	3.043	2.018
0.400	10.333	37.294	1.711	3.494	7.131	2.886

5.4.4 ^{31}P NMR

^{31}P NMR was performed on the full series of β-TCZP samples, and the resulting spectra are plotted in figure 5.10. There are a number of trends visible in the spectra as a function of composition, however it is not immediately obvious how these are quantitatively related to the composition, or whether they are consistent with the same model used previously to simplify the Rietveld refinement procedure. The same model was therefore employed to produce constrained fits to these spectra, to isolate the individual resonances and explore their properties as a function of composition. Additionally, it was initially assumed that substitution only occurred on a single site, i.e. there was no composition which showed partial substitution on the Ca(4) *and* Ca(5) sites. If the flow chart describing the ^{31}P NMR model for pure β-TCP in figure 4.10 is extended for Zn substitution following the Ca(5)-Ca(4) model, a predictable number of ^{31}P environments are created. The flow chart illustrating this case is shown in figure 5.11. This approach was previously considered by Jakeman et al. [2], albeit with fewer compositions and a less rigorous treatment.

For each spectrum, the number of peaks was fixed at the number predicted by the model, and the areas of the peaks were constrained based on the nominal composition and the multiplicity of the P and Ca sites causing the resonance. The widths of the peaks were not fixed; but were constrained to be similar to their values in the neighbouring
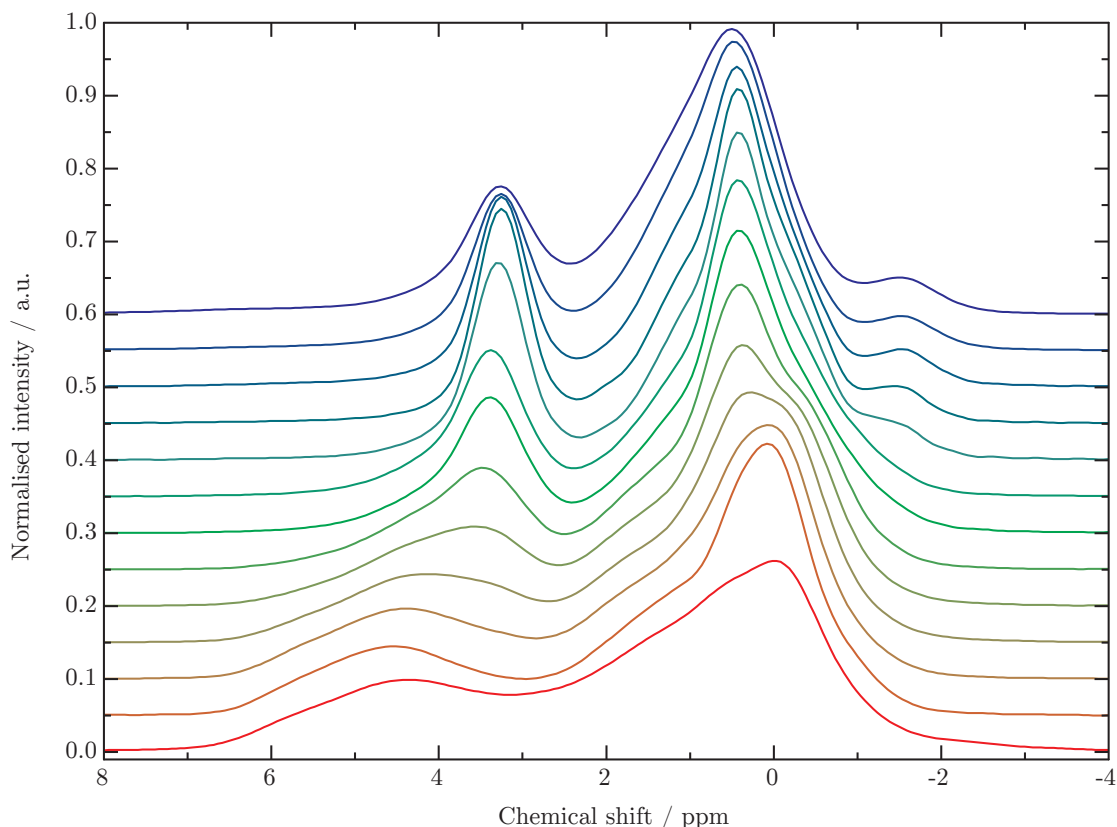
Figure 5.10 A stack plot of the ^{31}P NMR spectra, with the Zn concentration increasing to the top of the stack. There are clear trends in the spectra which can be quantitatively extracted if the spectra are fitted.

compositions. It was assumed that the Lorentzian component of the line-width would be approximately equal for all environments at all concentrations, since in β-TCP this width is almost entirely dependent on the spin-spin relaxation time T_2. As a result, the Gaussian-Lorentzian ratio in the pseudo-Voigt (PV) lineshape was set to a specific value based on the line-width of the resonance, since it was assumed that as the Gaussian line-width decreased, the PV would become more Lorentzian in character. This rule was relaxed slightly for some resonances, due to the slight difference of Lorentzian line-widths across the different environments. The series of fits are shown individually in figure 5.12, with the resulting parameters of the fits in table 5.7.
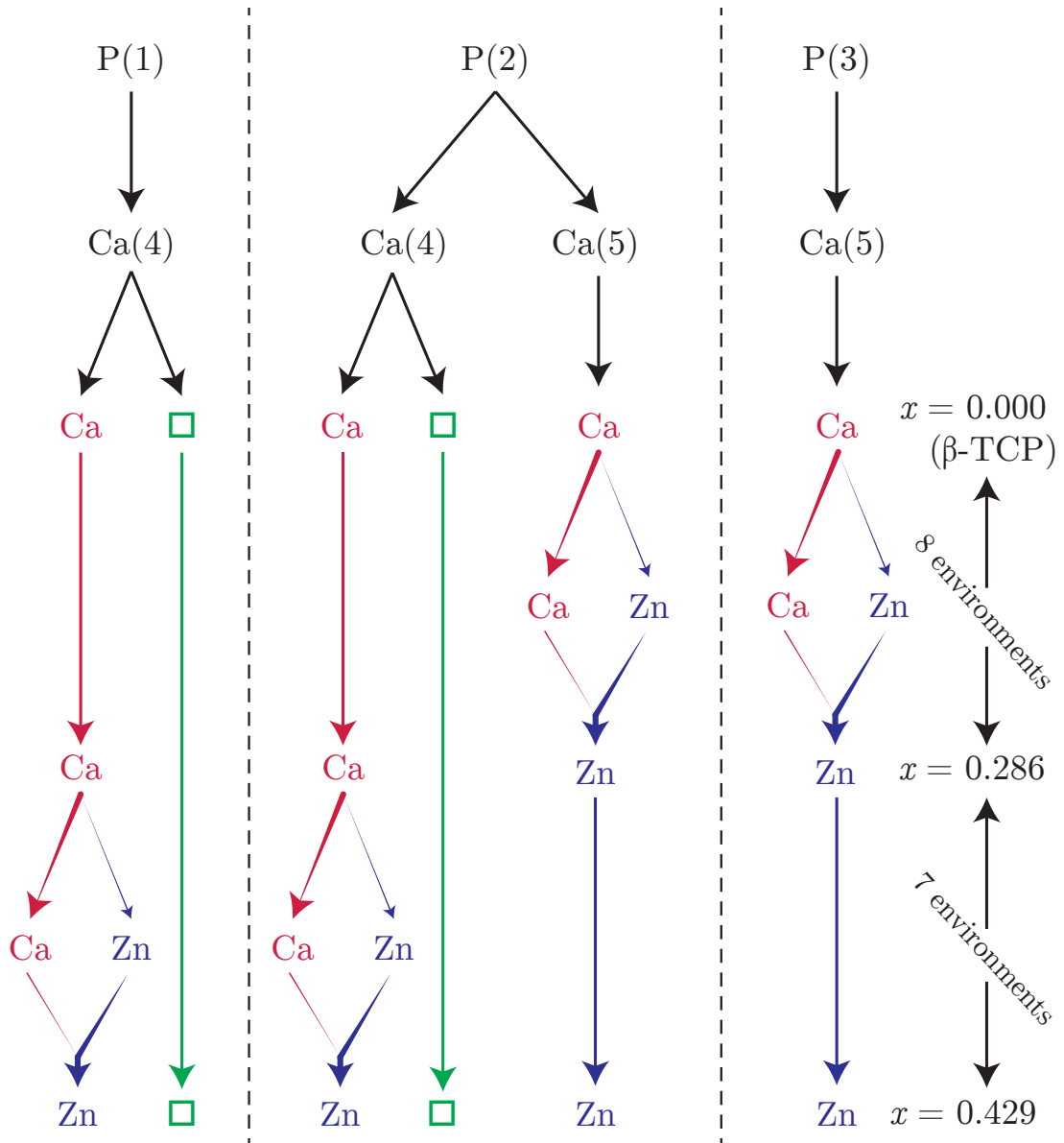
Figure 5.11 A flow diagram illustrating the Ca(5)-Ca(4) Zn substitution model of β-TCP, with the number of ^{31}P environments determined by the sum of the combinations of the next nearest neighbours of each P site. At the Ca(5) limit ($x = 0.286$) and the Ca(5)-Ca(4) limit ($x = 0.429$) five environments would be observed.

(a) $x = 0.033$ β-TCZP

(b) $x = 0.067$ β-TCZP

(c) $x = 0.100$ β-TCZP

(d) $x = 0.133$ β-TCZP

(e) $x = 0.167$ β-TCZP
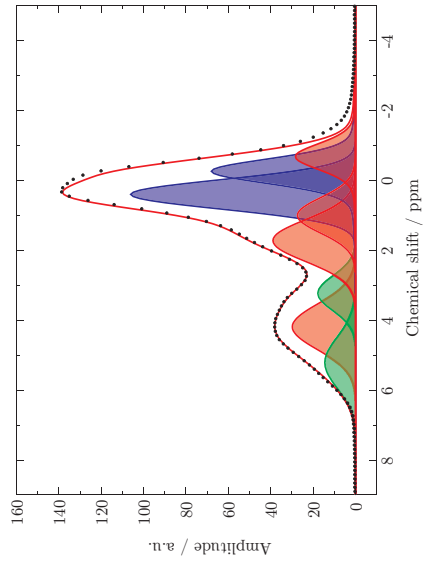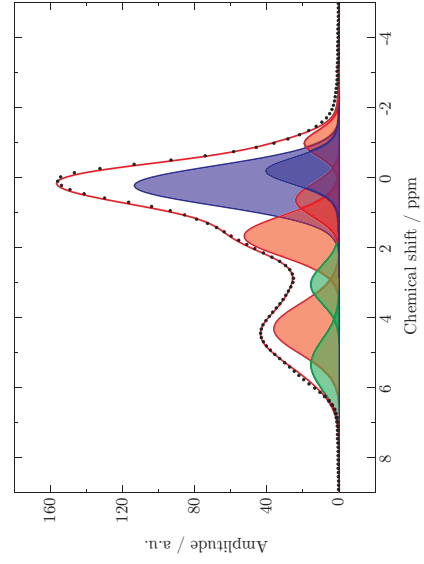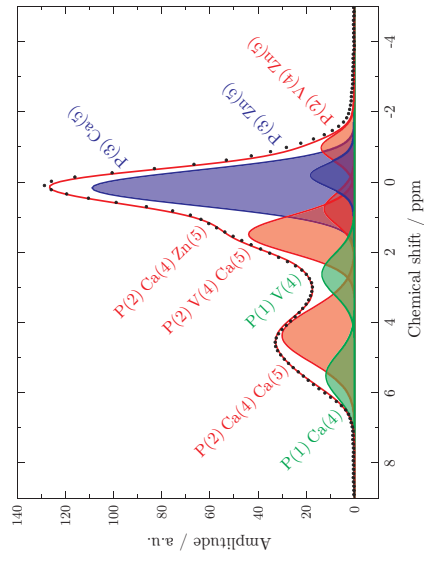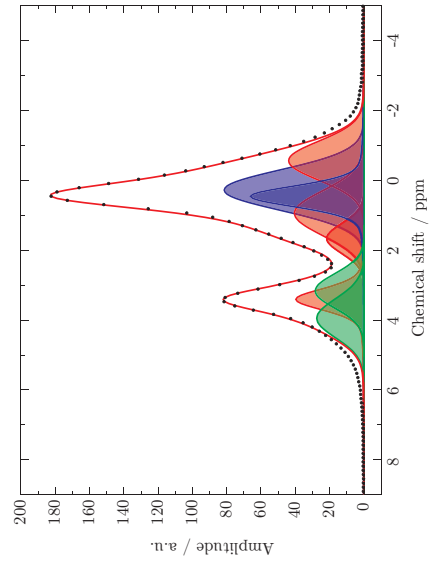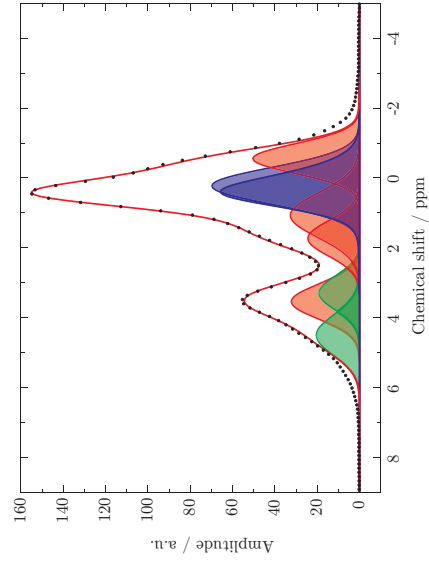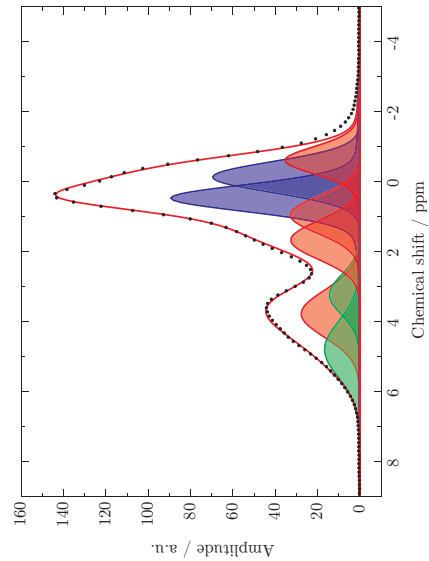
(f) $x = 0.200$ β-TCZP
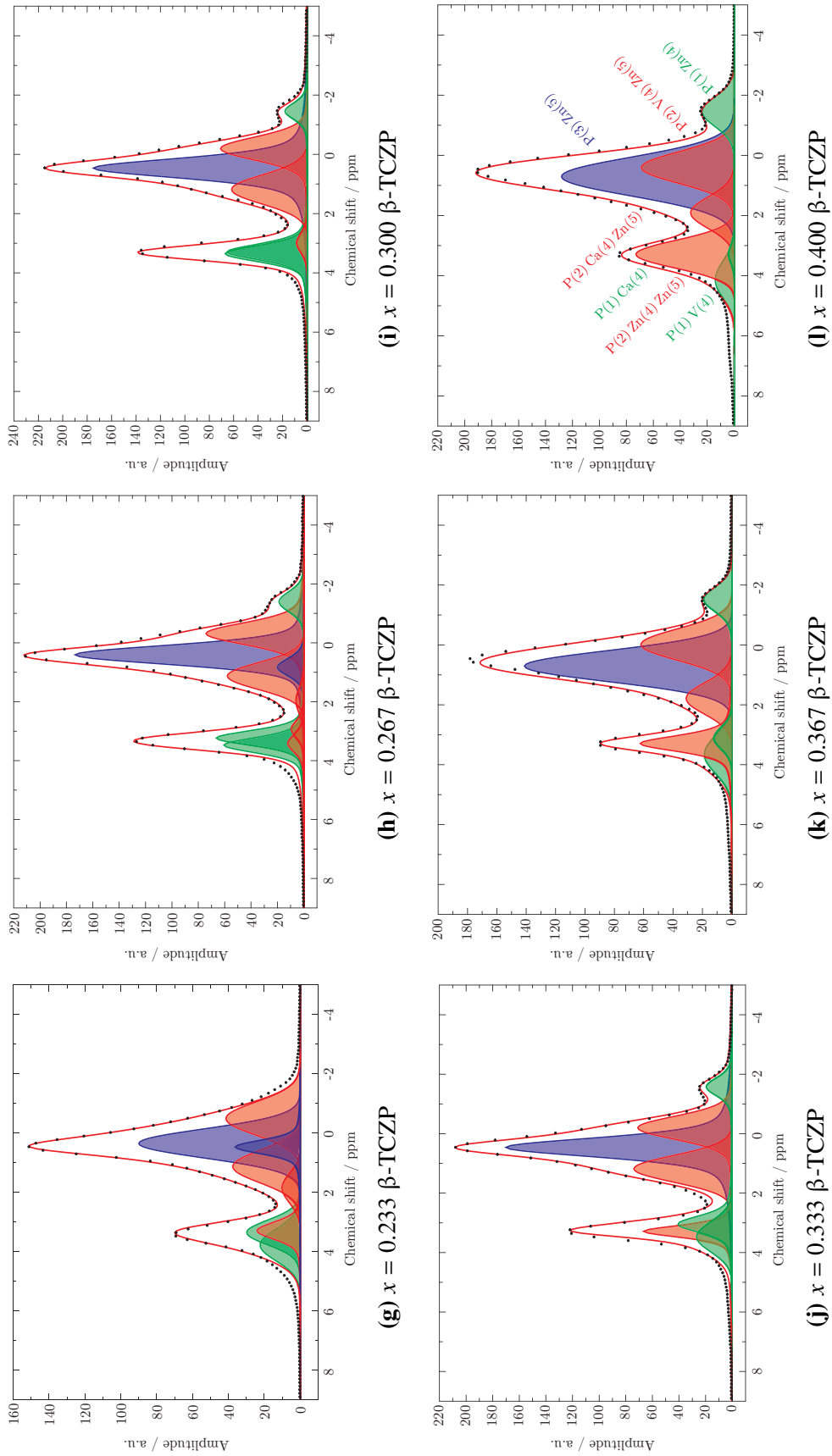
Figure 5.12 ^{31}P NMR spectra and fits of the β-TCZP series.

Table 5.7 The results from the fitting of the ^{31}P NMR spectra of the complete series of β-TCZP samples. The β-TCP results from the previous chapter are included for comparison. The chemical shift (δ) is rounded to 0.1 ppm with an uncertainty of ±0.05 ppm, the line-width (LW) is rounded to 5 Hz with an uncertainty of ±2.5 Hz, the area is rounded to 1 % with an uncertainty of ±0.5 %, and the Gaussian-Lorentzian ratio (PV) was set to a series of values based on the line-width.

Composition x	P(1) V(4) δ	Area	LW	PV	P(1) Ca(4) δ	Area	LW	PV	P(1) Zn(4) δ	Area	LW	PV	P(2) Ca(4) Ca(5) δ	Area	LW	PV	P(2) Ca(4) Zn(5) δ	Area	LW	PV
0.000	2.6	8 %	400	1.0	5.5	7 %	430	1.0					4.4	22 %	400	1.0				
0.033	2.7	6 %	290	1.0	5.6	6 %	280	1.0					4.5	19 %	255	1.0	0.8	5 %	210	0.9
0.067	3.1	7 %	345	1.0	5.4	5 %	265	1.0					4.4	18 %	275	1.0	0.7	7 %	230	1.0
0.100	3.3	7 %	350	1.0	5.3	6 %	240	1.0					4.3	16 %	285	1.0	1.0	10 %	240	1.0
0.133	3.2	9 %	380	1.0	4.9	5 %	265	1.0					3.9	12 %	260	1.0	1.0	12 %	250	1.0
0.167	3.3	8 %	275	1.0	4.5	6 %	230	1.0					3.6	8 %	240	0.7	1.1	14 %	300	1.0
0.200	3.2	10 %	265	1.0	4.0	9 %	230	1.0					3.5	6 %	205	0.7	1.0	16 %	300	1.0
0.233	3.4	10 %	255	1.0	3.9	11 %	200	1.0					3.4	4 %	240	0.6	1.2	17 %	260	1.0
0.267	3.3	11 %	125	0.9	3.5	12 %	120	1.0					3.5	2 %	205		1.2	16 %	215	1.0
0.300	3.4	11 %	125	0.6	3.4	9 %	105	0.6	−1.4	3 %	140	0.6					1.3	18 %	230	1.0
0.333	3.6	8 %	215	0.6	3.4	9 %	95	0.5	−1.5	4 %	150	0.6					1.3	18 %	180	0.8
0.367	3.7	7 %	305	1.0	3.3	3 %	175	0.8	−1.4	5 %	200	0.8					1.9	10 %	250	1.0
0.400	4.2	5 %	295	1.0	3.4	1 %	155	0.6	−1.5	6 %	235	1.0					2.0	7 %	250	1.0

Composition x	P(2) V(4) Ca(5) δ	Area	LW	PV	P(2) V(4) Zn(5) δ	Area	LW	PV	P(2) Zn(4) Zn(5) δ	Area	LW	PV	P(3) Ca(5) δ	Area	LW	PV	P(3) Zn(5) δ	Area	LW	PV
0.000	1.4	22 %	490	1.0									0.0	42 %	320	1.0	−0.1			
0.033	1.6	18 %	360	1.0	−0.9	4 %	180	0.8					0.2	43 %	240	1.0	−0.1	5 %	160	0.8
0.067	1.7	15 %	340	1.0	−0.9	5 %	180	0.8					0.3	38 %	270	1.0	−0.1	10 %	190	0.8
0.100	1.8	13 %	310	1.0	−0.6	8 %	180	0.8					0.5	30 %	200	1.0	−0.1	16 %	170	0.8
0.133	1.8	12 %	320	1.0	−0.5	10 %	190	0.8					0.5	25 %	185	0.8	0.3	20 %	205	1.0
0.167	1.8	11 %	235	1.0	−0.5	15 %	200	1.0					0.5	18 %	175	0.8	0.4	25 %	250	1.0
0.200	1.7	9 %	150	1.0	−0.5	15 %	265	1.0					0.5	14 %	145	0.7	0.4	30 %	270	1.0
0.233	1.9	6 %	140	1.0	−0.4	19 %	265	1.0					0.5	8 %	110	0.6	0.5	36 %	230	1.0
0.267	2.0	3 %	150	1.0	−0.2	19 %	180	1.0					0.9	4 %	145	0.7	0.5	38 %	155	0.7
0.300					−0.1	15 %	180	0.8	3.0	2 %	165	0.5					0.5	41 %	170	0.5
0.333					−0.1	17 %	190	0.8	3.1	6 %	135	0.5					0.5	39 %	155	0.5
0.367					0.1	19 %	245	1.0	3.4	12 %	125	0.5					0.8	44 %	245	1.0
0.400					0.5	19 %	245	1.0	3.4	18 %	215	1					0.8	44 %	305	1.0

(a) P(1) V(4)

(b) P(1) Ca(4)

(c) P(1) Zn(4)

(d) P(2) Ca(4) Ca(5)

(e) P(2) Ca(4) Zn(5)

(f) P(2) V(4) Ca(5)

(g) P(2) V(4) Zn(5)

(h) P(2) Zn(4) Zn(5)

(i) P(3) Ca(5)

(j) P(3) Zn(5)

Figure 5.13 The areas of the environments used in the fits presented in figure 5.12. The lines are theoretical trends based on the β-TCP structure and the Ca(5)-Ca(4) substitution model.
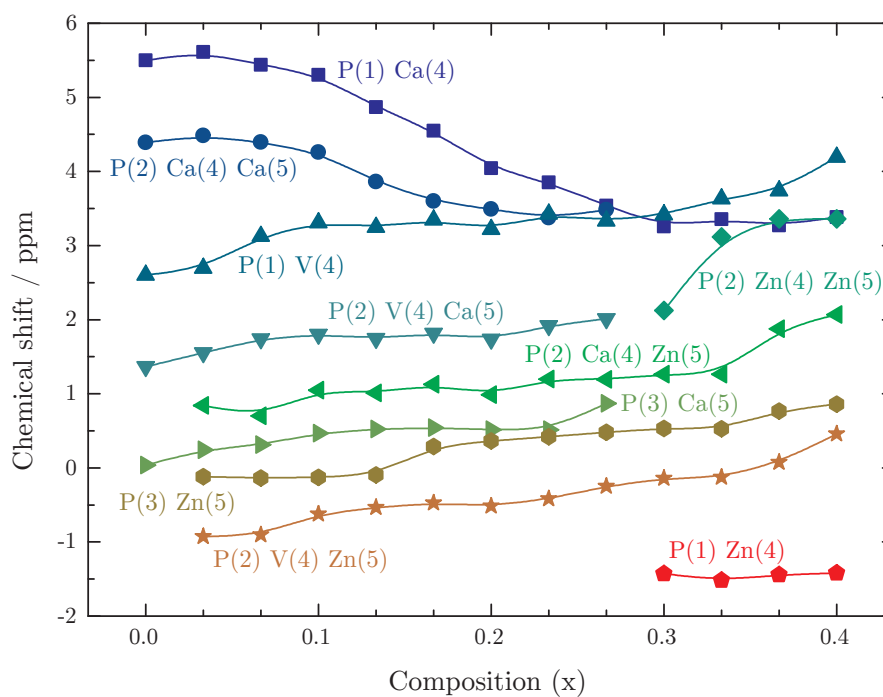
Figure 5.14 The chemical shifts of the individual ^{31}P resonances as a function of composition. The uncertainties in the fits are given by the size of the point, and a B-spline is used as a guide to the eye.
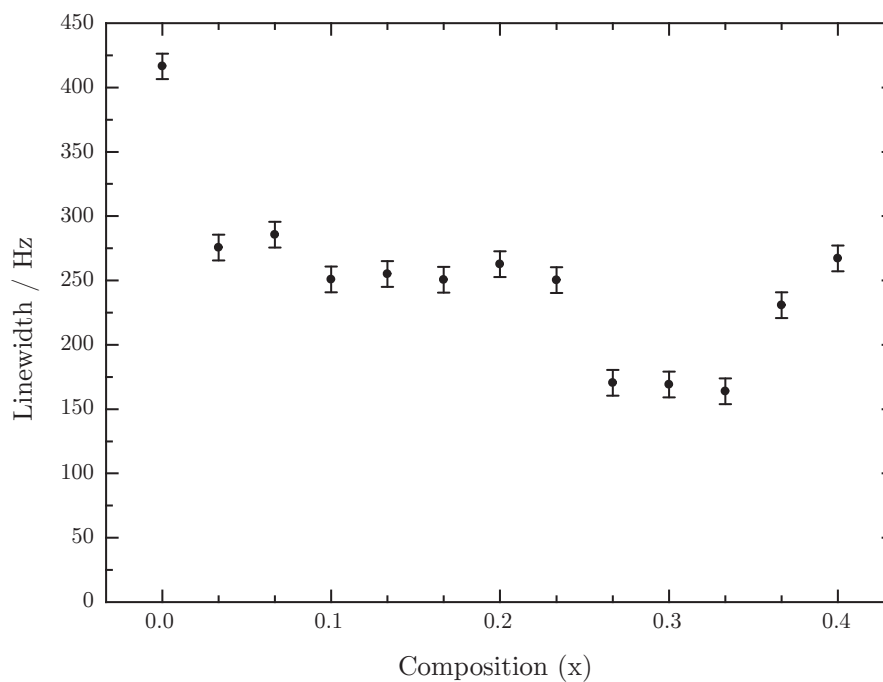
Figure 5.15 The average of the line-widths of the fitted resonances, weighted by the area of the resonance.

5.5   Discussion

5.5.1   NMR fitting

Figure 5.13 shows the areas of the peaks, with the theoretical trends for each resonance included for comparison. There is overall good agreement with the model over the full composition range for all the environments. Figure 5.14 shows the chemical shifts of the individual resonances. It is critical here to notice that the individual resonances do not move significantly and, with the exception of the P(1) Ca(4) environment, the ordering of the resonances does not change. Despite the seemingly arbitrary nature of fitting a broad spectrum to 7 or 8 pseudo-Voigt profiles, it becomes apparent that there is only one valid fit that is consistent over the complete compositional range which does not violate any of the constraints imposed on the process. Hence, it is apparent that the Ca(5)-Ca(4) model is consistent with the ^{31}P data.

The weighted average of the line-widths is plotted in figure 5.15, where the line-widths of each resonance were multiplied by their area before being summed. This produced a clear minimum at around $x = 0.300$, which is visible in the spectra themselves. Under the addition of Zn to the β-TCP structure, the average line-width reduces significantly, indicating a reduction of the disorder in the ^{31}P environments in the structure. The average line-width reaches a minimum at around $x = 0.300$, which is where the Ca(5) site becomes occupied entirely by Zn atoms, and substitution on the Ca(4) environment begins. As the Zn occupancy on the Ca(4) environment increases, the average line-width increases, which indicates an increase in disorder on the P sites. There is no significant difference between the trends of the widths of the individual P environments, indicating an increase in disorder of the β-TCZP structure as a whole.

Finally, since Zn substitution modulates the areas of the Ca(5) and Ca(4)-influenced ^{31}P resonances, this information can be used to fully assign all β-TCZP resonances, and hence the β-TCP resonances illustrated in chapter 4, figure 4.9, used as the starting condition for the series of fits presented here.

5.5.2 Zinc incorporation

In terms of the real-space ND patterns, the Zn-O correlation can be seen at around 2.11 Å, corresponding to a 6 coordinated Zn-O environment [5]. The existence of this 6 coordinated Zn-O correlation strongly indicates substitution into either the Ca(5) or Ca(4) site. Additionally, it is clear from figure 5.3 that the intensity of this correlation increases with the Zn content of the structure. Fits were attempted in order to determine the Zn coordination more precisely as in section 4.4.2. However the low intensity of the Zn-O correlation and its proximity to the Ca-O correlation made such fits unstable.

5.5.3 Lattice parameters

As Zn replaces Ca on the Ca(5) and Ca(4) sites, there is a clear effect on the lattice parameters, as is evident in figure 5.2a. The four reflections in this angular range are labelled, and three of the four undergo a steady increase in 2θ, indicating a contraction of the unit cell. The reflection (0 1 14) however does not follow this trend and reaches a maximum at $x = 0.300$, before decreasing upon further Zn substitution. Since this reflection is almost entirely in the c direction, it follows that while the a and b lattice directions contract over the entire compositional range, the c lattice parameter reaches a minimum at $x = 0.300$, before expanding with further Zn substitution.

The lattice parameters determined by Rietveld refinement are shown in figure 5.8a, and follow the same complex trend identified by examination of the XRD patterns themselves. This feature has been observed previously; Bigi et al. [3] reported similar behaviour around the $x = 0.300$ composition. The difference in the behaviour of the a and c lattice parameters beyond $x = 0.300$ is likely to be related to the columnar structure of the β-TCP structure, however the exact nature of this link is extremely subtle. It is interesting to note that, at the point where the c lattice parameter reaches a minimum, at $x = 0.300$, the volume also has a minimum. However, as opposed to increasing, as the c lattice parameter is shown to do, or decreasing, as the a lattice parameter is shown to do, it remains constant with increased substitution. This hints at electrostatic repulsion inhibiting any further contraction in the unit cell.

The χ^2 parameters for the XRD data sets in the Rietveld co-refinements presented here range from 1.1 to 1.5, indicating a good fit, with the exception of the $x = 0.233$,

$x = 0.267$, and $x = 0.367$ samples, with χ^2 values of 1.964, 1.826 and 1.825 respectively. The main flaw observable in these specific refinements is the error in peak height, which is consistent with a degree of preferred orientation. If the sample is not sufficiently finely ground, there may be significantly more crystallites in a certain direction, resulting in a greater than expected intensity of reflections in this same direction. Significantly however, this does not affect the lattice parameters, which are the major area of interest in this treatment. The χ^2 parameters for the ND data sets are sufficiently larger, which is likely caused by the similar effects introduced in section 4.5.3.

To examine the short-range structure resulting from the Rietveld refinements described above, total scattering plots were simulated from the structural parameters. The plots are shown in figure 5.9, with the simulation of the pure β-TCP sample included for comparison. The disagreement between the experimentally observed T(r) plots and the simulations from the refined β-TCZP structures increases as a function of Zn addition. The P-P and Ca-Ca correlations remain similar to those seen in the β-TCP T(r) plot, whereas the O-O correlation shows a marked departure from the correlation in β-TCP. The issue with the O-O correlation was observed with the pure β-TCP structure when compared to both the experimental data and the simulation produced from previously published structures, and so indicates that the oxygen positions are poorly known even with the addition of ND data.

The fundamental issue with allowing the short-range structure to vary on long-range scales is also visible in these simulated T(r) plots. When a mixed occupancy is allowed on a crystallographic site in Rietveld refinement, the assumption is made that the site and the surrounding atoms are identical for both site occupants. This is manifestly incorrect for the case of Zn substitution in β-TCP, since the 6 coordinated Ca-O and Zn-O bond lengths (Ca-O: 2.37 Å, Zn-O: 2.11 Å) are substantially different. As a result, the surrounding oxygen atoms will refine to a position equal to the weighted average of their Ca and Zn positions.

This is visible in figure 5.9b, where the Zn-O correlation in the experimental data is clearly visible at ~ 2 Å, however due to the assumption made above, the Zn(5)-O and Ca(5)-O correlations both constrained to the same value equal to the weighted average of their lengths. The same effect is visible in figure 5.9c, where the Zn(5)-O and Ca(5)-O correlations have moved to lower r due to the greater Zn concentration. As a result,

the positions of the oxygen atoms will never be known precisely, as only an average value of their positions can be determined by Rietveld refinement.

5.5.4 The anomalous c lattice parameter

Since the observed behaviour could be due to the rotation and/or distortion of the polyhedra in the structure, the precise location of the oxygen atoms is of critical importance, and hence ND patterns were vital in the refinements. The cause of the anomalous behaviour in the lattice parameters was investigated by examining correlations between the composition and any relevant bond lengths and angles in the refined structures. After completing the refinement, the resulting crystal structures were viewed in the CrystalMaker® software, where the relevant bond angles and lengths were computed [6]. It was decided to focus attention on the Ca(4) and Ca(5) sites since they share a column, and are also directly involved in the substitution. Whilst it was incorrect to assume that the Ca(1), Ca(2), and Ca(3) sites would be unaffected by the change in Ca(4,5) occupancy, it was decided that the effect would be most noticeable on the Ca(4) and Ca(5) sites. It was important to realise that there would be obvious correlations between certain parameters, such as lattice parameter and bond length, since even if the atoms are unmoved within the lattice, the simple act of reducing the lattice size will have the effect of reducing the bond lengths by an equivalent factor.

The torsion angle of the O(9)-P(1)-Ca(4)-O(9) cluster (the angle between the Ca(4)-O(9) and P(1)-O(9) bonds) was measured, and the results plotted figure 5.16a as a function of composition, with the geometry illustrated in figure 5.16b. This was shown to remain relatively unchanged throughout the entire compositional range, apart from a sudden decrease in the $x = 0.400$ sample. This is the composition where the c lattice parameter is at its greatest following the minimum at $x = 0.300$, and hence there is some tentative evidence that these two features are correlated. If the torsion angle were decreased, the two O(9) atoms would be forced closer together in the ab plane which, since there is likely to be a strong degree of repulsion between these two atoms, would result in them being forced apart in the c direction. This in turn would 'pull' the Ca(4) and P(1) atoms apart, resulting in the observed increase of the c lattice parameter. There is no evidence of a low torsion angle in pure β-TCP (with a similar c lattice parameter), and hence it is unlikely that the decrease in the torsion angle is merely the result of

the cluster of atoms in figure 5.16b 'relaxing' into this position, with some other force driving the increase in the c lattice parameter.

The spread of the data in figure 5.16a is quite large however, and so not only is any fine detail masked, but there is also the possibility that the change seen in the torsion angle is the result of a random fluctuation or an artefact of the refinement. A high degree of spread was expected, since not only is the unit cell extremely complex, causing many overlapping reflections in the diffraction patterns, but a high degree of correlation is seen in the z atomic positions. As such, any observed minimum in the z atomic positions will be displaced a small distance from the true minimum, causing not only imprecise, but also inaccurate oxygen positions. Additionally, the Rietveld refinements for the $x = 0.400$ sample produced large χ^2 values and a non-physical total scattering plot, indicating a large potential for error in the results. To further this investigation on the microscopic structure of the unit cell, one would require more precise and accurate oxygen positions. ^{17}O NMR would be a potential source of more precise oxygen positional information, however this would be challenging both in terms of cost and execution. Alternatively a Reverse Monte Carlo (RMC) approach could be used, where the structure is manipulated directly to fit the real-space $T(r)$ plots. This would require a number of years however, and is impractical as a component of this work.
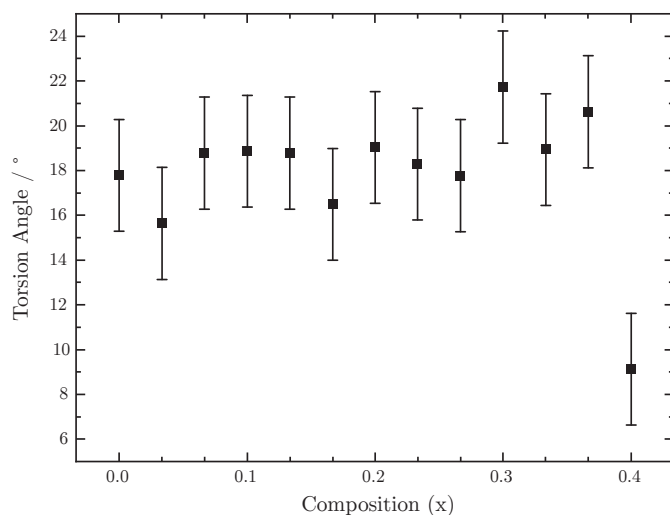
(a) The torsion angle as a function of composition in β-TCZP.
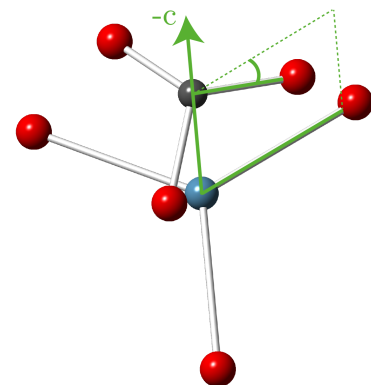
(b) An illustration of the torsion angle in β-TCP. The Ca(4)-O(9) and P(1)-O(9) bonds lie approximately in the *ab* plane, and the Ca(4)-P(1) bond is directed along the *c* direction.

Figure 5.16 The O(9)-P(1)-Ca(4)-O(9) torsion angle.

5.6 Summary

Samples of β-TCZP were successfully prepared using solid-state sintering, and it was observed that single phase samples could be prepared without the use of wet ball milling. Preliminary XRD and Rietveld refinement showed an initial contraction of the unit cell as a function of Zn concentration, followed by a continued decrease in a and an increase in c, resulting in a constant volume. This was later confirmed by a neutron and X-ray Rietveld co-refinement, and a refinement of the Ca(5) occupancy showed a linear change from Ca to Zn. However, even with the addition of ND data, it was not possible to observe the Ca(4) occupancy, despite clear evidence of substitution at this Zn concentration from the lattice parameters. The anomalous c lattice parameter was investigated in terms of the O positions around the Ca(4) site, which showed a possible correlation between the Ca(4)-P(1) torsion angle and Zn concentration, however the large uncertainties in the O position make it extremely difficult to draw firm conclusions.

The fit of the β-TCP ^{31}P NMR spectrum presented in the previous chapter was extended across the whole compositional range up to $x = 0.400$. Fits could be made to each spectrum that were consistent with initial substitution on the Ca(5) site, followed by substitution on the Ca(4) site. Since Zn substitution modulates the Ca(4) and Ca(5) Ca occupancy, the corresponding P(1) and P(2) resonances change in area. This enables a complete assignment of the resonances observed in the pure β-TCP ^{31}P experiment, which is not possible if the pure β-TCP ^{31}P NMR spectrum is taken in isolation. This assignment of the β-TCP ^{31}P spectrum has not previously been possible, due to the lack of a complete treatment of a series of samples. This full analysis of the β-TCZP spectra has not been performed previously, and has enabled the individual resonances to be isolated and assigned explicitly.

There was no second phase observed in these samples. It has previously been assumed that the generation of second phase is intrinsic to the system, however this has been shown not to be true.

References

[1] E. R. Kreidler and F. A. Hummel, *Inorganic Chemistry* **1103** (2), (1961), 524–528.

[2] R. J. B. Jakeman, A. K. Cheetham, N. J. Clayden and C. M. Dobson, *Journal of Solid State Chemistry* **78** (1), (1989), 23–34.

[3] A. Bigi, E. Foresti, M. Gandolfi, M. Gazzano and N. Roveri, *Journal of Inorganic Biochemistry* **66** (4), (1997), 259–265.

[4] R. J. B. Jakeman and A. K. Cheetham, *Journal of the American Chemical Society* **110**, (1988), 1140–1143.

[5] N. E. Brese and M. O'Keeffe, *Acta Crystallographica Section B Structural Science* **47** (2), (1991), 192–197.

[6] D. C. Palmer and S. E. Palmer, CrystalMaker® 2012.

CHAPTER 6

MAGNESIUM SUBSTITUTION

6.1 Introduction

The substitution of Mg into the β-TCP structure is also of interest since it too forms a major component of the waste streams, as outlined in section 2.3. The Mg-substituted β-TCP (β-TCMP) system has been studied in the past both in terms of the substitution mechanism and the macroscopic structure, with specific emphasis on how this is related to the biocompatibility of the material. However, the aim in this chapter was to prepare a range of β-TCMP samples, at different compositions, and to use a combination of XRD, neutron diffraction and ^{31}P NMR, all using the same samples, to extract more detailed structural information. Despite the large body of work previously published, there have been no ^{31}P NMR spectra fitted using the procedure described for β-TCZP in the previous chapter.

The first study on β-TCMP was by Ando [1], who described the phase diagram as a function of Mg substitution and observed a stabilisation of the β-TCP phase in relation to the α-TCP phase combined with a decrease in the liquidus temperature. Additionally, Ando observed a tricalcium trimagnesium phosphate (TCTMP) phase that formed at ∼ 10 mol% Mg, and existed in varying proportion with either β-TCP or trimagnesium phosphate over almost the entire compositional range.

Schroeder et al. [2] performed the first thorough analysis of the β-TCMP structure, making use of XRD and Rietveld refinement to determine the change in the structure under Mg substitution. They were the first to conclude that Mg preferentially enters the Ca(5) site as opposed to random substitution, and confirmed the existence of a TCTMP second phase. Subsequently, Terpstra et al. [3] summarised the results pre-

sented by Schroeder et al., and showed the change in lattice parameters as a function of Mg composition. A steady decrease was observed in the *a* lattice parameter, contrasted to an initial decrease followed by an increase in the *c* parameter (similar to the β-TCZP behaviour discussed in the previous chapter). This was posited to be related to the complete substitution of the Ca(5) site, with the change in substitutional site being responsible for the change in *c* behaviour.

The first ^{31}P NMR experiments on the β-TCMP system were presented by Jakeman et al. [4]; this paper was previously discussed in chapter 4. Due to the limited number of samples prepared and the relatively poor resolution of the spectra however, it was not possible to determine any detailed structural information based on these spectra.

Enderlea et al. [5] prepared a series of compositions up to $20 \, mol\%$ Mg, to investigate in more detail the phase diagram presented by Ando. They determined lattice parameters and transformation temperatures from β-TCP to α-TCP as a function of Mg composition, and also observed the change in Ca(4) and Ca(5) Mg occupancy as a function of substitution. This was shown to be consistent with substitution on the Ca(5) site, followed by the Ca(4) site. The same anomalous *c* lattice parameter behaviour was observed as in Terpstra et al. The phase diagram resulting from this work is shown in figure 6.1.

TCTMP was first isolated as a separate phase by Ando [1], who gave the chemical formula as $Ca_3Mg_3(PO_4)_4$. The unit cell has parameters of $a = 22.841(3) \, \text{Å}$, $b = 9.994(1) \, \text{Å}$, $c = 17.088(5) \, \text{Å}$, $\beta = 99.63(3)°$, and belongs to the monoclinic $C2/c$ space group. However, Dickens et al. showed that the structure can exist as a range of solid solutions, with a revised formula of $Ca_7Mg_9(Ca, Mg)_2(PO_4)_{12}$ [6].

6.2 Sample preparation

β-TCMP samples were prepared as described in the previous chapter for β-TCZP. $CaHPO_4$, $CaCO_3$ and magnesium oxide (MgO, 99+ %) were used. They were weighed on an analytical balance to $\pm 1 \, mg$ based on equation 6.1, before being mixed in an agate pestle and mortar for 10 minutes. The mixed powders were sintered in alumina crucibles for 4 hours at $1050 °C$, with heating and cooling rates of $300 °C \, h^{-1}$. This process was repeated twice, for a total of three heat treatments.

$$2\,\mathrm{CaH(PO_4)} + (1 - x)\,\mathrm{CaCO_3} + x\,\mathrm{MgO} \rightarrow$$
$$\rightarrow \mathrm{Ca_{(3-x)}Mg_x(PO_4)_2} + (1 - x)\,\mathrm{CO_2} + \mathrm{H_2O} \tag{6.1}$$
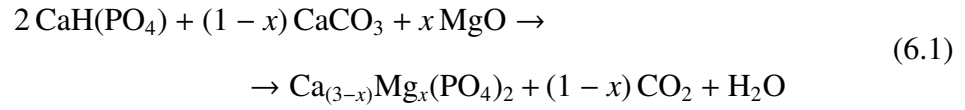
6.3   Experimental methods

A similar characterisation was attempted on the β-TCMP samples as was performed on the β-TCZP samples in the previous chapter. All experimental methods were identical to those described in section 5.3.
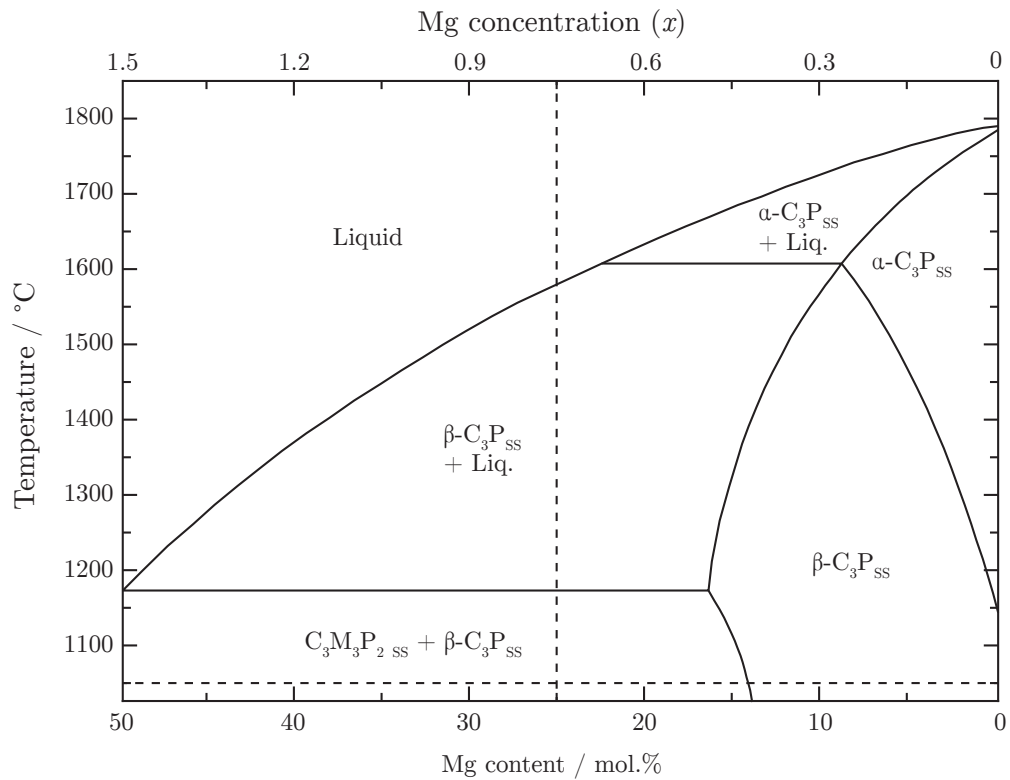
Figure 6.1   The phase diagram of Mg content in β-TCP published origi-nally by Ando, and subsequently modified by Enderlea et al. [1, 5]. The dashed lines indicate the limit of Mg content (25 mol%) and the sintering temperature used (1050 °C).
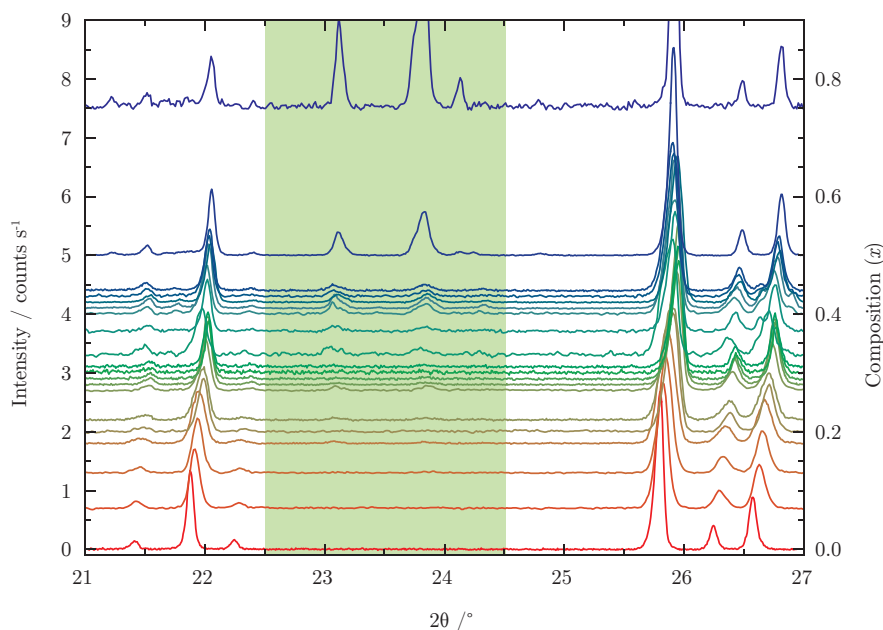
Figure 6.2 XRD patterns of β-TCMP as a function of Mg concentration. The unequal y offset reflects the unequal steps in composition used when preparing the samples. The region from 22.5° to 24.5° is highlighted, where reflections due to the TCTMP second phase are most visible.

6.4 Results

6.4.1 X-ray diffraction

XRD scans and preliminary Rietveld refinements were performed to determine the purity of the β-TCMP. The results are shown in table 6.1, with sections of the XRD patterns in figure 6.2. It is clear that a second phase is present, even at concentrations of Mg where the equivalent β-TCZP composition showed a single phase. This phase was confirmed as TCTMP by pattern matching. The proportion of second phase present was determined, and the corrected x value x_c in $Ca_{(3-x)}Mg_x(PO_4)_2$ was calculated. This has a large uncertainty attached to it however, estimated to be ±50 %, since not only is the precise composition of the TCTMP phase not known, but XRD can be a very poor tool in terms of quantitative phase analysis, especially with weak and overlapping reflections. This is confirmed by relatively large R-Bragg factors for the TCTMP phase, discussed in more detail below. The lattice parameters and their associated uncertainties are shown in table 6.1, and are plotted in figure 6.3.

6.4.2 Neutron diffraction

The same processing of the neutron data was performed as in the previous chapter to produce a series of T(r) plots. These are shown in figure 6.4, with labelled P-O, O-O, Ca-O and Mg-O correlations.

6.4.3 ^{31}P NMR

A stack plot of the NMR spectra is shown in figure 6.5. Initially a similar treatment of the β-TCMP ^{31}P NMR spectra was attempted as in the previous chapter, i.e. constrained fits as a function of composition. The spectra are shown as a stack plot in figure 6.5, and individually with their respective fits in figure 6.6. The parameters of the fits are shown in table 6.2, and areas of the individual resonances are plotted in figure 6.7.

Table 6.1 Results of the Rietveld refinements of the patterns shown in figure 6.2. x_c is calculated based on the quantity of TCTMP second phase, given in mol%. Relative uncertainties of ±25 % were assumed for the [TCTMP] values, which were then propagated to give estimations of the uncertainty in x_c. Both a and c lattice parameters have uncertainties ±0.005 Å. The TCTMP composition was assumed to be $Ca_3Mg_3(PO_4)_2$.

x	x_c	a / Å	c / Å	[TCTMP]	[β-TCMP]	χ^2	$\dfrac{R_B \text{ (TCTMP)}}{R_B \text{ (β-TCMP)}}$
0.000	0.000	10.439	37.375	0.0 %	100.0 %	2.236	-
0.067	0.067(1)	10.393	37.353	0.3 %	99.7 %	1.440	1.71
0.133	0.133(3)	10.380	37.306	0.5 %	99.5 %	1.582	2.56
0.180	0.179(4)	10.373	37.285	0.4 %	99.6 %	1.472	4.72
0.200	0.199(4)	10.363	37.241	0.5 %	99.5 %	1.414	1.81
0.220	0.219(4)	10.363	37.254	0.6 %	99.4 %	1.831	3.30
0.267	0.262(5)	10.352	37.197	1.4 %	98.6 %	2.162	2.19
0.280	0.278(6)	10.346	37.176	0.6 %	99.4 %	2.276	2.35
0.290	0.288(6)	10.340	37.165	0.6 %	99.4 %	1.878	1.81
0.300	0.299(6)	10.337	37.174	0.6 %	99.4 %	1.265	2.37
0.310	0.308(6)	10.340	37.170	0.7 %	99.3 %	1.481	2.32
0.333	0.332(7)	10.346	37.187	2.7 %	97.3 %	1.391	2.74
0.367	0.358(7)	10.336	37.187	2.1 %	97.9 %	1.453	2.29
0.400	0.382(8)	10.340	37.202	4.1 %	95.9 %	2.073	2.17
0.410	0.393(8)	10.336	37.207	3.8 %	96.2 %	3.314	5.02
0.420	0.404(8)	10.333	37.208	3.4 %	96.6 %	2.616	4.85
0.430	0.419(8)	10.331	37.223	2.3 %	97.7 %	2.140	4.01
0.440	0.428(9)	10.326	37.244	2.6 %	97.4 %	2.537	3.68
0.500	0.440(9)	10.323	37.253	11 %	89.0 %	2.215	2.22
0.750	0.518(10)	10.325	37.233	30 %	69.9 %	1.266	1.46
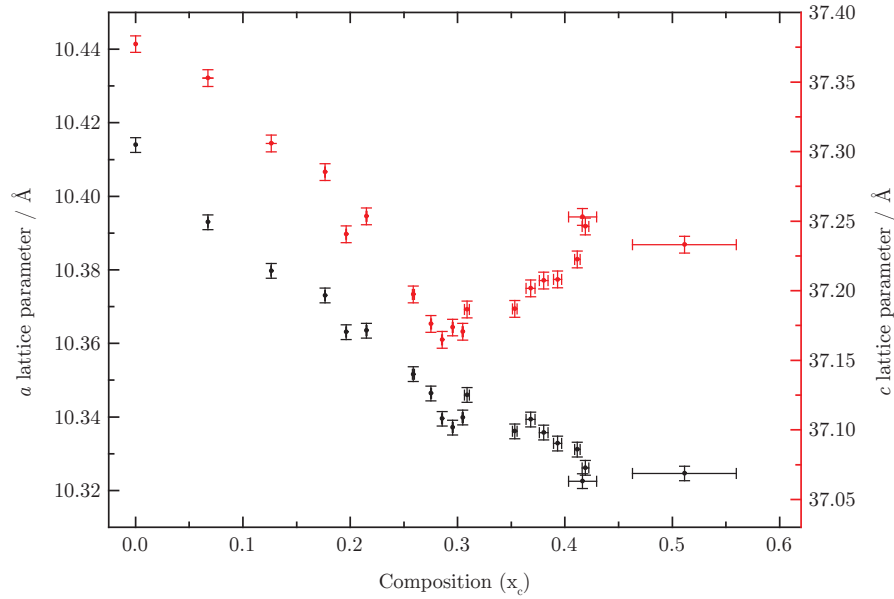
Figure 6.3 The *a* and *c* lattice paramters of β-TCMP as a function of Mg concentration. The *x* error bars are based on the uncertainty in the TCTMP concentration, which is estimated to be ±50 %.
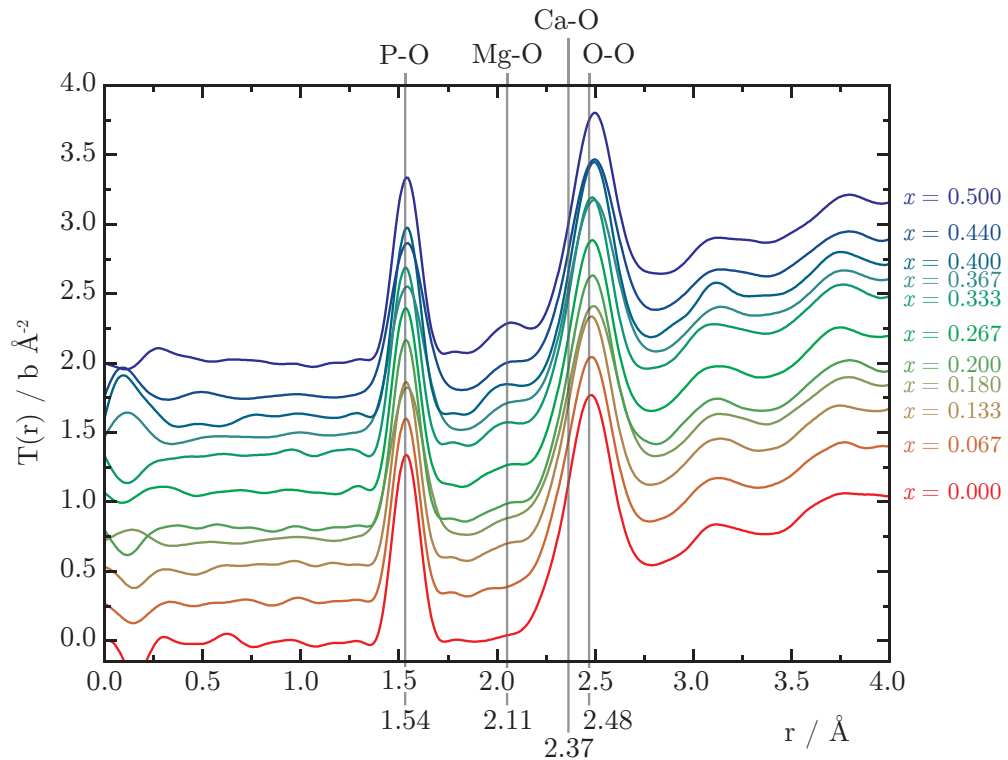
Figure 6.4 A stack plot of neutron T(r) plots of the β-TCMP samples. The increase in the Mg-O correlation at 2.10 Å is visible, and again the non-regular *y* offset is used to indicate the non-regular steps in effective composition.

101
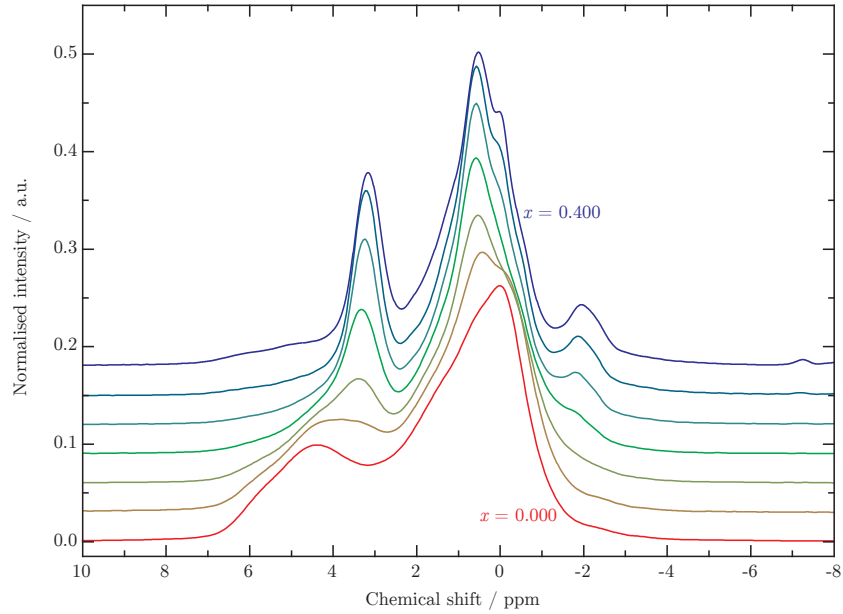
Figure 6.5 ^{31}P NMR spectra of β-TCMP over a series of compositions.

(a) β-TCMP $x = 0.067$

(b) β-TCMP $x = 0.133$

(c) β-TCMP $x = 0.200$

(d) β-TCMP $x = 0.267$
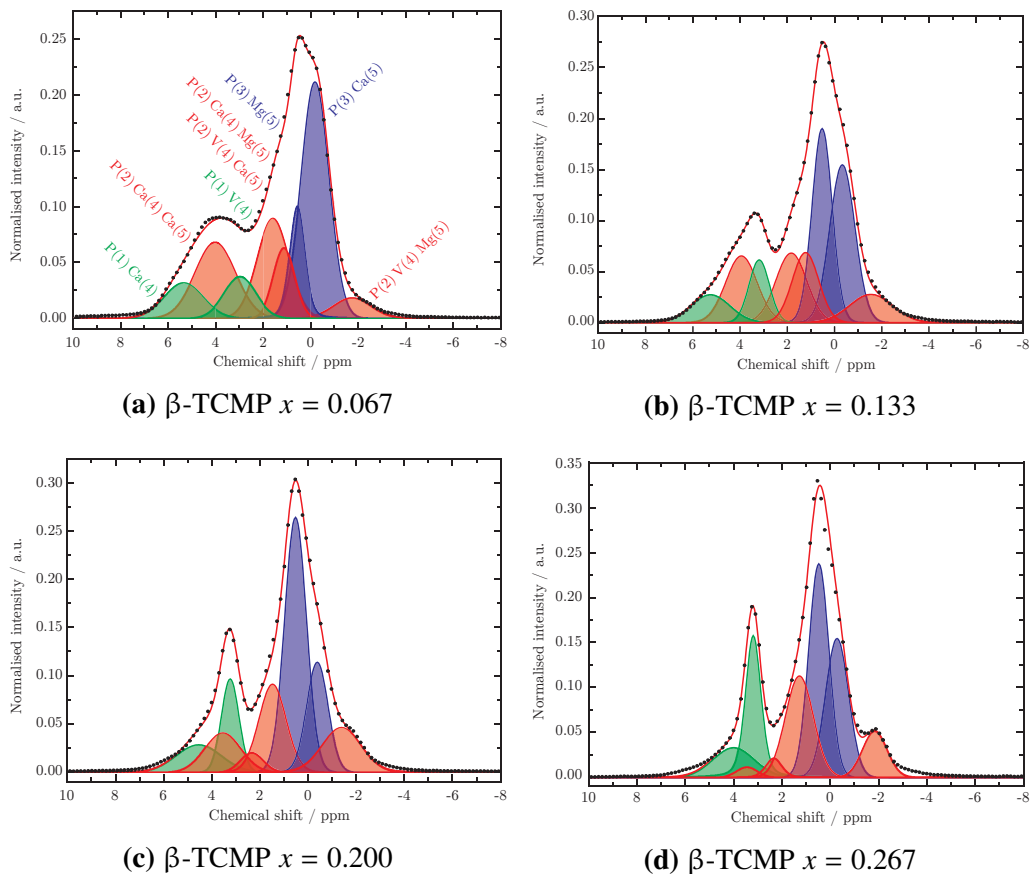
Figure 6.6 ^{31}P NMR fits of β-TCMP compositions. Due to the existence of TCTMP second phase, the results of these fits do not agree with the simulated areas beyond $x = 0.200$.

Table 6.2 The parameters used in the fits presented in figure 6.6. The β-TCP results from chapter 4 are included for comparison. The chemical shift (δ) is rounded to 0.1 ppm with an uncertainty of ±0.05 ppm, the line-width (LW) is rounded to 5 Hz with an uncertainty of ±2.5 Hz, the area is rounded to 1 % with an uncertainty of ±0.5 %, and the Gaussian-Lorentzian ratio (PV) was set to a series of values based on the line-width.

| Composition | P(1) V(4) | | | | P(1) Ca(4) | | | |
x_c	δ	Area	LW	PV	δ	Area	LW	PV
0.000	2.6	7 %	430	1.0	5.5	8 %	400	1.0
0.067	3.0	7 %	385	1.0	5.4	7 %	470	1.0
0.133	3.3	6 %	245	1.0	5.4	6 %	470	1.0
0.200	3.7	7 %	425	1.0	4.6	7 %	530	1.0
0.267	3.3	16 %	145	0.7	4.1	8 %	405	1

x_c	P(2) V(4) Ca(5)				P(2) V(4) Mg(5)			
0.000	1.4	22 %	400	1.0				
0.067	1.6	16 %	255	1.0	−1.7	7 %	275	1.0
0.133	1.9	13 %	225	1.0	−1.4	11 %	240	1.0
0.200	2.4	3 %	210	1.0	−1.3	14 %	215	1.0
0.267	2.4	2 %	160	0.7	−1.7	18 %	245	1.0

x_c	P(2) Ca(4) Ca(5)				P(2) Ca(4) Mg(5)			
0.000	4.4	22 %	490	1.0				
0.067	4.0	16 %	485	1.0	1.1	7 %	255	1.0
0.133	4.1	12 %	380	1.0	1.1	11 %	320	1.0
0.200	3.4	10 %	205	0.8	1.6	14 %	320	1.0
0.267	3.5	1 %	205	1.0	1.4	7 %	120	0.6

x_c	P(3) Ca(5)				P(3) Mg(5)			
0.000	0.0	43 %	320	1.0				
0.067	−0.1	33 %	335	1.0	0.6	9 %	185	0.8
0.133	−0.3	22 %	305	1.0	0.6	22 %	240	1.0
0.200	−0.2	14 %	255	1.0	0.6	33 %	265	1.0
0.267	−0.2	20 %	225	1.0	0.6	27 %	200	1.0

(a) P(1) V(4)

(b) P(1) Ca(4)

(c) P(2) Ca(4) Ca(5)

(d) P(2) Ca(4) Mg(5)

(e) P(2) V(4) Ca(5)

(f) P(2) V(4) Mg(5)

(g) P(3) Ca(5)

(h) P(3) Mg(5)
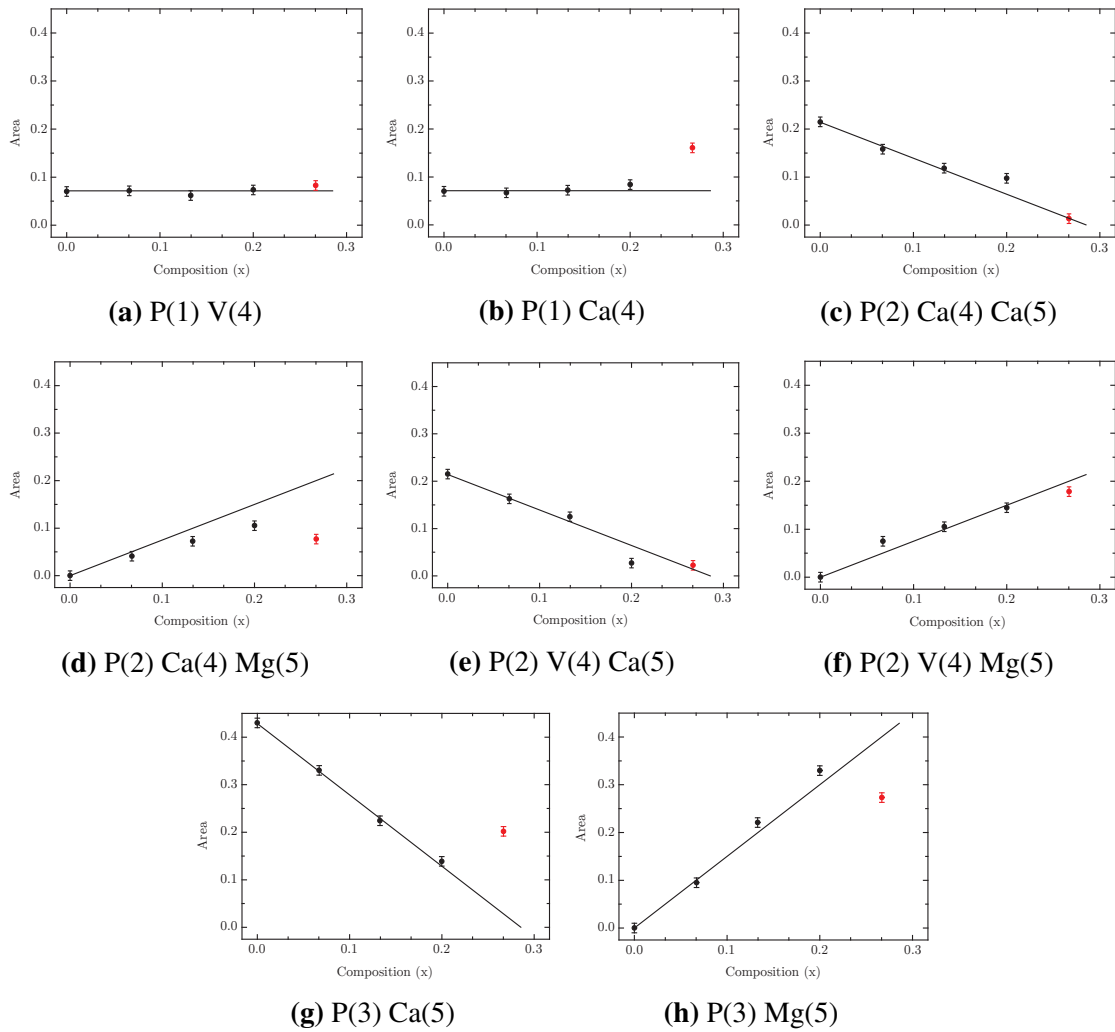
Figure 6.7 The areas of the environments used in the fits presented in figure 6.6. The data points corresponding to the β-TCMP x = 0.267 composition are highlighted red, and are clearly in error for the P(1)Ca(4), P(2)Ca(4)Mg(5), and both P(3) environments.

6.5 Discussion

6.5.1 Magnesium substitution

Due to the time constraints imposed when using a central facility, only a smaller subset of the samples were used in the ND experiment. These were not distributed equally in composition, and the unequal stepping in the stack plot in figure 6.4 reflects this. The 6 coordinated Mg-O correlation can be seen at 2.10 Å [7], and steadily increases with composition. This is expected since, even though a poorly known fraction of the sample is TCTMP second phase, the Mg is 6 coordinated in both phases. As a result, the only information one can extract from the T(r) plot is that the Mg in the sample is 6 coordinated. The resolution in the real-space plot is insufficient to distinguish the different Mg-O correlation lengths in β-TCMP and TCTMP.

6.5.2 The formation of tricalcium trimagnesium phosphate

As is clear in figure 6.2, there are visible quantities of TCTMP second phase in the β-TCMP samples. However, it can also be noted that the amount of TCTMP does not increase smoothly with composition; there appear to be compositions with more second phase than would be expected ($x = 0.267$) and compositions with less second phase ($x = 0.43$ and $x = 0.44$). These anomalies are large with respect to the relative uncertainties of ±25 % placed on the TCTMP content, however are within the limits of this uncertainty. As a result, there is a chance they are merely due to statistical uncertainties. However, a tentative explanation can be formed, assuming these anomalies are real.

These anomalous TCTMP compositions appear around the point of complete substitution on the Ca(5) ($x = 0.285$) and Ca(4) ($x = 0.429$) sites. It is possible that, due to potential ordering of both the Mg^{2+} on the substitutional sites and the vacant Ca(4) sites, substitution becomes less favourable than TCTMP formation as the substitution limit is reached; this is analogous to the effect observed in the electron orbital occupancy of the anomalous transition elements. It is possible that a similar effect occurs in the substitution examined here, where Mg occupancy of the Ca(5) and Ca(4) sites becomes less favourable than the formation of TCTMP until there is sufficient Mg to *fully* occupy a Ca site.

Rietveld refinement was also attempted on the data, however it was realised that this would not be able to provide more accurate results on the compositions of the samples. Rietveld refinement relies on accurate amplitudes of Bragg peaks, in addition to their position. Since the unit cells of β-TCMP and TCTMP are both large, many of their peaks overlap. In order to determine the relative quantities of the second phase precisely, one must know its composition and the positions of every atom in each unit cell exactly, such that the only unknown parameter in the material is the relative quantity of each phase. In practice this is not possible, since even with a nominally perfect sample with the complexity and disorder of TCTMP, the atomic positions vary enough to result in a high level of uncertainty in the resulting composition.

The χ^2 parameters for the dual-phase XRD Rietveld refinements were similar to the refinements presented in the previous two chapters, varying from 1.2 to 1.6. However, a significant increase in the χ^2 parameters was observed for the compositions near $x_n =$ 0.27 and 0.43, approaching complete substitution on the Ca(5) and Ca(4) sites. These refinements have χ^2 values from 1.8 to 3.3, indicating an extremely poor fit to the data. This correlates with increase in the proportion of the TCTMP second phase at these compositions. The χ^2 parameters are given in table 6.1.

If the individual R-Bragg (R_B) parameters are examined over the entire range of refinements, it is clear that the β-TCMP reflections have a much lower R_B parameter in general, indicating a much better fit for the β-TCMP phase than the TCTMP phase. The ratios of the TCTMP to β-TCMP R_B values are shown in table 6.1, and are within 2-5 for all refinements excluding the $x_n = 0.75$ sample. The poor fit of the TCTMP patterns indicated by this high ratio is probably due to the low intensity of the reflections, making the contrast between local and global minima extremely poor. It is observed in the diffraction patterns themselves (figure 6.2) that there is significantly more TCTMP in the compositions with poor χ^2 parameters and so the effect of the poor TCTMP fit on the χ^2 parameter is amplified. It is important to note that in the $x_n = 0.75$ β-TCMP sample, the χ^2 parameter is extremely low, despite the large quantity of TCTMP. At this composition the concentration of TCTMP is comparable with that of β-TCMP, and, as a result, the TCTMP reflections are much more conducive to the refinement avoiding local minima, and so achieving a lower residual. Indeed, in this refinement, the R_B parameters are similar for both the β-TCMP and TCTMP phases.

6.5.3 ^{31}P NMR

As is clear from the results of the fits plotted in figure 6.7, the treatment shown to be successful in the previous chapter could not be applied here. The 8 peak Ca(5) model can be successfully applied to the spectra up to $x = 0.200$ inclusive, however beyond this point the model breaks down. This is due to the presence of the TCTMP second phase described above. This phase has a minimum of 6 ^{31}P NMR resonances for the compositions $Ca_9Mg_9(PO_4)_{12}$ or $Ca_7Mg_{11}(PO_4)_{12}$, rising to at least 10 for other compositions due to Ca-P interatomic distances of less than 3.6 Å between the mixed occupancy Ca,Mg site and the surrounding P sites. This threshold distance was chosen after looking at the Ca-P interatomic distances in β-TCP and could be overly conservative.

At the time of writing, there are no published ^{31}P NMR spectra of TCTMP available for comparison, so a sample with composition $Ca_3Mg_3(PO_4)_4$ was prepared. It was not possible to use the same precursors as in section 6.2, since when the proportion of MgO is increased such that the Ca:Mg ratio is 1:1 there is insufficient phosphate in the mixture. As a result, $Mg_3(PO_4)_2$ was used as a precursor, and made to equation 6.2, with the same procedure outlined in section 6.2. XRD shows a single phase consistent with the phase published by Dickens et al. [6], with no β-TCMP phase evident.

$$2\,CaH(PO_4) + CaCO_3 + Mg_3(PO_4)_2 \rightarrow Ca_3Mg_3(PO_4)_4 + CO_2 + H_2O \qquad (6.2)$$

It is clear that the ^{31}P NMR spectra in figure 6.5 bear a similarity to the equivalent ^{31}P NMR spectrum of β-TCZP shown in figure 5.10. In particular, the feature at -2 ppm is consistent to both, which was shown in the Zn case to be the P(1) Zn(4) environment. Evidence of this peak is visible at $x = 0.200$, would could indicate Ca(4) substitution at this composition. This is less than the limit of the Ca(5) substitution at $x = 0.286$, and the existence of the TCTMP second phase would extend the region of Ca(5) substitution, since there is proportionally less Mg in the β-TCMP phase.

There are also similarities between the β-TCMP and TCTMP spectra shown in figure 6.8, with a main central peak at 0 ppm, and peaks at -2.5 ppm, 3 ppm, and 5 ppm. Importantly, the peak at -2.5 ppm is in a similar position to the P(1) Zn(4) environment mentioned above. This may be merely a coincidence, or an indication of a more significant link between the two structures. It is however impossible to determine the crystallographic environments responsible for these resonances with only one sample,
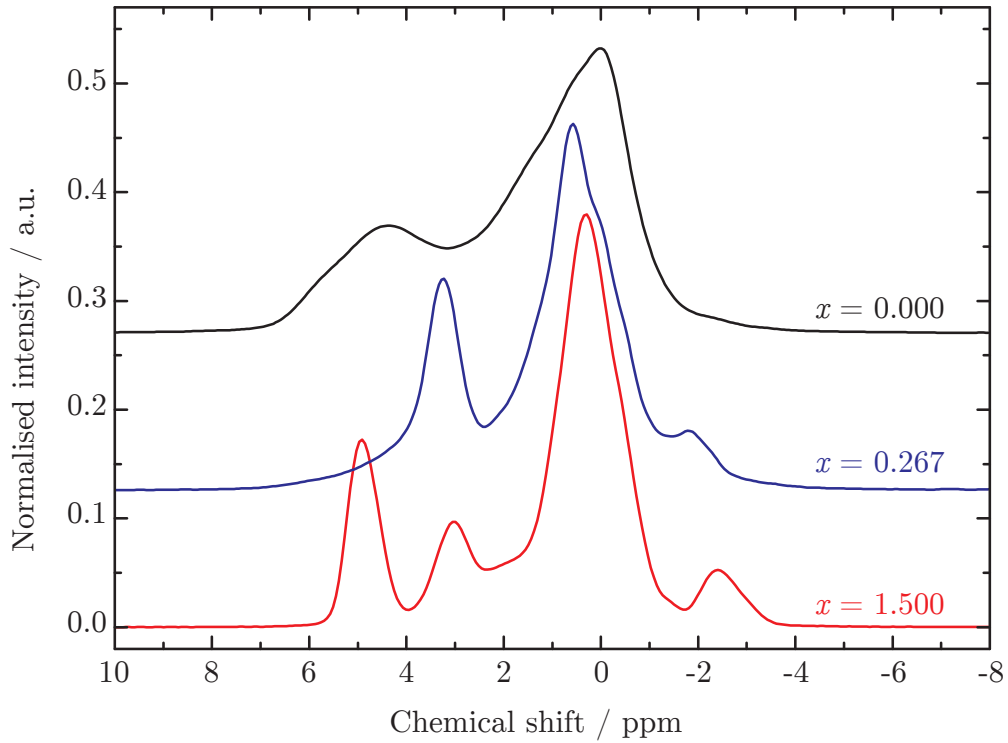
Figure 6.8 A comparison of the ^{31}P NMR spectra of β-TCP, x_n = 0.267 β-TCMP, and TCTMP.

and a full treatment of the solid solution range in TCTMP is outside the scope of this thesis. It is likely however that any subtle change in composition in this solid solution region will have a large effect on the resonances, as is clear in the change of the ^{31}P NMR spectra between β-TCP and β-TCMP over a similar compositional range. As a result, any simple subtraction of the TCTMP ^{31}P NMR spectrum from the β-TCMP spectrum would introduce far more uncertainty than it would eliminate.

6.6   Summary

Despite the similarities between the β-TCMP and β-TCZP systems, it is not possible to treat them similarly. Once the β-TCMP composition exceeds $x = 0.200$, a TCTMP second phase forms with the Ca:Mg ratio 1:1, resulting in an effective decrease in the amount of Mg in the β-TCMP phase. Since the β-TCMP and TCTMP unit cells are both large, any correction to the β-TCMP composition is inherently imprecise. It can be done however, and the lattice parameters can be plotted against a corrected Mg content, and follow a similar trend as shown in the previous chapter. This implies a similar sub-

stitution model as to the Zn case, with substitution initially on the Ca(5) site, followed by the Ca(4) site.

A sample of TCTMP was prepared in order to study the ^{31}P NMR spectrum. It was confirmed that the spectra significantly overlapped, due to the P existing as orthophosphate in both samples. Some similarities were observed in the β-TCMP and TCTMP ^{31}P NMR spectra, making any further interpretation of the β-TCMP system extremely difficult.

References

[1] J. Ando, *Bulletin of the Chemical Society of Japan* **31**, (1958), 201–205.

[2] L. W. Schroeder, B. Dickens and W. E. Brown, *Journal of Solid State Chemistry* **22** (3), (1977), 253–262.

[3] R. A. Terpstra, F. C. M. Driessens, H. G. Schaeken and R. M. H. Verbeeck, *Zeitschrift fur anorganische und allgemeine Chemie* **507** (12), (1983), 206–212.

[4] R. J. B. Jakeman, A. K. Cheetham, N. J. Clayden and C. M. Dobson, *Journal of Solid State Chemistry* **78** (1), (1989), 23–34.

[5] R. Enderlea, F. Gotz-Neunhoeffer, M. Gobbels, F. A. Müller and P. Greil, *Biomaterials* **26**, (2005), 3379–3384.

[6] B. Dickens and W. E. Brown, *Mineralogy and Petrology* **16**, (1971), 79–104.

[7] N. E. Brese and M. O'Keeffe, *Acta Crystallographica Section B Structural Science* **47** (2), (1991), 192–197.

CHAPTER 7

ALUMINIUM & GALLIUM SUBSTITUTION

7.1 Introduction

In contrast to the previous two chapters, this chapter deals exclusively with trivalent cations. The substitution of Al^{3+} into the β-TCP structure is important since the ultimate wasteform will consist of a β-TCP-like phase encapsulated in sodium aluminoborophosphate (NABP) glass. This process is examined in more detail in the following chapter, however for this chapter it is sufficient to realise that during encapsulation of β-TCP in NABP glass, some Al^{3+} will inevitably diffuse into the β-TCP structure. The investigation of Ga^{3+} substitution however, is motivated by the same reason as the Mg^{2+} and Zn^{2+} substitution discussed previously, i.e. its existence in the waste stream. In this work, the naturally occurring non-radioactive isotopes are used.

In the case of a trivalent cation substitution, for every two trivalent cations M^{III} introduced, three calcium Ca^{2+} cations are removed and one vacancy is created [1]:

$$3Ca^{2+} \Rightarrow 2M^{III} + \square, \tag{7.1}$$

Since the trivalent ions investigated here are smaller than Ca^{2+} (Ca^{2+}: 1.0 Å, Al^{3+}: 0.50 Å, Ga^{3+}: 0.62 Å; all 6-coordinated Pauling radii) then substitution on Ca(4) and/or Ca(5) can be assumed. If substitution is exclusively on the Ca(5) site the problem can be simplified by assuming vacancies are created on the Ca(4) site only, since vacancies are present on this site in pure β-TCP:

$$2Ca^{2+}_{Ca(5)} + Ca^{2+}_{Ca(4)} \Rightarrow 2M^{III}_{Ca(5)} + \square_{Ca(4)}. \tag{7.2}$$
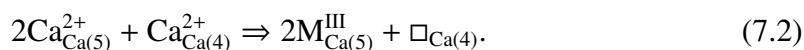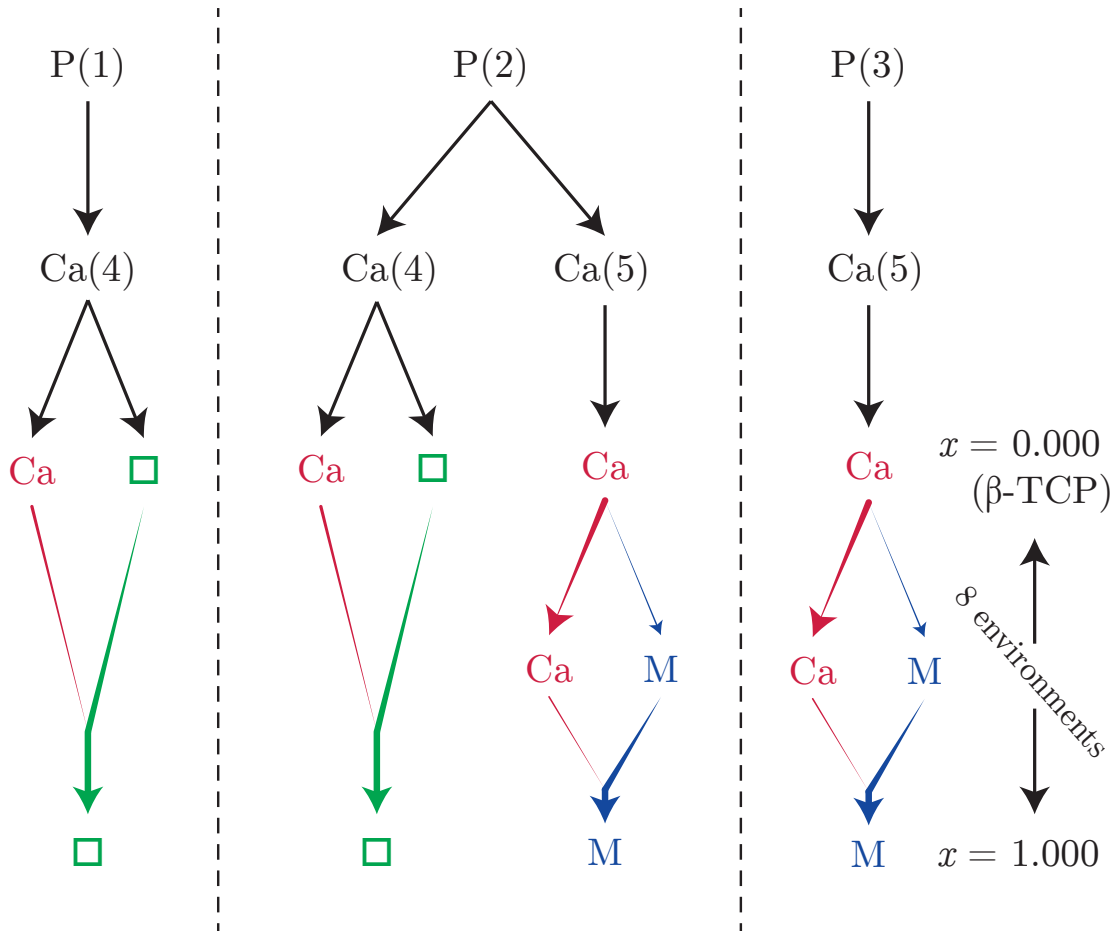
Figure 7.1 The proposed substitution of a trivalent cation M (Al or Ga), and the number of distinct ^{31}P NMR environments at each stage of the substitution.

Under full substitution of the Ca(5) site, the Ca(4) site would be entirely vacant. Since the Ca(1,2,3) sites are considered to be always fully occupied by Ca^{2+} ions, there are 54 unchanged Ca^{2+} ions. Under complete substitution, with Ca(4) vacant, and Ca(5) fully occupied by M^{3+} ions, there is hence a ratio of 54:6 Ca^{2+}:M^{3+} ions, or 9:1. The compositional formula $Ca_9M_x(PO_4)_{6+x}$ is a modified version of that used in the divalent case studied previously, and is commonly used in other studies of trivalent β-TCP substitution.

Total M^{3+} substitution on the Ca(5) site means that three ^{31}P environments would be observed due to the different nnn, rising to 8 distinct ^{31}P environments with partial Ca(5) substitution. This model is referred to as the Ca(5) model. A flow diagram illustrating this model and its expected ^{31}P environments is shown in figure 7.1.

The case of trivalent substitution in β-TCP has been well studied, and a review

of the relevant literature is given in section 2.4. The aim of this chapter is to extend this work by using a relatively new 2D NMR experiment known as rotary resonance recoupled heteronuclear multiple quantum coherence (R^3-HMQC), augmenting the 1D ^{31}P NMR experiments performed in the previous two chapters.

Recently Mellier et al. [2] performed this very experiment, i.e. using R^3-HMQC to investigate the substitution of Ga into the β-TCP structure. The 2D reconstructed ^{31}P NMR spectrum (i.e. the P environments experiencing dipolar coupling with Ga atoms) appears under the high field region of the 1D ^{31}P spectrum only. The resonances comprising the 2D spectrum are identified as being due to the P(2) and P(3) sites, and hence the Ga substitution site was identified as Ca(5).

We have carried out R^3-HMQC experiments on an Al substituted β-TCP sample as well as on a Ga substituted sample similar to that of Mellier et al. [2] to determine the substitutional site directly, based on knowledge of the ^{31}P NMR resonances in β-TCP from the 1D spectra in conjunction with results presented in the previous two chapters.

7.2 Sample synthesis

A series of Ga and Al doped β-TCP samples (β-TCGP and β-TCAP respectively) were made to the stoichiometric formula $Ca_9M_{x_n}(PO_4)_{6+x_n}$, where M is Ga and Al respectively with x_n, the nominal value of x, varying from 0.2 to 1.0 in 0.2 increments. Calcium hydrogen phosphate ($CaHPO_4$) and calcium carbonate ($CaCO_3$) were used as precursors, with gallium oxide (Ga_2O_3) and aluminium phosphate ($AlPO_4$) included in stoichiometric proportions given by the equations 7.3 and 7.4. The powders were ground in an agate pestle and mortar for 10 minutes, before being heat treated in an alumina crucible for 4 hours at 1050 °C. The grinding and heat treatments were repeated a further four times, to eliminate as much cation phosphate second phase as possible.

$$3CaCO_3 + 6CaHPO_4 + x_n AlPO_4.4H_2O \rightarrow Ca_9Al_{x_n}(PO_4)_{6+x_n} + (3+4x_n)H_2O + 3CO_2 \quad (7.3)$$

$$(3-x_n)\,CaCO_3 + (6+x_n)\,CaHPO_4 + \left(\frac{x_n}{2}\right)(Ga_2O_3) \rightarrow$$

$$\rightarrow Ca_9Ga_{x_n}(PO_4)_{6+x_n} + \left(\frac{6+x_n}{2}\right)H_2O + (3-x_n)\,CO_2$$

$$(7.4)$$
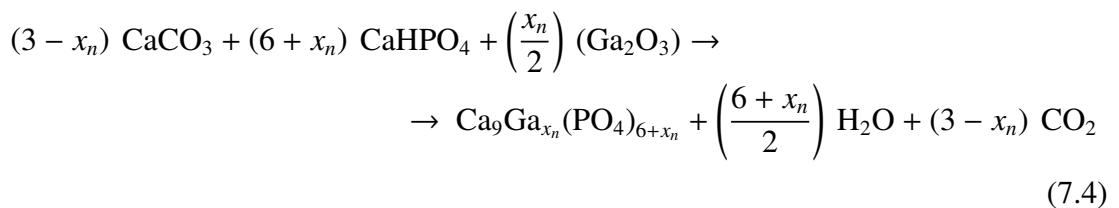
7.3 Experimental methods

7.3.1 ^{27}Al NMR

^{27}Al NMR spectra were acquired at 156.20 MHz with a $\pi/12$ pulse of length 0.5 µs. 3.2 mm rotors were used with a spinning rate of 20 kHz, and a delay of 5 s between pulses was used. The spectra were referenced to the symmetric 6 co-ordinated aluminium site in yttrium aluminium garnet ($Y_3Al_5O_{12}$) at 0.7 ppm with respect to 1 mol aq. $Al(H_2O)_6 \uparrow$.

7.3.2 ^{71}Ga NMR

^{71}Ga NMR spectra were acquired at 61.02 and 152.51 MHz (4.7 T and 11.75 T) with short, low power pulses of 1.3 and 1.75 µs, and 4 mm and 3.2 mm rotors were used with MAS spinning rates of 10 kHz and 17.5 kHz respectively. A delay of 2 s between pulses was used in both cases, with 90-180 Hahn echos to preserve the broad nature of the spectrum. The spectra were referenced to the primary reference 1 mol aq. $Ga(H_2O)_6 \uparrow$.

7.3.3 ^{43}Ca NMR

Natural abundance ^{43}Ca NMR was performed for the β-TCAP $x_c = 0.86$ composition on a Bruker Avance III 850 MHz spectrometer at 57.22 MHz (20 T), and for the β-TCGP $x_c = 0.8$ sample on a Bruker 830 MHz (19.6 T) spectrometer at the NHMFL, Tallahassee. In both cases, a delay of 5 s between pulses was used, with 7 mm rotors at an MAS spinning rate of 5 kHz. Since the natural abundance of ^{43}Ca is only 0.135 %, signal enhancement techniques were used to improve the signal to noise ratio. The rotary-assisted population-transfer (RAPT) [3] sequence was used (5 pairs of Gaussian shaped pulses offset by ±200 kHz) for the β-TCAP sample, and 5 ms frequency-swept chirp pulses (250 kHz below the Larmor frequency with a nutation frequency of 20 kHz) were used for the β-TCGP sample. A 1.5 µs solids $\pi/2$ pulse was used for β-TCAP, with 30 000 acquisitions resulting in a total experimental time of 41 hours. A 3 µs $\pi/2$ pulse was used for β-TCGP, with 61 440 acquisitions resulting in a total experimental time of 85 hours. Both spectra were referenced to the primary reference 0.1 mol aq. $CaCl_2 \cdot H_2O$.

7.3.4 R^3-HMQC

R^3-HMQC was performed using a 4 mm probe. The quadrupolar nuclei were used as the observe nucleus, due to their much shorter T_1 relaxation times, with the single quantum coherence on the indirect (^{31}P) nucleus. The RF power required for the $q = 2$ R^3 resonance was determined by observing the minimum in observed signal as a function of applied power on a spin-lock pulse [4]. Selective π and $\pi/2$ pulses were used for the ^{71}Ga and ^{27}Al spin-echo so as to only excite the central transition. Spectral widths of 100 kHz and 12.5 kHz were used in the cation (X) and ^{31}P (Y) dimensions respectively, where the spectral width of the Y dimension was chosen to be equal to the MAS rate, at 12.5 kHz. In the case of the ^{71}Ga experiment, 1000 acquisitions with a pulse delay of 0.5 s were collected for each of the 128 T_1 increments, with a complete experimental time of 18 hours. For the ^{27}Al experiment, 192 acquisitions with a pulse delay of 1 s were observed for 256 T_1 increments, with a complete experimental time of 14 hours. The States hyper-complex processing method [5] was used for sign discrimination.

Since the $x_c = 0.93$ Ga sample contained $\sim 7\%$ $GaPO_4$ second phase, the $x_c = 0.80$ Ga sample was chosen for the R^3-HMQC experiment. The $x_c = 0.86$ Al sample was retained as the upper limit of the Al series, despite the presence of second phase, since the receptivity and general ease of study of ^{27}Al is far more favourable to detecting small quantities of $AlPO_4$, and identifying it amongst the major β-TCP phase.

7.4 Results

7.4.1 X-ray diffraction

XRD was performed to determine the phase composition; a detailed Rietveld refinement has been performed previously by Mee [6]. Second phase was present in the form of $AlPO_4$ in the $x_n = 0.8$ and 1.0 β-TCAP samples, and as $GaPO_4$ in the $x_n = 1.0$ β-TCGP sample. The relative phase concentrations were determined by ^{27}Al NMR (for the Al samples) and Rietveld refinement. The proportions of second phase and the adjusted cation concentration in the β-TCP phase are given in table 7.1. For $x_n = 1.0$ the effective aluminium substitution was reduced to $x_c = 0.86$ due to the $AlPO_4$ second phase, where x_c is the corrected x value.

Table 7.1   Cation phosphate second phase at each composition is given as at.%, with the corrected x values referred to as x_c, and [ ] denotes the concentration.

Composition	β-TCAP		β-TCGP	
x_n	$[AlPO_4] \pm 1\%$	$x_c \pm 0.01$	$[GaPO_4] \pm 1\%$	$x_c \pm 0.01$
0.20	0 %	0.20	0 %	0.20
0.40	0 %	0.40	0 %	0.40
0.60	0 %	0.60	0 %	0.60
0.80	2 %	0.79	0 %	0.80
1.00	14 %	0.86	7 %	0.93

7.4.2 ^{31}P NMR

Stack plots of the ^{31}P NMR spectra are shown in figures 7.2a and 7.2b. An 8 peak model was used to fit the Al and Ga substituted spectra as described in figure 7.1, using the corrected composition computed in section 7.4.1. The fitted β-TCAP and β-TCGP ^{31}P NMR spectra are shown in figures 7.3 and 7.4 respectively, with the fit parameters given in table 7.2. In the case of the β-TCGP fits, the linewidths of the individual peaks become significantly narrower with substitution, requiring a pseudo-Voigt profile to fit the spectra. In these cases, the Gaussian/Lorentzian mixing ratio was fixed for a given overall peak linewidth, similar to the β-TCZP and β-TCMP ^{31}P NMR fits presented in chapters 5 and 6.

(a) β-TCAP
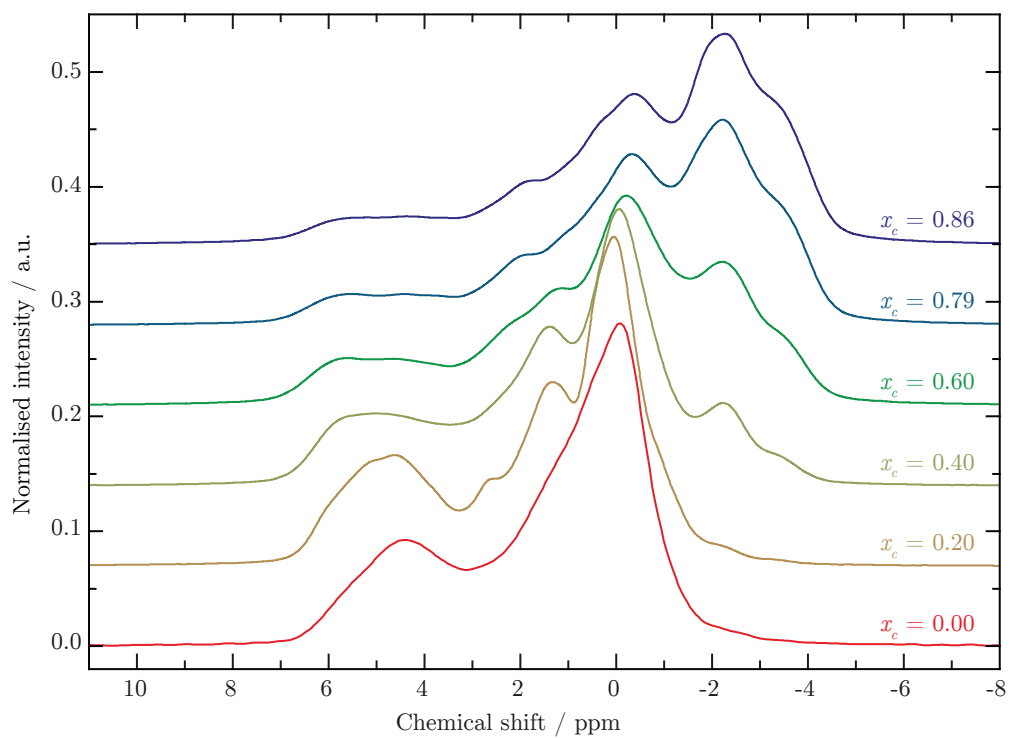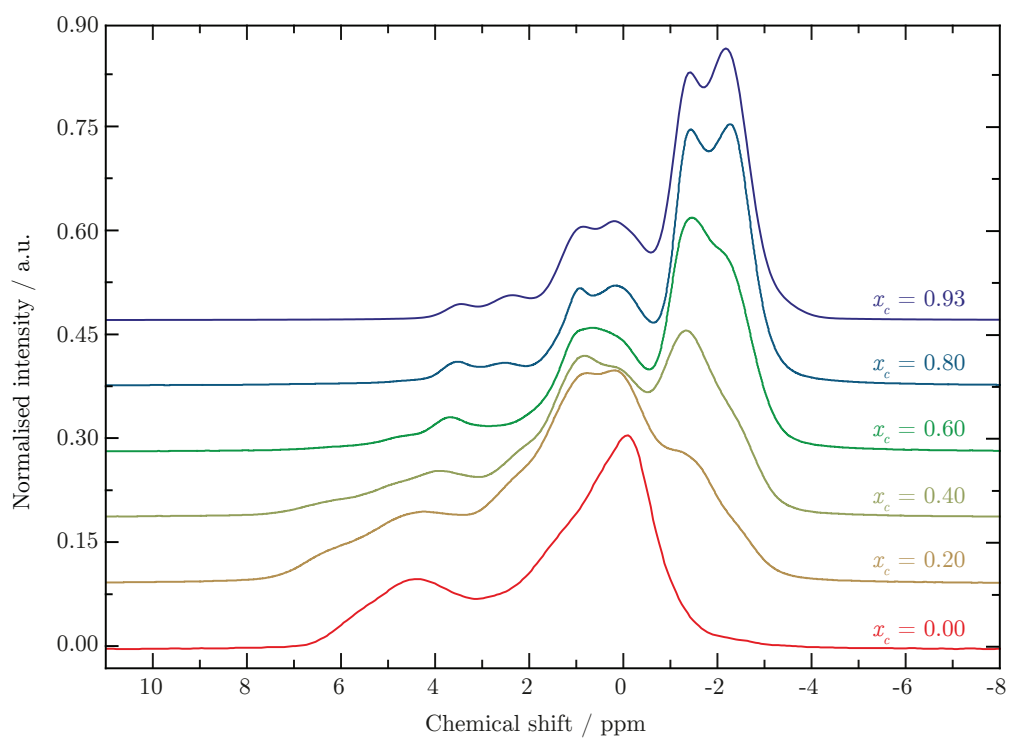
(b) β-TCGP

Figure 7.2 Stack plots of β-TCAP and β-TCGP ^{31}P NMR spectra.

(a) β-TCAP $x_c = 0.20$

(b) β-TCAP $x_c = 0.40$

(c) β-TCAP $x_c = 0.60$

(d) β-TCAP $x_c = 0.79$

(e) β-TCAP $x_c = 0.86$
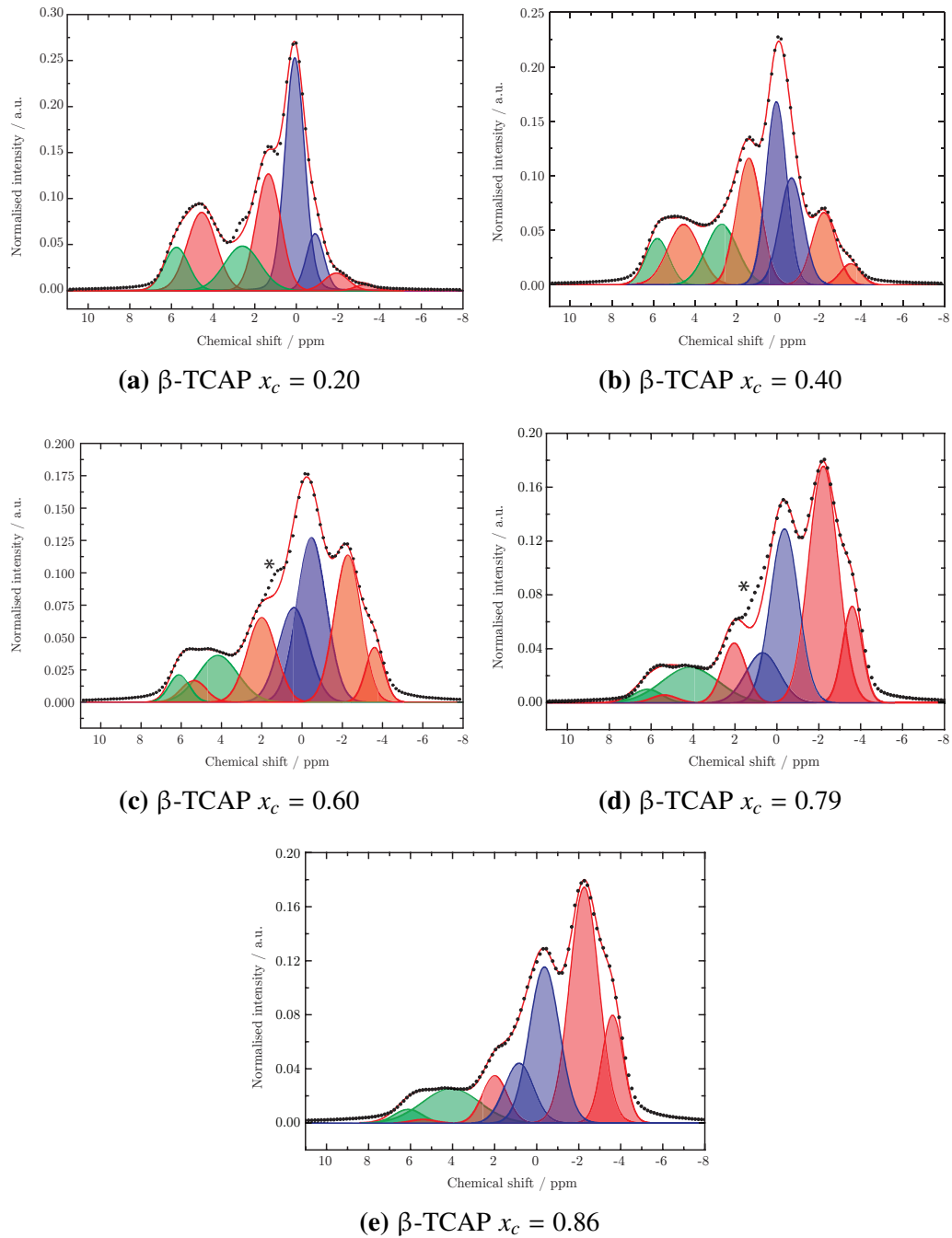
Figure 7.3 ^{31}P NMR fits of the β-TCGP series. The corrected composition x_c was used to calculate and fix the areas of the individual resonances. The ∗ at 1.3 ppm in the $x_c = 0.79$ and 0.86 spectra denote brushite second phase.

(a) β-TCGP $x_c = 0.20$

(b) β-TCGP $x_c = 0.40$

(c) β-TCGP $x_c = 0.60$

(d) β-TCGP $x_c = 0.80$

(e) β-TCGP $x_c = 0.93$
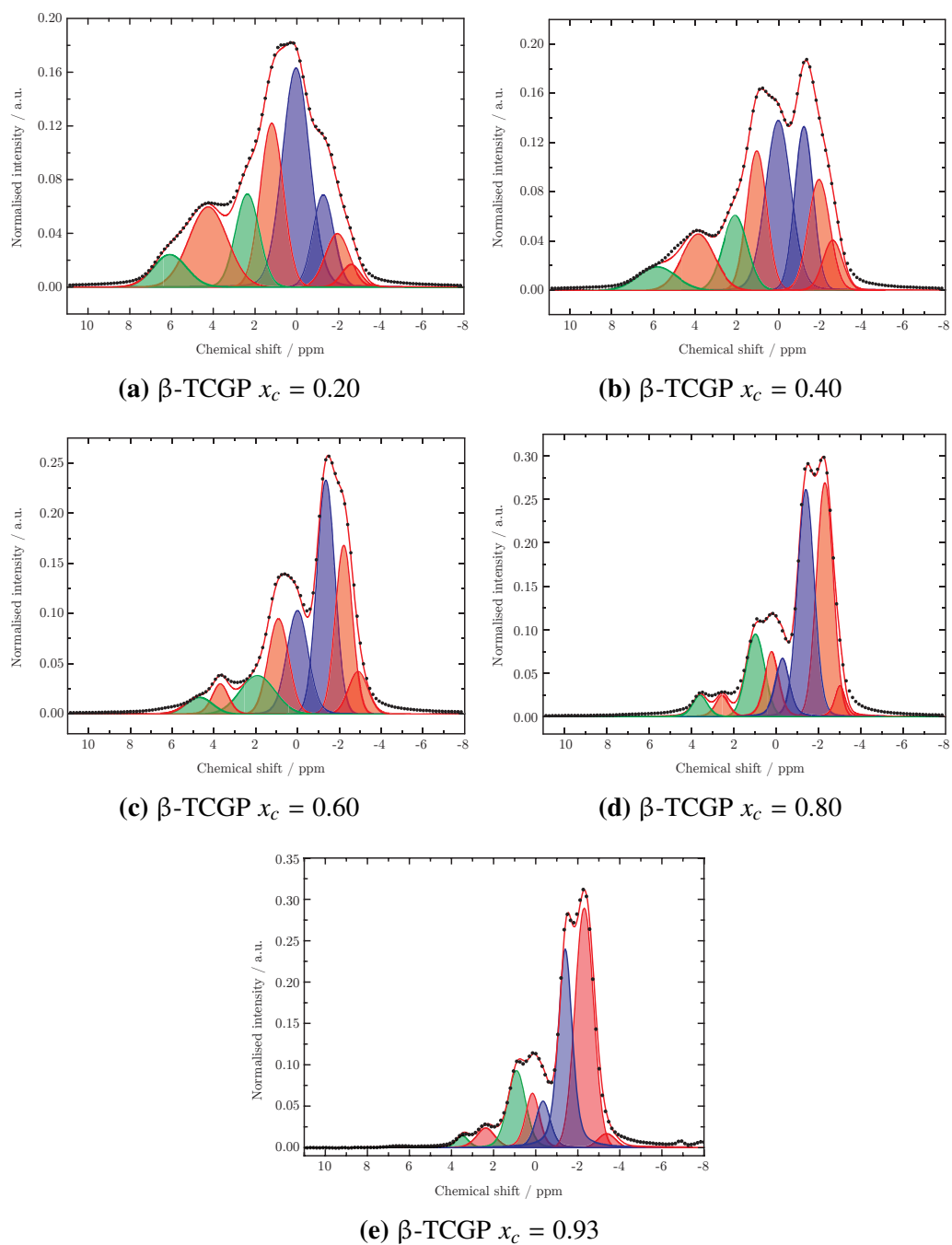
Figure 7.4 ^{31}P NMR fits of the β-TCGP series. The corrected composition x_c was used to calculate and fit the areas of the individual resonances.

Table 7.2 The results of the fits for β-TCAP (left) and β-TCGP (right), from figures 7.3 and 7.4 respectively. The β-TCP results from chapter 4 are included for comparison. The chemical shift (δ) is rounded to 0.1 ppm with an uncertainty of ±0.05 ppm, the line-width (LW) is rounded to 5 Hz with an uncertainty of ±2.5 Hz, the area is rounded to 1 % with an uncertainty of ±0.5 %, and the Gaussian-Lorentzian ratio (PV) was set to a series of values based on the line-width.

β-TCAP (left)

Comp. x_c	P(1) V(4) δ	Area	LW	PV	P(1) Ca(4) δ	Area	LW	PV
0.00	2.6	7 %	430	1.0	5.5	8 %	400	1.0
0.20	2.7	9 %	260	1.0	5.7	8 %	255	1.0
0.40	2.8	10 %	380	1.0	5.8	6 %	250	1.0
0.60	2.4	10 %	395	1.0	6.9	6 %	275	1.0
0.79	4.1	8 %	645	1.0	6.2	1 %	320	1.0
0.86	4.1	8 %	650	1.0	6.1	2 %	320	1.0

Comp. x_c	P(2) V(4) Ca(5) δ	Area	LW	PV	P(2) V(4) Al(5) δ	Area	LW	PV
0.00	1.4	23 %	400	1.0				
0.20	1.4	21 %	240	1.0	-2.1	2 %	275	1.0
0.40	1.4	19 %	265	1.0	-2.2	10 %	270	1.0
0.60	1.3	12 %	260	1.0	-2.3	20 %	315	1.0
0.79	2.0	5 %	305	1.0	-2.2	40 %	320	1.0
0.86	2.0	5 %	285	1.0	-2.3	42 %	320	1.0

Comp. x_c	P(2) Ca(4) Ca(5) δ	Area	LW	PV	P(2) Ca(4) Al(5) δ	Area	LW	PV
0.00	4.4	26 %	490	1.0				
0.20	4.5	16 %	305	1.0	-3.2	1 %	255	1.0
0.40	4.6	11 %	345	1.0	-3.4	2 %	180	0.9
0.60	4.5	6 %	305	1.0	-3.5	6 %	220	1.0
0.79	5.4	8 %	290	1.0	-3.6	7 %	220	1.0
0.86	5.4	4 %	290	1.0	-3.6	9 %	240	1.0

Comp. x_c	P(3) Ca(5) δ	Area	LW	PV	P(3) Al(5) δ	Area	LW	PV
0.00	0.0	44 %	320	1.0				
0.20	0.1	34 %	205	1.0	-0.9	9 %	215	1.0
0.40	0.1	25 %	210	1.0	-0.6	17 %	265	1.0
0.60	0.1	16 %	235	1.0	-0.7	25 %	335	1.0
0.79	0.1	10 %	385	1.0	-0.5	28 %	310	1.0
0.86	0.1	7 %	325	1.0	-0.4	28 %	340	1.0

β-TCGP (right)

Comp. x_c	P(1) V(4) δ	Area	LW	PV	P(1) Ca(4) δ	Area	LW	PV
0.00	2.6	7 %	430	1.0	5.5	8 %	400	1.0
0.20	2.4	11 %	270	1.0	6.1	5 %	385	1.0
0.40	2.2	10 %	280	1.0	6.0	5 %	360	1.0
0.60	1.9	9 %	350	1.0	4.7	3 %	305	1.0
0.80	1.0	12 %	210	0.9	3.6	3 %	170	0.8
0.93	0.6	12 %	205	0.9	3.2	1 %	145	0.7

Comp. x_c	P(2) V(4) Ca(5) δ	Area	LW	PV	P(2) V(4) Ga(5) δ	Area	LW	PV
0.00	1.4	23 %	400	1.0				
0.20	1.2	19 %	255	1.0	-1.9	6 %	275	1.0
0.40	1.1	16 %	225	1.0	-1.9	13 %	240	1.0
0.60	0.9	14 %	210	1.0	-2.2	21 %	215	1.0
0.80	0.2	8 %	160	0.7	-2.3	31 %	185	0.8
0.93	-0.1	7 %	155	0.7	-2.6	34 %	200	0.9

Comp. x_c	P(2) Ca(4) Ca(5) δ	Area	LW	PV	P(2) Ca(4) Ga(5) δ	Area	LW	PV
0.00	4.4	26 %	490	1.0				
0.20	4.3	15 %	440	1.0	-2.6	2 %	220	1.0
0.40	4.1	9 %	375	1.0	-2.6	5 %	220	1.0
0.60	3.7	4 %	185	0.8	-3.1	6 %	220	1.0
0.80	2.5	3 %	155	0.7	-3.0	3 %	120	0.6
0.93	2.1	3 %	180	0.8	-3.6	2 %	200	1.0

Comp. x_c	P(3) Ca(5) δ	Area	LW	PV	P(3) Ga(5) δ	Area	LW	PV
0.00	0.0	44 %	320	1.0				
0.20	0.1	32 %	310	1.0	-1.3	10 %	235	1.0
0.40	0.1	23 %	280	1.0	-1.2	17 %	205	1.0
0.60	0.1	15 %	230	1.0	-1.4	29 %	200	1.0
0.80	-0.3	8 %	155	0.7	-1.4	32 %	185	0.8
0.93	-0.6	6 %	170	0.8	-1.7	35 %	170	0.8

(a) P(1) V(4) **(b)** P(1) Ca(4) **(c)** P(2) Ca(4) Ca(5) **(d)** P(2) Ca(4) Al(5)

(e) P(2) V(4) Ca(5) **(f)** P(2) V(4) Al(5) **(g)** P(3) Ca(5) **(h)** P(3) Al(5)

Figure 7.5 The areas of the environments used in the fits presented in figure 7.3. The final two data points show a significant deviation from the calculated trend for some environments, and are highlighted red. The statistical error is given by the size of the data point.

(a) P(1) V(4) **(b)** P(1) Ca(4) **(c)** P(2) Ca(4) Ca(5) **(d)** P(2) Ca(4) Ga(5)

(e) P(2) V(4) Ca(5) **(f)** P(2) V(4) Ga(5) **(g)** P(3) Ca(5) **(h)** P(3) Ga(5)
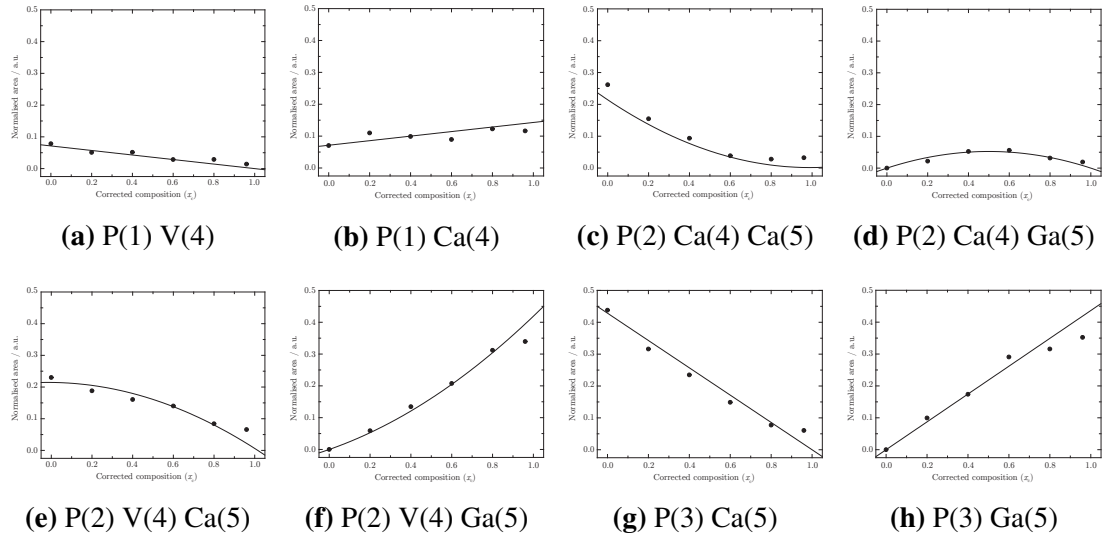
Figure 7.6 The areas of the environments used in the fits presented in figure 7.4. A good agreement between the fit and the calculated areas is seen over the entire compositional range. The statistical error is given by the size of the data point.

120

7.4.3 ^{27}Al NMR

^{27}Al NMR was performed on the complete set of Al substituted samples. A narrow resonance at -10 ppm with a width of ~ 200 Hz was observed to increase with increasing Al content and, in the higher concentration Al $x_c = 0.79$ and $x_c = 0.86$ samples a small additional resonance at 40 ppm due to AlPO$_4$ was observed. The small linewidth of the resonance at -10 ppm implies C_q must be less than 1 MHz, indicating a highly symmetric environment. The spectrum of the $x_c = 0.86$ sample is shown in figure 7.7.
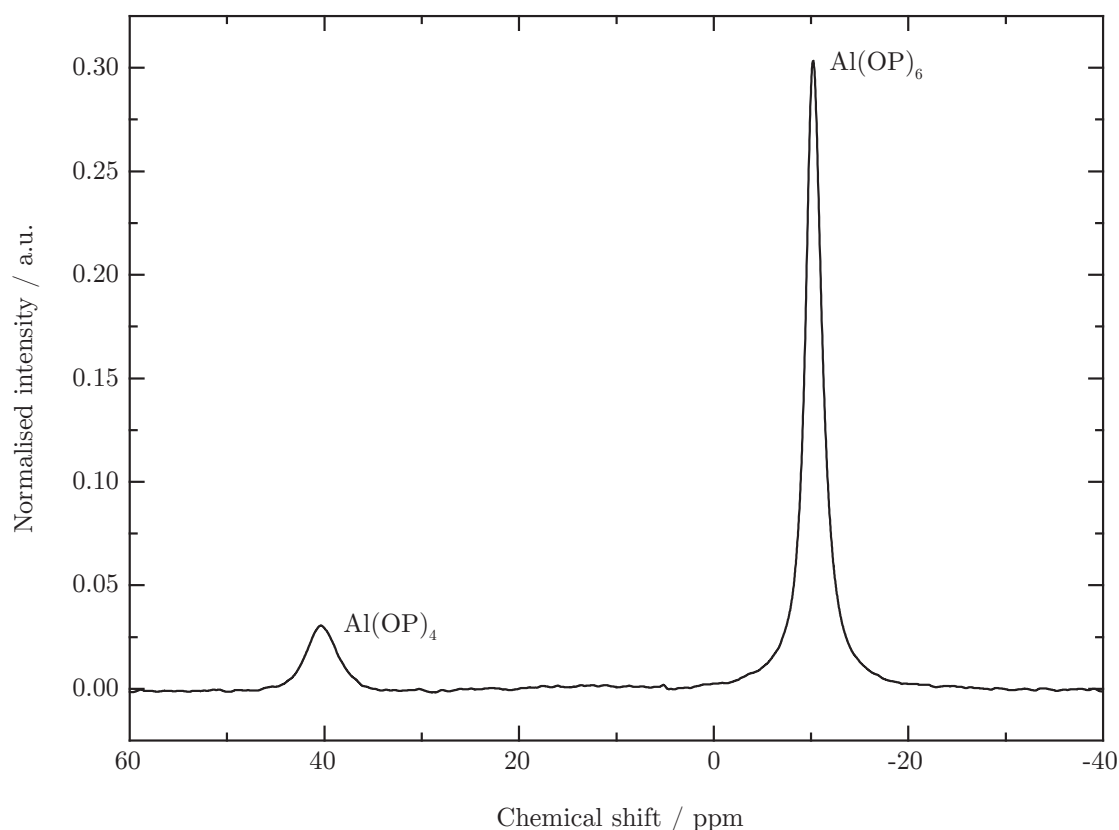
Figure 7.7 The ^{27}Al NMR spectrum of the $x_c = 0.86$ β-TCAP sample. The linewidth of the 6 coordinated Al(OP)$_6$ environment is dominated by Lorentzian broadening due to the T$_2$ relaxation time. As a result, only an upper limit can be put on the C_q, indicating an extremely symmetric site.

7.4.4 ^{71}Ga NMR

Initially ^{71}Ga was performed at high field (11.75 T), however due to the significant contribution to the linewidth by chemical shift dispersion from the range of environments present it was decided to also perform the experiment at low field. A 3.2 mm probe was used to provide a faster spinning speed of 17.5 kHz to counter the increased quadrupolar broadening at the lower field. Thus, the additional ^{71}Ga NMR experiment mentioned above was performed on the Ga $x_c = 0.80$ sample, however due to the proportionally broader lineshape a faster spinning speed of 17.5 kHz was required. Both spectra were fitted using the QuadFit software [7] with identical C_q and η_q distributions used in both fits. Gaussian line broadening was used to model the effects of shift dispersion. The fits at both 11.75 T and 4.7 T are shown in figure 7.8, where $C_q = 4.0$ MHz, $\Delta C_q = 1.3$ MHz, $\eta_q = 0.39$, $\Delta \eta_q = 0.10$, and 10 ppm of Gaussian line broadening was used to produce the fits.
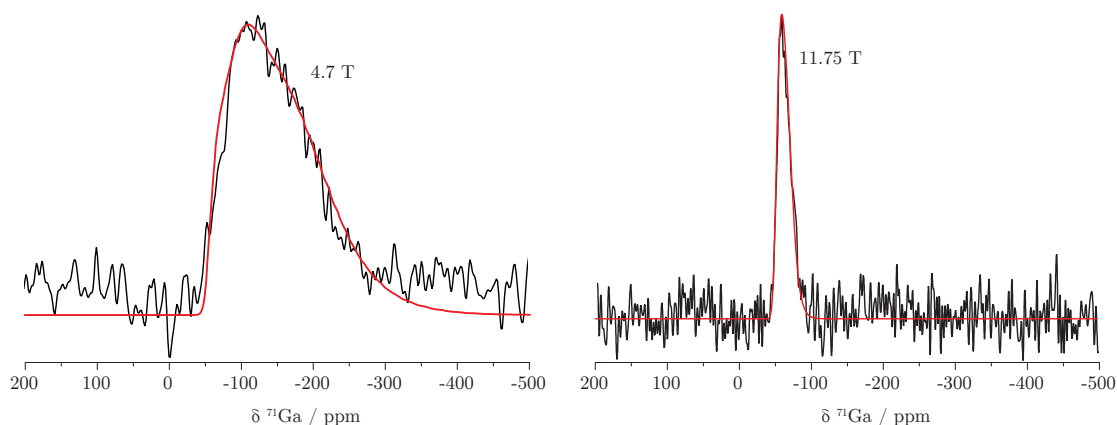
Figure 7.8 The ^{71}Ga spectra of the $x = 0.8$ β-TCGP sample collected at 4.7 T and 11.75 T. The fit in red uses a Gaussian distribution of quadrupolar coupling parameters. $C_q = 4.0$ MHz, $\Delta C_q = 1.3$ MHz, $\eta_q = 0.39$ and $\Delta \eta_q = 0.10$.

7.4.5 ^{43}Ca NMR

^{43}Ca NMR β-TCAP and β-TCGP spectra are shown in figure 7.9 alongside the pure β-TCP ^{43}Ca NMR spectrum presented previously in chapter 4. The spectra were fitted to 5 Gaussian line shapes, with areas determined by the relative number of Ca sites in the β-TCP structure, and the predicted β-TCAP and β-TCGP structures.

(a) β-TCP

(b) β-TCAP

(c) β-TCGP
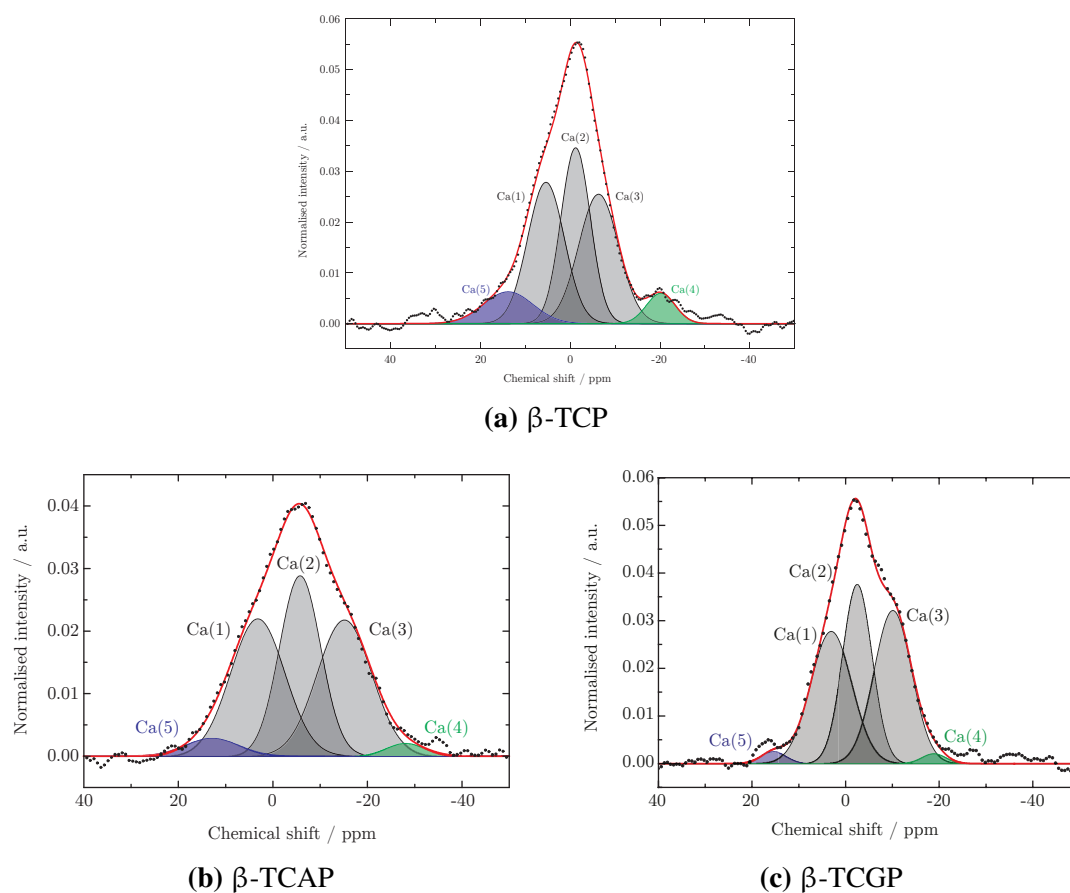
Figure 7.9 ^{43}Ca NMR spectra and simulations of β-TCP, x_c = 0.86 β-TCAP, and x_c = 0.8 β-TCGP.

7.4.6 R^3-HMQC

Contour plots of the results of the R^3-HMQC experiments are shown in figure 7.10, and skyline projections are shown for both dimensions. Slices taken at the maximum intensity in the cation dimension are shown in figure 7.11, with the 1D spectra from figures 7.3e and 7.4d respectively. The contour plots have the same ^{31}P axis limits as the one dimensional ^{31}P spectra.

(a) β-TCGP

(b) β-TCAP
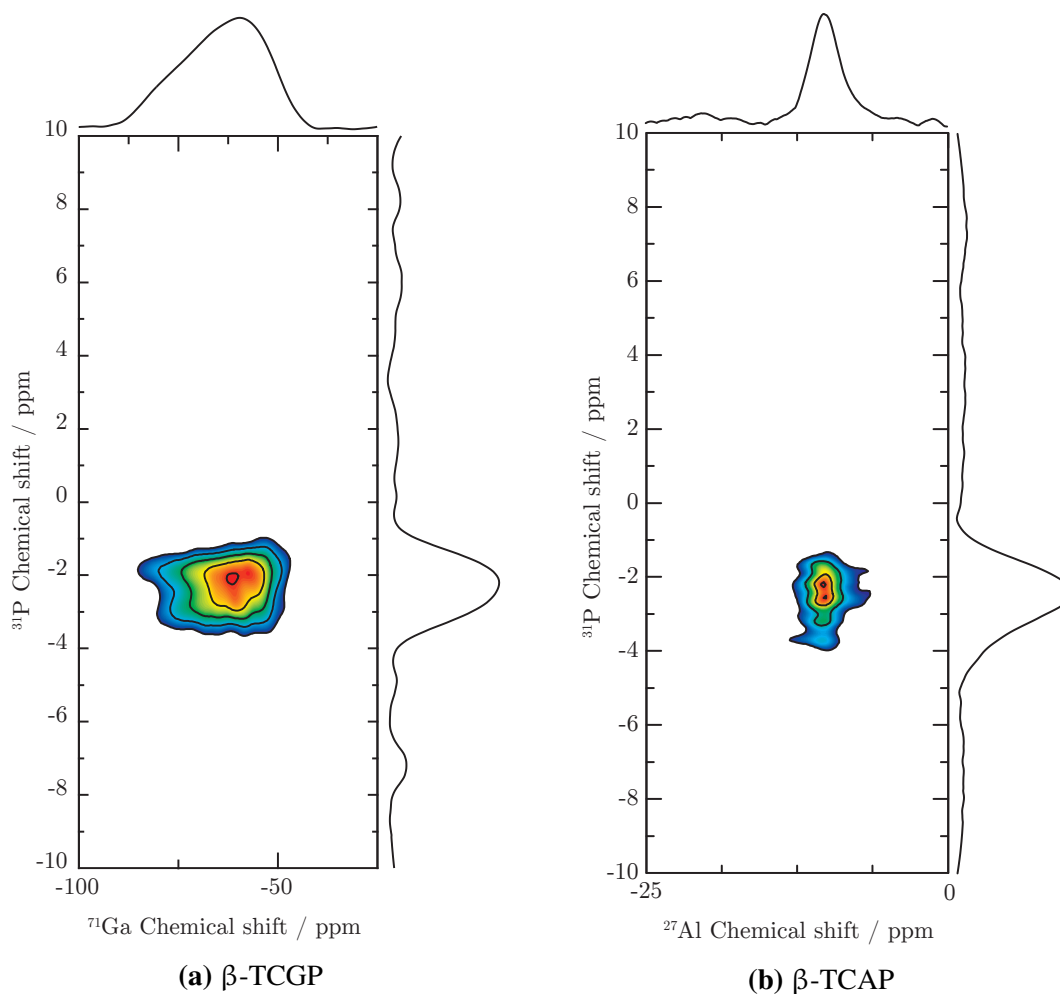
Figure 7.10   2D contour plots with skyline projections for the ^{27}Al-$\left\{^{31}\text{P}\right\}$ R^3-HMQC and ^{71}Ga-$\left\{^{31}\text{P}\right\}$ R^3-HMQC experiments.

(a) β-TCGP

(b) β-TCAP
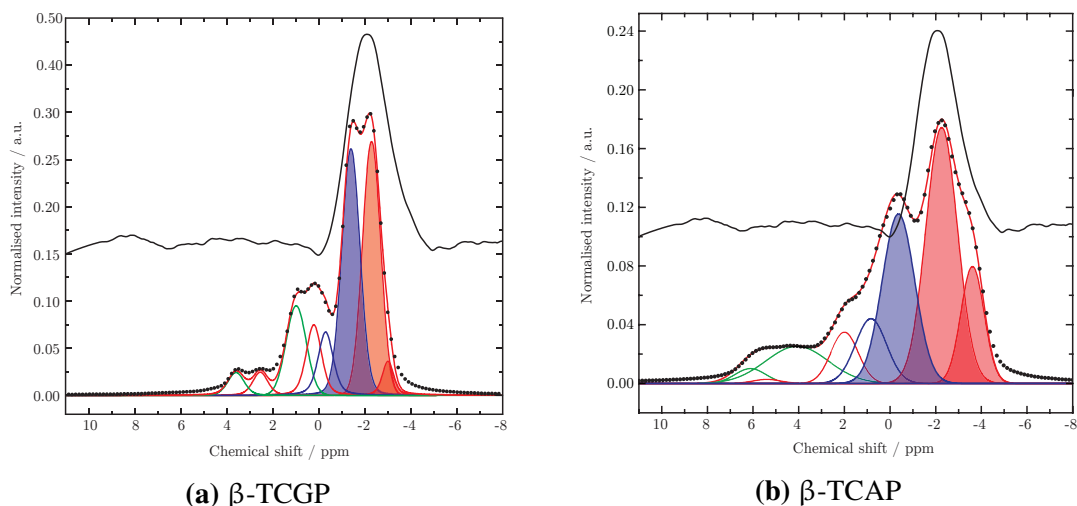
Figure 7.11 1D slices taken from the respective plots in figure 7.10 at the maximum cation intensity. The 1D fits are shown for comparison, where only the ^{31}P environments with cation nnn are shaded.

7.5 Discussion

7.5.1 ^{43}Ca NMR

The ^{43}Ca spectra of the Ga and Al substituted samples can be simulated using a model similar to that which is shown in figure 7.1, with the simplification that the Ca environments are only sensitive to their nearest neighbours, i.e. number and position of oxygen neighbours. For substitution of trivalent cations, the number of vacant Ca sites must increase at half the rate of the substitution in order to maintain charge neutrality of the unit cell. Hence, under substitution of a trivalent cation, a decrease in the area of the Ca environments is expected from both the replacement of Ca atoms with substituent cations, and the introduced vacancies for charge balancing. These two mechanisms of removing Ca^{2+} cations from Ca environments are indistinguishable by ^{43}Ca NMR.

Nevertheless, the ^{43}Ca NMR data show that substitution and vacancy generation on Ca(1), Ca(2), and Ca(3) sites do not occur, proving that the assumption of substitution only on Ca(4+5) is correct. Figure 7.9 shows the simulations produced for unsubstituted β-TCP, β-TCAP $x_c = 0.86$ and β-TCGP $x_c = 0.8$ compositions. The major change from figure 7.9a to both figures 7.9b and 7.9c is the reduction of intensity of the peaks at the most extreme positive and negative shifts, which have been assigned to Ca(5)

and Ca(4) respectively. No conclusion can be made as to the distribution of Al or Ga between these environments, however the absence of Ca intensity is clear. There appears to be little change in the areas of the central three environments, though there are changes in their chemical shift and linewidth.

The linewidths of the β-TCGP ^{43}Ca spectrum is unchanged from the pure β-TCP ^{43}Ca NMR spectrum, however the linewidths of the β-TCAP samples are approximately 50 % larger whilst still being Gaussian (i.e. no indication of any quadrupolar broadening). This indicates a greater disorder at the Ca environments under Al substitution as opposed to both β-TCP and β-TCGP, which could be due to the difference between the Al^{3+} and Ca^{2+} cation radii (0.5 Å), strongly distorting the structure.

7.5.2 ^{31}P NMR

The relative areas of the environments were constrained according to the sample composition, and the pure β-TCP spectrum was used as the initial fitting condition for the series. It is key to note that the resonances in the pure β-TCP ^{31}P spectrum moved less than 1 ppm in the simulations for the Al and Ga substituted samples, only changes in area and linewidth were allowed. The x_c = 0.6 and 0.8 β-TCAP ^{31}P spectra show small peaks at 1.7 ppm, consistent with the dicalcium phosphate dihydrate, or brushite, (CaHPO$_4 \cdot$ 2 H$_2$O) ^{31}P NMR chemical shift [8, 9]. The amount of this phase determined by the ^{31}P NMR spectrum is < 1 %, and hence was not observed with the preliminary XRD scans.

The existence of AlPO$_4$ in samples with x_c = 0.79 and 0.86 substitution, with no corresponding GaPO$_4$ phase at this substitution level, indicates that Al substitution is less favourable than Ga substitution. This is probably due to the large difference in ionic radius between Al^{3+} and Ca^{2+} (0.5 Å). The difference between Ga^{3+} and Ca^{2+} is smaller (0.38 Å), but a substitution limit was reached for both cations below the structural maximum. This is unsurprising, since calculations by Jay et al. show a relatively high solution energy for Al^{3+} and Ga^{3+} under substitution into the β-TCP unit cell compared to other substituent cations [10].

The linewidths of the individual resonances are dependent on the substituent cation. In the case of the ^{31}P spectra, the β-TCAP ^{31}P NMR linewidths remain unchanged from the pure β-TCP ^{31}P spectrum. The β-TCGP ^{31}P linewidths become much narrower,

which can be attributed to the decrease of the Ca(4) occupancy, resulting in a Ca(4) site dominated by vacancies. Since the difference between the Ga^{3+} and Ca^{2+} cation size is smaller than the Al^{3+} and Ca^{2+} difference (discussed above), one could imagine the Ga substituted structure would be dominated by the change in Ca(4) occupancy, as opposed to any distortion caused by cation size.

7.5.3 ^{27}Al & ^{71}Ga NMR

The ^{27}Al NMR spectrum shown in figure 7.7 shows two clear environments; a peak due to 6-coordinated Al (substituted in the β-TCP phase) is visible at -10 ppm, and a peak due to 4-coordinated Al (in the 4 coordinated $AlPO_4$ second phase) is visible at 42 ppm. The 6-coordinated environment has a C_q of less than 1 MHz, implying a highly symmetric site with a small electric field gradient, consistent with the Ca(5) site. Similarly, the ^{71}Ga NMR fits in figure 7.8 are consistent with a single substituent environment, strongly indicating the existence of substitution on one Ca site only. Furthermore, the small C_q value from this fit is consistent with substitution onto the relatively symmetric 6-coordinated Ca(5) site.

7.5.4 R^3-HMQC

The 2D contour plots of the β-TCAP and β-TCGP samples shown in figure 7.10 clearly show a ^{31}P NMR signal confined to a narrow chemical shift range around -2 ppm, consistent with the resonances caused by P(3) and P(2) with substituent cation nnn. This is more easily seen if slices are taken through the 2D spectrum, as shown in figure 7.11b and 7.11a. The ^{31}P slices through the spectra at maximum cation resonance intensity, which show only those P environments with a dipolar coupling to the substituted cation, exist only in the shift range from -1 to -4 ppm. This region of the ^{31}P 1D lineshape has been assigned to P(2) and P(3) environments coupled to the substituent cation on the Ca(5) site, shown previously in section 7.4.2. There is no observed intensity at lower field from -1 to 5 ppm, where resonances assigned to P(1) and P(2) environments coupled to Ca on the Ca(4) and Ca(5) sites are found. Thus Ca(5) must be the only substituent site, and there is no substitution on the Ca(4) site, only vacancy formation.

7.6   Summary

The results of the 2D NMR experiments clearly show that Al and Ga substitute only on the Ca(5) site. By extending the pure β-TCP ^{31}P spectrum to Al and Ga substituted β-TCP ^{31}P spectra with tight constraints, the individual resonances comprising the broad ^{31}P NMR resonance previously reported in the literature can be assigned. The ^{27}Al-$\left\{^{31}P\right\}$ and ^{71}Ga-$\left\{^{31}P\right\}$ R^3-HMQC experiments then show only the regions of the 1D ^{31}P spectra assigned to P resonances with Al or Ga cation nnn respectively.

The Ca(5) site is the site of substitution, and the occupancy of the Ca(4) site reduces towards zero to conserve electroneutrality of the unit cell. The elimination of Ca from the Ca(4) site leads to narrowing of the resulting resonances. Furthermore, it has been shown that Al and Ga β-TCP can be readily formed up to $Ca_9M_{0.8}(PO_4)_{6.8}$, and the resulting single phase polycrystalline material undergoes substitution on one specific environment.

References

[1] K. Yoshida, H. Hyuga, N. Kondo, H. Kita, M. Sasaki, M. Mitamura, K. Hashimoto and Y. Toda, *Journal of the American Ceramic Society* **89** (2), (2006), 688–690.

[2] C. Mellier, F. Fayon, V. Schnitzler, P. Deniard, M. Allix, S. Quillard, D. Massiot, J.-M. Bouler, B. Bujoli and P. Janvier, *Inorganic Chemistry* **50** (17), (2011), 8252–60.

[3] Z. Yao, H.-T. Kwak, D. Sakellariou, L. Emsley and P. J. Grandinetti, *Chemical Physics Letters* **327** (1-2), (2000), 85–90.

[4] M. Baldus, D. Rovnyak and R. G. Griffin, *The Journal of Chemical Physics* **112** (13), (2000), 5902.

[5] D. States, R. Haberkorn and D. Ruben, *Journal of Magnetic Resonance* **48** (2), (1982), 286–292.

[6] M. Mee, *Trivalent cation substitution of β-tricalcium phosphate*, Ph.D. thesis, University of Warwick 2011.

[7] T. F. Kemp and M. E. Smith, *Solid State Nuclear Magnetic Resonance* **35** (4), (2009), 243–52.

[8] W. P. Rothwell, J. S. Waugh and J. P. Yesinowski, *Journal of the American Chemical Society* **102** (8), (1980), 2637–2643.

[9] A. P. Legrand, H. Sfihi, N. Lequeux and J. Lemaître, *Journal of Biomedical Materials Research. Part B, Applied Biomaterials* **91** (1), (2009), 46–54.

[10] E. E. Jay, P. M. Mallinson, S. K. Fong, B. L. Metcalfe and R. W. Grimes, *Journal of Nuclear Materials* **414** (3), (2011), 367–373.

CHAPTER 8

ENCAPSULATION OF β-TCP IN PHOSPHATE GLASS

8.1 Introduction

In order to create a chemically inert and physically resilient wasteform, the substituted β-TCP is encapsulated in a sodium aluminoborophosphate (NABP) glass matrix at 800 °C. During processing, there is significant interdiffusion between the β-TCP particles and the glass matrix leading to concentration gradients at the interface between the two materials. The processes occurring at this interface are of intense interest since diffusion of cations from the glass into the crystal can displace the immobilised waste cations. Similarly, both calcium and waste cations can diffuse from the crystal host into the glass encapsulant and result in precipitated phases which might compromise the chemical durability. As part of the approach to understanding this problem, the glass forming range of the NABP:β-TCP system was studied.

The encapsulating glass used in this study was developed as a result of a series of optimisations in terms of thermal stability and melting point [1]. B_2O_3 was included in the glass to increase its thermal resilience while maintaining the inherent chemical durability of the sodium aluminophosphate (NAP) base composition, since any devitrification will threaten the structural integrity of the wasteform. Whilst there are no detailed models of the structure of NABP, the structure of NAP has been studied extensively. Brow et al. [2] investigated a range of compositions, including 40:20:40 $Na_2O:Al_2O_3:P_2O_5$, the composition most closely matched to the glass used in this study. A clear preference towards the formation of 4-coordinated aluminium $[Al(OP)_4]$, and to a lesser extent 6-

a) Pyrophosphate   b) Orthophosphate
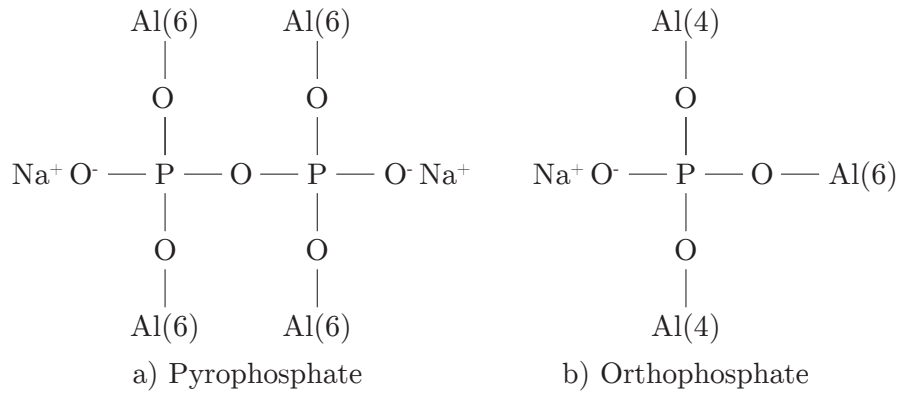
Figure 8.1 The two structural units commonly observed in sodium aluminophosphate glasses. Mixtures of the two can form stable networks ranging from $Na_2O{:}\frac{1}{3}Al_2O_3{:}P_2O_5$ to $Na_2O{:}\frac{2}{3}Al_2O_3{:}P_2O_5$.

coordinated $[Al(OP)_6]$, was observed. This was explained by the relative proportion of orthophosphate and pyrophosphate-type structures in the glass (figure 8.1). In the case of the 40:20:40 composition, this model suggests $1/3\ Q^1$ and $2/3\ Q^0$. The Q^n notation is used here, where n is the number of phosphorus nnn, or bridging oxygen bonds.

There have been studies published on the nature of borophosphate glass, by Carta et al. [3] and Raskar et al. [4] (sodium borophosphate), and Jin et al. [5] (lithium borophosphate). All three studies come to the conclusion that boron and phosphorus readily form a mixed network, strongly preferring the $P{-}O{-}B$ configuration, as opposed to $P{-}O{-}P$ or $B{-}O{-}B$. At low concentrations $([B]/([B] + [P]) > 0.3)$, boron exists exclusively in a $[BO_4]^-$ (B^4) state, with no $[BO_3]$ (B^3) observed. It is therefore clear that at the boron concentration used in this study, the boron environments would be expected to be almost exclusively 4 coordinated.

8.2 Sample preparation

NAP glass was produced by AWE initially melting a mixture of Na_2HPO_4 and $AlPO_4$ to yield a nominal composition of 40.8:19.4:39.8 $Na_2O{:}Al_2O_3{:}P_2O_5$ mol%. This was heated to 1250 °C at a rate of 250 °C h^{-1}, and quenched in deionised water. 2 mol% B_2O_3 was then added to the glass, producing a final nominal composition of 40:19:39:2 $Na_2O{:}Al_2O_3{:}P_2O_5{:}B_2O_3$ mol%. This was heated to 200 °C at 200 °C h^{-1}, held for 12 hours, before being heated to 1100 °C, again at a rate of 200 °C h^{-1}, and held for 2 hours. This was then quenched in deionised water, and ground to a particle size of

$< 45\,\mu m$. The β-TCP and $x = 0.8$ β-TCGP powders were prepared as in chapters 4 and 7.

The two components were mixed together by weight, since this method is the usual industrial practice. β-TCP:NABP ratios from 10 % β-TCP and 10 % β-TCGP (10C, 10G) to 80 % β-TCP and 80 % (80C, 80G) were prepared. The β-TCP-containing compositions are detailed in table 8.1, and the β-TCGP-containing samples were prepared to the same proportions. The compositions from 10C to 60C and 10G to 60G were heated to 1400 °C before being roller quenched [6], a method which produces cooling rates approaching $10^6\,K\,s^{-1}$, vital to maintain the vitreous state at the highest crystalline concentrations. Compositions 70C, 80C, 70G and 80G were heated to 1500 °C before roller quenching, due to the viscosity of the melt inhibiting pouring at lower temperatures. Composition 85C was successfully melted, however the sample crystallised before it could be roller quenched. Composition 85G was successfully melted and poured, however the sample devitrified significantly while pouring, making further analysis of the sample prohibitive. At high β-TCP and β-TCGP compositions, some isolated regions of devitrification were formed in even the successfully prepared samples, despite the fast cooling rate of the roller quenching method. These regions were separated from the glass flakes, and were not used in subsequent experiments.

8.3 Experimental methods

8.3.1 X-ray diffraction

XRD was initially used to examine the resultant glass flakes for any evidence of residual crystallinity. The flakes produced by the roller quencher were ground, in an agate pestle and mortar, to a powder suitable for XRD. In the case of the β-TCP glasses, a Bruker D5005 diffractometer was used, with a CuKα anode under Bragg-Brentano geometry. For the β-TCGP compositions, a Panalytical X'Pert Pro diffractometer was used, with CuKα$_1$radiation under θ-2θ geometry. Scans were taken from 20°-40° 2θ, with a step size of 0.014° and a time per step of 5 s. The technique was also used to determine the crystal phases formed by controlled devitrification of the 60C and 70G samples.

8.3.2 Energy dispersive X-ray spectroscopy

Energy dispersive X-ray analysis (EDX) was performed on the β-TCP-containing samples after carbon coating to determine their composition, since it was possible that alumina diffused into the melts from the crucible. A Zeiss Supra 55VP FEG SEM was used with an accelerating potential of 10 kV for the electron beam. EDAX Genesis software was used for analysis.

8.3.3 Differential thermal analysis

DTA was performed to determine the effects β-TCP and β-TCGP incorporation had on the thermal characteristics of the samples. A Mettler Toledo TGA/DSC 1 STARe System was used, with the temperature increased from 20 °C to 1400 °C at 10 °C min^{-1}, under nitrogen atmosphere.

8.3.4 NMR

NMR was performed on the resulting glasses to determine the structural units present as a function of β-TCP and β-TCGP incorporation. ^{31}P NMR was performed on a CMX360 spectrometer at 8.5 T (360 MHz) in the case of the boron-free NAP glass, and a Bruker Avance III spectrometer at 11.75 T (500 MHz) for all other samples. In both cases, the experiments were performed as described in section 4.3.4.

^{27}Al NMR, ^{23}Na NMR and ^{11}B NMR were performed on a Bruker Avance II+ spectrometer at 14.1 T. ^{27}Al NMR was performed using a Bruker 3.2 mm probe with an MAS spinning rate of 20 kHz. A solids 90° pulse length of 0.5 μs was used with a delay of 5 s between pulses. The spectra were referenced to the symmetric 6 co-ordinated aluminium site in yttrium aluminium garnet ($Y_3Al_5O_{12}$) at 0.7 ppm with respect to 1 mol aq. $Al(H_2O)_6$↑.

^{23}Na NMR was performed using a Bruker 4 mm probe with an MAS spinning rate of 10 kHz. A solids 90° pulse length of 4 μs was used with a delay of 5 s between pulses. The spectra were referenced to solid NaCl at 7.2 ppm with respect to the primary reference 0.1 mol aq. NaCl.

^{11}B NMR was performed using a Varian T3 4 mm probe with an MAS spinning rate of 11 kHz. A small angle pulse length of 1 μs was used with a delay of 4 s between

pulses. The spectra were referenced to BPO_4 at -3.3 ppm with respect to the primary reference 15 % $BF_3 \cdot O(Et)_2$ in $CDCl_3$.

^{71}Ga NMR was performed on a Bruker Avance III spectrometer at 11.75 T using a Bruker 4 mm probe with an MAS spinning rate of 10 kHz. A rotor synchronised 90°-180° spin echo pulse sequence was used, with a 90° pulse length of 1.5 μs, 6 rotor cycles between the 90° and 180° pulses and a 13 s delay between cycles. The spectra were referenced to the primary reference 1 mol aq. $Ga(H_2O)_6 \uparrow$.

For all nuclei, the number of pulses per spectrum was sufficient to give a S/N ratio better than 75.

8.3.5   Raman spectroscopy

Raman spectra were collected on a Renishaw inVia Reflex Raman microscope with an excitation wavelength of 442 nm from a He-Cd laser in TEM00 mode with an output of 100 mW. An N Plan EPI 50x/0.75 objective was used, producing a laser spot on the sample of ~ 1 μm. 10 accumulations of 10 s were taken at four different positions on the sample, and an average was taken after the exclusion of any anomalous spectra.

8.4   Results

8.4.1   X-ray diffraction

XRD patterns taken of the roller-quenched samples showed all samples to be amorphous, with the exception of 70C and 80C. The patterns were smoothed using the Savitzky-Golay filter with a 60 point window and a polynomial of order 1 [7]. The scans are shown in figure 8.2. These samples showed evidence of devitrification, with Bragg peaks consistent with α-TCP, illustrated by a pattern calculated from the structure determined by Mathew et al. [8]. α-TCP is thermodynamically stable at temperatures above 1400 °C [9] but is retained as a metastable phase at room temperature by the rapid quench rate used [10]. Bragg peaks were not visible in any Ga-containing samples.

(a) β-TCP-containing compositions.

(b) β-TCGP-containing compositions.
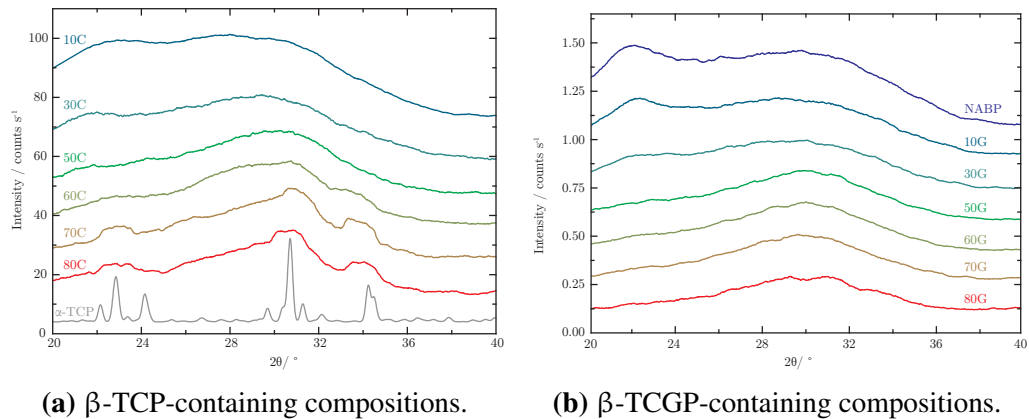
Figure 8.2 XRD patterns of the successfully prepared glass compositions. The β-TCP-containing samples are compared to a simulated α-TCP pattern based on the crystal structure published by [8]. The difference in count rate between the two sets of patterns is caused by the different diffractometer used for the two experiments.

8.4.2 Energy dispersive X-ray spectroscopy

The composition of each β-TCP sample was computed from the EDX data in at.% for Al, Na, P and Ca and the values are compared with the nominal compositions in table 8.1. O concentrations were calculated based on known cation oxidation states, and B concentrations were omitted entirely, due to the difficulty in obtaining quantitative results for these species. The Na, P and Ca results agree well with the trend predicted from the combination of the known compositions of the end members. There are significant systematic discrepancies in the Al contents however, which can be explained by a reaction of the melt with the alumina crucible. Physical evidence of this was seen in the form of an etch-line at the meniscus of the melt. Importantly, EDX gives initial direct confirmation that β-TCP has been incorporated into the amorphous phase.

8.4.3 Differential thermal analysis & recrystallisation

Heating curves are shown in figure 8.4. Both a glass transition T_g and two crystallisation events T_{x1} and T_{x2} are visible for most samples, and generally these increase in temperature with increasing β-TCP and β-TCGP concentration. The intensity of the glass transition reduces as the β-TCP and β-TCGP contents increase, which is concomitant with changes in the relative areas of the two crystallisation events; the higher temperature event increases with β-TCP and β-TCGP concentration, while the lower
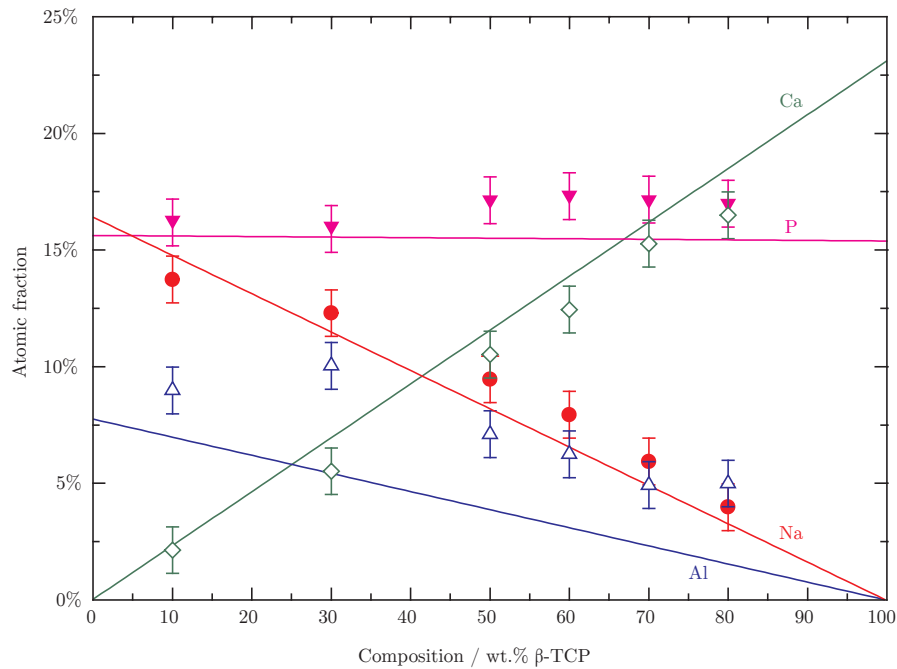
Figure 8.3 The results of the EDX analysis. All species show an agreement with the predicted compositions, except Al which was more abundant than expected. This was determined to be due to attack on the alumina crucible by the melt at the meniscus line. B and O were not detected, due to the difficulty inherent in using EDX to probe the concentration of light nuclei.

Table 8.1 Nominal and measured compositions for the samples used. Nominal compositions were renormalized by neglecting boron content. Actual compositions were determined by EDX and are shown in brackets; oxygen was calculated based on known cation:oxygen ratios. EDX measurements are ±1 %.

Sample ID		NABP	10T	30T	50T	60T	70T	80T	β-TCP
NABP (wt%)		100	90	70	50	40	30	20	0
β-TCP (wt%)		0	10	30	50	60	70	80	100
Nominal (observed) composition / at.%	Na	16	15 (14)	11 (12)	8 (9)	6 (8)	5 (6)	3 (4)	0
	Ca	0	2 (2)	7 (6)	12 (11)	14 (12)	16 (15)	18 (16)	23
	Al	8	7 (9)	5 (10)	4 (7)	3 (6)	2 (5)	2 (5)	0
	P	16	16 (16)	16 (16)	16 (17)	16 (17)	16 (17)	15 (17)	15
	O	60	60 (59)	61 (56)	61 (56)	61 (56)	61 (57)	61 (58)	62
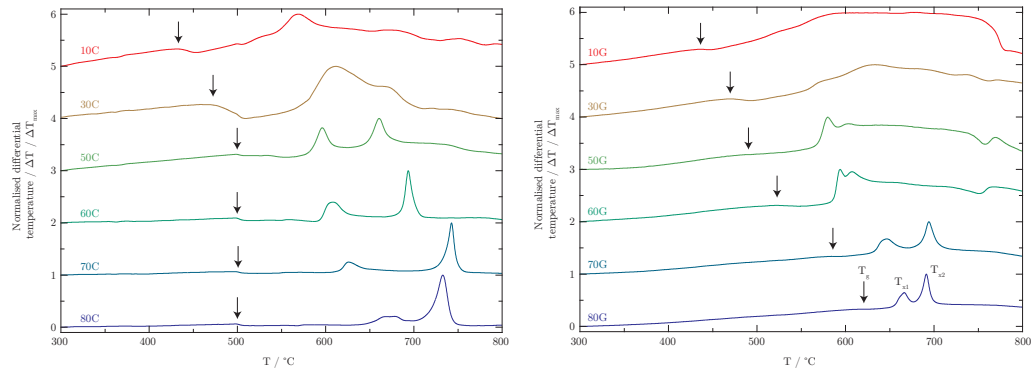
(a) DTA heating curves shown for the β-TCP-containing compositions.

(b) DTA heating curves shown for the β-TCGP-containing compositions.

Figure 8.4 For β-TCP and β-TCGP concentrations of 50 wt.% and above, two crystallisation events are clearly visible. T_g is indicated by an arrow.

Table 8.2 Glass transition and crystallisation temperatures for the compositions made in this study, as a function of β-TCP and β-TCGP concentration. Values for the NABP composition were taken from Donald et al. [1].

Sample ID	NABP	10C	30C	50C	60C	70C	80C
T_g / °C	428(1)	434(3)	472(3)	498(2)	501(2)	500(2)	501(2)
T_{x1} / °C	558(2)	569(2)	611(3)	596(2)	608(3)	626(2)	678(7)
T_{x2} / °C	663(3)	668(5)	667(3)	660(2)	693(1)	743(1)	733(2)

Sample ID		10G	30G	50G	60G	70G	80G
T_g / °C		434(3)	435(3)	489(10)	522(3)	588(10)	621(10)
T_{x1} / °C		527(10)	570(10)	580(3)	594(2)	645(5)	664(1)
T_{x2} / °C		ND	ND	603(3)	608(2)	694(1)	691(1)

temperature event decreases. Table 8.2 lists the values for the glass transition temperature, T_g, and the two crystallisation temperatures T_{x1} and T_{x2}.

Two samples each of the 60C and 70G compositions were devitrified at each of the two crystallisation temperatures observed in the DTA curve, T_{x1} = 608 °C and T_{x1} = 693 °C for the 60C sample, and T_{x1} = 645 °C and T_{x2} = 694 °C for the 70G sample. The samples were heated separately in alumina crucibles. The 60C samples were heated for two hours, with heating and cooling rates of 600 °C h^{-1}. The 70G samples were heated for four hours, with heating and cooling rates of 300 °C h^{-1}.

For the 60C samples, XRD pattern matching and ^{31}P NMR were used to identify the phases present. The XRD plots are shown in figure 8.5, and the ^{31}P NMR spectra are shown in figure 8.6. The lower temperature event T_{x1} for the 60C sample

(larger at low β-TCP concentration) was shown to be crystallisation of calcium sodium phosphate ($Ca_5Na_2(PO_4)_4$) [11] and monoclinic $AlPO_4$ [12] by XRD pattern matching. To the best of the authors' knowledge, there is no published NMR spectrum available for $Ca_5Na_2(PO_4)_4$, and so the presence of this phase cannot be verified by ^{31}P NMR. The peaks centred at ∼ 0 ppm probably arise from this phase due to the orthophosphate P environments, however there may be other contributions to the feature. The ^{31}P NMR spectrum does show a resonance at ∼ −30(1) ppm however, consistent with $[Al(OP)_4]$ [31]P environments in $AlPO_4$. This feature comprises 16 % of the ^{31}P NMR spectrum, which corresponds to 16 % of the sample if all phases are assumed to be orthophosphate-based.

The higher temperature event T_{x2} for the 60C sample (larger at high β-TCP concentration) was shown by XRD pattern matching to be due to formation of a substituted β-TCP. The composition of the phase is difficult to elucidate with XRD alone but can be compared to previous ^{31}P NMR spectra of substituted β-TCP formulations. The spectrum is very similar to that of $Ca_{2.4}Al_{0.3}Na_{0.3}(PO_4)_2$, which is consistent with the contracted unit cell observed in the XRD pattern and the cations present in the 60C glass. Again, $AlPO_4$ was visible in the ^{31}P NMR spectrum and XRD pattern. The $AlPO_4$ comprised 3 % of this spectrum, again corresponding to 3 % of the phase.

Some residual amorphous P environments were also observed for both compositions consistent with Q^2 environments; it is not possible to determine the quantity due to overlap with the crystalline orthophosphate phases discussed above and the low intensity of the resonance.

In the case of the 70G samples both T_{x1} and T_{x2} crystallisation events resulted in an identical phase composition. ^{27}Al NMR spectra are shown in figure 8.7. Aluminium is present primarily in a 4 coordinated $[Al(OP)_4]$ environment, with additional $[Al(OP)_6]$, $[Al(O)_6]$, $[Al(OP)_5]$ and $[Al(O)_4]$ phases. Again, it is not possible to give quantitative values for these phases due to the extensive overlap of amorphous and crystalline resonances. Conversely, the [71]Ga NMR spectrum shown in figure 8.8 shows Ga primarily in a 6 coordinated $[Ga(OP)_6]$ environment, with 85(5) % $[Ga(OP)_6]$ and 15(5) % $[Ga(OP)_4]$. The ^{31}P NMR spectra are similar to that of the 60C T_{x2} sample in terms of the β-TCP feature around 0 ppm, albeit with less fine structure. This is probably due to the addition of Ga introducing a greater variety of P environments in the structure.

(a) 60C T_{x1}

(b) 60C T_{x2}

(c) 70G T_{x1} and T_{x2}
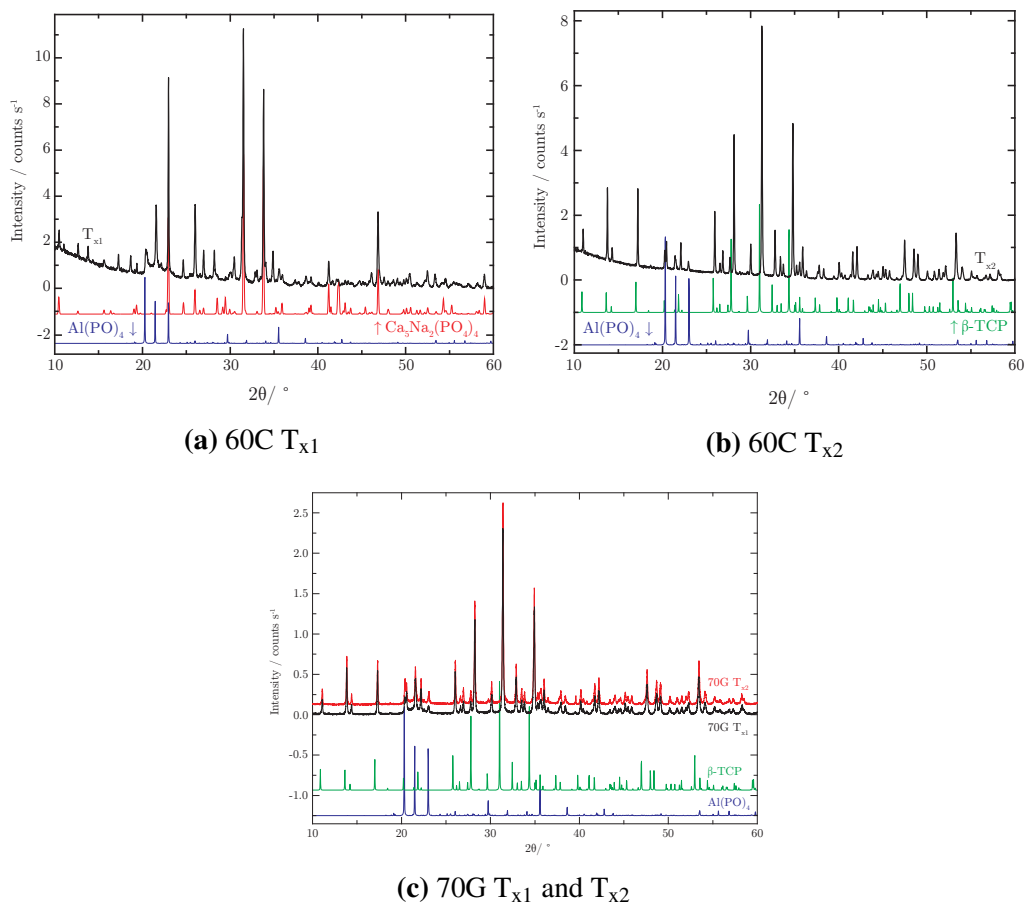
Figure 8.5 XRD patterns taken of the recrystallised samples. 60C T_{x1} and 60C T_{x2} are both compared to a simulated pattern of monoclinic $AlPO_4$ [12], and simulated patterns of $Ca_5Na_2(PO_4)_4$ [11] and β-TCP [13] respectively. 70C T_{x1} and 70C T_{x2} are both compared to monoclinic $AlPO_4$ and β-TCP. The non-linear offset in position reflects a difference in unit cell size.

The resonance previously assigned to $AlPO_4$ in the ^{31}P NMR spectra comprises 9 % of the spectrum, however the $GaPO_4$ resonance will exist in a similar chemical shift range to the $AlPO_4$ resonances. The concentration of Ga in this sample is very small (~ 1.5 at.%), and as a result the feature is primarily due to the $AlPO_4$ phase, and hence $AlPO_4$ shows a greater affinity for formation than in the 60C sample. This composition is consistent with XRD patterns of the two samples, which show reflections due to a cation-substituted β-TCP phase and monoclinic $AlPO_4$, as in the T_{x2} 60C sample discussed above.
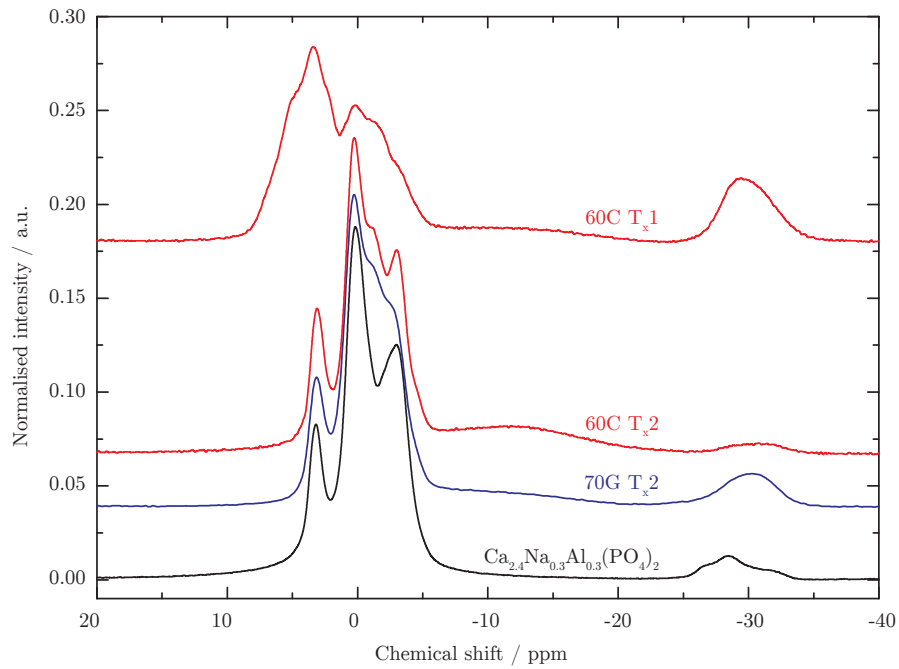
Figure 8.6 ^{31}P NMR spectra of three devitrified samples. 60C T$_{x1}$ contains mostly orthophosphate-type structures dominated by Ca$_5$Na$_2$(PO$_4$)$_4$, with AlPO$_4$ visible at −27 ppm. 70C T$_{x2}$ and 70G T$_{x2}$ are compared to experimental data of Ca$_{2.4}$Al$_{0.3}$Na$_{0.3}$(PO$_4$)$_2$.
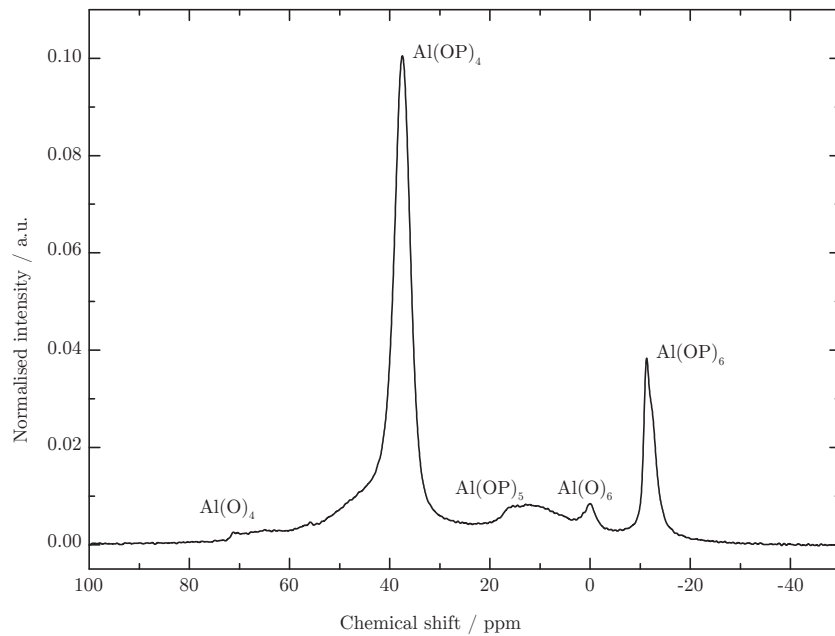
Figure 8.7 The ^{27}Al NMR spectrum of 70G T$_{x2}$. The various Al environments are labelled, where the [Al(O)$_4$] environment has a width of ∼ 20 ppm, indicative of a large C_q value and a very asymmetric site.
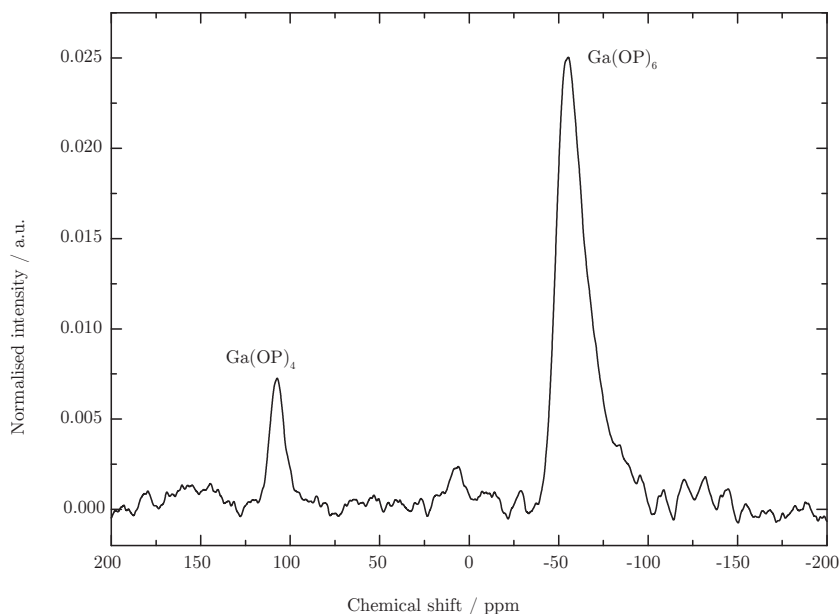
Figure 8.8   The ^{71}Ga NMR spectrum of 70G T_{x2}. Ga is primarily 6 co-ordinated in the sample, showing a tendency to exist in the β-TCP phase observed by ^{31}P NMR and XRD.

8.4.4   NMR

8.4.4.1 ^{31}P NMR

Figure 8.9 shows ^{31}P NMR data of the amorphous samples, normalised to an area of unity. For both the pure β-TCP and β-TCGP series of samples, as the calcium phosphate content increases the spectrum maxima move to lower field, consistent with depolymerisation of the network. The spectra can be deconvolved into four Gaussian lineshapes, corresponding to Q^0, Q^1, Q^2 and Q^3 species; the concentrations of each are summarised in figure 8.10 and fits are shown in figures 8.12 and 8.13 for the β-TCP and β-TCGP-based samples respectively. During the fitting procedure, the difference in peak position between compositions was constrained to be small, and the changes in area and linewidth of the peaks were constrained to be smoothly varying as a function of composition. All peaks could not be allowed to refine independently due to the overlapping nature of the spectrum. The Gaussian profile parameters are shown in table 8.3 and 8.4.

(a) β-TCP compositions

(b) β-TCGP compositions
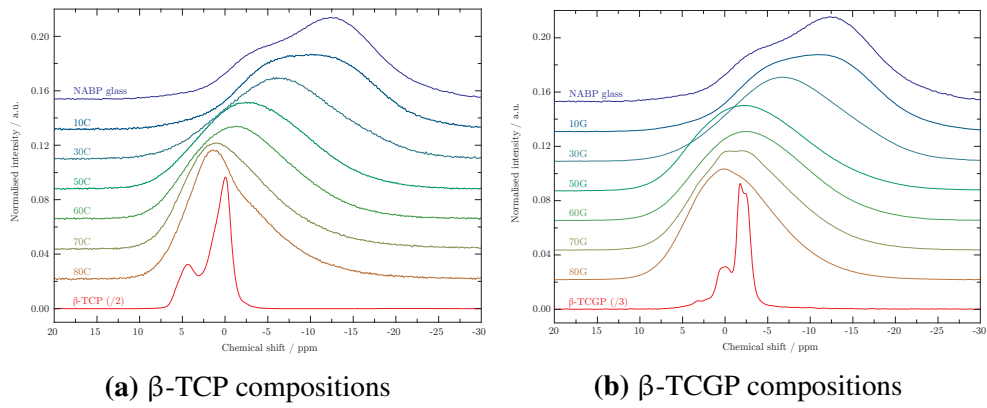
Figure 8.9 ^{31}P NMR spectra of the β-TCP and β-TCGP series of glasses. The peak maxima move to lower field as the β-TCP and β-TCGP concentrations increase. All spectra are normalised to equal area (β-TCP and β-TCGP are plotted at one half and one third intensity respectively).

(a) β-TCP compositions

(b) β-TCGP compositions
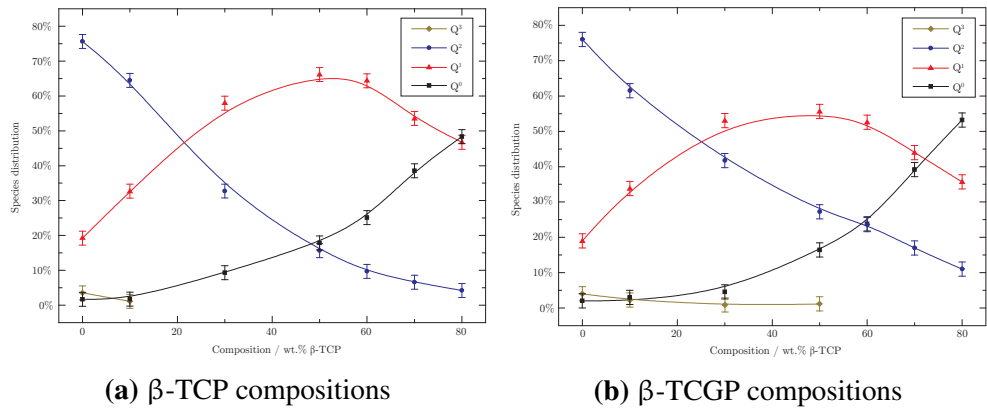
Figure 8.10 The phosphorus species distribution. A steady depolymerisation of the structure is observed.

(a) NAP

(b) NABP
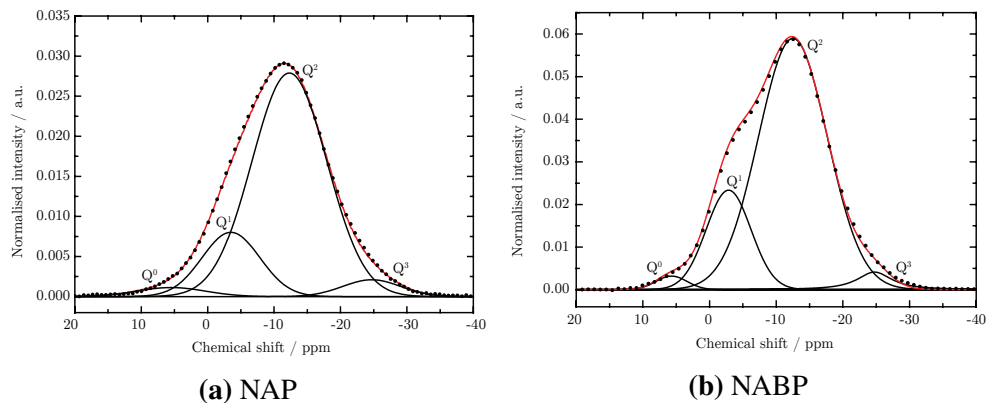
Figure 8.11 The ^{31}P NMR spectra and fits of the NAP and NABP glasses. There is no significant difference in the *proportions* of the species, however the inclusion of B into the NAP network reduces the *disorder* in the P environments.

141

Table 8.3 Parameters of the Gaussian lineshapes used in the fitting of the β-TCP-based ^{31}P NMR spectra. All areas have an absolute uncertainty of ±2%, chemical shifts and FWHMs an uncertainty of ±0.5 ppm. The ABO column shows the average number of bonding oxygens.

Sample	Q^3			Q^2			Q^1			Q^0			ABO
	Area	δ_{iso}	LW	Area	δ_{iso}	LW	Area	δ_{iso}	LW	Area	δ_{iso}	LW	
NAP	4 %	−24.7	10.3	76 %	−12.3	13.3	17 %	−3.5	10.3	3 %	5.5	12.2	1.81
NABP	4 %	−24.7	6.2	76 %	−12.5	12.2	19 %	−2.7	7.9	2 %	5.8	5.5	1.81
10C	1 %	−26.9	7.0	64 %	−12.7	13.3	33 %	−4.4	10.6	2 %	5.7	5.9	1.65
30C		ND		33 %	−12.7	14.0	58 %	−5.3	11.8	9 %	2.4	9.7	1.23
50C		ND		16 %	−11.9	13.3	66 %	−3.8	12.6	18 %	1.4	9.6	0.97
60C		ND		9 %	−12.2	12.3	64 %	−3.3	12.6	26 %	1.5	9.0	0.84
70C		ND		7 %	−14.1	9.9	54 %	−3.0	11.9	39 %	2.2	7.6	0.67
80C		ND		4 %	−13.4	7.9	45 %	−3.4	10.9	50 %	2.0	6.9	0.55

Table 8.4 Parameters of the Gaussian lineshapes used in the fitting of the β-TCGP-based ^{31}P NMR spectra. All areas have an absolute uncertainty of ±2%, chemical shifts and FWHMs an uncertainty of ±0.5 ppm. The ABO column shows the average number of bonding oxygens.

Sample	Q^3			Q^2			Q^1			Q^0			ABO
	Area	δ_{iso}	LW	Area	δ_{iso}	LW	Area	δ_{iso}	LW	Area	δ_{iso}	LW	
NAP	4 %	−24.7	10.3	76 %	−12.3	13.3	17 %	−3.5	10.3	3 %	5.5	12.2	1.81
NABP	4 %	−24.7	6.2	76 %	−12.5	12.2	19 %	−2.7	7.9	2 %	5.8	5.5	1.81
10C	2 %	−24.5	8.2	62 %	−13.0	13.3	34 %	−4.5	10.6	2 %	4.9	5.9	1.64
30C	1 %	−24.7	9.6	42 %	−12.2	14.0	53 %	−4.9	11.8	5 %	3.1	9.7	1.39
50C	1 %	−25.1	9.6	27 %	−10.2	13.3	55 %	−2.9	12.6	16 %	2.2	9.6	1.13
60C		ND		24 %	−10.5	12.3	52 %	−3.7	12.6	24 %	1.8	9.0	1.00
70C		ND		17 %	−10.4	9.9	44 %	−4.0	11.9	39 %	1.1	7.6	0.78
80C		ND		11 %	−10.0	7.9	36 %	−4.0	10.9	53 %	1.4	6.9	0.58
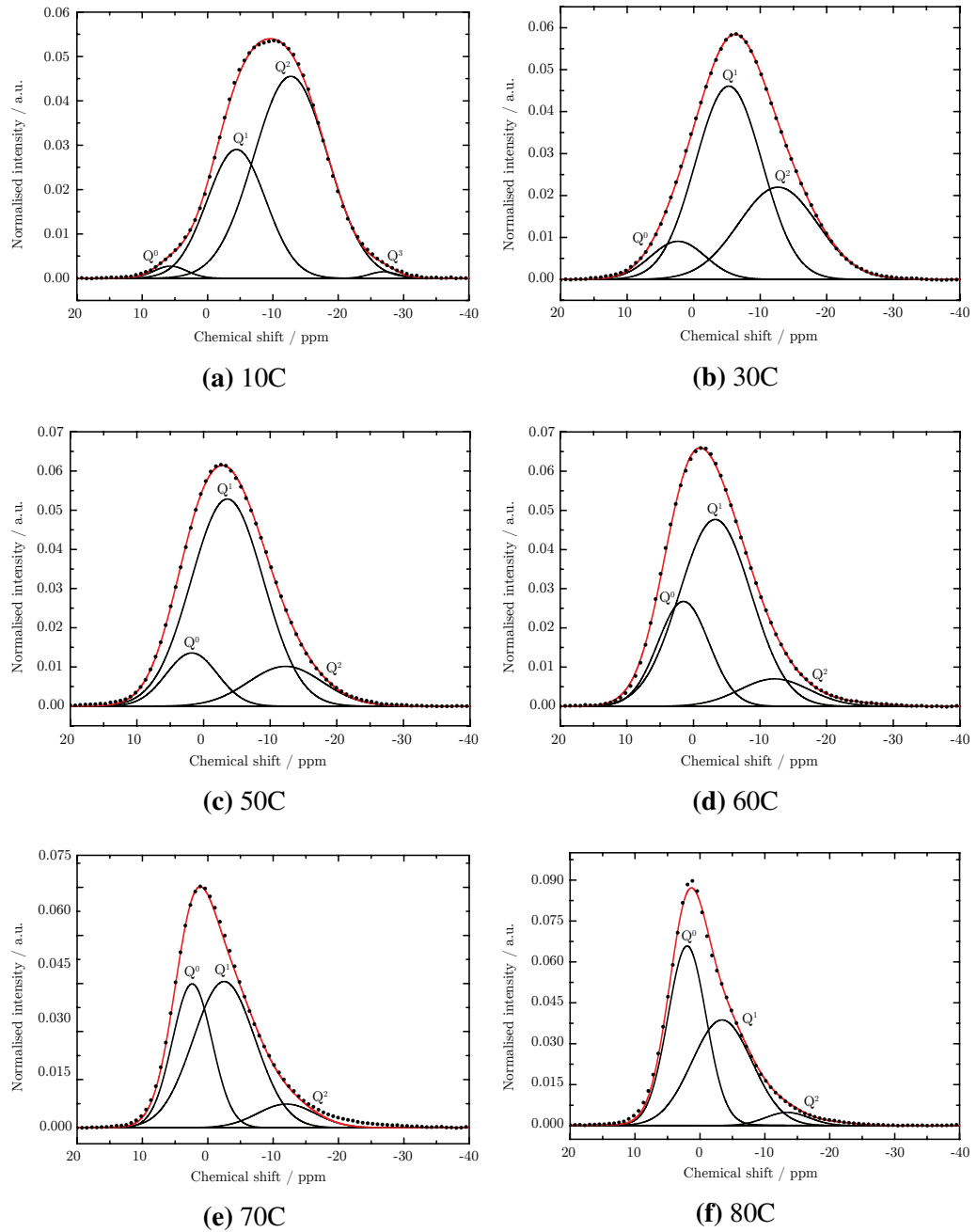
Figure 8.12 Fits to ^{31}P NMR spectra for the β-TCP series of samples. Gaussian profiles were used for all ^{31}P NMR fits since the broadening is almost entirely due to disorder, with no residual Lorentzian broadening visible.
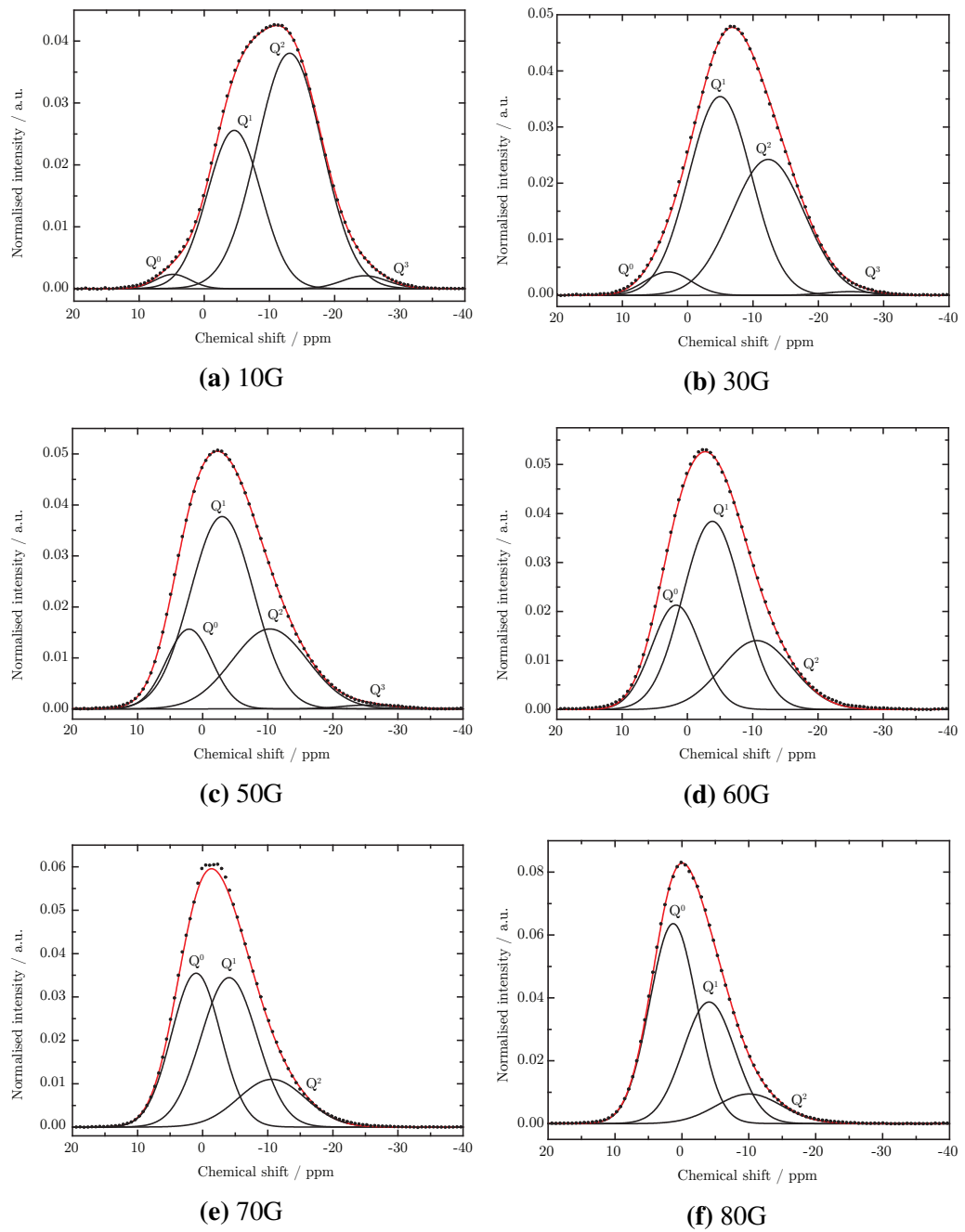
Figure 8.13 Fits to ^{31}P NMR spectra for the β-TCGP series of samples. Gaussian profiles were used for all ^{31}P NMR fits since the broadening is almost entirely due to disorder, with no residual Lorentzian broadening visible.

8.4.4.2 ^{27}Al NMR

The spectra in figure 8.15 show three distinct peaks corresponding to three aluminium phosphate environments [Al(OP)$_n$], where n is 4, 5, and 6 [14]. Due to the quadrupolar nature of the ^{27}Al nucleus and the disorder inherent in the glass, it was necessary to fit the ^{27}Al spectra using a distribution of quadrupolar C_q parameters. The QuadFit software was used, which provides such a functionality [15]. It was critical to fit spectra collected at multiple magnetic fields to ensure the resulting fit is non-ambiguous; a fit to a single spectrum with a distribution of C_q parameters can have many possible solutions. Hence, additional ^{27}Al NMR spectra were collected of the 30C and 70C samples at 20 T (850 MHz), with a spectrometer frequency of 221.55 MHz. A 0.8 μs pulse was used, resulting in a small tip angle to ensure a quantitative spectrum. The 30C and 70C fits are shown in figure 8.16, the remaining fits are shown in figure 8.17 and 8.18 for β-TCP and β-TCGP respectively.

The C_q distributions used in the spectra collected at a single field were constrained to be similar to the 30C and 70C fits, with only small changes in the distribution parameters allowed. The figure 8.19 shows the coordination concentration as a function of β-TCP and β-TCGP weight percent, with the values summarised in table 8.5 and 8.6. The peaks become significantly broader as shown by the increase in C_q, ΔC_q and the line broadening as the crystalline concentration increases, indicating a greater distribution of environments beyond a simple change in coordination. The peak maxima show a clear trend of moving to more positive shift as the β-TCP and β-TCGP concentration increases, and hence as the aluminium concentration decreases. This was also observed by Brow et al. [16] for a range of NAP compositions.

The boron-free NAP glass was also fitted and compared with the results presented by Brow et al. and the NABP fit. This illustrates the significant effect which the boron addition has in reducing the fraction of [Al(OP)$_6$] in the NABP glass. These data are shown in table 8.7. The distribution of Al coordinations presented here is in agreement with the 40:20:40 Na$_2$O:Al$_2$O$_3$:P$_2$O$_5$ composition presented by Brow et al.

(a) NAP

(b) NABP
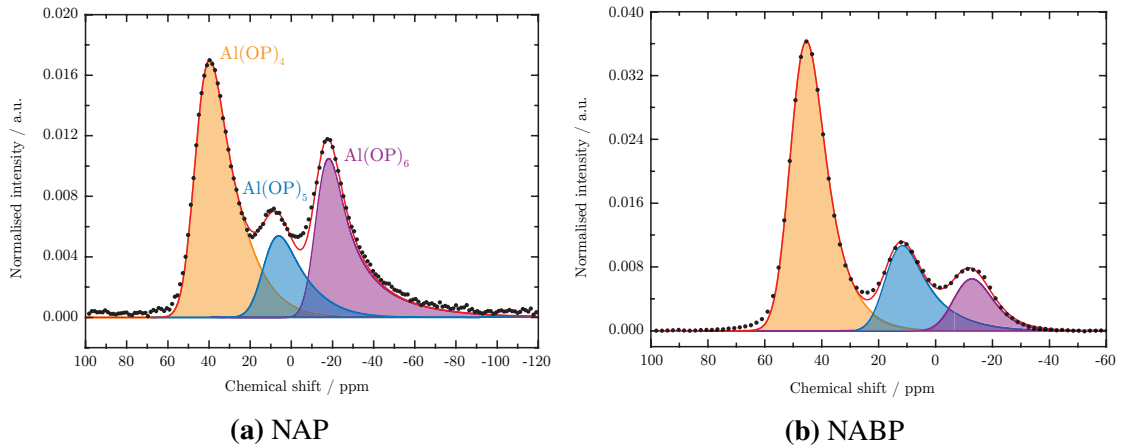
Figure 8.14 A comparison between the NAP (8.5 T) and NABP (14.1 T) ^{27}Al NMR spectra, with fits based on the results in figure 8.16.

(a) β-TCP compositions

(b) β-TCGP compositions
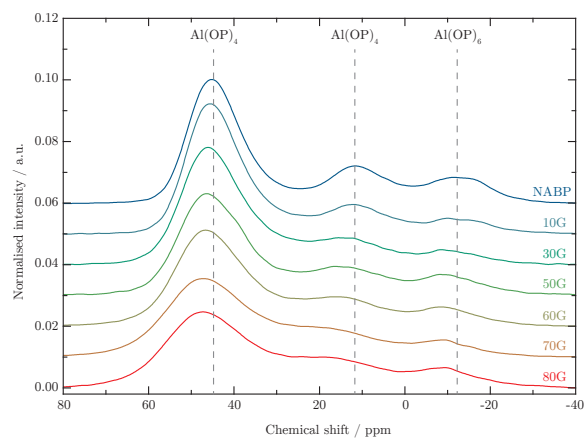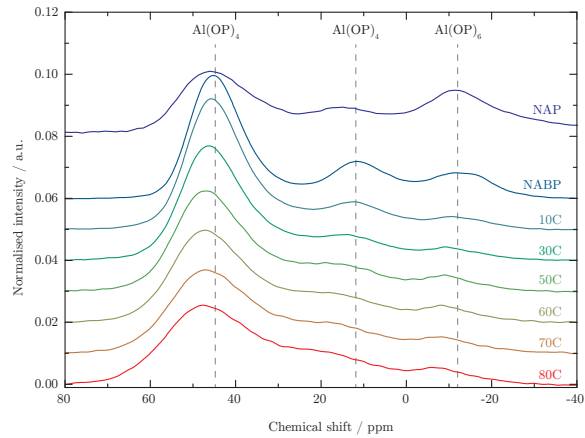
Figure 8.15 ^{27}Al NMR spectra taken at 14.1 T (the NAP spectrum was taken at 8.5 T). The positions of the Al(OP)$_4$, Al(OP)$_5$ and Al(OP)$_6$ peaks are labelled.

(a) 30C - 14.1 T

(b) 30C - 20 T

(c) 70C - 14.1 T

(d) 70C - 20 T
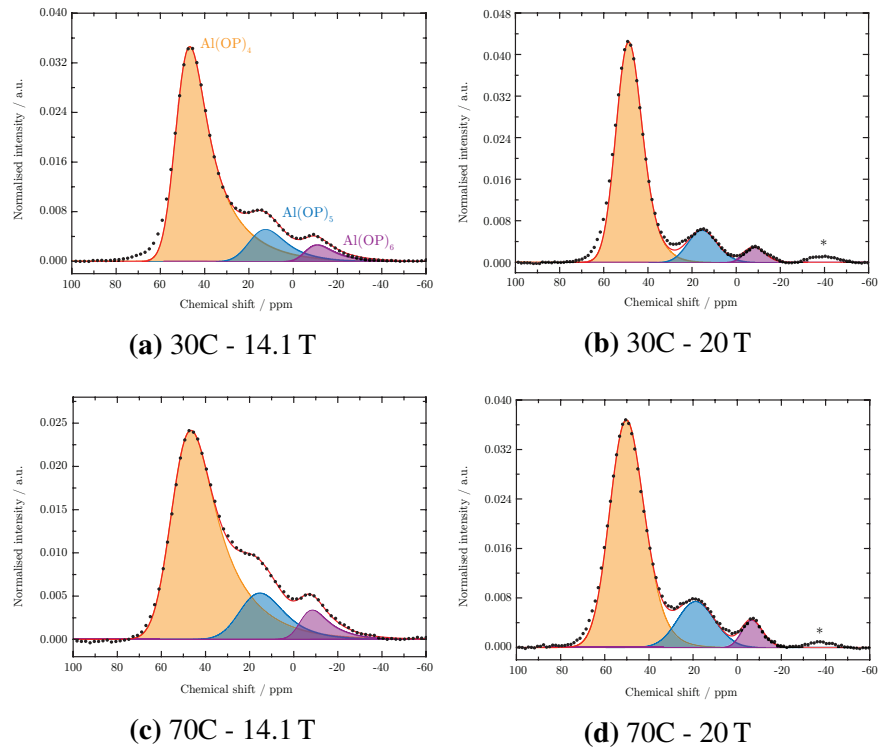
Figure 8.16 The 30C and 70C ^{27}Al NMR spectra recorded at low (14.1 T) and high (20 T) fields. ∗ denotes a spinning sideband.

(a) 10C

(b) 50C
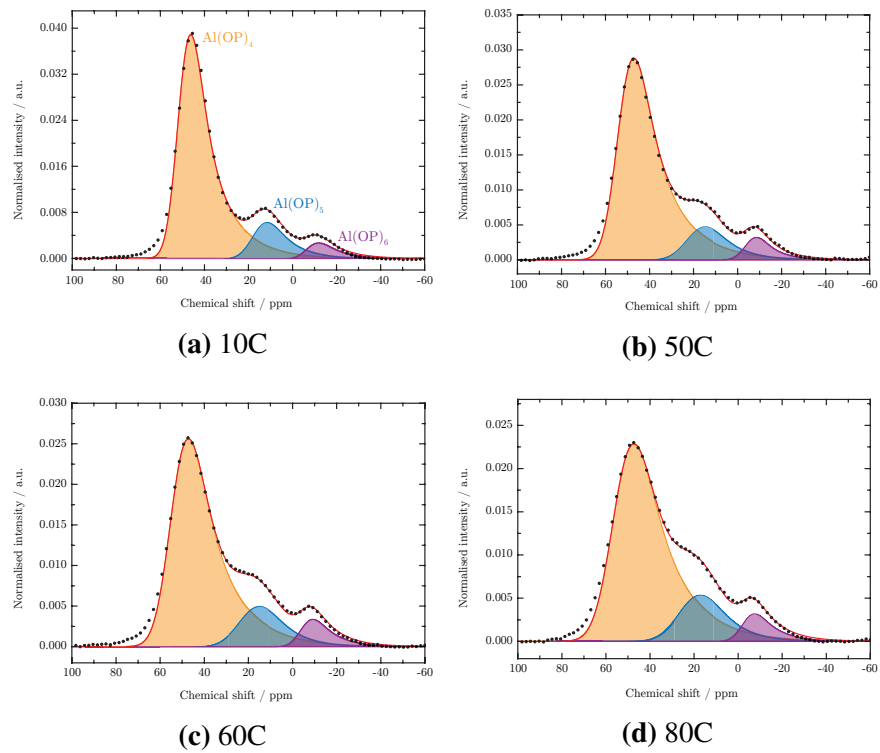
(c) 60C

(d) 80C

Figure 8.17 10C, 50C, 60C and 80C ^{27}Al NMR spectra recorded at low (14.1 T) field.

147

(a) 10G **(b)** 30G **(c)** 50G

(d) 60G **(e)** 70G **(f)** 80G
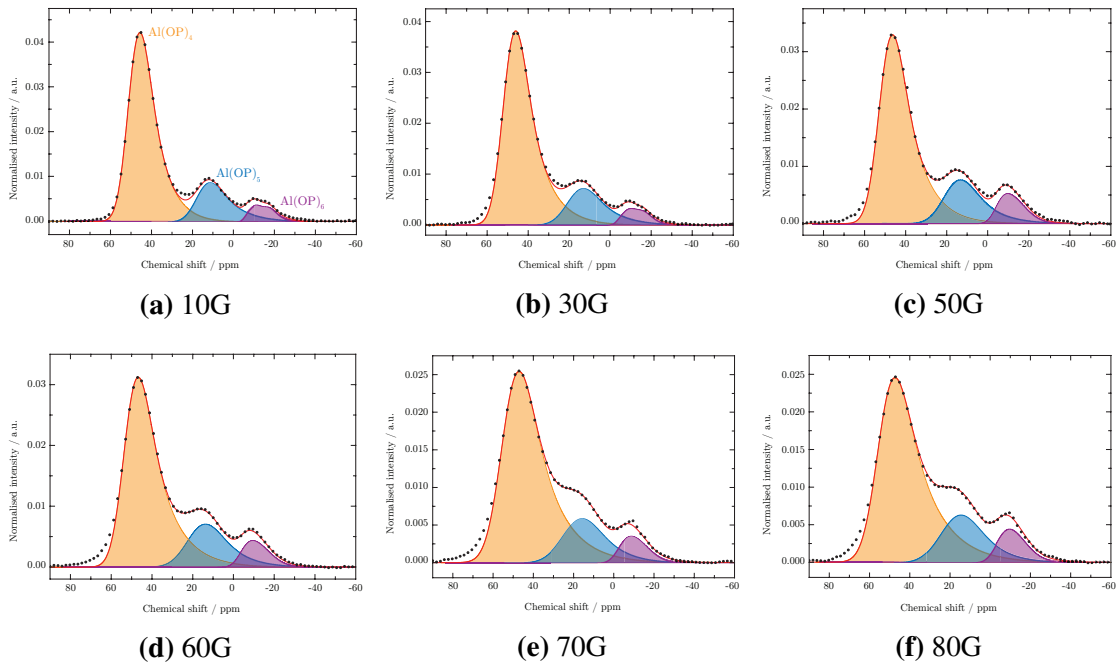
Figure 8.18 ^{27}Al NMR spectra of β-TCGP-containing NABP glasses recorded at low (14.1 T) field.
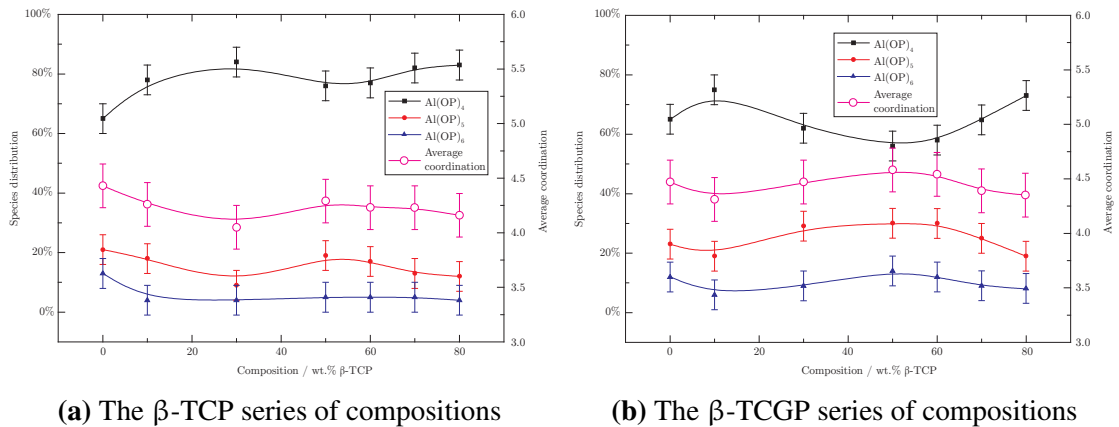
(a) The β-TCP series of compositions **(b)** The β-TCGP series of compositions

Figure 8.19   Distribution of [Al(OP)$_n$] species and average coordination numbers for β-TCP (left) and β-TCGP (right) incorporation derived from the ^{27}Al spectra in figure 8.15 fitted using a distribution of C_q parameters.

Table 8.5 Proportions of aluminium coordinations extracted from figure 8.15a for β-TCP incorporation. The areas have an absolute uncertainty of ±5%. Chemical shifts have an uncertainty of ±0.5 ppm. The shaded columns indicate a fit performed at both low and high field, and as a result the uncertainties for these fits are reduced. For all fits $\eta_q = \Delta\eta_q = 0$.

Sample	[Al(OP)$_4$]					[Al(OP)$_5$]					[Al(OP)$_6$]					AC
	Area	δ_{iso}	C_q	ΔC_q	LB	Area	δ_{iso}	C_q	ΔC_q	LB	Area	δ_{iso}	C_q	ΔC_q	LB	
NABP	65%	49.8	5.0	5.0	11	23%	17.0	6.0	6.0	11	12%	−7.8	5.0	4.0	13	4.47
10C	81%	50.3	5.3	8.1	11	14%	17.1	6.0	6.0	12	5%	−6.4	5.0	6.0	10	4.24
30C	82%	51.6	6.0	8.0	12	13%	18.5	6.0	6.0	14	5%	−5.4	5.0	6.0	10	4.23
50C	81%	53.0	6.4	7.8	13	13%	21.0	6.0	6.0	16	6%	−4.7	5.0	6.0	10	4.25
60C	78%	53.8	6.7	7.6	15	15%	21.7	6.0	6.0	18	7%	−3.7	5.0	6.0	10	4.29
70C	78%	54.2	7.1	7.5	16	16%	22.0	6.0	6.0	18	7%	−3.0	5.0	6.0	10	4.34
80C	77%	55.4	7.2	7.4	17	16%	24.0	6.0	6.0	19	7%	−2.0	5.0	6.0	10	4.30

Table 8.6 Proportions of aluminium coordinations extracted from figure 8.15b for β-TCGP incorporation. The areas have an absolute uncertainty of ±5%. Chemical shifts have an uncertainty of ±0.5 ppm. The shaded columns indicate a fit performed at both low and high field, and as a result the uncertainties for these fits are reduced. For the [Al(OP)$_6$] fits from 10G to 80G $\eta_q = 0.4$ and $\Delta\eta_q = 0.02$.

Sample	[Al(OP)$_4$]					[Al(OP)$_5$]					[Al(OP)$_6$]					AC
	Area	δ_{iso}	C_q	ΔC_q	LB	Area	δ_{iso}	C_q	ΔC_q	LB	Area	δ_{iso}	C_q	ΔC_q	LB	
NABP	65%	49.8	5.0	5.0	11	23%	17.0	6.0	6.0	11	12%	−7.8	5.0	4.0	13	4.47
10G	75%	50.3	5.2	5.0	11	19%	17.1	6.0	6.0	12	5%	−4.0	6.5	1.0	4	4.25
30G	63%	51.0	5.5	5.8	12	29%	19.2	6.0	6.0	15	9%	−2.6	6.5	1.0	5	4.51
50G	56%	51.8	5.8	5.9	12	30%	19.5	6.0	6.0	15	14%	−2.0	6.5	2.0	7	4.58
60G	58%	52.5	6.1	6.5	13	30%	20.3	6.0	6.0	17	12%	−1.5	6.5	2.0	8	4.54
70G	65%	54.0	6.6	7.0	16	25%	22.5	6.0	6.0	19	9%	−0.5	6.5	2.0	9	4.39
80G	73%	54.8	7.0	7.0	15	19%	21.5	6.0	6.0	20	8%	−1.2	6.5	2.0	10	4.35

Table 8.7 Aluminium coordinations compared with Brow et al. [16]. Shifts given for Brow data are peak maxima. Percentage area has an absolute uncertainty of ±5 % (±10 % for Brow et al.), and chemical shifts have an uncertainty of ±0.5 ppm (unknown for Brow et al.).

Sample	$[Al(OP)_4]$					$[Al(OP)_5]$					$[Al(OP)_6]$				
	Area	δ_{iso}	C_q	ΔC_q	LB	Area	δ_{iso}	C_q	ΔC_q	LB	Area	δ_{iso}	C_q	ΔC_q	LB
Brow et al.	58 %	47.2	-	-	-	16 %	13.5	-	-	-	25 %	13.4	-	-	-
NAP	51 %	48.3	4.5	3.0	12	17 %	15.0	4.5	3.0	13	32 %	−13.0	4.0	5.5	11
NABP	65 %	49.8	5.0	5.0	11	23 %	17.0	6.0	6.0	11	12 %	−7.8	5.0	4.0	13

8.4.4.3 ^{11}B NMR

Despite the small fraction of boron in the NABP glass, ^{11}B NMR spectra can be collected in a reasonably short length of time. Figure 8.20a shows the spectra collected from the NABP glass and 10C, 30C, 50C and 80C samples. The NABP glass initially favours 4-coordinated $[BO_4]^-$, with the fraction of 4-coordinated boron (N_4) equal to 0.7. The addition of 10 wt.% β-TCP shifts this to a predominantly 3-coordinated $[BO_3]$ structure, with N_4 falling to 0.2. This falls to 0.1 for the 30 wt.% β-TCP sample, and remains unchanged with further β-TCP addition. In the NABP and 10C spectra, two $[BO_4]^-$ resonances are visible, indicating ^{11}B environments with different numbers of P nnn. A similar trend is seem in the β-TCGP series of compositions shown in figure 8.20b only up to the 60G sample. The 80G sample is dominated by $[BO_4]^-$ structural units, and as a result has an N_4 value of 0.68, similar to that of NABP.

(a) β-TCP compositions

(b) β-TCGP compositions
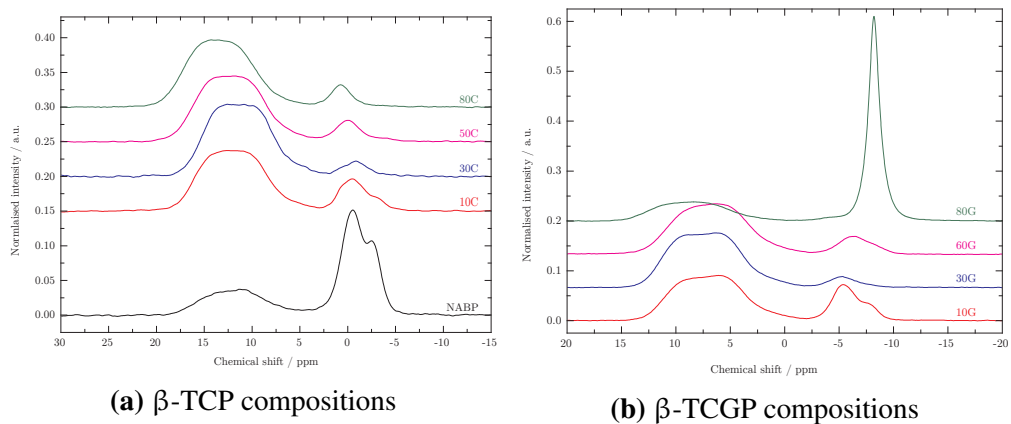
Figure 8.20 ^{11}B NMR spectra. A stark contrast is visible between the B^3 dominated Ca-containing compositions, and the B^4 dominated Ca-free base glass.

8.4.4.4 ^{23}Na NMR

^{23}Na NMR is problematic due to its very small chemical shift range. Combined with broad lines characteristic of its quadrupolar nature, extracting information from ^{23}Na spectra of glasses can be extremely challenging. The ^{23}Na NMR spectra shown in figure 8.21 show small but clear trends in both the width and position of the peak maximum as a function of β-TCP concentration. As this increases, the peak maximum moves downfield by 0.5 ppm, from -11.7 ppm in the NABP glass, to -11.2 ppm in the 80C composition and the FWHM increases, from 24.8 ppm in the NABP glass to 25.9 ppm in the 80C composition, indicating that the range of ^{23}Na environments increases slightly.
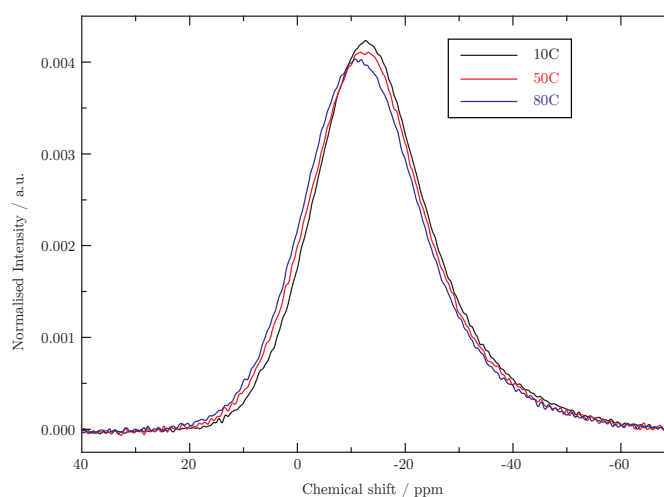
Figure 8.21 ^{23}Na NMR spectra of three compositions of the β-TCP series of glasses. The spectra are normalised to equal area, so an increase in height reflects a decrease in width.

8.4.5   Raman spectroscopy

Three characteristic vibrational frequencies of a Q^1 $(P_2O_7)^{4-}$ group in a calcium phosphate glass are shown on the lower *x* axis [17, 18] of figure 8.22, and the four main vibrational frequencies of a free Q^0 $[PO_4]^{3-}$ tetrahedron are shown on the upper *x* axis [19–21]. The NABP glass spectrum agrees well with vibrations observed in the literature for $2\,CaO{:}P_2O_5$ [17, 18], shown to be almost exclusively $[P_2O_7]^{4-}$ based, indicating the presence of similar structural units. The spectra shown in figure 8.22 are broader, probably caused by the more complex composition of the samples, resulting in a greater
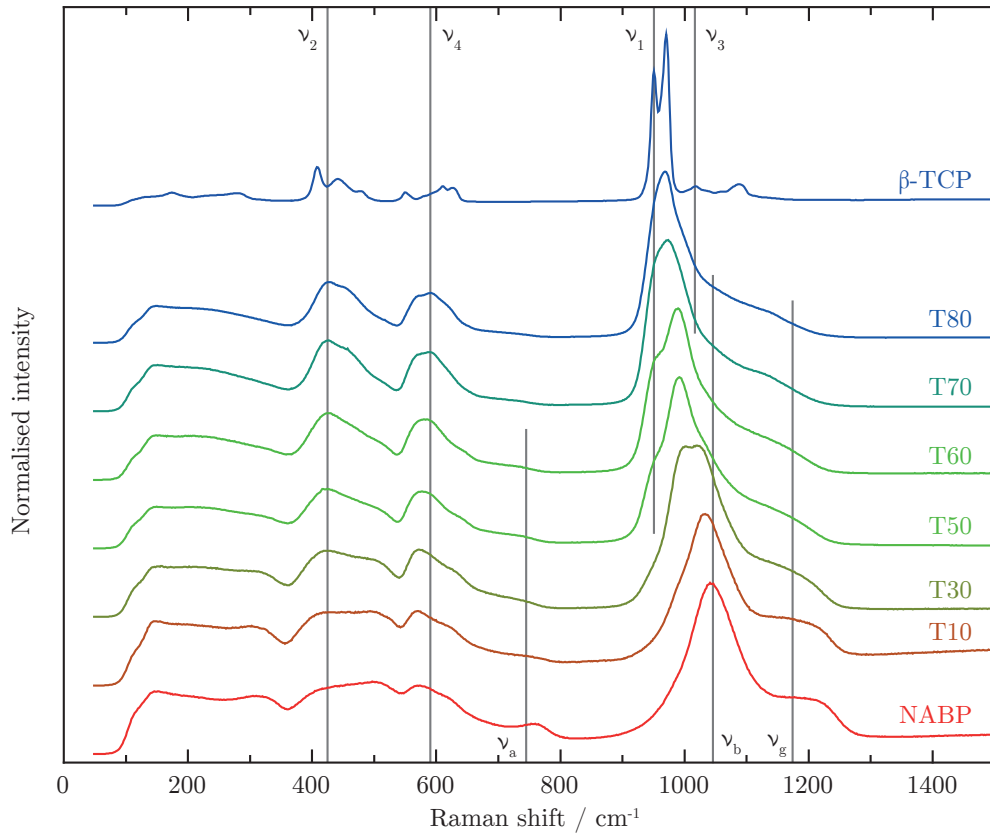
Figure 8.22   Raman spectra illustrating the progression from a Q^2 dominated glass structure, through Q^1 to a Q^0 structure. The labels ν_α, ν_β and ν_γ refer to the 3 characteristic vibrational frequencies of a Q^1 $(P_2O_7)^{4-}$ group in a calcium phosphate glass, whilst ν_1, ν_2, ν_3 and ν_4 refer to the four main vibrational frequencies of a free Q^0 $(PO_4)^{3-}$ tetrahedron.

range of vibrational modes. These $[P_2O_7]^{4-}$ modes decrease as a function of β-TCP content, in contrast to the $[PO_4]^{3-}$ modes which show a corresponding increase in intensity. This behaviour ceases at 50 wt.% β-TCP content, whereupon the $[P_2O_7]^{4-}$ modes have reduced beyond the detection limit. There is little change in the spectra over the range of 50 wt.% to 100 wt.% β-TCP content, showing an unchanged $[PO_4]^{3-}$. This is corroborated by the ^{31}P NMR data presented in section 8.4.4.1. The Q^2 phosphate units observed by ^{31}P NMR are not of a high enough concentration to be observed in the Raman spectra.

8.5 Discussion

8.5.1 Structure of sodium aluminoborophosphate glasses

There is no observable difference between the boron-free 40.8:19.4:39.8 NAP glass studied here and the 40.0:20.0:40.0 composition studied by Brow [16], in terms of the Al coordinations and P structural units.

In terms of the formation of the NABP phase, the major structural difference between the boron-free NAP composition and the 40.0:19.0:39.0:2.0 NABP composition is the relative area of the ^{27}Al peaks. The proportion of $[Al(OP)_6]$ is reduced by a significant amount, with a corresponding increase of $[Al(OP)_5]$ and $[Al(OP)_4]$. This results in a change in average Al-O coordination from 4.81 to 4.47 under the incorporation of B_2O_3 into the glass network; the addition of boron is causing aluminium to behave more as a network former than a network modifier.

The favoured boron environment is $[BO_4]^-$ on small additions of B_2O_3 to the NAP glass. This is expected, and has been seen previously in borophosphate glasses [3]. The region of the ^{11}B NMR spectrum due to $[BO_4]^-$ groups clearly shows two environments with resonances at -0.5 ppm and -2.8 ppm corresponding to B_{2P}^4 ($[BO_4]^-$ with two phosphorous nn) and B_{3P}^4 ($[BO_4]^-$ with three phosphorous nn) respectively, as described by Carta et al. [3] providing direct evidence for boron incorporation into the phosphate network. There is some $[BO_3]$ visible however, which was not observed at this boron concentration in their work.

The influence of the boron on the phosphate network is also visible in the change in T_g between the NAP and NABP glass from 405 °C to 428 °C [1] reflecting increased network cross-linking.

8.5.2 Structural effects of calcium and calcium gallium substitution on the sodium aluminoborophosphate glass network

Since the cation:phosphorus ratios are similar for the glass and β-TCP (1.51 and 1.50 respectively), one can effectively treat the concentration of phosphorus, [P], as unchanged, with a linear substitution of [Na+Al] by [Ca]. This change results in a depolymerisation of the lattice, reflected in the changes to the Raman spectra and also

the downfield shift of the ^{31}P NMR spectra as a consequence of the changes in the phosphorus Q speciation. The cation:phosphorus ratio in β-TCGP is slightly less than β-TCP due to the increase in vacancies on the Ca(4) site due to the trivalent nature of Ga. The ratio is 1.44 in comparison to the pure β-TCP of 1.5. As a result, a similar effect is observed under the addition of β-TCGP, with only small changes in the rate of depolymerisation.

The aluminium environments in the NABP glass under β-TCP incorporation are dominated by [Al(OP)$_4$] throughout the compositional range. As the Al concentration decreases, the environments become less ordered, caused by an increase in the number of possible nnn. Under the initial addition of β-TCP to the NABP structure, the relative fraction of [Al(OP)$_4$] increases from 65 % in NABP to 81 % in 10C, reducing the average coordination of Al in the structure from 4.45 to 4.25. Under further addition of β-TCP the fraction of [Al(OP)$_4$] changes very little, decreasing linearly within experimental error to 77 % at 80C, resulting in an increase of the average Al coordination from 4.25 to 4.35.

Under the addition of β-TCGP to the NABP structure a much more significant change is seen. At 10G again the [Al(OP)$_4$] fraction increases, however only to 75 %, significantly less than in the β-TCP case. This then decreases to a value of 57 % at 50G, before increasing to 72 % at 80G. As a result, the average Al coordination is significantly greater with the addition of Ga, remaining at or above 4.35 at all compositions.

The boron spectra become dominated by B^3 after only 10 % incorporation of β-TCP. Previous work has shown [BO$_3$] is only visible beyond [B]/([B] + [P]) > 0.3 [3], but this ratio in our samples is always < 0.05. The implication is that these species either associate with the [Al(OP)$_n$] species or there are boron rich regions of the structure as observed for Pyrex$^®$ [22]. This is in stark contrast to the case with no β-TCP incorporation, where the boron was shown to exist primarily in the phosphorus network. The same trend is observed for the Ga-containing glasses, however the 80G sample has a B^4 concentration similar to that of the NABP glass itself, indicating B is again forming an intrinsic part of the network. Additionally, a decrease in the chemical shift of the B^4 resonances are seen over the entire compositional range as a function of β-TCGP addition.

8.5.3 The phases present in recrystallisation

The presence of Ga produces a significant difference in terms of the recrystallization of the samples. All β-TCP compositions and all but the 10G β-TCGP compositions show two clear recrystallization events.

Two very distinct compositions are formed at the two events observed for the 60C sample. Monoclinic $AlPO_4$ was present in both recrystallized phases, indicating the stability of the $AlPO_4$ structure over a range of temperatures. At T_{x1} the sodium-rich calcium sodium phosphate $Ca_5Na_2(PO_4)_4$ phase forms. This can be identified explicitly by XRD due to its distinct structure, and shows that at the lower temperature Al is more likely to exist in a separate phase, and hence $Ca_5Na_2(PO_4)_4$ is more stable than a mixed calcium sodium aluminium phosphate. At T_{x2}, most of the Al recombines with the calcium and sodium, forming a sodium aluminium-substituted β-TCP phase, with much less residual $AlPO_4$. ^{27}Al NMR showed two resonances with small C_q values, consistent with the $[Al(OP)_4]$ and $[Al(OP)_6]$ environments in $AlPO_4$ and β-TCP respectively.

Under the substitution of Ca by Ga in the initial β-TCP structure, the resulting recrystallization behaviour is dramatically altered. The NMR spectra and XRD patterns of the T_{x1} and T_{x2} are identical excluding statistical variations. Since the temperatures T_{x1} and T_{x2} for the 70G sample are separated by 50 °C, and it expected that the furnace used for heat treatment should be able to maintain a stable temperature of ±5 °C, the distinct crystallisation events visible in the DTA spectrum must not be due to different phases crystallising as was the case for the 60C sample. In contrast to the 60C sample, the ^{27}Al NMR 70G spectra showed six resonances. The $[Al(OP)_4]$ and $[Al(OP)_6]$ resonances observed above were again present as $AlPO_4$ and β-TCP, but with an additional broad $[Al(OP)_5]$ resonance, and $[Al(O)_4]$ and $[Al(O)_6]$ resonances. In terms of the Ga environment itself, the [71]Ga NMR spectrum shows $[Ga(OP)_4]$ and $[Ga(OP)_6]$ resonances, existing in approximately the opposite ratios to the corresponding [27]Al spectrum. Gallium shows a clear preference to exist in the β-TCP structure as 6 coordinated $[Ga(OP)_6]$ as opposed to 4 coordinated $[Ga(OP)_4]$ in $GaPO_4$, thus displacing the Al from the 6 coordinated β-TCP environment to the 4 coordinated $AlPO_4$ environment. $GaPO_4$ reflections were not observed in XRD, consistent with a low concentration of $GaPO_4$ in the recrystallized 70G sample.

8.6 Summary

This work was performed to identify the structural changes that could occur as a result of compositional changes at the interface of a crystalline β-TCP region during encapsulation in a matrix of NABP glass. The situation was simplified by fully dissolving the β-TCP in the NABP glass, as opposed to the calcination and encapsulation process used in industrial-scale processes.

Initially the NABP glass was studied, produced by addition of B_2O_3 to NAP glass. The boron is present primarily in a $[BO_4]^-$ environment and forms an intrinsic part of the phosphate network, which explains the increase in physical stability of the glass under heating.

Vitreous calcium sodium aluminoborophosphate and calcium sodium aluminoborogallophosphate glasses were successfully prepared using the roller quenching technique, with incorporation up to 80 wt.% β-TCP and β-TCGP. Despite the successful quenching, some devitrification was observed in the XRD patterns of the 70 wt.% and 80 wt.% β-TCP-containing samples. Both ^{31}P NMR and, in the case of the β-TCP-based samples Raman spectroscopy, show a clear trend from a mixture of Q^2 and Q^1 phosphate units to a Q^0 dominated structure as the β-TCP concentration increases, caused by the increase in modifier concentration and reduction in the Al_2O_3 network former. Aluminium itself has been shown to exist in three different coordinations; $Al(OP)_4$, $Al(OP)_5$, and $Al(OP)_6$. In terms of the overall structure of the glass, no evidence of macroscopic phase separation is observed but clustering of $[BO_4]^-$ units may occur.

Devitrification of the 60C sample showed the crystallisation of $Ca_5Na_2(PO_4)_4$ and substituted β-TCP with the approximate formula $Ca_{2.4}Al_{0.3}Na_{0.3}(PO_4)_2$, depending on the heating temperature, indicating a tendency for the cations in the glass to enter the crystalline phases. Importantly, under the addition of Ga to the system, the Ga was shown to displace the Al in the recrystallised β-TCP phase, resulting in $AlPO_4$ formation. Since Ga is present in the waste stream, this provides an excellent demonstration of the suitability of NABP and β-TCP as a wasteform.

References

[1] I. W. Donald, B. L. Metcalfe, S. K. Fong and L. A. Gerrard, *Journal of Non-Crystalline Solids* **352** (28-29), (2006), 2993–3001.

[2] R. K. Brow, R. J. Kirkpatrick and G. L. Turner, *Journal of the American Ceramic Society* **76** (4), (1993), 919–928.

[3] D. Carta, D. Qiu, P. Guerry, I. Ahmed, E. A. Abou Neel, J. C. Knowles, M. E. Smith and R. J. Newport, *Journal of Non-Crystalline Solids* **354** (31), (2008), 3671–3677.

[4] D. B. Raskar, M. T. Rinke and H. Eckert, *Journal of Physical Chemistry C* **112** (32), (2008), 12530–12539.

[5] J. Yifen, C. Xiangsheng and H. Xihuai, *Journal of Non-Crystalline Solids* **112**, (1989), 147–150.

[6] A. J. Havel, S. A. Feller, M. Affatigato and M. Karns, *Glass Technology-European Journal of Glass Science and Technology Part A* **50**, (2009), 227–229.

[7] A. Savitzky and M. J. E. Golay, *Analytical Chemistry* **36** (8), (1964), 1627–1639.

[8] M. Mathew, L. W. Schroeder, B. Dickens and W. E. Brown, *Acta Crystallographica Section B Structural Crystallography and Crystal Chemistry* **33** (5), (1977), 1325–1333.

[9] J. Ando, *Bulletin of the Chemical Society of Japan* **31**, (1958), 201–205.

[10] R. G. Carrodeguas and S. de Aza, *Acta biomaterialia* **7** (10), (2011), 3536–46.

[11] G. Celotti and E. Landi, *Journal of the European Ceramic Society* **23**, (2003), 851–858.

[12] H. Graetsch, *Acta crystallographica. Section C, Crystal structure communications* **56** (4), (2000), 401–3.

[13] M. Yashima, A. Sakai, T. Kamiyama and A. Hoshikawa, *Journal of Solid State Chemistry* **175** (2), (2003), 272–277.

[14] S. H. Risbud, R. J. Kirkpatrick, A. P. Taglialavore and B. Montez, *Journal of the American Ceramic Society* **70** (1), (1987), C10–C12.

[15] T. F. Kemp and M. E. Smith, *Solid State Nuclear Magnetic Resonance* **35** (4), (2009), 243–52.

[16] R. K. Brow, *Journal of the American Ceramic Society* **76** (4), (1993), 913–918.

[17] A. Saranti, I. Koutselas and M. Karakassides, *Journal of Non-Crystalline Solids* **352** (5), (2006), 390–398.

[18] N. Vedeanu, O. Cozar, I. Ardelean, B. Lendl and D. Magdas, *Vibrational Spectroscopy* **48** (2), (2008), 259–262.

[19] P. N. de Aza, C. Santos, A. Pazo, S. de Aza, R. Cuscó and L. Artus, *Chemistry of Materials* **4756** (10), (1997), 912–915.

[20] K. Nakamoto, *Infrared and Raman Spectra of Inorganic and Coordination Compounds* (John Wiley & Sons, New Jersey, 2009), 6th ed.

[21] D. M. Adams and I. R. Gardner, *Journal of the Chemical Society, Dalton Transactions* **14**, (1974), 1505.

[22] A. P. Howes, N. M. Vedishcheva, A. Samoson, J. V. Hanna, M. E. Smith, D. Holland and R. Dupree, *Physical chemistry chemical physics : PCCP* **13** (25), (2011), 11919–28.

CHAPTER 9

CONCLUSIONS & FURTHER WORK

9.1 Substitution of cations into β-tricalcium phosphate

Chapters 4 to 7 have dealt with the structure of β-TCP itself, and the effect that substitution of cations has on the structure. All samples used in these chapters were prepared for this study with commercial reagent-grade materials. Solid state sintering of calcium hydrogen phosphate and calcium carbonate in an alumina crucible was used as a preparation route for the pure β-TCP sample, with the addition of cation-containing compounds in the case of substituted samples. In all cases a β-TCP-like phase was formed as a primary phase, however small quantities of second phase were observed in some samples.

9.1.1 Zinc and magnesium substituted β-tricalcium phosphate

The β-TCMP samples formed a tricalcium trimagnesium phosphate (TCTMP) phase at compositions in excess of $Ca_{2.8}Mg_{0.2}(PO_4)_2$. The presence of TCTMP was previously described by Enderlea et al. [1], confirming that a lower energy is required to form this phase than to create more highly-substituted β-TCMP.

Significantly, no second phase was observed in the β-TCZP series of compositions, even at high Zn composition. All samples up to $Ca_{2.6}Zn_{0.4}(PO_4)_2$ showed a single β-TCP-like phase with no trace of the $CaZn_2(PO_4)_2$ previously shown to exist [2, 3]. This shows that the previous studies into the β-TCZP system probably did not use a sufficiently high sintering temperature; Kreidler & Hummel [2] used 900 °C and Jakeman et al. [3] used 800 °C cf. 1050 °C and 1150 °C used for the samples in this study. This difference in the second phase is likely related to the relative ionic radii of the Zn^{2+}

158

(0.74 Å) and Mg^{2+} (0.65 Å) cations compared to Ca^{2+} (1.00 Å). Since the difference between Zn^{2+} and Ca^{2+} is less than that between Mg^{2+} and Ca^{2+}, one would expect the substitution of Zn to be more energetically favourable, and hence possible up to a higher concentration. In both cases, substitution was observed initially on the Ca(5) site, followed by substitution on the Ca(4) site.

In both cases, the previously observed contraction of the lattice parameters was observed in the samples prepared in this study. The β-TCZP system was analysed with a smaller step size in sample composition than previous studies however, and has shown in more detail the increasing c lattice parameter under substitution on the Ca(4) site beyond $x = 0.3$. This anomalous behaviour was also observed in the case of the β-TCMP samples, albeit masked by the presence of the TCTMP second phase causing a reduction in the Mg concentration in the β-TCMP primary phase. A combined XRD and ND Rietveld refinement was carried out on β-TCZP to probe the short-range structure as a function of composition, with a view to understanding the mechanism driving the increase in c under Ca(4) substitution. The O(9)-P(1)-Ca(4)-O(9) torsion angle was examined as a function of Zn concentration, and some evidence of a change was observed for the highest Zn concentration sample. Detailed examination of the O-O distances in the structure however, cast significant doubt on this observation.

Total scattering neutron diffraction experiments were also performed on the β-TCZP and β-TCMP samples, with a view to examining the short-range structure directly. Fits were attempted of the total scattering plots to determine correlation lengths and coordination numbers, however the overlapping nature of the correlations prohibited stable solutions. A fit of the P-O correlation was successfully performed for the β-TCP sample, however any additional peaks modelling the Ca-O or O-O correlations resulted in instabilities. It was also not possible to fit the Zn-O and Mg-O correlations in even the highest Zn and Mg concentrations, due to the low intensity of the peaks in the total scattering plots. In order to make further progress, additional information is required, such as high energy X-ray diffraction data with high Q_{max} and good resolution. However, it was possible to compare the structure resulting from Rietveld refinement of the β-TCZP structures to the total scattering plot in real space; a good agreement was observed in all but the highest Zn concentrations, indicating an error in the assumptions of long-range order used for Rietveld refinement at these compositions. The error was

observed primarily in the O-O positions, and was assigned to the large difference between the Zn and Ca correlation lengths, most likely resulting in a movement of the Zn atom from the nominal position of the Ca site, an effect Rietveld refinement cannot account for.

^{31}P NMR experiments were performed on both β-TCZP and β-TCMP samples; the β-TCZP experiments were again the most successful due to the purity of the samples. A model was constructed based on the probable substitution sites and the known Ca nnn of the P environments, and this was used to determine the number of ^{31}P resonances and their respective intensities as a function of substitution. An excellent agreement was observed between the predicted and observed intensities of the resonances.

9.1.2 Aluminium and gallium substituted β-tricalcium phosphate

The β-TCAP and β-TCGP samples also showed evidence of second phase formation at high substitution levels, which was shown to be due to $AlPO_4$ and $GaPO_4$ respectively. $AlPO_4$ formed at a lower substitution level than $GaPO_4$, indicating a lesser tendency for Al^{3+} to substitute into the β-TCP lattice than Ga^{3+}. In both cases, there is an equilibrium of the form

$$Ca_9M_x(PO_4)_{6+x} \rightleftharpoons xMPO_4 + 3\,Ca_3(PO_4)_2. \tag{9.1}$$

The effects of Al and Ga substitution on the long-range order of the β-TCP lattice have previously been examined by Mee [4], a former member of the research group, and as a result were not re-examined in this work. The main crux of chapter 7 was to re-evaluate the ^{31}P NMR spectra of the samples, and to use the R^3-HMQC NMR experiment to aid the identification of the individual resonances in the ^{31}P NMR spectrum.

Since the individual resonances in the β-TCP spectrum were unambiguously identified in chapter 5, this β-TCP ^{31}P spectrum was used as a starting condition for the β-TCAP and β-TCGP fits as a function of Al and Ga substitution. These fits were successfully applied to the ^{31}P NMR spectra over the range of single-phase samples; the ^{31}P NMR spectra of the β-TCAP samples which showed $AlPO_4$ second phase could not be successfully fitted. Since each resonance had a unique dependence on the substitution level, it was possible to identify the resonances in terms of their respective P environment. These series of fits showed evidence of Al^{3+} and Ga^{3+} substitution on the Ca(5) site, with vacancy generation on the Ca(4) site.

The R^3-HMQC experiment was successfully performed. This experiment had the effect of only showing ^{31}P intensity from a P environment if it is coupled to the cation site, in this case by the dipolar interaction. By this method it was shown unequivocally that the results inferred by the 1D ^{31}P NMR experiments were indeed correct; the Al^{3+} and Ga^{3+} cations are substituting for Ca^{2+} cations on the Ca(5) site. This experiment was performed on a β-TCGP sample at about the same time by Mellier et al. [5]. The ^{27}Al-$\{^{31}P\}$ R^3-HMQC spectrum of β-TCAP is however entirely novel, and provides the first direct evidence of Al^{3+} substitution on the Ca(5) environment. Additionally, the R^3-HMQC experiment was performed on Na-substituted β-TCP (but not reported in detail here). Due to the monovalent nature of Na^+, substitution results in an *increase* of the Ca(4) Ca occupancy. This was observed with ^{31}P, and the Ca(5) site was again positively identified as the substitutional site *via* ^{23}Na-$\{^{31}P\}$ R^3-HMQC.

9.2 Encapsulation of β-tricalcium phosphate in NABP glass

An entirely novel study was carried out into the effects of dissolving β-TCP and β-TCGP in a sodium aluminoborophosphate (NABP) melt, and investigating the structure of the resulting glass. However, initial work was performed into determining the structure of the NABP glass itself.

^{11}B NMR showed 4-coordinated $[BO_4]^-$, indicating that the boron is present primarily in B-O-P environments, and hence forms an intrinsic part of the phosphate network. This addition of cross-linking caused by the boron addition is probably the cause of the increase in the glass transition temperature T_g from 409(1) °C to 428(1) °C [6]. The two crystallisation events T_{x1} and T_{x2} were also observed to increase in temperature from 502(1) °C and 612(2) °C to 558(2) °C and 668(3) °C respectively.

Vitreous samples were successfully prepared up to 80 wt.% β-TCP and β-TCGP, confirmed by XRD. ^{31}P NMR and Raman spectroscopy showed that under the addition of β-TCP and β-TCGP the phosphorus network was depolymerised, with the average number of bonding oxygens per phosphorus site decreasing linearly as a function of β-TCAP and β-TCGP addition. Fits of the ^{27}Al NMR spectra were determined unambiguously by performing the experiment at two fields, and showed the Al environments

were mostly 4 coordinated [Al(OP)$_4$] sites, indicating the tendency for Al to exist in the phosphate network.

^{11}B NMR experiments showed B to exist as a predominantly 3 coordinated [BO$_3$] environment, in contrast to the pure NABP composition. Since it is very difficult to accommodate [BO$_3$] environments in a phosphate network, the implication is that B exists in a micro-phase separated environment. However, under 80 wt.% β-TCGP incorporation, the glass once again becomes dominated by 4 coordinated [BO$_4$]$^-$. At this limit of composition, there is the indication that the B is once again forming part of the phosphate network. Alternatively, this could be crystalline BPO$_4$; the concentration of this phase would be too small to detect by XRD, however the width of the [11]B resonance would be expected to be < 1 ppm.

9.2.1 Recrystallisation

Differential thermal analysis (DTA) was performed on all samples, and a trend of increasing T$_g$ and crystallisation temperatures T$_{x1}$ and T$_{x2}$ was observed. To determine the crystalline phases formed at these temperatures, the 60 wt.% β-TCP and 70 wt.% β-TCGP samples were sintered at the T$_{x1}$ and T$_{x2}$ temperatures observed in the DTA spectra.

In the case of the β-TCP-based sample, two distinct phases were observed at T$_{x1}$ and T$_{x2}$. The phase present at T$_{x1}$ was composed mainly of a calcium sodium phosphate phase with composition Ca$_5$Na$_2$(PO$_4$)$_4$, with monoclinic AlPO$_4$ second phase. At T$_{x2}$, the Ca$_5$Na$_2$(PO$_4$)$_4$ phase was replaced by a Na Al co-substituted β-TCP phase, and the proportion of monoclinic AlPO$_4$ was shown to reduce.

Contrastingly, the β-TCGP-based sample showed a single phase at both T$_{x1}$ and T$_{x2}$. Both samples showed a Na Ga Al co-substituted β-TCP phase, albeit with a much lower Al concentration than the β-TCP case. This was shown by [71]Ga NMR, which indicated the existence of Ga in a predominantly 6 coordinated [Ga(OP)$_6$] environment, consistent with the β-TCP phase observed by ^{31}P NMR and XRD. ^{27}Al NMR showed Al to exist in mainly a 4 coordinated [Al(OP)$_4$] environment, again consistent with monoclinic AlPO$_4$ observed by XRD.

9.3 Applications to nuclear waste encapsulation

The main application of this work is to develop a viable waste form for halogenated nuclear waste. Critically, this work has shown that Zn, Mg, and Ga can be substituted into β-TCP, with maximum limits of substitution determined such that the substituent cation remains in the β-TCP phase. These values are shown in table 9.1 both in terms of cation fractions and metal oxide contents.

Table 9.1 Substitution limits determined in this thesis, given in terms of cation proportion and metal oxide content. * denotes that a limit was not reached.

Waste component	Max. cation sub. / at.%	Max. metal oxide content / wt.%
ZnO	13.3*	1.7
MgO	6.7	0.4
Ga_2O_3	8.9	2.7
Al_2O_3	6.7	1.1

The formation of a predominantly vitreous phase has been shown under substantial loading of β-TCP and β-TCGP. In industrial-scale processes the wasteform will naturally not be roller quenched, however similar phases are expected to form at the interface between the NABP and β-TCP phases. It is unsurprising however that a decrease in the temperature difference between T_{x1} and T_g is observed under β-TCP and β-TCGP loading, indicating a decrease in the thermal stability of the glass. Additionally, under devitrification of the β-TCGP-based glass samples, the Ga waste was shown to recrystallise in the β-TCP phase, as opposed to a separate $GaPO_4$ phase.

It must be stated however that only the Ca(4) and Ca(5) sites feature in these studies, and since these sites together comprise one sixth of the total calcium content of β-TCP, hence a relatively low limit is imposed on the substitution. The other calcium sites *are* involved in the substitution of the heavier environments in the waste streams, but since the elements studied here comprise more than one sixth the content of waste streams II and IV (table 2.2), they will still become the limiting factor on the maximum substitution in β-TCP.

9.4 Future work

9.4.1 The short-range structure of β-tricalcium phosphate

The effect of cation substitution on the long-range structure of β-TCP is well under-
stood. This can be determined by Rietveld refinement of XRD and ND data, and nu-
merous studies have been published of lattice parameters as a function of various cation
substitutions. The key area which is still relatively unknown however, is that of the the
structure. Specifically, the nature of vacancy ordering in the pure β-TCP, and how this
changes under substitution.

A key sample for consideration is that of the 'novel' phase of β-TCP prepared by a
previous student of the research group. This was discussed briefly in chapter 4, however
it was not possible to examine the sample in detail due to the time constraints of the
Ph.D. This sample is of particular interest because of the similarity of the XRD patterns
(figure 9.1a), contrasted with the obvious disparity of the ^{31}P NMR spectra (figure 9.1b).
This is a clear example of the potential variety in the short-range structure of β-TCP,
whilst maintaining an established and conventional long-range structure.

This sample has previously been prepared by one other research group [7], however
the majority of published β-TCP ^{31}P NMR spectra are that of the conventional β-TCP
structure. An essential avenue of research is to determine how this novel phase forms,
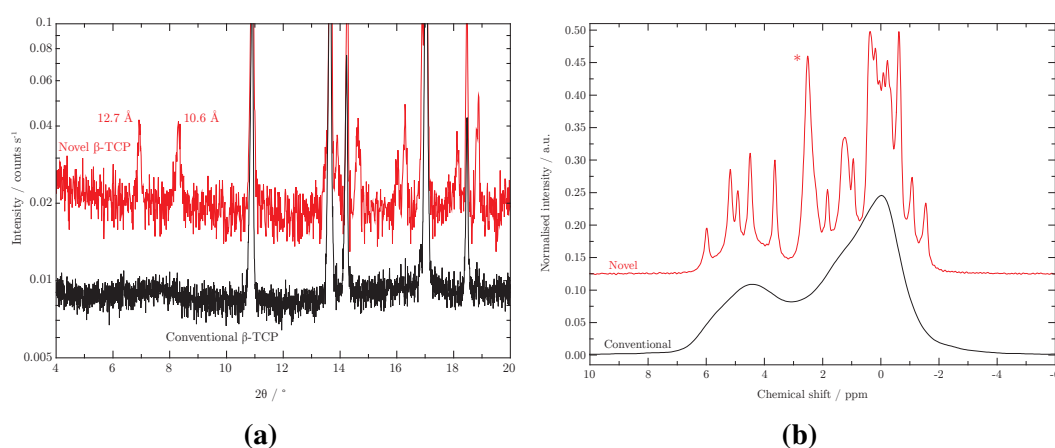
Figure 9.1   XRD patterns (left) and ^{31}P NMR spectra (right) of the con-
ventional and novel β-TCP phases. The extra reflections in the novel XRD
pattern above 10° and the peak in the ^{31}P NMR spectrum marked with ∗ are
due to HAp second phase.

and whether its formation can be controlled. Secondly, total scattering ND experiments should be performed, to observe if there is any difference in the real-space total scattering plot when compared to that of conventional β-TCP. Any significant difference could be explored by a Reverse Monte Carlo (RMC) real-space structural refinement of the total scattering plot. This would enable the structure to relax beyond its long-range ordered symmetry, which is highly likely to be an approximation of the real structure of β-TCP.

Additionally, RMC could be used to probe the short-range structure in substituted β-TCP samples. Rietveld refinement makes the implicit assumption that the long-range order of the sample is unchanged under mixed occupancy of a site, however this is shown to be manifestly untrue in the case of Zn and Mg substitution; the Zn-O and Mg-O correlations are at a different position to that of Ca-O. A solution to this problem is to allow a supercell of substituted β-TCP to refine in real space, which could result in a more accurate representation of the structure.

9.4.2   Co-substitution of β-tricalcium phosphate

Only a small subset of the elements present in the predicted waste streams have been examined in this thesis, and only in terms of individual substitution. A study into co-substitution of β-TCP has previously been performed by Mee [4], however compositions were chosen where a single-phase sample was guaranteed. A potentially insightful study would be in the regime of 'competitive' co-substitution, where the total cation substitution is above the substitution limit observed in the single substitution case. An ideal system to study would be that of Al and Ga co-substitution, since the individual substitution is well understood, and R^3-HMQC experiment could be applied to examine the ^{31}P NMR spectra in detail.

9.4.3   Simulation of NMR spectra

Initial studies were carried out into the practicality of simulating ^{31}P and ^{43}Ca NMR spectra using the CASTEP code [8, 9]. Due to the presence of vacancies in the β-TCP unit cell, the available computing power has only recently become available for such calculations. Simulations of the β-TCP ^{31}P and ^{43}Ca NMR spectra were performed, however the results did not agree with the experimental observations for either nucleus.

It is unclear as to whether this is a fault with the structural model or the simulation process, and a great deal of work would be necessary to produce the first successful simulation of the ^{31}P and ^{43}Ca NMR spectra of β-TCP.

References

[1] R. Enderlea, F. Gotz-Neunhoeffer, M. Gobbels, F. A. Müller and P. Greil, *Biomaterials* **26**, (2005), 3379–3384.

[2] E. R. Kreidler and F. A. Hummel, *Inorganic Chemistry* **1103** (2), (1961), 524–528.

[3] R. J. B. Jakeman, A. K. Cheetham, N. J. Clayden and C. M. Dobson, *Journal of Solid State Chemistry* **78** (1), (1989), 23–34.

[4] M. Mee, *Trivalent cation substitution of β-tricalcium phosphate*, Ph.D. thesis, University of Warwick 2011.

[5] C. Mellier, F. Fayon, V. Schnitzler, P. Deniard, M. Allix, S. Quillard, D. Massiot, J.-M. Bouler, B. Bujoli and P. Janvier, *Inorganic Chemistry* **50** (17), (2011), 8252–60.

[6] I. W. Donald and B. L. Metcalfe, *Journal of Non-Crystalline Solids* **348**, (2004), 118–122.

[7] L. Obadia, P. Deniard, B. Alonso, T. Rouillon, M. Julien, D. Massiot, B. Bujoli and J.-M. Bouler, *Chemistry of Materials* **18** (7), (2006), 1425–1433.

[8] C. J. Pickard and F. Mauri, *Physical Review B* **63** (24), (2001), 1–13.

[9] M. D. Segall, P. J. D. Lindan, M. J. Probert, C. J. Pickard, P. J. Hasnip, S. J. Clark and M. C. Payne, *Journal of Physics: Condensed Matter* **2717**.

APPENDIX A

TOPAS INPUT FILES

A.1 XRD Refinement

```
'-------------------------------------------------------------
'Input File for simple Rietveld Refinement
'Use save/set current button then run with F6 in topas
'Replace $ and # symbols with text/numbers as needed
'-------------------------------------------------------------

r_wp 0 r_exp 0 r_p 0 r_wp_dash 0 r_p_dash 0 r_exp_dash 0 gof 0

'-------------------------------------------------------------
'General information about refinement here
'Remove comments as required
'-------------------------------------------------------------

iters 100000
chi2_convergence_criteria 0.001
do_errors

'-------------------------------------------------------------
'Information on datafile etc here
'Check that default weighting is appropriate for your data
'-------------------------------------------------------------
xdd DATAFILE.xy
x_calculation_step = Yobs_dx_at(Xo); convolution_step 4
bkg @ 0 0 0 0 0 0
Zero_Error(!zero,0)
Specimen_Displacement(height,0)
LP_Factor(!th2_monochromator, 27.26)
CuKa1(0.0001)
Simple_Axial_Model(axial, 0)

'-------------------------------------------------------------
'Information on structure
'Type in phase/space group/cell etc
'Comment in/out sections as needed
'-------------------------------------------------------------
str
a 10.4352
b 10.4352
c 37.4029
al 90
be 90
ga 120
volume 3527.2605
space_group "R3c"
site Ca1    x 0.7259   y 0.8618   z 0.1663    occ Ca+2 1.     beq 0.38
site Ca2    x 0.6188   y 0.8255   z -0.0332   occ Ca+2 1.     beq 0.27
site Ca3    x 0.7266   y 0.8514   z 0.0611    occ Ca+2 1.     beq 0.76
site Ca4    x 0        y 0        z -0.0851   occ Ca+2 0.43   beq 2.00
site Ca5    x 0        y 0        z 0.7336    occ Ca+2 1.     beq 0.76
```

```
site P1     x 0        y 0        z 0        occ P+5  1.    beq 0.41
site P2     x 0.6872   y 0.8606   z 0.8685   occ P+5  1.    beq 0.29
site P3     x 0.6530   y 0.8464   z 0.7668   occ P+5  1.    beq 0.14
site O1     x 0.7256   y -0.0944  z -0.0917  occ O-2  1.    beq 1.79
site O2     x 0.7674   y 0.7833   z 0.8548   occ O-2  1.    beq 1.66
site O3     x 0.7298   y 0.0088   z 0.8486   occ O-2  1.    beq 0.77
site O4     x 0.5221   y 0.7608   z 0.8627   occ O-2  1.    beq 1.25
site O5     x 0.5987   y -0.0488  z 0.7794   occ O-2  1.    beq 0.44
site O6     x 0.5738   y 0.6930   z 0.7850   occ O-2  1.    beq 1.32
site O7     x 0.0803   y 0.8990   z 0.7771   occ O-2  1.    beq 0.27
site O8     x 0.6320   y 0.8258   z 0.7268   occ O-2  1.    beq 0.84
site O9     x 0.0057   y 0.8624   z -0.0115  occ O-2  1.    beq 1.36
site O10    x 0        y 0        z 0.0421   occ O-2  1.    beq 1.06
PVII_Peak_Type(@, 0.02,@, 0.02,@, 0.02,@, 0.02,@, 0.02,@, 0.02)
```

A.2 Combined XRD and ND refinement

```
r_wp 0 r_exp 0 gof 0

#define USE_BANK3
#define USE_BANK4
#define USE_BANK5
#define USE_BANK6
#define USE_XRD

do_errors

#ifdef USE_BANK3
xdd bank3.xye
r_wp 0 r_exp 0 gof 0
start_X 1400.0 finish_X  19000.0
bkg @  0 0 0 0 0 0

local !two_theta 34.11
local !t1 = 505.556829 flight_path Sin(0.00872664626 two_theta) ;
local !t2 -0.89835
local !tauf_1  6.79610

scale_pks 1.00000
TOF_2FP_Voigt( , 43.18146,   , 334.35537)

neutron_data
x_calculation_step 1
TOF_LAM(0.0001)
extra_X_left 100

TOF_x_axis_calibration(!t0, -4.74776, , t1, , t2)

TOF_MIC(!tauf_0, 2.41035, , tauf_1, !taus_0, 0.02901, !taus_1, 0.01365,
!t_eff, 248.11862, !hhh, 0.03999, !double_pulse, 0.14658, two_theta)
scale_pks = D_spacing^4;

str
    Dummy_Peak_Type
  TOF_CS_L(!cl_size_phase1,10000.0 , t1)
  'TOF_CS_G(cg_size_phase1, 10000, t1)
  TOF_Strain_L(strain_phase1, 0.001, t1)
  TOF_Strain_G(gstrain_phase1, 0.03, t1)
    MVW( 343.899_0.000, 127.22013_0.00393281678, 100.000_0.000)
#endif

#ifdef USE_BANK4
xdd bank4.xye
r_wp  5.251 r_exp  0.626 gof  8.385
start_X 2700.0 finish_X  15700.0
bkg @ 0 0 0 0 0 0

local !flight_path 18.218
local !two_theta 61.381
local !t1 = 505.556829 flight_path Sin(0.00872664626 two_theta) ;
local !t2 -7.02201'_0.07434
local !tauf_1  9.08220'_0.07551

scale_pks 1.0
TOF_2FP_Voigt( , 36.35451,   , 348.41450)

***as above***

#endif

#ifdef USE_BANK5
xdd bank5.xye
r_wp  4.200 r_exp  0.589 gof  7.136
start_X 4000.0  finish_X  16300.0
bkg  @  0 0 0 0 0 0
```

```
local !flight_path 18.37939298152923
local !two_theta 91.4219436645507
local !t1 = 505.556829 flight_path Sin(0.00872664626 two_theta) ;
local !t2  0.25515`_0.15495
local !tauf_1  2.41665`_0.09189

scale_pks @  0.000623504093`_4.10674352e-006
TOF_2FP_Voigt( , 21.52327,  , 330.15311)

***as above***

#endif

#ifdef USE_BANK6
xdd bank6.xye
r_wp  11.074 r_exp  1.066 gof  10.386
start_X 4800.0 finish_X  16700.0
bkg @  0 0 0 0 0 0

local !flight_path 18.6381
local !two_theta 146.10
local !t1 = 505.556829 flight_path Sin(0.00872664626 two_theta);
local !t2 -5.22697
local !tauf_1 -0.04981

scale_pks @  0.000623504093`_4.10674352e-006
TOF_2FP_Voigt( , 21.52327,  , 330.15311)

***as above***

#endif


#ifdef USE_XRD
xdd xrd.xy
r_wp  10.575 r_exp  4.723 gof  2.239
x_calculation_step = Yobs_dx_at(Xo); convolution_step 4

bkg @ 0 0 0 0 0 0
LP_Factor(27.3)
CuKa1(0.0001)
   Radius(240)

Simple_Axial_Model(sam, 0)
Zero_Error(!zero,0)
Specimen_Displacement(disp, 0)

str
scale @  1.0000
r_bragg  0
PVII_Peak_Type(@, 0.02,@, 0.02,@, 0.02,@, 0.02,@, 0.02,@, 0.02)
#endif

for xdds {

for strs {

***structure***

}
}
```

A.3 Custom macros

```
macro TOF_2FP_Voigt(lc, lv, gc, gv)
{
  #m_argu lc
  #m_argu gc
  If_Prm_Eqn_Rpt(lc, lv, min .0001 max = 2 Val + 1; del = 0.05 Val + .0001; )
  If_Prm_Eqn_Rpt(gc, gv, min .0001 max = 2 Val + 1; del = 0.05 Val + .0001; )

local !l2tan = (flight_path-17) Tan(0.00872664626 two_theta);
lor_fwhm = CeV(lc, lv) D_spacing Constant(t1) .000014 / l2tan ;
  gauss_fwhm = CeV(gc, gv) D_spacing Constant(t1) .000014 / l2tan ;
}

macro Dummy_Peak_Type
{
peak_type pv pv_lor 0 pv_fwhm 0.01
}

macro TOF_MIC(tauf_0, tauf_1, taus_0, taus_1, t_eff, hhh, double_pulse, two_theta)
{
local !lam = 2 D_spacing Sin(0.00872664626 two_theta);
user_defined_convolution = X^2 Exp(-X / (tauf_0 + tauf_1 lam));
min 0
max = 10 (tauf_0 + tauf_1 lam);
local !storage = Exp( -950 /(t_eff lam^2)) hhh;
push_peak
hat=double_pulse ;
scale_top_peak = (1 - storage)/double_pulse;
bring_2nd_peak_to_top
exp_conv_const = -Ln(0.001) / (taus_0 +  taus_1 / lam^2);
scale_top_peak = storage/double_pulse;
add_pop_1st_2nd_peak
}

macro TOF_MIC(tauf_0, tauf_0v, tauf_1, tauf_1v, taus_0, taus_0v, taus_1, taus_1v,
t_eff,  t_effv, hhh, hhhv, double_pulse, double_pulsev, two_theta)
{
   #m_argu tauf_0
   #m_argu tauf_1
   #m_argu taus_0
   #m_argu taus_1
   #m_argu t_eff
   #m_argu hhh
   #m_argu double_pulse
   If_Prm_Eqn_Rpt(tauf_0, tauf_0v, min .01 max = 2 Val + 1; del = 0.05 Val + 1; )
   If_Prm_Eqn_Rpt(tauf_1, tauf_1v, min .01 max = 2 Val + 1; del = 0.05 Val + 1; )
   If_Prm_Eqn_Rpt(taus_0, taus_0v, min .01 max = 2 Val + 1; del = 0.05 Val + 1; )
   If_Prm_Eqn_Rpt(taus_1, taus_1v, min .01 max = 2 Val + 1; del = 0.05 Val + 1; )
   If_Prm_Eqn_Rpt(t_eff, t_effv, min 10.0 max = 2 Val + 1; del = 0.05 Val + 1; )
   If_Prm_Eqn_Rpt(hhh, hhhv, min .001 max = 2 Val + 1; del = 0.05 Val + 1; )
   If_Prm_Eqn_Rpt(double_pulse, double_pulsev, min .001 max = 2 Val + 1; del = 0.05 Val + 1; )
TOF_MIC(CeV(tauf_0, tauf_0v), CeV(tauf_1, tauf_1v), CeV(taus_0, taus_0v), CeV(taus_1, taus_1v),
  CeV(t_eff,  t_effv), CeV(hhh, hhhv), CeV(double_pulse, double_pulsev), two_theta)
}

macro TOF_Strain_L(c, v, t1)
{
   #m_argu c
   If_Prm_Eqn_Rpt(c, v, min 0.0001 max .1)
   lor_fwhm = Constant((t1) .1) D_spacing * CeV(c, v);
}

macro TOF_Strain_G(c, v, t1)
{
   #m_argu c
   If_Prm_Eqn_Rpt(c, v, min 0.0001 max .1)
   gauss_fwhm = Constant((t1) .1) D_spacing * CeV(c, v);
}
```

APPENDIX B

ZINC SUBSTITUTED β-TCP RIETVELD REFINEMENT RESULTS

Table B.1 Refined structure of $x = 0.033$ β-TCZP. Values without uncertainties were not refined.

Site	x	y	z	Species	Occ.	U_{iso}
Ca1	0.728 59(61)	0.858 16(122)	0.166 18(22)	Ca^{2+}	1.0	0.4130(574)
Ca2	0.622 85(66)	0.824 86(137)	−0.033 42(101)	Ca^{2+}	1.0	0.4130(574)
Ca3	0.731 40(95)	0.848 98(127)	0.063 94(36)	Ca^{2+}	1.0	0.4130(574)
Ca4	0	0	−0.081 81(145)	Ca^{2+}	0.5	†
Ca5	0	0	0.734 63(73)	Zn^{2+}	0.12	2.3719(23495)
				Ca^{2+}	0.88	
P1	0	0		P^{5+}	1.0	3.4367(8418)
P2	0.687 45(112)	0.861 23(149)	0.868 30(68)	P^{5+}	1.0	0.4429(394)
P3	0.656 87(79)	0.845 82(172)	0.765 94(69)	P^{5+}	1.0	0.4429(394)
O1	0.717 17(77)	−0.094 56(77)	−0.092 93(20)	O^{2-}	1.0	1.9503(1026)
O2	0.769 66(63)	0.782 51(57)	0.854 83(21)	O^{2-}	1.0	1.0678(420)
O3	0.727 55(57)	−0.003 81(133)	0.847 88(20)	O^{2-}	1.0	1.0678(420)
O4	0.520 64(230)	0.757 85(59)	0.861 58(25)	O^{2-}	1.0	1.0678(420)
O5	0.600 94(58)	−0.043 11(292)	0.779 20(23)	O^{2-}	1.0	1.0678(420)
O6	0.576 29(62)	0.692 51(63)	0.784 21(23)	O^{2-}	1.0	1.0678(420)
O7	0.079 83(53)	0.899 38(48)	0.775 46(23)	O^{2-}	1.0	1.0678(420)
O8	0.625 82(253)	0.820 97(306)	0.726 18(88)	O^{2-}	1.0	1.0678(420)
O9	0.014 03(266)	0.866 17(210)	−0.011 96(100)	O^{2-}	1.0	1.5573(6836)
O10	0	0	0.041 86(185)	O^{2-}	1.0	0.3745(5135)

† $U_{11} = 0.000\,00(806)$, $U_{22} = 0.000\,00(806)$, $U_{33} = 0.092\,81(5376)$, $U_{12} = 0.000\,00(403)$, $U_{13} = 0$, $U_{23} = 0$

Table B.2 Refined structure of $x = 0.067$ β-TCZP. Values without uncertainties were not refined.

Site	x	y	z	Species	Occ.	U_{iso}
Ca1	0.725 09(171)	0.858 16(61)	0.167 22(129)	Ca^{2+}	1.0	0.4777(638)
Ca2	0.618 74(182)	0.819 04(139)	−0.032 57(118)	Ca^{2+}	1.0	0.4777(638)
Ca3	0.728 33(123)	0.849 28(53)	0.066 30(75)	Ca^{2+}	1.0	0.4777(638)
Ca4	0	0	−0.083 24(161)	Ca^{2+}	0.5	†
Ca5	0	0	0.734 75(118)	Zn^{2+}	0.23	1.6562(20024)
				Ca^{2+}	0.77	
P1	0	0		P^{5+}	1.0	3.5901(14403)
P2	0.691 11(105)	0.871 20(213)	0.869 30(131)	P^{5+}	1.0	0.2236(406)
P3	0.663 46(131)	0.852 37(151)	0.766 44(128)	P^{5+}	1.0	0.2236(406)
O1	0.731 55(151)	−0.086 56(490)	−0.089 02(189)	O^{2-}	1.0	2.9385(14962)
O2	0.770 63(616)	0.785 83(279)	0.858 06(177)	O^{2-}	1.0	0.7468(408)
O3	0.722 50(543)	0.004 43(523)	0.848 46(165)	O^{2-}	1.0	0.7468(408)
O4	0.519 74(394)	0.762 95(591)	0.863 10(185)	O^{2-}	1.0	0.7468(408)
O5	0.600 17(108)	−0.045 35(514)	0.780 46(176)	O^{2-}	1.0	0.7468(408)
O6	0.577 79(532)	0.683 09(161)	0.785 75(173)	O^{2-}	1.0	0.7468(408)
O7	0.074 01(620)	0.900 34(561)	0.778 16(65)	O^{2-}	1.0	0.7468(408)
O8	0.623 38(86)	0.827 26(171)	0.731 53(93)	O^{2-}	1.0	0.7468(408)
O9	0.002 95(146)	0.853 27(84)	−0.018 46(67)	O^{2-}	1.0	3.1805(12326)
O10	0	0	0.041 90(39)	O^{2-}	1.0	1.3225(2206)

† $U_{11} = 0.000\,02(760)$, $U_{22} = 0.000\,02(760)$, $U_{33} = 0.152\,29(2738)$, $U_{12} = 0.000\,01(380)$, $U_{13} = 0$, $U_{23} = 0$

Table B.3 Refined structure of $x = 0.133$ β-TCZP. Values without uncertainties were not refined.

Site	x	y	z	Species	Occ.	U_{iso}
Ca1	0.726 22(60)	0.858 03(85)	0.171 20(53)	Ca^{2+}	1.0	0.2412(493)
Ca2	0.619 34(66)	0.824 54(95)	−0.033 80(19)	Ca^{2+}	1.0	0.2412(493)
Ca3	0.733 79(76)	0.852 99(74)	0.060 38(38)	Ca^{2+}	1.0	0.2412(493)
Ca4	0	0	−0.081 77(80)	Ca^{2+}	0.5	†
Ca5	0	0	0.735 02(43)	Zn^{2+}	0.23	0.6506(3487)
				Ca^{2+}	0.77	
P1	0	0	0	P^{5+}	1.0	1.3488(4510)
P2	0.685 98(75)	0.861 08(134)	0.873 44(29)	P^{5+}	1.0	0.4382(376)
P3	0.650 43(107)	0.863 99(112)	0.766 08(42)	P^{5+}	1.0	0.4382(376)
O1	0.740 97(176)	−0.089 03(57)	−0.091 47(58)	O^{2-}	1.0	−0.5965(2005)
O2	0.764 19(263)	0.776 34(108)	0.856 05(52)	O^{2-}	1.0	1.0864(390)
O3	0.728 33(241)	0.009 40(230)	0.846 52(54)	O^{2-}	1.0	1.0864(390)
O4	0.519 46(167)	0.760 90(106)	0.863 96(74)	O^{2-}	1.0	1.0864(390)
O5	0.599 82(70)	−0.043 42(194)	0.778 98(62)	O^{2-}	1.0	1.0864(390)
O6	0.571 12(240)	0.684 82(110)	0.784 70(60)	O^{2-}	1.0	1.0864(390)
O7	0.078 58(263)	0.904 58(250)	0.777 95(30)	O^{2-}	1.0	1.0864(390)
O8	0.627 24(155)	0.822 97(202)	0.726 50(60)	O^{2-}	1.0	1.0864(390)
O9	0.017 38(69)	0.870 81(55)	−0.005 09(47)	O^{2-}	1.0	2.6790(4706)
O10	0	0	0.043 77(29)	O^{2-}	1.0	1.4428(2144)

† $U_{11} = 0.000\,02(992)$, $U_{22} = 0.000\,02(992)$, $U_{33} = 0.083\,32(3355)$, $U_{12} = 0.000\,01(496)$, $U_{13} = 0$, $U_{23} = 0$

Table B.4 Refined structure of $x = 0.167$ β-TCZP. Values without uncertainties were not refined.

Site	x	y	z	Species	Occ.	U_{iso}
Ca1	0.725 61(120)	0.860 94(147)	0.166 01(26)	Ca^{2+}	1.0	0.4656(628)
Ca2	0.617 31(123)	0.825 44(158)	−0.030 02(71)	Ca^{2+}	1.0	0.4656(628)
Ca3	0.727 32(50)	0.845 54(114)	0.061 51(76)	Ca^{2+}	1.0	0.4656(628)
Ca4	0	0	−0.078 62(164)	Ca^{2+}	0.5	†
Ca5	0	0	0.736 11(85)	Zn^{2+}	0.58	1.5936(5491)
				Ca^{2+}	0.42	
P1	0	0	0	P^{5+}	1.0	2.8351(9068)
P2	0.683 62(129)	0.853 84(179)	0.870 56(84)	P^{5+}	1.0	0.3725(441)
P3	0.668 06(120)	0.844 44(214)	0.767 77(83)	P^{5+}	1.0	0.3725(441)
O1	0.738 36(334)	−0.092 34(85)	−0.091 71(117)	O^{2-}	1.0	1.7187(3187)
O2	0.762 95(473)	0.774 95(410)	0.856 90(43)	O^{2-}	1.0	1.3204(470)
O3	0.733 75(465)	−0.007 31(110)	0.848 68(102)	O^{2-}	1.0	1.3204(470)
O4	0.524 20(171)	0.762 71(412)	0.864 72(141)	O^{2-}	1.0	1.3204(470)
O5	0.603 20(434)	−0.034 31(112)	0.779 70(119)	O^{2-}	1.0	1.3204(470)
O6	0.577 81(412)	0.692 13(490)	0.787 75(32)	O^{2-}	1.0	1.3204(470)
O7	0.083 14(454)	0.908 94(445)	0.775 34(109)	O^{2-}	1.0	1.3204(470)
O8	0.624 60(80)	0.823 33(135)	0.731 29(55)	O^{2-}	1.0	1.3204(470)
O9	0.017 52(69)	0.863 67(58)	−0.008 49(54)	O^{2-}	1.0	2.3460(8857)
O10	0	0	0.042 83(30)	O^{2-}	1.0	1.7271(2816)

† $U_{11} = 0.239\,21(8286)$, $U_{22} = 0.239\,21(8286)$, $U_{33} = 0.079\,47(5437)$, $U_{12} = 0.119\,61(4143)$, $U_{13} = 0$, $U_{23} = 0$

Table B.5 Refined structure of $x = 0.233$ β-TCZP. Values without uncertainties were not refined.

Site	x	y	z	Species	Occ.	U_{iso}
Ca1	0.727 60(56)	0.857 86(59)	0.171 09(44)	Ca^{2+}	1.0	0.4220(409)
Ca2	0.617 20(45)	0.823 20(61)	−0.033 51(20)	Ca^{2+}	1.0	0.4220(409)
Ca3	0.732 27(66)	0.851 85(51)	0.060 33(30)	Ca^{2+}	1.0	0.4220(409)
Ca4	0	0	−0.080 18(48)	Ca^{2+}	0.5	†
Ca5	0	0	0.735 04(30)	Zn^{2+}	0.82	0.7126(1342)
				Ca^{2+}	0.18	
P1	0	0	0	P^{5+}	1.0	2.6167(3335)
P2	0.687 73(49)	0.861 83(127)	0.873 06(38)	P^{5+}	1.0	0.3713(333)
P3	0.653 81(70)	0.858 47(99)	0.764 77(33)	P^{5+}	1.0	0.3713(333)
O1	0.744 75(116)	−0.092 66(72)	−0.090 02(43)	O^{2-}	1.0	−0.9027(1671)
O2	0.760 92(160)	0.771 46(98)	0.856 82(36)	O^{2-}	1.0	0.7200(335)
O3	0.722 64(135)	0.003 11(138)	0.847 45(37)	O^{2-}	1.0	0.7200(335)
O4	0.516 77(109)	0.762 17(103)	0.865 68(53)	O^{2-}	1.0	0.7200(335)
O5	0.603 77(65)	−0.042 47(128)	0.778 96(43)	O^{2-}	1.0	0.7200(335)
O6	0.576 41(145)	0.688 24(97)	0.785 13(40)	O^{2-}	1.0	0.7200(335)
O7	0.070 45(156)	0.899 79(144)	0.776 99(28)	O^{2-}	1.0	0.7200(335)
O8	0.622 19(105)	0.820 91(139)	0.726 49(44)	O^{2-}	1.0	0.7200(335)
O9	0.015 24(59)	0.866 90(45)	−0.005 92(39)	O^{2-}	1.0	1.5866(2854)
O10	0	0	0.046 22(59)	O^{2-}	1.0	1.5030(2055)

† $U_{11} = 0.000\,20(573)$, $U_{22} = 0.000\,20(573)$, $U_{33} = 0.000\,20(1373)$, $U_{12} = 0.000\,10(287)$, $U_{13} = 0$, $U_{23} = 0$

Table B.6   Refined structure of x = 0.267 β-TCZP. Values without uncertainties were not refined.

Site	x	y	z	Species	Occ.	U_{iso}
Ca1	0.728 59(51)	0.859 74(65)	0.169 86(61)	Ca^{2+}	1.0	0.3976(444)
Ca2	0.617 22(51)	0.824 77(70)	−0.033 17(21)	Ca^{2+}	1.0	0.3976(444)
Ca3	0.735 34(60)	0.853 05(57)	0.059 41(32)	Ca^{2+}	1.0	0.3976(444)
Ca4	0	0	−0.079 42(61)	Ca^{2+}	0.5	†
Ca5	0	0	0.734 89(34)	Zn^{2+}	0.93	0.6946(1430)
				Ca^{2+}	0.07	
P1	0	0	0	P^{5+}	1.0	1.5257(3541)
P2	0.685 64(57)	0.852 23(123)	0.874 29(41)	P^{5+}	1.0	0.3263(343)
P3	0.654 60(84)	0.855 72(120)	0.765 00(35)	P^{5+}	1.0	0.3263(343)
O1	0.748 81(136)	−0.090 27(68)	−0.092 90(49)	O^{2-}	1.0	−0.6245(1892)
O2	0.756 87(211)	0.768 60(98)	0.855 44(41)	O^{2-}	1.0	0.7489(340)
O3	0.725 36(170)	0.005 48(160)	0.846 31(42)	O^{2-}	1.0	0.7489(340)
O4	0.516 14(136)	0.760 86(113)	0.865 97(60)	O^{2-}	1.0	0.7489(340)
O5	0.600 08(69)	−0.040 53(147)	0.778 18(48)	O^{2-}	1.0	0.7489(340)
O6	0.572 72(183)	0.689 35(96)	0.784 34(46)	O^{2-}	1.0	0.7489(340)
O7	0.072 60(194)	0.902 37(180)	0.776 70(39)	O^{2-}	1.0	0.7489(340)
O8	0.623 47(119)	0.821 08(160)	0.724 98(50)	O^{2-}	1.0	0.7489(340)
O9	0.013 71(57)	0.865 51(48)	−0.005 18(45)	O^{2-}	1.0	1.9990(3631)
O10	0	0	0.044 85(60)	O^{2-}	1.0	1.1557(1990)

† U_{11} = 0.000 00(685), U_{22} = 0.000 00(685), U_{33} = 0.008 29(1638), U_{12} = 0.000 00(343), U_{13} = 0, U_{23} = 0

Table B.7   Refined structure of x = 0.333 β-TCZP. Values without uncertainties were not refined.

Site	x	y	z	Species	Occ.	U_{iso}
Ca1	0.726 95(48)	0.861 89(123)	0.172 74(41)	Ca^{2+}	1.0	0.5763(463)
Ca2	0.618 50(113)	0.823 41(133)	−0.033 03(17)	Ca^{2+}	1.0	0.5763(463)
Ca3	0.733 80(58)	0.849 31(122)	0.058 91(88)	Ca^{2+}	1.0	0.5763(463)
Ca4	0	0	−0.081 35(117)	Ca^{2+}	0.32	†
				Zn^{2+}	0.18	
Ca5	0	0	0.735 17(89)	Zn^{2+}	1.0	0.4190(2529)
P1	0	0	0	P^{5+}	1.0	4.5770(9092)
P2	0.692 06(102)	0.861 96(100)	0.873 94(34)	P^{5+}	1.0	0.3295(338)
P3	0.664 51(157)	0.863 68(83)	0.762 23(95)	P^{5+}	1.0	0.3295(338)
O1	0.758 25(364)	−0.088 32(66)	−0.093 07(132)	O^{2-}	1.0	0.2650(1702)
O2	0.743 35(369)	0.771 27(69)	0.857 89(101)	O^{2-}	1.0	0.9144(347)
O3	0.720 08(368)	−0.001 26(321)	0.846 22(107)	O^{2-}	1.0	0.9144(347)
O4	0.515 42(243)	0.760 71(79)	0.868 14(131)	O^{2-}	1.0	0.9144(347)
O5	0.599 27(61)	−0.044 88(297)	0.778 68(107)	O^{2-}	1.0	0.9144(347)
O6	0.568 56(302)	0.691 95(78)	0.784 19(109)	O^{2-}	1.0	0.9144(347)
O7	0.071 34(351)	0.902 86(325)	0.777 21(30)	O^{2-}	1.0	0.9144(347)
O8	0.610 01(267)	0.813 24(371)	0.726 27(124)	O^{2-}	1.0	0.9144(347)
O9	0.016 44(52)	0.870 20(47)	−0.003 74(43)	O^{2-}	1.0	1.6162(7325)
O10	0	0	0.043 90(45)	O^{2-}	1.0	3.4634(2174)

† U_{11} = 0.000 00(1078), U_{22} = 0.000 00(1078), U_{33} = 0.000 00(2469), U_{12} = 0.000 00(539), U_{13} = 0, U_{23} = 0

Table B.8 Refined structure of $x = 0.400$ β-TCZP. Values without uncertainties were not refined.

Site	x	y	z	Species	Occ.	U_{iso}
Ca1	0.866 83(161)	0.866 83(161)	0.141 69(730)	Ca^{2+}	1.0	−2.6267(1173)
Ca2	0.777 83(134)	0.777 83(134)	−0.067 67(362)	Ca^{2+}	1.0	−2.6267(1173)
Ca3	0.859 24(172)	0.859 24(172)	0.040 72(403)	Ca^{2+}	1.0	−2.6267(1173)
Ca4	0	0	−0.092 23(412)	Ca^{2+}	0.40	†
				Zn^{2+}	0.10	
Ca5	0	0	0.680 41(403)	Zn^{2+}	1.0	20.0000(18540)
P1	0	0	0	P^{5+}	1.0	19.9722(74811)
P2	0.883 32(289)	0.883 32(289)	0.857 57(699)	P^{5+}	1.0	5.9326(2916)
P3	0.859 74(530)	0.859 74(530)	0.751 31(435)	P^{5+}	1.0	5.9326(2916)
O1	−0.126 80(151)	−0.126 80(151)	−0.148 13(427)	O^{2-}	1.0	0.3391(5334)
O2	0.831 15(328)	0.831 15(328)	0.850 50(468)	O^{2-}	1.0	0.4737(1095)
O3	−0.128 08(473)	−0.128 08(473)	0.789 17(472)	O^{2-}	1.0	0.4737(1095)
O4	0.731 35(347)	0.731 35(347)	0.847 71(358)	O^{2-}	1.0	0.4737(1095)
O5	0.034 48(559)	0.034 48(559)	0.805 52(454)	O^{2-}	1.0	0.4737(1095)
O6	0.658 77(224)	0.658 77(224)	0.745 78(411)	O^{2-}	1.0	0.4737(1095)
O7	0.986 91(8604)	0.986 91(8604)	0.691 20(712)	O^{2-}	1.0	0.4737(1095)
O8	0.755 60(521)	0.755 60(521)	0.688 72(483)	O^{2-}	1.0	0.4737(1095)
O9	0.937 48(306)	0.937 48(306)	−0.007 38(692)	O^{2-}	1.0	6.0450(25041)
O10	0	0	0.003 46(1045)	O^{2-}	1.0	−1.2911(6162)

† $U_{11} = 0.000\,00(2059)$, $U_{22} = 0.000\,00(2059)$, $U_{33} = 0.000\,00(4368)$, $U_{12} = 0.000\,00(1030)$, $U_{13} = 0$, $U_{23} = 0$
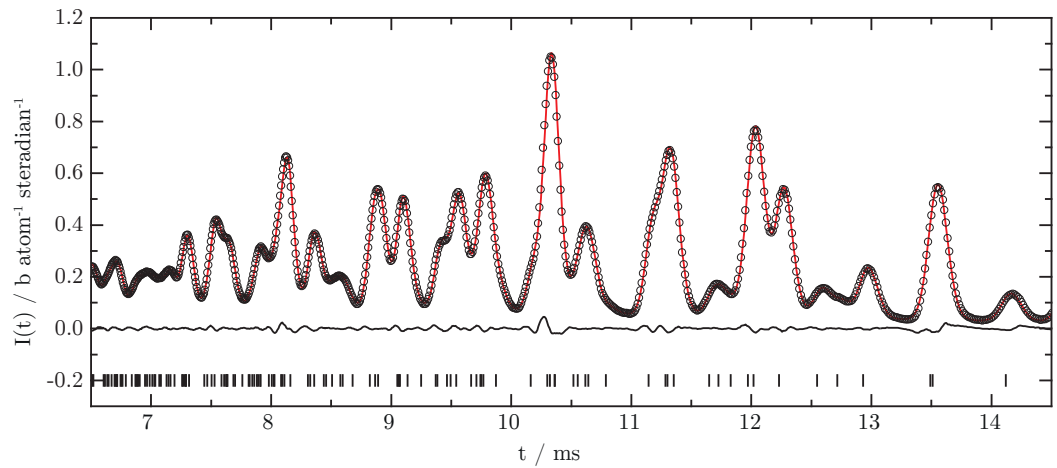
(a) ND: Bank 4
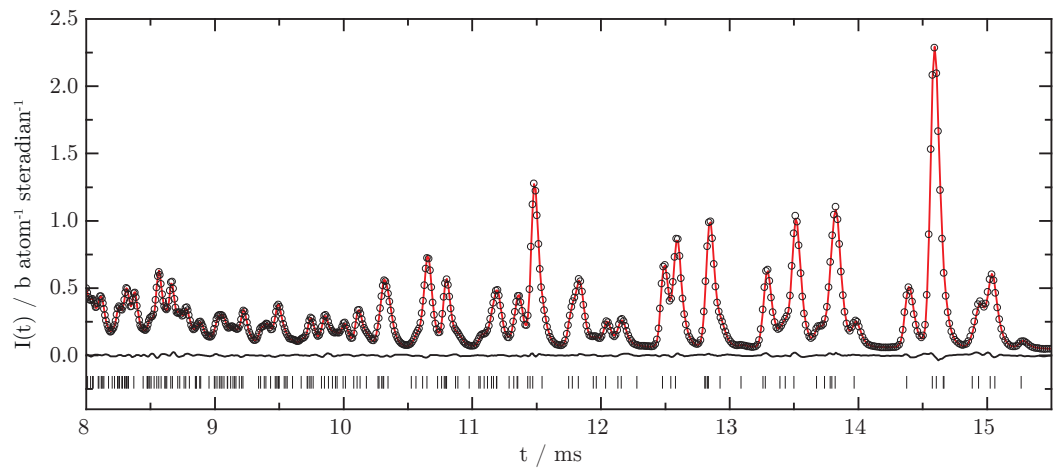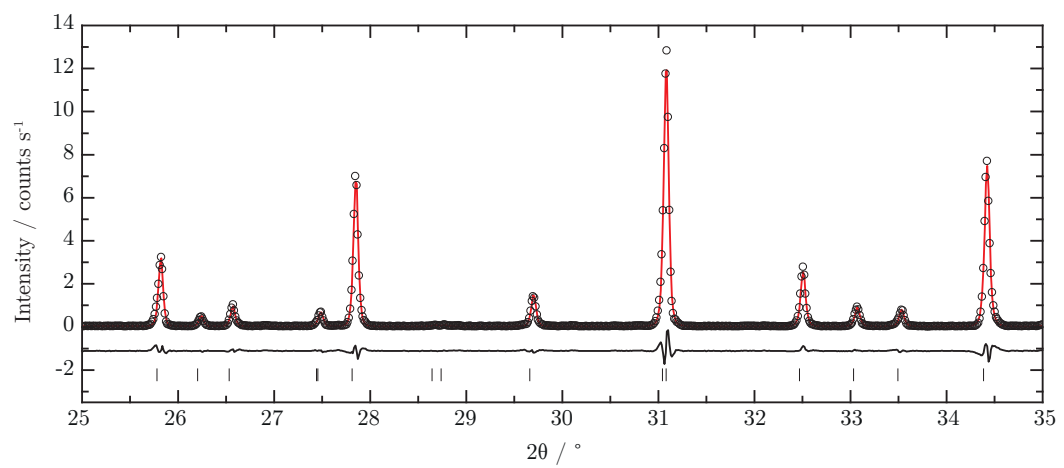
(b) ND: Bank 5

(c) XRD

Figure B.1   Rietveld refinement results from x = 0.033 β-TCZP.

A11
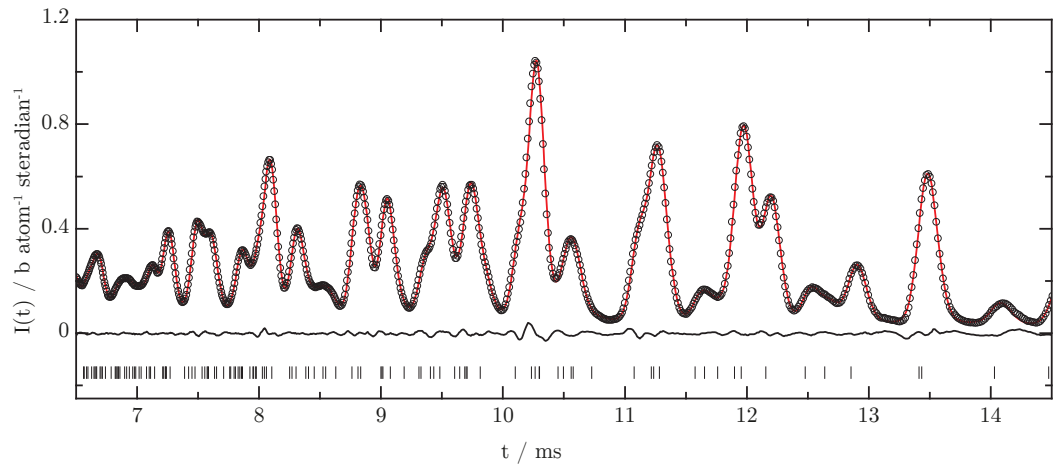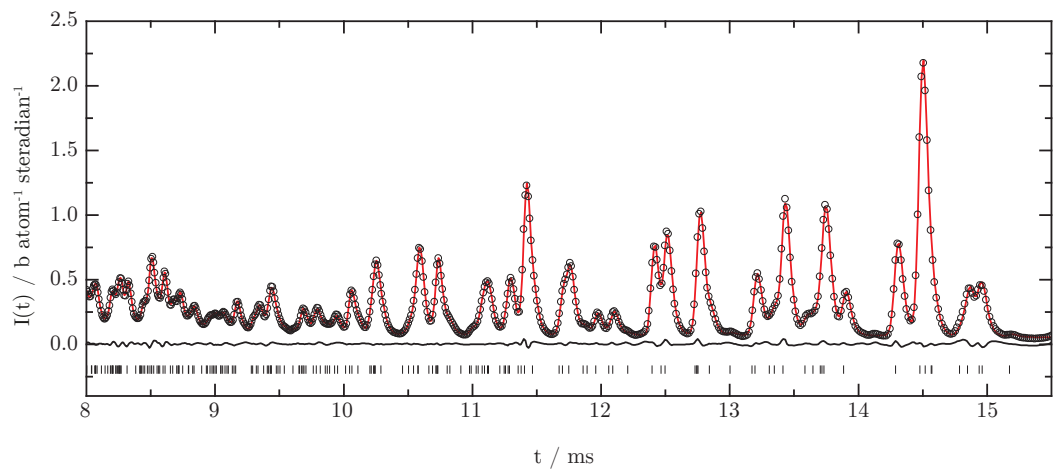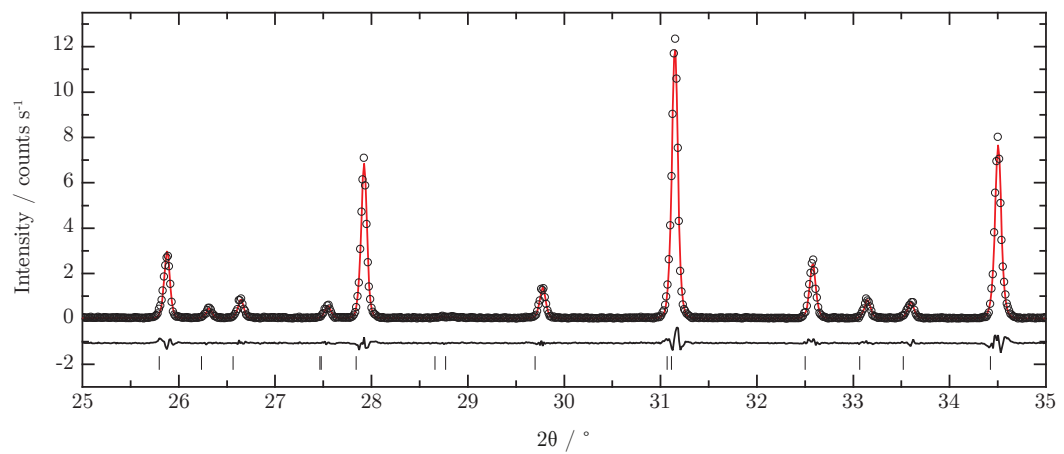
(a) ND: Bank 4

(b) ND: Bank 5

(c) XRD

Figure B.2   Rietveld refinement results from $x = 0.067$ β-TCZP.
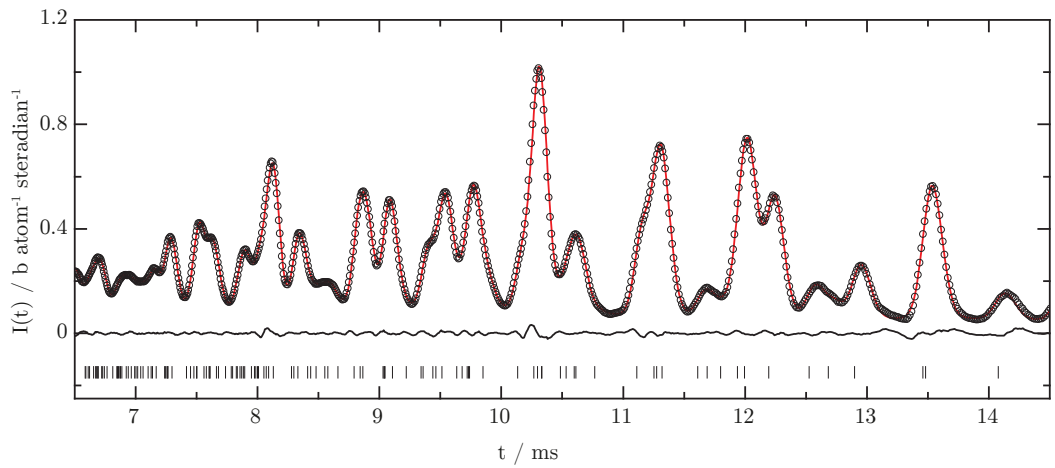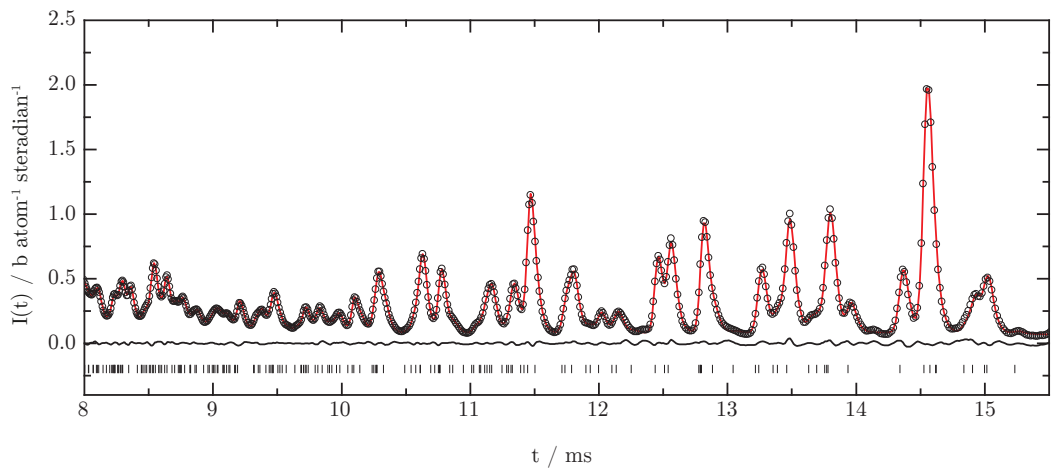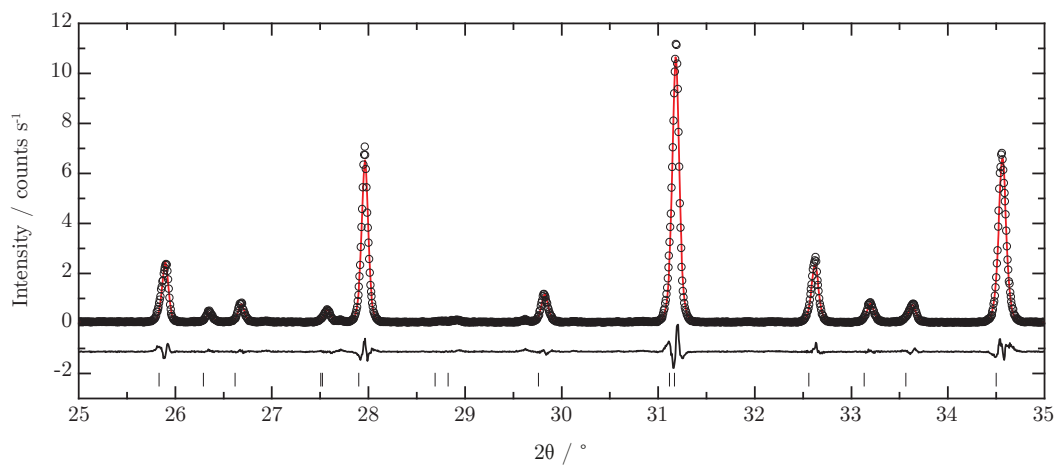
(a) ND: Bank 4

(b) ND: Bank 5

(c) XRD

Figure B.3 Rietveld refinement results from *x* = 0.133 β-TCZP.
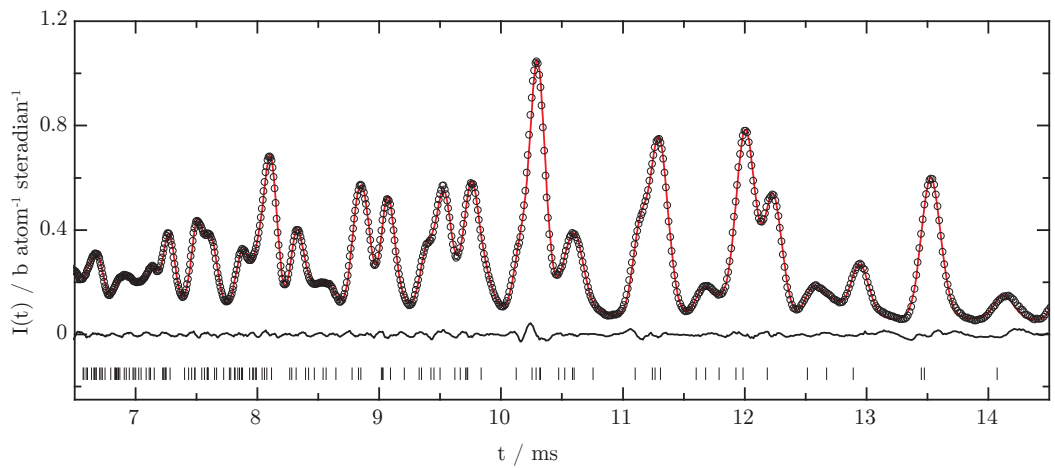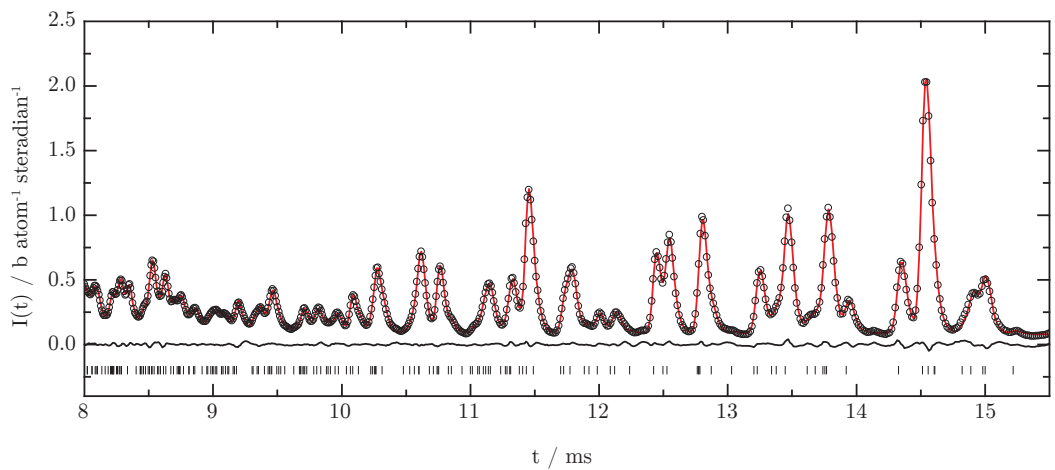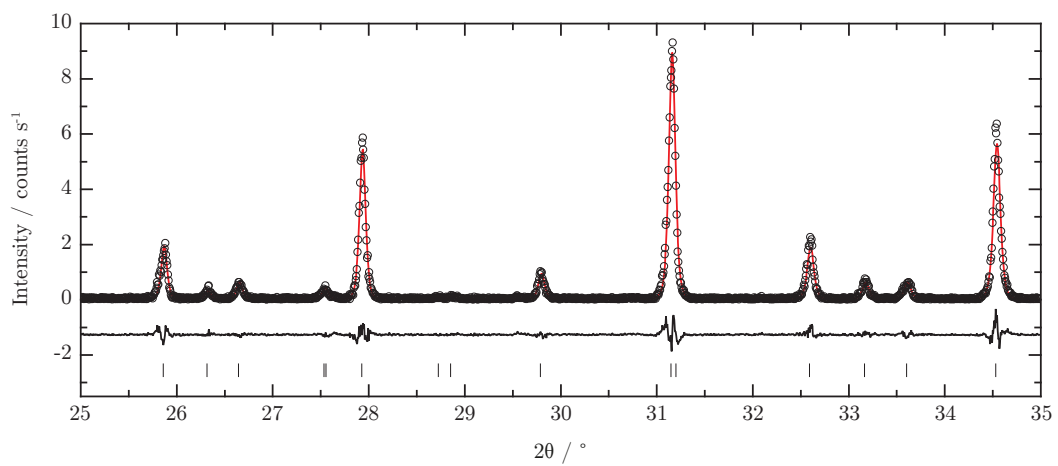
(a) ND: Bank 4

(b) ND: Bank 5

(c) XRD

Figure B.4   Rietveld refinement results from *x* = 0.167 β-TCZP.
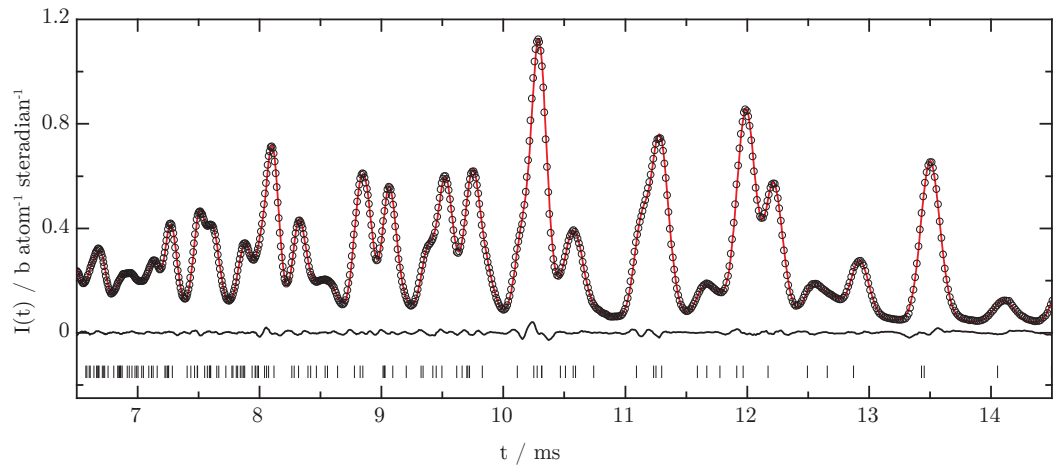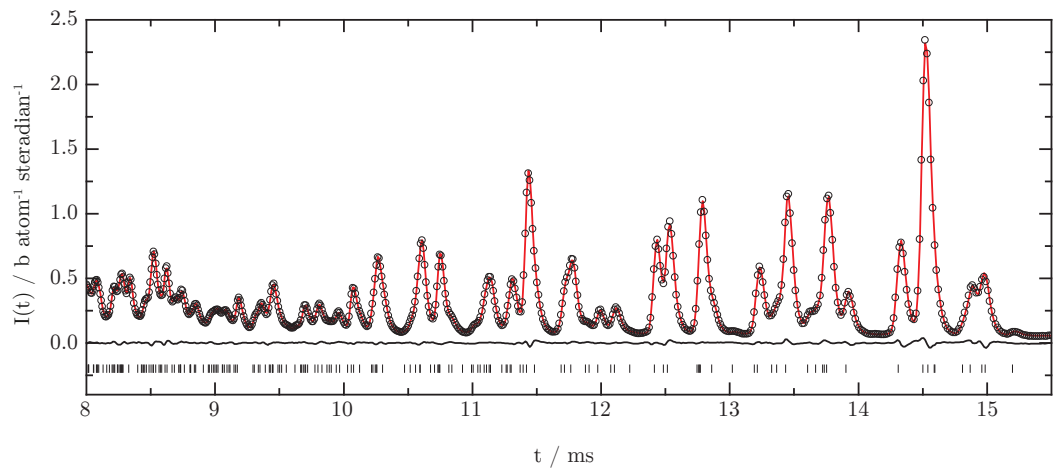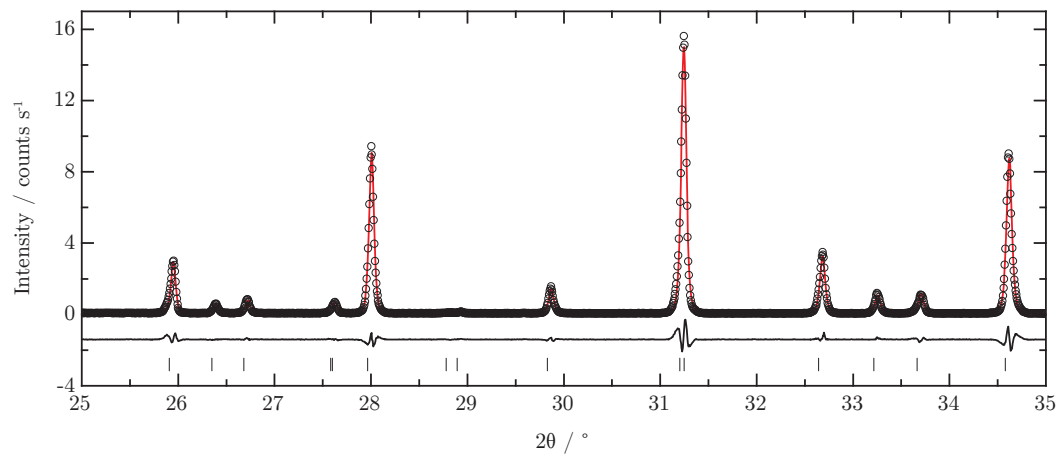
(a) ND: Bank 4

(b) ND: Bank 5

(c) XRD

Figure B.5 Rietveld refinement results from $x = 0.233$ β-TCZP.
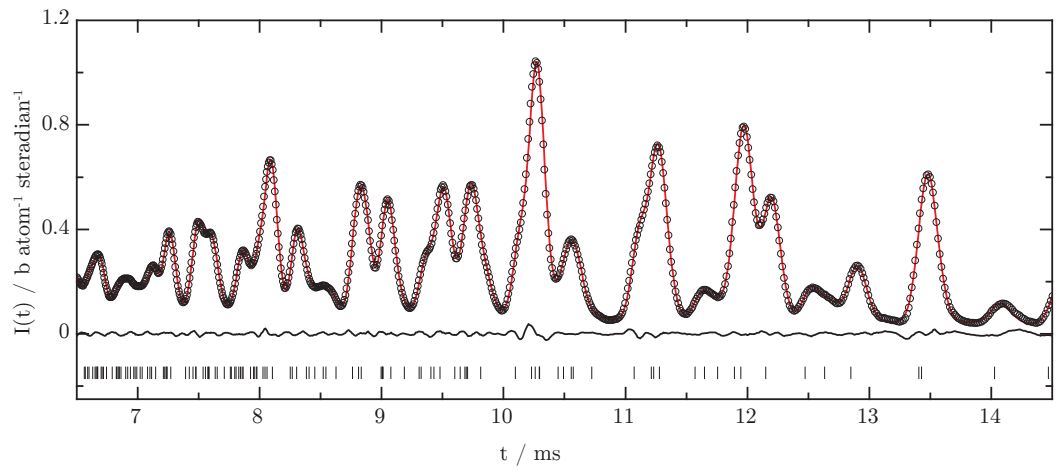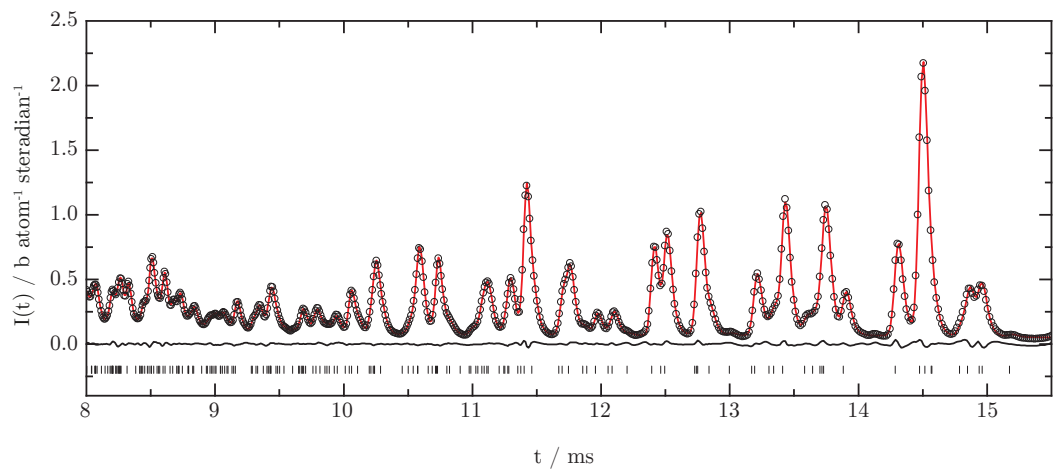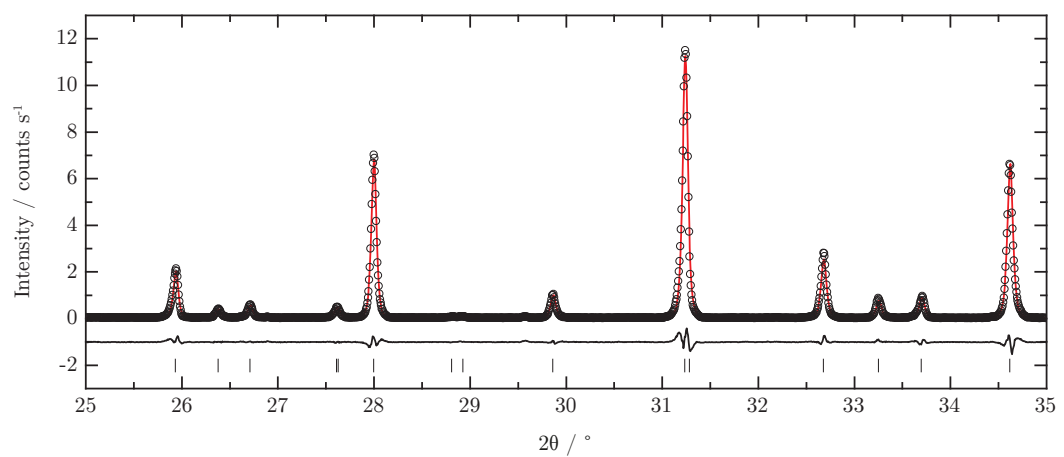
(a) ND: Bank 4

(b) ND: Bank 5

(c) XRD

Figure B.6 Rietveld refinement results from $x = 0.267$ β-TCZP.
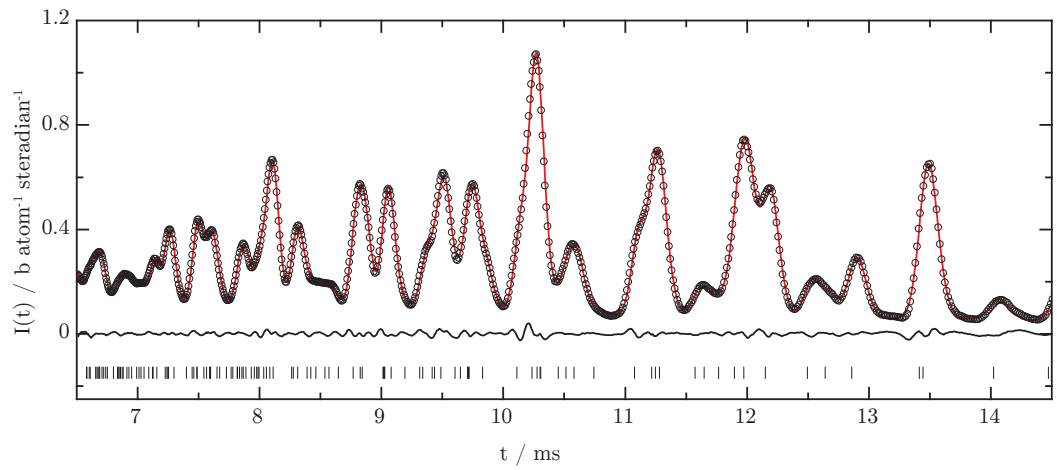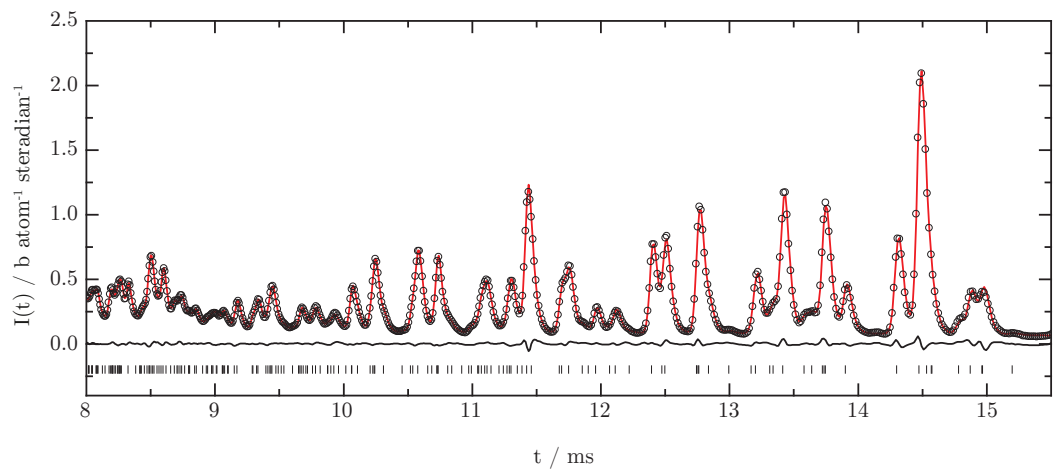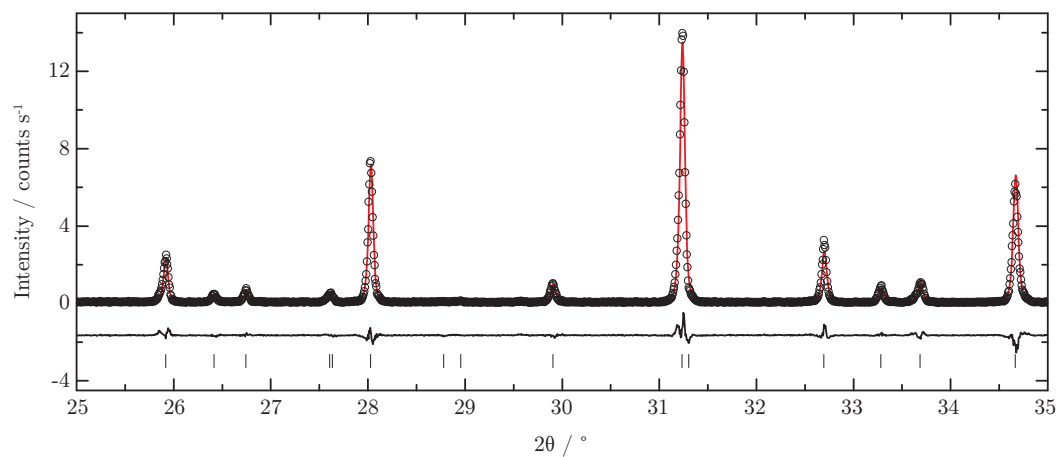
(a) ND: Bank 4

(b) ND: Bank 5

(c) XRD

Figure B.7 Rietveld refinement results from $x = 0.333$ β-TCZP.
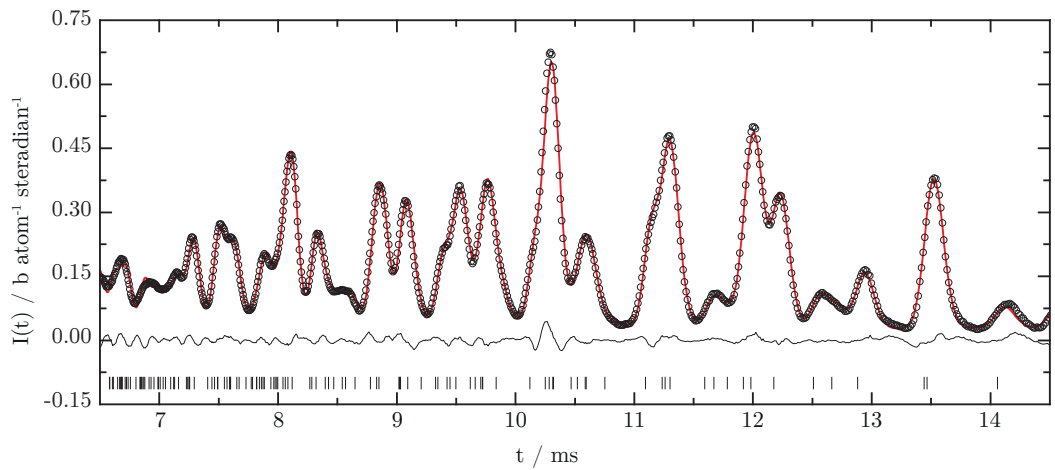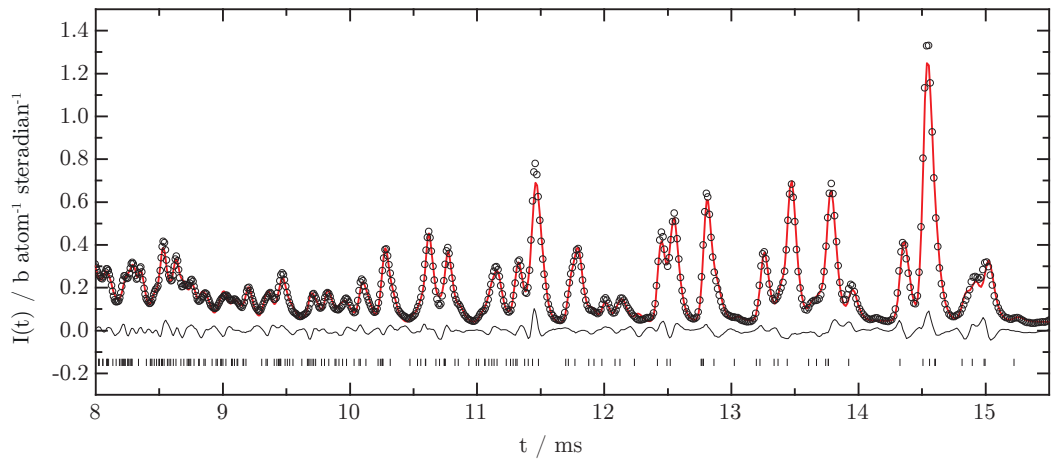
(a) ND: Bank 4

(b) ND: Bank 5
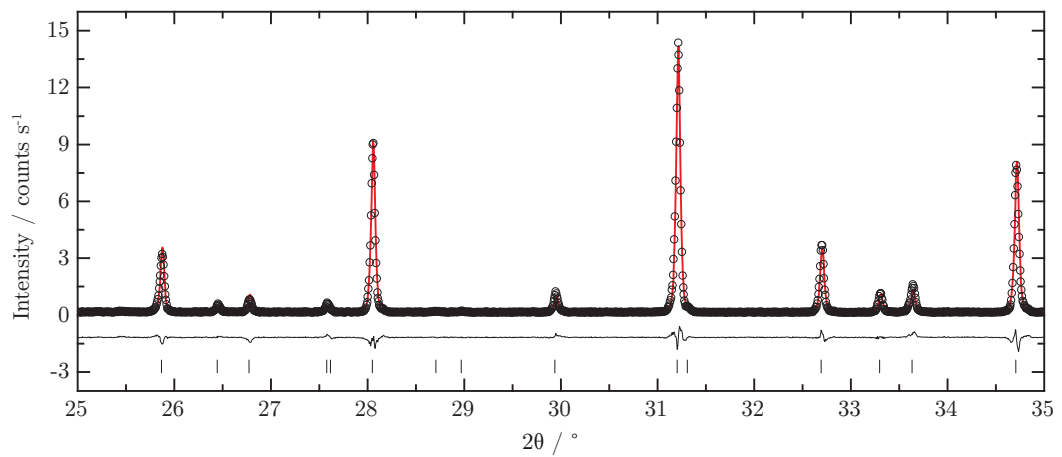
(c) XRD

Figure B.8 Rietveld refinement results from $x = 0.400$ β-TCZP.